Novel Molecular MRI Approaches to the Detection of Brain Metastasis



Niloufar Zarghami

University College

Department of Oncology

A thesis submitted to the University of Oxford in partial fulfilment of the requirements for the degree of *Doctor of Philosophy*

Trinity Term 2019

Instructions for living a life:

Pay attention.

Be astonished.

Tell about it.

- Mary Oliver, Sometimes

Acknowledgment

It is said that the purpose of education is to replace an empty mind with an open one. My mind certainly has been opened by some incredible people that I have had the pleasure to interact with over the past four years. I have many colleagues, family, and friends to thank, who deserve to be listed as co-authors of this thesis. Without them, this thesis would not have been possible, and I would like to take this opportunity to acknowledge their significant contributions to both this work and my scientific and personal development.

First and foremost, I would like to express my utmost gratitude to my D.Phil. supervisor, Prof. Nicola Sibson, for taking a chance on me four years ago. I consider myself extremely lucky to have had the opportunity to work and learn in your lab. My personal growth as a researcher has been highly influenced by your incredible mentorship. Niki - Thank you for not only your supervision, but also your friendship.

I am also grateful for the invaluable advice and guidance provided by the post-docs in the Sibson lab. To my great mentor, Manuel - Thanks for your unconditional support (even from Seville), and for giving me valuable lessons not only about science but life. To Sasha - your passion for science is contagious. Thank you for encouraging an open and flexible approach to research where curiosity always leads the way. To my chemist advisors Paco and Luca – I really appreciate your expertise and willingness to share it with me. And finally, to James – Thanks for your guidance and presence throughout this journey.

I consider myself extremely lucky to be a part of Sibson family. To mon amie Manon - I am not sure what D.Phil. would have looked like without you by my side. Thanks for being the ultimate best office neighbour, gym partner, conference and travel fellow, therapist, dance buddy and a person I am very proud to call my friend. My beloved Sarah (Saartje) – Thanks for always answering all my questions with a big smile and being the ultimate support during the last four years. Dear Christina - Thanks for always believing in me, I truly value our friendship. To my fellow Sibsonites, past and present – Anne-Marie, Axel, Claire, Helen, Jess, Kevin, Kleo, Maria, Mario, Mio, Vanessa, Vas, Vinton and Yasemin; we have had many adventures and memories that I will never forget. It has been an honour to work with you all. I would also like to acknowledge Imaging Core Group, Paul, Stu and Sean, and also RRI BMS facilitators, Karla and Magda for their assistance and support.

I have been fortunate to be a member of the University College, where I have met incredibly talented people and had unforgettable experiences. I would like to thank old members of college and GA Paul scholarship, for making all my conference travels possible. To my fellow Univites, Joanna, Naiara, Laura, Dan and Vicky - I cherish all of our memories and thanks for all the dinners and good laughs.

A special thank you to my family for their support not only during this journey, but always.
پدر و مادر عزیزم ، علیرضا و مامانی – از تمام زحماتتون متشکرم. ازینکه با وجود دوری همیشه پشتیبانم واولین مشوق من در هر زمینه ای بودید قدردانی میکنم. امیدوارم باعث افتخارتون شده باشم و بتوانم روزی این فداکاریها را جبران کنم.
Mas'oud – I am so grateful for your support, understanding, belief and unconditional love. Thank you for being a wonderful partner in this life of ours, for often carrying more than your fair share during my crazy experiments and this thesis preparation and cheering me on the whole way. I hope I have made all of you proud.
Last but not least, I appreciate the financial support that was generously given to me throughout my D.Phil. from the Cancer Research UK, and the University College Radcliffe Scholarship.

Abstract

Novel Molecular MRI Approaches to the Detection of Brain Metastasis
A thesis submitted in partial fulfillment for the requirements of the degree of
Doctor of Philosophy Trinity Term 2019
Niloufar Zarghami, University College

Secondary brain cancer (brain metastasis) is a leading cause of cancer morbidity and mortality. As treatments for primary tumours and systemic metastatic disease improve, the significance of brain metastasis as a cause of death increases. The poor survival of patients with brain metastasis is partly attributed to the unique microenvironment of the brain, includes the blood-brain barrier (BBB), which limits penetration of systemics cancer therapies and imaging contrast agents, and partly to the late stage of diagnosis. Current diagnosis relies on breakdown of the BBB, which only occurs at later stages of metastasis progression and, thus, delaying the introduction of potential treatments. To address this critical issue, development of novel molecular magnetic resonance imaging (MRI) contrast agents for the detection of brain metastasis at the early stages of formation was the overall focus of this thesis.

Inflammation is a hallmark of many neurological disorders, and expression of cell adhesion molecules on blood vessels is a key component of this process. Brain endothelial activation can readily be targeted by iron oxide particles *in vivo* and unmasked using routine MRI acquisition methods. A number of different types of iron oxide particles, MRI sequences and magnetic field strengths have been used previously for visualising this endothelial activation. Hence, in this thesis, the initial aim was to optimise each of these parameters to further improve molecular MRI in mouse brain.

Endothelial activation is also an early event in the development of brain metastasis. Two adhesion molecules, activated leukocyte cell adhesion molecule (ALCAM) and E-selectin, were assessed in brain metastasis models from three primary tumours (breast, melanoma and lung) as potential biomarkers for detection of brain micrometastases in the preclinical models. Iron oxide based microparticles against these surrogate biomarkers of brain metastases were developed, validated and applied *in vivo*.

The results of this work demonstrated that targeting both ALCAM and E-selectin can reveal brain metastases at the microscopic level, and before conventional imaging methods. The advances in our ability to detect early brain metastatic stages using molecular MRI, and the presented contrast agents in this body of work is likely to yield substantial improvements in patient survival.

Research Outcomes

Peer-reviewed Journal Articles

- **N. Zarghami**, M. Sarmiento Soto, F. Perez-Balderas, A.A. Khrapitchev, C. Simoglou Karali, V.A. Johanssen, O. Ansorge and N.R. Sibson, "Activated Leukocyte Cell Adhesion Molecule (ALCAM) as an MRI biomarker for early detection of brain metastases", *Journal of Neuro-Oncology*, Under review.

- S. Gilchrist, P. Kinchesh, **N. Zarghami**, A.A. Khrapitchev, N.R Sibson, V. Kersemans, S.C. Smart, "Improved detection of molecularly targeted iron oxide particles in mouse brain using B_0 field stabilised high resolution MRI", *Magnetic Resonance Imaging*, Under review.

- S. Melemenidis, J.C. Knight, V. Kersemans, F. Perez-Balderas, **N. Zarghami**, M. Sarmiento Soto, B. Cornelissen, R.J. Muschel and N.R. Sibson, "In vivo PET detection of lung micrometastases by targeting endothelial VCAM-1" *European Journal of Nuclear Medicine and Molecular Imaging*, Under review.

- **N. Zarghami**, A.A. Khrapitchev, F. Perez-Balderas, M. Sarmiento Soto, J.R. Larkin, L. Bau and N.R. Sibson, "Optimization of molecularly targeted MRI in the brain: empirical comparison of sequences and particles", *International Journal of Nanomedicine*, vol. 13, pp. 4345 - 4359, 2018.

Peer-reviewed Conference Abstracts and Presentations

- **N. Zarghami**, M. Sarmiento Soto, F. Perez-Balderas, A.A. Khrapitchev and N.R. Sibson, "Targeting inflammation biomarkers for brain micrometastasis detection", Brain Metastasis Research Symposium, June 2019, Vienna, Austria.

- **N. Zarghami**, M. Sarmiento Soto, A.A. Khrapitchev and N.R. Sibson, "Finding brain tumours using magnetic dyes", STEM for Britain, March 2019, Westminster, London, United Kingdom.

- **N. Zarghami**, M. Sarmiento Soto, F. Perez-Balderas, A.A. Khrapitchev and N.R. Sibson, "Targeting inflammation biomarkers for brain micrometastasis detection", European Molecular Imaging Meeting, March 2019, Glasgow, United Kingdom.

- **N. Zarghami**, M. Sarmiento Soto, F. Perez-Balderas, A.A. Khrapitchev and N.R. Sibson, "Activated leukocyte cell adhesion molecule (ALCAM) as a potential MRI biomarker for detection of brain micrometastases", 8th Annual Conference of Brain Metastases Research, September 2018, Marseille, France.

- C. Simoglou Karali, M. Munoz Pinto, V. Cheng, **N. Zarghami**, D. Beard, D.C. Anthony and N.R. Sibson "Towards TNFR1-selective permeabilisation of the blood-brain barrier", 8th Annual Conference of Brain Metastases Research, September 2018, Marseille, France.

- **N. Zarghami**, M. Sarmiento Soto and N.R. Sibson, "Activated leukocyte cell adhesion molecule (ALCAM) as a potential MRI biomarker for detection of brain micrometastases", British-Chapter ISMRM, September 2018, Oxford, UK.

- J. Buck, A.A. Khrapitchev, **N. Zarghami**, F. Perez-Balderas and N.R. Sibson, "Molecular imaging of integrin αvβ3 upregulation in a mouse model of brain metastasis", 25th European Association for Cancer Research Congress, July 2018, Amsterdam, Netherlands.

- **N. Zarghami**, M. Sarmiento Soto and N.R. Sibson, "Activated leukocyte cell adhesion molecule (ALCAM) as a potential MRI biomarker for detection of brain micrometastases", Monitoring Molecules in Neuroscience, March 2018, Oxford, United Kingdom.

- **N. Zarghami**, M. Sarmiento Soto, F. Perez-Balderas, A.A. Khrapitchev and N.R. Sibson, "Activated leukocyte cell adhesion molecule (ALCAM) as a potential MRI biomarker for detection of brain micrometastases", European Molecular Imaging Meeting, March 2018, San Sebastián, Spain.

- P. Kinchesh, S. Gilchrist, **N. Zarghami**, A.A. Khrapitchev, N.R. Sibson and S.C. Smart, "Respiratory-gated B_0 field stabilization for high resolution mouse brain imaging", European Molecular Imaging Meeting, March 2018, San Sebastián, Spain.

- **N. Zarghami**, M. Sarmiento Soto and N.R. Sibson, "Activated leukocyte cell adhesion molecule (ALCAM) as a potential MRI biomarker for detection of brain micrometastases", CRUK/MRC Oxford Institute for Radiation Oncology Symposium, September 2017, Oxford, United Kingdom

- C. Simoglou Karali, V. Cheng, **N. Zarghami**, M. Sarmiento Soto, Y. Couch, D.C. Anthony and N.R. Sibson "The impact of brain metastasis on endothelial cell function", 12th International Conference on Cerebral Vascular Biology, November 2017, Melbourne, Australia; and also presented at 20th International Symposium on Signal Transduction at the Blood-Brain Barriers, September 2017, Krakow, Poland.

- **N. Zarghami**, A.A. Khraptichev, F. Perez-Balderas, M. Sarmiento Soto and N.R. Sibson, "Comparison of USPIO and MPIO for molecular MPIO across different field strengths", International Society for Magnetic Resonance Imaging, April 2017, Honolulu, Hawaii, United States.

- A.A. Khrapitchev, R. Virgincar, JR. Larkin, **N. Zarghami**, S. Wallington, A. Gomes, S. Gilchrist, P. Kinchesh, S.C. Smart and N.R. Sibson, "Development and comparison of 19F and hyperpolarized 129Xe lung MRI for preclinical application in mice", International Society for Magnetic Resonance Imaging, April 2017, Honolulu, Hawaii, United States.

- **N. Zarghami**, A.A. Khraptichev, M. Sarmiento Soto, and N.R. Sibson, "Evaluation of bSSFP3D sequence to detect micron-sized paramagnetic iron oxide in a brain cancer model", British-Chapter ISMRM, September 2016, Leeds, United Kingdom.

List of Contents

Acknowledgment ..... **i**

Abstract ..... **iii**

Research Outcomes ..... **iv**

List of Contents ..... **vi**

List of Figures ..... **xi**

List of Tables ..... **xiv**

List of Abbreviations ..... **xv**

1 Introduction **1**

1.1 Motivation and Thesis Overview 2

1.2 Cancer 3
1.2.1 Cancer Metastasis 3

1.3 Brain Metastasis 4
1.3.1 Epidemiology of Brain Metastasis 4
1.3.2 Diagnosis of Brain Metastasis 5
1.3.3 Management of Brain Metastases 6

1.4 Metastasis Mechanism 7
1.4.1 The Process of Metastasis 8
1.4.2 Role of Blood-Brain Barrier in Brain Metastasis 11

1.5 Cell Adhesion Molecules in Brain 13
1.5.1 Cell Adhesion Molecules and Neuroinflammation 13
1.5.2 Cell Adhesion Molecules in Brain Metastasis 14
1.5.3 Activated Leukocyte Cell Adhesion Molecule (ALCAM) 15
1.5.4 E-selectin 17
1.5.5 Vascular Cell Adhesion Molecule (VCAM-1) 18

1.6 Mouse Models of Brain Metastasis 19

1.7 Cellular and Molecular Imaging 20
1.7.1 Targeted Molecular Imaging in CNS Diseases 21
1.7.2 Molecular Targeted MRI 22
1.7.3 Targeted Molecular MRI in CNS 26

1.8 Purpose of This Thesis 29
1.8.1 Specific Hypotheses 30

2 Materials and Methods **31**

2.1 Buffers 32

2.2 Injectable Agents 32
2.2.1 Antibody Conjugation to Carboxylic MPIO 32
2.2.2 Total Antibody Loading on MPIO 34

2.3 Cell Lines and Cell Culture 35
2.3.1 Brain Metastasis Cell Lines 35
2.3.2 Endothelial Cell lines 36
2.3.3 Cell Handling 36
2.3.4 Three-dimensional (3D) Cell Culture and Fluorescent Staining 37
2.4 Animal work 38
2.4.1 Animal Husbandry 38
2.4.2 Mouse Brain Metastasis Model 39
2.4.3 Mouse Neuroinflammation Model 40
2.4.4 Perfusion-Fixation and Tissue Handlings 41
2.5 Immunohistochemistry (IHC) 42
2.5.1 Mouse Tissue Preparation 42
2.5.2 Immunohistochemistry Protocol: Mouse Tissue 42
2.5.3 Immunohistochemistry Protocol: Human Tissue 43
2.5.4 Perls' Prussian Blue Staining 44
2.5.5 Immunohistochemical Analyses 45
2.5.6 Fluorescent Immunohistochemistry Protocol 45
2.5.7 Fluorescent Immunocytochemistry Protocol 46
2.6 Pre-clinical MRI 48
2.6.1 Mouse MRI Set-Up 48
2.6.2 MRI Scanners Specifications 48
2.6.3 MRI Sequences 49
2.6.4 MRI Data Processing 51
2.6.5 MRI and Histology Co-Registration 52

3 Optimisation of Molecularly Targeted MRI in the Brain: Empirical Comparison of MRI Sequences and Iron Oxide Particles 53

3.1 Introduction 54
3.2 Methods and Materials 56
3.2.1 MPIO Comparison 56
3.2.2 VCAM-MPIO Synthesis 57
3.2.3 VCAM-USPIO Synthesis Steps 57
3.2.4 Physicochemical Properties of VCAM-MPIO and VCAM-USPIO 59
3.2.5 Iron Content Per Particle and Estimation of Per Particle Properties 60
3.2.6 Assessment of VCAM Antibody Loading on MPIO and USPIO 61
3.2.7 Determination of MPIO and USPIO Relaxivity in Agarose Gel 61
3.2.8 Mouse Neuroinflammation Model 62
3.2.9 MRI of Neuroinflammation Model 62
3.2.10 Assessment of VCAM-MPIO and USPIO Binding 63
3.2.11 Image Reconstruction 63
3.2.12 Image and Data Analysis 63

3.2.13 Perls' Prussian Blue Staining Validation of Iron Oxide Particles....64
3.2.14 Blood Circulatory Half-Life: VCAM-MPIO, VCAM-USPIO and Untagged USPIO....64
3.2.15 Statistical Analyses....65
3.3 Results....65
3.3.1 MPIO Comparison....65
3.3.2 Physicochemical Properties of VCAM-MPIO and VCAM-USPIO....67
3.3.3 Comparison of MRI Sequences and Field Strengths for Detection of Iron Oxide Particles....70
3.3.4 Comparing Sensitivity and Specificity of VCAM-MPIO and VCAM-USPIO....73
3.3.5 Blood Circulatory Half-Life: VCAM-MPIO, VCAM-USPIO and Untagged USPIO....75
3.3.6 Perls' Prussian Blue Staining for Detection of Iron Oxide Particles....77
3.4 Discussion....79
3.5 Summary of Chapter 3....82
4 Activated Leukocyte Cell Adhesion Molecule (ALCAM) as an MRI Biomarker for Early Detection of Brain Metastases....83
4.1 Introduction....84
4.2 Methods....85
4.2.1 Cell Lines....85
4.2.2 ALCAM Response to Cytokines; *In Vitro*....85
4.2.3 Endothelial ALCAM Response to Proinflammatory Agents; *In Vivo*....86
4.2.4 Endothelial ALCAM Response in Presence of Tumour Cells; *In Vitro*....86
4.2.5 Mouse Brain Metastasis Models....87
4.2.6 Immunohistochemistry and Immunofluorescence; Mouse Tissue....87
4.2.7 Immunohistochemistry; Human Tissue....88
4.2.8 ALCAM-MPIO Synthesis....88
4.2.9 ALCAM-MPIO Binding Assay under Static and Flow Conditions....89
4.2.10 *In vivo* Brain Imaging....90
4.2.11 MRI and Histology Co-Registration....91
4.2.12 Statistical Analysis....91
4.3 Results....92
4.3.1 Evaluating Endothelial ALCAM Upregulation in Response to Cytokines....92
4.3.2 Endothelial ALCAM Response in Presence of TCM and Tumour Cells....97
4.3.3 ALCAM Expression in Breast, Melanoma and Lung Brain Metastasis Models....99
4.3.4 Assessment of ALCAM Expression in Human Brain metastasis Biopsies....106
4.3.5 Optimisation and Binding Assessment of ALCAM-MPIO Conjugate....108
4.3.6 *In Vivo* Detection of Micrometastases Using ALCAM-MPIO....111
4.3.7 Sensitivity Assessment of ALCAM-MPIO Imaging in Tumour Models....116
4.3.8 Growth Pattern of Melanoma Brain Metastases....118
4.4 Discussion....119
4.5 Summary of Chapter 4....123

5 Targeting E-selectin for Early Detection of Brain Metastases 124

5.1 Introduction 125

5.2 Methods 128

5.2.1 Cell Lines 128

5.2.2 E-selectin Response to Cytokines; *In Vitro* 128

5.2.3 E-selectin Response to Proinflammatory Agents; *In Vivo* 128

5.2.4 E-selectin-MPIO Synthesis 128

5.2.5 E-selectin-MPIO and Control IgG-MPIO Binding Assay; *In Vitro* 129

5.2.6 E-selectin Imaging in an Acute Neuroinflammation Model 130

5.2.7 E-selectin Expression on Endothelial Cells in the Presence of Tumours 131

5.2.8 Mouse Brain Metastasis Models 132

5.2.9 Immunohistochemistry and Immunofluorescence; Mouse Tissue 132

5.2.10 Immunohistochemical Analyses 132

5.2.11 Immunohistochemistry; Human Tissue 133

5.2.12 E-selectin Imaging in the Brain Metastasis Models 133

5.2.13 MRI and Histology Co-Registration 134

5.2.14 Dual Targeted Imaging in the Brain Metastasis Models 135

5.2.15 Statistical Analysis 135

5.3 Results 135

5.3.1 E-selectin Upregulation in Response to Cytokines; *In Vitro* and *In Vivo* 135

5.3.2 Optimisation and Binding Assessment of E-selectin-MPIO Conjugate 138

5.3.3 Binding Assessment of E-selectin Conjugate; *In Vivo* 140

5.3.4 E-selectin Expression in Breast, Melanoma and Lung Brain Metastasis Models 143

5.3.5 E-selectin Expression in Human Brain Metastasis Biopsies 147

5.3.6 *In Vivo* Detection of Micrometastases Using E-selectin-MPIO 148

5.3.7 Sensitivity Assessment of E-selectin-MPIO Imaging in Tumour Models 153

5.3.8 Targeting Dual Adhesion Molecules for Detection of Brain Micrometastases 155

5.4 Discussion 158

5.5 Summary of Chapter 5 163

6 Discussion and Future Directions 164

6.1 Optimisation of Targeted Molecular Imaging in a Mouse Neuroinflammation Model 165

6.2 ALCAM Targeted MRI 166

6.3 E-selectin Targeted MRI 168

6.4 Comparing VCAM-1, ALCAM and E-selectin for Brain Micrometastases Detection 170

6.5 Limitations and Considerations 174

6.6 Clinical Translation 174

6.7 Future Directions 176

6.8 Closing Remarks 177

Bibliography **179**

Appendices **193**

List of Figures

Figure 1.1: Brain metastasis process (i-v) from breast, melanoma and lung primary tumours. . 11

Figure 1.2: ALCAM protein expression in cancer tissues [84]. 16

Figure 1.3: Cancer cell adhesion cascade and the representative adhesion molecules in brain. 19

Figure 1.4: Iron oxide particles used for molecular MRI applications. 24

Figure 2.1: Synthesis of VCAM-/ALCAM-/E-selectin-MPIO. 33

Figure 2.2: Quantification of antibody loading on MPIO. 35

Figure 2.3: Ultrasound guided intracardiac injection of brain tropic tumour cells into the mouse left ventricle. 40

Figure 2.4: Intracerebral injection of the proinflammatory agent to the striatum. 41

Figure 2.5: Pulse diagram of T_2*W-MGE3D sequence. 49

Figure 2.6: Pulse diagram of bSSFP3D sequence. 50

Figure 2.7: Pulse diagram of SEMS2D sequence. 50

Figure 2.8: Automatic processing of iron oxide induced hypointensities. 51

Figure 2.9: Volumetric histology and MRI co-registration. 52

Figure 3.1: Multistep synthesis of VCAM-USPIO. 57

Figure 3.2: Aggregation analysis of MPIO in vitro. 66

Figure 3.3: Aggregation of carboxylic MPIO in vivo. 67

Figure 3.4: Relaxivity measurements of MPIO and USPIO in agarose gel. 68

Figure 3.5: Effect of sonication on antibody loading. 69

Figure 3.6: Representative in vivo images from mice 1 hour post VCAM-MPIO injection at different magnetic fields. 71

Figure 3.7: Representative in vivo images from mice 13 hours post VCAM-USPIO injection at different magnetic fields. 72

Figure 3.8: Quantitative comparison of MRI sequences for detection of VCAM-MPIO/-USPIO. 73

Figure 3.9: Comparison of VCAM-MPIO and VCAM-USPIO sensitivity and specificity. 75

Figure 3.10: Blood clearance half-life of VCAM-MPIO, VCAM-USPIO and USPIO generations. 76
Figure 3.11: VCAM-USPIO blood circulation in an inflammation model and naïve mouse..... 77
Figure 3.12: Perls' Prussian blue staining validation for detection of MPIO and USPIO..... 78
Figure 4.1: ALCAM imaging experimental plan in the brain metastasis models. 91
Figure 4.2: ALCAM response to cytokines on mouse and human endothelial cells. 93
Figure 4.3: ALCAM response to proinflammatory agents in vivo. 95
Figure 4.4: VCAM-1 response to proinflammatory agents in vivo. 96
Figure 4.5: ALCAM response to tumour-conditioned medium (TCM). 97
Figure 4.6: Three-dimensional culture of mouse brain endothelial cells and tumour cells. 98
Figure 4.7: ALCAM upregulation in mouse brain metastases from breast, melanoma and lung. 100
Figure 4.8: ALCAM co-localisation with three different BBB endothelial markers. 101
Figure 4.9: Classification of intratumoural and peritumoural vessels. 102
Figure 4.10: ALCAM and CD31 co-localisation in the breast cancer brain metastases model. 104
Figure 4.11: ALCAM and CD31 co-localisation in the melanoma brain metastases model.... 105
Figure 4.12: ALCAM and CD31 co-localisation in the lung brain metastases model. 106
Figure 4.13: ALCAM positive vessels in human brain metastasis biopsies..... 107
Figure 4.14: ALCAM-MPIO static binding ability in vitro. 109
Figure 4.15: ALCAM-MPIO flow binding ability in vitro. 110
Figure 4.16: Detection of brain micrometastases using ALCAM-MPIO. 112
Figure 4.17: Tumour bearing mice injected with IgG-MPIO. 113
Figure 4.18: MRI BBB permeability assessment in the brain metastasis models. 114
Figure 4.19: ALCAM-MPIO in vivo binding and detection of brain metastases. 115
Figure 4.20: Graphs indicating volume of metastases from breast, melanoma and lung that were endothelial ALCAM +/- and MRI hypointense +/-. 117
Figure 4.21: Histological comparison of two growth patterns in melanoma brain metastasis. 118

Figure 5.1: Flow chamber setup for binding assessment of E-selectin-MPIO. 130
Figure 5.2: Experimental plan for E-selectin imaging in the neuroinflammation model. 131
Figure 5.3: Experimental plan for E-selectin imaging in the brain metastasis models..... 134
Figure 5.4: E-selectin response to the inflammatory cytokines on mouse brain endothelial cells. 136
Figure 5.5: E-selectin response to proinflammatory agents in vivo. 137
Figure 5.6: E-selectin-MPIO binding ability in vitro..... 139
Figure 5.7: Temporal upregulation of E-selectin in the mouse neuroinflammation model. 140
Figure 5.8: E-selectin binding in the neuroinflammation model. 142
Figure 5.9: E-selectin expression on endothelial cells in presence of cancer cells in vitro. 143
Figure 5.10: E-selectin expression in brain metastasis models..... 146
Figure 5.11: E-selectin and CD31 co-localisation in brain metastasis models. 146
Figure 5.12: Representative E-selectin staining for human brain metastasis biopsies. 147
Figure 5.13: Detection of brain micrometastases using E-selectin-MPIO. 149
Figure 5.14: Brain metastasis tumour bearing mice injected with IgG-MPIO. 150
Figure 5.15: MRI BBB permeability assessment in the brain metastases models..... 151
Figure 5.16: E-selectin-MPIO in vivo binding and detection of brain metastases. 152
Figure 5.17: Graphs indicating volume of metastases from breast, melanoma and lung that were endothelial E-selectin +/- and MRI hypointense +/-. 154
Figure 5.18: Targeting E-selectin and VCAM-1 adhesion molecules for early detection of brain micrometastases [221]. 156
Figure 5.19: Detection of brain metastases using dual target (VCAM-/E-selectin-MPIO) MRI agent. 157
Figure 6.1: Schematic of endothelial VCAM-1, ALCAM and E-selectin upregulation in brain metastasis. 173

List of Tables

Table 2.1: List of the antibodies conjugated to MPIO. 34

Table 2.2: Immunohistochemistry antibodies. 47

Table 2.3: MRI scanners specifications. 48

Table 3.1: Summary of different commercially available MPIO. 66

Table 3.2: Physiochemical properties of MPIO and USPIO. 69

Table 5.1: Sensitivity of targeted adhesion molecule MRI contrast agents in detection of brain micrometastases. 155

Table 6.1: Expression of VCAM-1, ALCAM and E-selectin adhesion molecules on tumour-associated vessels. 170

Table 6.2: Sensitivity of cell adhesion molecules targeted MRI compounds in detection of brain metastases. 171

List of Abbreviations

3D	3-dimensional
ABC	Avidin-biotin complex
AD	Alzheimer's disease
ALCAM	Activated leukocyte cell adhesion molecule
ALCAM-MPIO	MPIO coated with multiple ALCAM antibodies
ANGPTL4	Angiopoietin-like 4
ANOVA	Analysis of variance
BALB/c	Bagg albino mouse strain
BBB	Blood-brain barrier
BEN	Bursal epithelium and neuron
bEnd-3	Mouse brain endothelial cell line derived from BALB/c
BSA	Bovine serum albumin
CAM	Cell adhesion molecule
CD	Cluster of differentiation
CLA	Cutaneous lymphocyte antigen
CNR	Contrast-to-noise ratio
CNS	Central nervous system
CT	Computed tomography
CTC	Circulating tumour cell
CTLA-4	Cytotoxic T-lymphocyte-associated protein 4
CLIO	Crosslinked iron oxide
CV	Coefficient of variation
DAB	3,3'-Diaminobenzidine
DAPI	4'-6-diamidino-2-phenylidole
dH_2O	Distilled water
DLS	Dynamic light scattering
DMEM	Dulbecco's Modified Eagle Medium
DMSO	Dimethyl sulfoxide
DTPA	Diethylenetriaminepentaacetic acid
DPX	Distyrene plasticiser xylene
E-selectin	Endothelial-selectin
E-selectin-MPIO	MPIO coated with multiple E-selectin antibodies
EAE	Experimental autoimmune encephalomyelitis
ECM	Extracellular matrix
EDC	N-(3-Dimethylaminoproyl)-N-ethylcarbodiimide hydrochloride
EDTA	Ethylenediaminetetraacetic acid
EGFR	Epidermal growth factor receptor
ELAM-1	Endothelial leukocyte adhesion molecule-1
EMT	Epithelial-mesenchymal transition
ESL	E-selectin ligand
FACS	Fluorescence-activated cell sorting
FBS	Foetal bovine serum
FSC	Forward scatter
FDA	Food and drug administration
Fe	Iron

FoV	Field-of-view
Gd	Gadolinium
GE3D	Gradient-echo 3D sequence
GFP	Green fluorescent protein
GLUT-1	Glucose transporter-1
^{1}H	Proton
H1_DL2	Human-derived brain metastasis melanoma cell line
HCELL	Haematopoietic cell E-selectin/L-selectin ligand
hCMEC/D3	Human cerebral microvascular endothelial cells, clone D3
HEPES	4-(2-hydroxyethyl) piperazine-1-ethanesulfonic acid
HD	Huntington's disease
HUVEC	Human umbilical vein endothelial cells
ICAM-1	Intercellular adhesion molecule-1
ICP-OES	Inductively couple plasma optical emission spectrometry
ID	Inner diameter
IF-γ	Interferon-gamma
IgG1	Immunoglobulin G subclass 1
Ig-SF	Immunoglobin superfamily
IHC	Immunohistochemistry
IL-1β	Interleukin-1β
iv	Intravenous
KO	Knock out
LPS	Lipopolysaccharide
MDA-MB-231-Br	Subclone of MDA231Br human metastatic breast carcinoma cell line
MEMD	Melanoma metastasis clone D
MES	2-(N-morpholino)ethanesulfoci acid
MGE3D	Multiple gradient-echo 3D
MION	Monocrystalline iron oxide nanocompounds
MPIO	Microparticles of iron oxide
mMPIO	Multimeric MPIO
MRI	Magnetic resonance imaging
MRS	Magnetic resonance spectroscopy
MS	Multiple sclerosis
NE	Number of echoes
NF-κB	Nuclear factor-κB
NK	Natural killer cells
NO	Nitric oxide
NSCLC	non-small cell lung cancer
OD	Outer diameter
PBS	Phosphate buffered saline
PBST	Phosphate buffered saline with 0.01% Tween-20
PD-1	Programmed cell death protein 1
PD	Parkinson's disease
PET	Positron emission tomography
PFA	Paraformaldehyde
pH	Power of hydrogen
PIL	Procedure Individual Licence

PLP	Periodate-lysine paraformaldehyde
PSGL	P-selectin glycoprotein ligand
PPL	Procedure Project Licence
RDG	Arginine-aspartic acid-glycine
RF	Radio frequency
rpm	Revolutions per minute
RES	Reticulo-endothelial system
SCID	Severe combined immunodeficiency
SD	Standard deviation
SEBTA-001	Human-derived brain metastasis lung adenocarcinoma cell line
sEnd-1	Mouse skin-derived endothelial cells
SEM	Standard error of the mean
SEER	Surveillance, epidemiology and end results
sLex	Sialyl Lewis x
SNMMI	Society of Nuclear Medicine and Molecular Imaging
SNR	Signal-to-noise ratio
SPECT	Single photon emission computed tomography
SPIO	Superparamagnetic particles of iron oxide
SqrtSOS	Square root of the sum of squares
SRS	Stereotactic radiosurgery
STR	Short tandem repeat
SW	Spectral width
T_1	Time constant, Mz recovers the 63% of its equilibrium value
T_2	Time constant, Mxy drops to 37% of its original magnitude
T_2*	Time constant, T_2 dependency of the inhomogeneities
TCM	Tumour-conditioned medium
TE	Echo time
TE_2	Second echo time
TFF	Tangential flow filtration
TGF-1β	Tumour growth factor-1β
TJ	Tight junction
TNB	Tris-NaCl buffer
TNF	Tumour necrosis factor
TR	Repetition time
TSA-BIO	Tyramide signal amplification–biotin
TSPO	Translocator protein
USPIO	Ultrasmall superparamagnetic iron oxide
VCAM-1	Vascular cell adhesion molecule 1
VCAM-MPIO	MPIO coated with multiple VCAM-1 antibodies
VEGF	Vascular endothelial growth factor
VLA-4	Very late antigen-4
VSOP	Very small superparamagnetic iron oxide particles
WBRT	Whole brain radiation therapy
WHO	World health organisation

CHAPTER 1

Introduction

This thesis develops and advances molecular magnetic resonance imaging (MRI) contrast agents for the non-invasive, *in vivo* detection of brain micrometastases, using mouse brain metastasis models. This introductory Chapter discusses brain metastasis, the role of adhesion molecules, and molecular MRI techniques to provide background and motivation for the research presented in this body of work.

1.1 Motivation and Thesis Overview

Brain metastasis is a complex disease, and, upon diagnosis, these tumours are generally beyond treatment intervention. Although MRI is a sensitive screening tool used for the detection of brain metastasis clinically [1], this method largely relies on contrast enhancement, which often occurs in the late stages of tumour development. Early detection of brain metastases would enable choices for appropriate treatment options and potentially improve survival in these patients. Molecular MRI is an evolving field of research, with the capacity to enable early diagnosis of diseases at the cellular and molecular levels. The overall aims of the work presented here were to optimise molecular imaging in the brain, to develop and validate new molecular MRI methodology for early detection of brain micrometastasis in preclinical models.

In this thesis, novel targeted molecular MRI contrast agents were developed to study cell adhesion molecules as imaging biomarkers, and to investigate their role in brain metastasis. Chapter 1 gives an introduction to brain metastases, the role of adhesion molecules, and basis of molecular MRI. In Chapter 2 general material and experimental methods used throughout this thesis are described. Chapter 3 compares two widely used iron oxide particles for targeted molecular imaging application, and verifies the optimal MRI sequence and magnetic field, with respect to detecting and visualising targeted MRI contrast agents. Chapter 4 examines a novel adhesion molecule, ALCAM, as an MRI surrogate for early diagnosis of brain metastasis. This work extends to Chapter 5, where the sensitivity of a second adhesion molecule, E-selectin is determined for *in vivo* detection of brain micrometastasis in preclinical models. Further, this Chapter demonstrates application of concurrent targeting of two adhesion molecules using molecular MRI. Finally, Chapter 6 summarises the conclusions and significance of this work, discusses experimental limitations and presents ideas for future work to build on the results presented in this thesis.

1.2 Cancer

Cancer is a broad term, referring to more than 277 different types of disease. It describes the group of diseases that result when cellular changes cause the uncontrolled, abnormal growth and division of normal cells. The evolution by which normal cells progressively transform to malignant ones requires sequential mutations, which result in damaging of the genome. The question of "what causes cancer" has intrigued scientists for generations. We now know that the genomic damage could be the result of endogenous processes such as hereditary genetic disorders (BRCA1 and BRCA2 in breast and ovarian cancer) or it could result from interaction with exogenous (physical or chemical) stimuli such as ionising radiation or tobacco.

Cancer is a major public health problem and is the second leading cause of death globally. Based on the World Health Organisation (WHO) report in 2018, 9.6 million people died due to cancer worldwide; this is 1 in 6 deaths due to this disease.

1.2.1 Cancer Metastasis

The term "Metastasis", a Greek word for "displacement", was first used by Joseph Récamier in 1829 to describe the spread of cancer. Metastasis is thought to be the ultimate manifestation of a neoplastic cell revolution. Despite almost 200 years of study, the process of metastasis has remained controversial. Metastasis is still the primary cause of morbidity and mortality in patients diagnosed with cancer [2]–[4]. In most patients, metastasis has occurred by the time of diagnosis and, due to inherent diagnostic limitations, it may not manifest itself clinically. In fact, cure of most cancers is mostly probable before they have spread to distant organs, at which point it is deemed to be incurable [5]. The Surveillance, Epidemiology and End Results (SEER) program revealed that the 5-year relative survival rate in female patients with localised breast cancer is 98.7%, but that this drops to merely 27% in metastatic breast cancer patients [6].

In 1889, Stephan Paget, tried to answer the question "what decides which organ suffers from disseminated cancer cells?" [7]. He suggested the "seed and soil" theory, where he proposed that the metastatic patterns do not simply follow blood flow distribution and tumour cell emboli as

suggested by Rudolf Virchow in 1858 [8]. A quote from Paget's paper says: " when a plant goes to seed, its seed are carried in all directions but they can only live and grow if they all fall on congenial soil" [7]. Now in the 21st century, Paget's theory is still the basis of ongoing research. The term "seed" is now used as, progenitor cells, cancer stem cells and metastatic cells and the "soil" is the host factor or the organ microenvironment. Despite the terminology used, the outcome of the metastatic process depends substantially on the cross-talk between metastatic cancer cells and the secondary organ microenvironment [8], [9].

1.3 Brain Metastasis

1.3.1 Epidemiology of Brain Metastasis

Brain metastasis develops following the spread of primary cancer cells to the brain. It is the most common intracranial neoplasm in adults, and its prevalence is followed by primary tumours such as high-grade glioma and medulloblastoma. Despite recent advances in the management of cancer patients, brain metastasis is an increasing challenge in modern oncology. Depending on the primary tumour, the median survival in these patients ranges from 2-27 months following diagnosis [10].

Recent epidemiologic studies have shown that the incidence of brain metastasis has increased in the last 20 years [11], [12]. The reason for such a trend is poorly studied, however, there are possible explanations. First, patients with metastatic cancer live longer owing to advances in systemic treatment strategies, which result in control of extracranial diseases [13]. A second explanation is the improvement in the quality of brain metastasis diagnosis with advances in neuroimaging [14].

It has been estimated that 9-20% of cancer patients will develop brain metastasis, however the true incidence is believed to be higher owing to underestimation of asymptomatic brain metastases or symptomatic but ignored brain metastases [15], [16]. The most common types of primary tumours to metastasise to brain are lung cancers (20-56%), followed by breast (5-20%),

melanoma (7-16%), renal and colorectal cancer [15]. Amongst these types of cancers, melanoma is the most likely to metastasise to the brain (75% based on autopsy reports) [17].

1.3.2 Diagnosis of Brain Metastasis

The clinical presentation of brain metastasis is similar to the presentation of any intracranial lesion associated with brain compression and mass effect. Depending on the number of lesions and their anatomical location, most patients experience headache followed by neurological disorders such as weakness, numbness and seizure [18]. Nevertheless, the symptoms of brain metastasis could be subtle. As a general rule, brain metastasis could be suspected in any patient with a history of known systemic cancer. These patients are referred to as “at risk” patients in this body of work. Detection of brain metastasis remains a significant limitation in the clinical setting. Brain MRI without and with intravenous administration of contrast agent is the method of choice for the detection and assessment of all brain metastases. MRI compared to contrast-enhanced CT has a superior sensitivity for lesions in the posterior fossa where bone artefacts can occur, and also for multiple punctate and leptomeningeal metastases [1], [19]. Other techniques such as proton MR spectroscopy (MRS) can additionally distinguish neoplastic and non-neoplastic brain masses, however this method is not reliable for differentiating different types of malignant tumours (brain metastasis *vs.* high-grade glioma) [1], [20].

Routinely two MRI sequences are used for the detection of brain metastasis in the clinic: (1) T_1-weighted acquisition after intravenous injection of a gadolinium-based contrast agent, which displays regions with blood-brain barrier (BBB) disruption; and (2) T_2-weighted fluid attenuated inversion recovery (T_2W-FLAIR) which highlights oedema around the tumour [20]. These sequences cannot detect brain metastases with a non-permeable BBB (no gadolinium leakage), and these lesions need to have reached a minimum 2-5 mm in diameter before they become visible on MRI [21]. The appearance of brain metastases on contrast-enhanced MRI often includes ring enhancement with prominent peritumoural oedema, and a fairly spherical, well-encapsulated shape [15]. However, these radiological features are not specific to metastasis,

and MRI cannot unequivocally differentiate metastases and primary brain tumours (gliomas) from non-neoplastic conditions (abscesses, infections, demyelinating diseases and vascular lesions) [15]. Additionally, some brain metastases can display particular imaging characteristics that can complicate radiological assessment. For example, brain metastases from melanoma can demonstrate high signal on non-contrast T_1-weighted images owing to the paramagnetic effect of melanin and the same radiological features could be found for cerebral haemorrhage [1]. In cases where imaged-based diagnosis are uncertain, histological evaluation via needle biopsy is performed. However, this method also cannot deliver a definitive diagnosis, owing to sampling errors and heterogeneity between tumours [22]. There is an urgent need therefore, to advance imaging modalities and to identify biomarkers that provide information about structural and functional changes in brain metastases at the molecular level. These molecular biomarkers not only assist with more definitive and early diagnosis of brain metastasis, but they also have the potential to be used for evaluating treatment response and enabling treatment strategies within an effective therapeutic time-window.

1.3.3 Management of Brain Metastases

Standard brain metastasis treatment often includes surgery, whole brain radiation therapy (WBRT), stereotactic radiosurgery (SRS), or a combination of these modalities. Since the 1970's, radiation therapy has remained as a mainstay treatment for brain metastasis. Historically, WBRT technique has been utilised to treat the whole brain (both tumour and normal tissues), but is associated with neurocognitive decline and even dementia for patients that survive longer [23]. Nevertheless, WBRT remains the preferred treatment option for multiple brain metastases (more than 3 brain metastases) and for prophylactic cranial radiation for primary histology (e.g. small-cell lung carcinoma) prone to development of micrometastasis [24]. Over the last 15 years, stereotactic radiosurgery (SRS) has become increasingly popular owing to lower neurotoxicity compared to WBRT. SRS delivers multiple convergent beams of high dose radiation to the tumour with a rapid fall off that minimises the risk of damage to the normal surrounding tissue.

SRS is now the treatment of choice for patients with ≤ 3 brain metastases, where the largest lesion is smaller than 4 cm in maximum diameter [25]. Surgery is preferred for patients with controlled disease and good condition, however, brain metastases > 3 cm in diameter or those causing local compression, would also benefit from this modality [26]. The initial line of treatment for brain metastases relies heavily on local therapies, as described above. The presence of an intact or partially intact BBB limits penetration of systemic chemotherapy drugs owing to their large molecular weight. Nevertheless, advances in understanding molecular pathways and the tumour microenvironment has shifted the treatment paradigm in these patients. In melanoma and non-small cell lung cancer (NSCLC) monoclonal antibodies against CTLA-4 (check point on T cells; ipilimumab) and PD-1 (check point on T cells; nivolumab, pembrolizumab) are examples of novel immunotherapy drugs where removing inhibition of the anti-tumour immune response will bolster the natural physiological response to tumours [26]. Combination of SRS with nivolumab or ipilimumab has been associated with improved efficacy and overall survival compared to SRS alone, in melanoma brain metastasis patients [27]. Based on recent advances, systemic treatment using targeted therapy is moving to the front line of management of brain metastases. Thereby, early confirmation of brain metastasis using novel techniques would provide a window-of-opportunity for early and effective intervention and personalising cancer treatment [28], [29].

1.4 Metastasis Mechanism

The process of metastasis begins long before the secondary or even primary tumours are detectable. The question of "when do cancer cells metastasise?" has been challenged many times [30], [31], with a long-held notion that metastasis is a sequential evolution of cancer cells that occurs in the later stages of tumour progression. However, with the heterogeneities observed in primary tumours, it is now believed that a subpopulation of cancer cells may evolve in parallel with progression of the primary tumours and that these leave the primary site at an early stage of primary tumour formation [32]. These cells may stay dormant long before manifesting

themselves as a metastatic burden. The highly complex, pathological metastatic cascade has resulted in the definition of the "hallmarks of metastasis" [33]. The three hallmarks of metastasis, (i) motility and invasion; (ii) modulation of microenvironment; and (iii) plasticity and colonisation, are distinctive for metastasis compared to the well-recognised "hallmarks of cancer" as described by Hanahan and Weinburg [34]. Below I discuss the metastatic process, and the interaction of tumour cells with the host microenvironment.

1.4.1 The Process of Metastasis

Metastasis is the end result of a series of dynamic and systematic events, for which all steps must be successfully completed (Figure 1.1):

(i). Dissemination and local invasion

Dissemination is the initial step of the metastatic cascade. During dissemination, cancer cells acquire the ability to leave the primary tumour location, to invade nearby tissues and to travel to distant locations. This process requires that the primary cancer cells loosen their cell-cell adhesion and gain mobility. One of the first steps in dissemination, is a change in the phenotype of migratory cells. These cells undergo a reversable transition from epithelial to mesenchymal phenotype, by losing their epithelial markers and gaining motility. The epithelial to mesenchymal transition (EMT) process is orchestrated by EMT-induced transcription factors such as SNAIL, TWIST, and ZEB1, and it was first observed in vertebrate embryonic development [35], [36]. As the result of EMT-induced transcription factors, cancer cells experience various alterations in their gene expression. For example, E-cadherin and various integrins are downregulated, which enables them to detach from neighbouring cells, remodel intracellular cytoskeletal molecules, and degrade the basal membrane in order to penetrate into the surrounding stromal matrix [37].

(ii). Intravasation

Single, or clusters of, migratory cancer cells that have successfully gained the motile ability, can actively intravasate into the surrounding vessels and reach their secondary host via the circulatory system. These cells may disseminate into blood vessels or lymphatics. Either route can lead to

venous circulation, as lymphatics drain into blood [38]. There are many pathways that regulate intravasation. This process can be facilitated by enzymes (proteases), the epidermal growth factor receptor (EGFR) family and the biophysical condition of the local microenvironment and vasculature [39].

(iii). Survival in the circulation

Once cancer cells have intravasated into blood vessels, they travel via venous and arterial circulation, and are known as circulating tumour cells (CTCs). In recent years, there has been an explosion of interest in the detection of CTCs during haematogenous transport and, thus, targeting of the metastatic process. Transit within the blood vessels is the most vulnerable time for migrating cells. There are publications showing that 1 million cancer cells per 1 gram of tumour can spread to the blood daily [40], [41]. However, it appears that only a small fraction of these cells can survive within the blood stream and, subsequently, extravasate into distant organs. The low survival rate for CTCs is primarily a result of haemodynamic turbulence (i.e. blood shear stress), immunological attack (e.g. natural killer cells) and collision with host tissue cells (e.g. endothelial cell lining) [42]. Over time, migratory cancer cells have developed strategies to overcome these hurdles. By activating mechanotransduction signalling during extravasation, CTCs are more resistant to haemodynamic stresses than normal cells [43]. The gain of immunohibitory molecules and the loss of immunostimulatory molecules are other abilities that facilitate resistance to immune cell attack [44]. For example, CTCs can associate with activated platelets, which secret protective signals and react to the main threats in blood.

(iv). Extravasation

After survival in the blood stream, tumour cells become arrested in the vessels of secondary organs and extravasate into the parenchyma of distant tissue. Since the size of CTCs is usually larger than the microvasculature, they are likely to become trapped [45]. For brain metastases, most CTCs (85%) are trapped at grey-white matter junctions, where progressive narrowing of blood vessels are located [46]. The tumour cells can promote their extravasation by secreting angiopoietin-like 4 (ANGPTL4), which permeabilises vascular structures and facilitates

extravasation [47]. Active adhesion processes between tumour cell and the endothelium is required for this process. This attachment is essential for tumour cells to transmigrate through the endothelial wall of the secondary organ and it determines the locations of secondary tumour seeding [48]. In Section 1.5, I will discuss these interactions in more detail.

(v). Micrometastasis and colonisation

Extravasated cancer cells have to survive to form micrometastases at the secondary site. The microenvironment of a secondary organ is different from the microenvironment of the primary tumour location. For example, the brain is full of interstitial fluid, which is high in chloride, and in which most epithelial cells cannot survive. As a result, the brain attracts cells with neuroepithelial origin, such as lung and melanoma [49]. For metastatic cancer cells to survive in the secondary location, they need to adapt to the new microenvironment such as stromal cells, extracellular matrix components, cytokines, chemokines, and growth factors. Even if tumour cells can survive in the secondary location, the proliferation of tumour cells and formation of macrometastases is not guaranteed. Tumour cells can be in a long-term (months or years) dormancy state (G_0 phase) and remain as small colonies. These cells are resistant to chemotherapy, as they are not actively dividing [50].

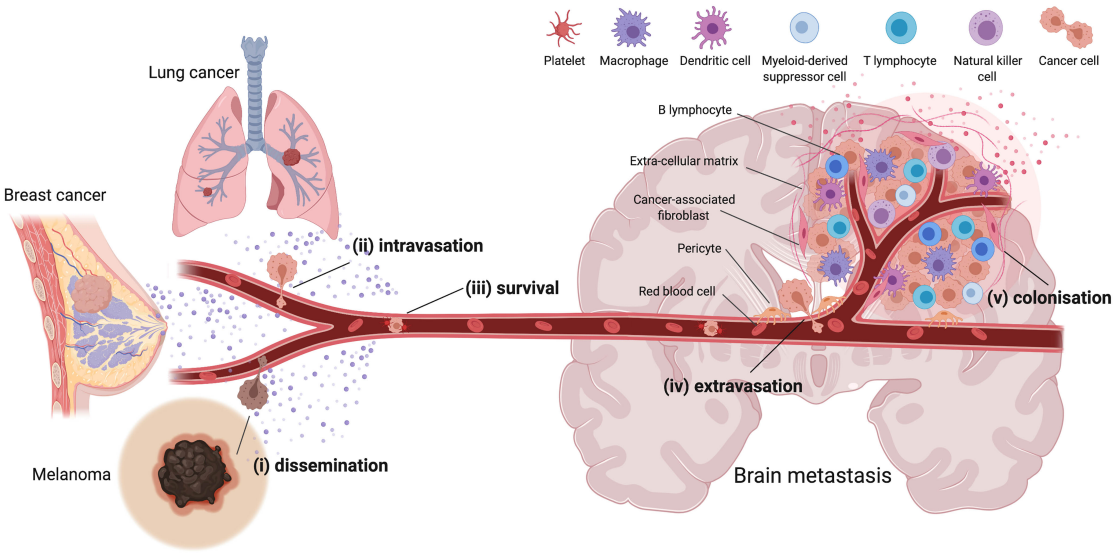


Figure 1.1: Brain metastasis process (i-v) from breast, melanoma and lung primary tumours.[*] Metastasis is a multistep process. Cancer cells leave the primary organ (breast, skin, lung) **(i)**, and then intravasate **(ii)** into the circulatory system. CTCs need to survive **(iii)** shear stress and evade clearance by the immune system to reach to the secondary organ. Cancer cells then attach to the host endothelial cells, which facilitate their extravasation **(iv)**. Tumour cells must survive in the secondary microenvironment (brain) to establish micrometastases **(v)**.

1.4.2 Role of Blood-Brain Barrier in Brain Metastasis

The blood-brain barrier (BBB) restricts traffic of solutes and cellular elements between the systemic circulation and neural tissue. The smallest molecules that can pass the BBB need to have lipophilicity and a molecular weight of less than 400-500 Da [51]. The most essential components of the BBB are a monolayer of endothelial cells, astrocytes and pericytes. In particular, the absence of fenestrations and presence of tight junctions (TJ) between endothelial cells are indispensable for the barrier role. Pericytes and the endfeet of astrocytes also play a crucial role in the properties of the BBB, as well as regulation of blood flow. Given the function of the BBB, it is surprising that CTCs are able to cross it and form brain metastases. It has been shown that the BBB can be supportive of transmigration of migratory cancer cells by secreting chemokines and cytokines favourable for metastasis [52].

[*] All illustrations of this thesis were designed by N. Zarghami using BioRender.com [221].

The process of extravasation into the brain takes longer than for other organs, and can take up to 14 days for melanoma and lung cancer cells [53], [54]. It is thought that transmigration of CTCs occurs primarily by transendothelial migration in a similar manner to leukocyte extravasation into areas of disease or injury. This process will be discussed in more detail in Section 1.5.

After the transmigration (diapedesis) step, the proximity of tumour cells to the blood-brain/tumour barrier is crucial for their survival. Proliferation of brain metastases was only observed in transmigrated brain metastatic cells in a position similar to pericytes and in close contact to endothelial cells [54]. Long-lasting proximity of metastatic tumour cells and endothelial cells provides: (i) support for growth of tumours before they form *de novo* tumour vasculature; (ii) protection from the immune system. After transmigration into the brain, breast cancer cells align along blood vessels on the extraluminal side, and melanoma cells continue their movement beneath the endothelial cell layer [52]. This pattern of growth, where tumour cells migrate along pre-existing vessels of the host organ to provide tumour blood supply is termed vessel "co-option", and has been observed in breast and melanoma primary tumour cells [54]–[56]. In contrast, lung brain metastases present early angiogenesis, a process whereby the tumour develops its own blood vessels [57]. This suggests different growth patterns of brain metastases depending on their origin.

The BBB remains intact during this micrometastatic growth stage and its integrity is only altered once larger tumours are formed. The intact BBB contributes to diagnostic and therapeutic challenges. Delivery of imaging contrast agents and systemic drugs (chemotherapy, immunotherapy, monoclonal antibody therapy) is not possible in the early stages of tumour formation. As the diagnosis of brain metastases heavily relies on the passive extravasation of the contrast agent across a disrupted BBB, an intact BBB leads to the inability of brain micrometastases detection at standard imaging resolutions. Consequently, brain metastases are usually detected at a later stage, where treatment options are limited. However, evidence is emerging to support the concept that treatment of brain metastases at microscopic stage would be most effective [58].

Nevertheless, the BBB could become transiently permeable using various strategies including physical methods (e.g. focused ultrasound and microbubble), chemical methods (aromatic substances; borneol), and nanoparticles [59]. Moreover, Connell *et.al* demonstrated that is possible to selectively permeabilise the BBB at sites of brain metastases through systemic injection of tumour necrosis factor (TNF), whilst remaining brain vasculature stays intact [60]. Upon detection of brain micrometastases, these strategies could be employed for delivering therapeutic drugs across the BBB.

1.5 Cell Adhesion Molecules in Brain

Cell adhesion molecules (CAMs) have a fundamental role in the development and maintenance of the nervous system. These transmembrane glycoproteins mediate cell-to-cell and/or cell-to-extracellular matrix (ECM) interactions, and regulate apoptosis, establishment of the BBB, inflammation, proliferation, and tumorigenesis. These adhesions are important for brain morphology and functions, including learning and memory [61]. Most CAMs belong to one of the five major classes: cadherins, immunoglobin superfamily (Ig-SF), selectins, integrins and mucins. CAMs can have homophilic (homotypic) interactions, like cadherins, or heterophilic (heterotypic) interactions, like selectins [62].

1.5.1 Cell Adhesion Molecules and Neuroinflammation

Inflammation is a physiological response to many CNS diseases, including stroke, traumatic brain injury, neurodegenerative disease and infection [63]. As described earlier in Section 1.4.2, under normal physiological conditions, cell trafficking into the CNS is limited by presence of an intact BBB. However, under pathophysiological conditions the integrity of the BBB collapses and leukocytes aggregate at the injury site, which is the key development of neuroinflammation. Upon tissue injury, immune cells release cytokines and chemokines, endothelial cells at the site of injury get activated, immune cells stop on surface of the blood vessels, transmigrate, and reach to the inflammatory foci [64]. The leukocyte adhesion cascade consists of several steps, including

tethering, rolling, firm adhesions and transmigration [64]. Different CAMs mediate each step, and the correct molecules must interact within a short period of time for a successful recruitment of leukocytes to the site of inflammation [65]. Selectins mediate tethering and rolling, integrins promote firm adhesions, and integrins together with Ig-SF facilitate transmigration of immune cells [64], [65].

1.5.2 Cell Adhesion Molecules in Brain Metastasis

CAMs also play a significant role in metastasis establishment and progression. It has been suggested that during the metastatic cascade, tumour cells use the same machinery and steps (i.e. rolling, adhesion and transmigration) as leukocyte-endothelial cell interaction during inflammation [66]. Although the mechanisms certainly differs between these two processes, the CAMs involved in contact formation on endothelial cells are potentially the same [62].

Since modulation of adhesive interactions between metastatic tumour cells and brain endothelial cells is pivotal throughout a successful metastatic process, correctly timed up and/or downregulation of CAMs is considered to be one of the major determinants of successful establishment of brain metastases. Extravasation of tumour cells, similar to leukocytes, is a multistep cascade. Soluble factors secreted by cancer cells, activate endothelial cells that favours lodging of the cells to the endothelium. Rolling of CTCs on the endothelium is mainly regulated by the selectin family [66]. During rolling, integrins are activated and permit subsequent tight junctions to form between endothelial and tumour cells. Additionally, members of the Ig-SF are expressed and help with tight binding of tumour cells [67], [68].

Evidence from liver and lung metastasis models suggests that CTCs, use CAMs on the vascular endothelium to enable extravasation from the blood [69], [70]. However, little is known of their role in brain metastasis. In 2014, Sarmiento Soto *et al.* determined the role of twelve CAMs and their ligands in early stages of breast cancer brain metastasis formation [56]. Results showed a subset of CAMs are upregulated on the cerebral endothelium at the early stages of brain metastasis seeding. From this group, activated leukocyte cell adhesion molecule (ALCAM),

E-selectin and vascular cell adhesion molecule-1 (VCAM-1) were highly upregulated on the cerebral endothelium, whilst their ligands were upregulated on metastatic tumour cells [56]. Moreover, blocking specific CAMs (e.g. VLA-4, ALCAM) reduced the number of tumours seeding to the brain. In the following Sections, I introduce these three CAMs in more detail.

1.5.3 Activated Leukocyte Cell Adhesion Molecule (ALCAM)

Activated leukocyte cell adhesion molecule (ALCAM; 110 kDa), also referred as BEN (bursal epithelium and neuron), CD166, SC1, rat KG-CAM, chicken DM-GRASP, fish neurolin, SB10, and human melanoma metastasis clone D (MEMD) in the literature, is a type I transmembrane protein and a member of the Ig-SF. ALCAM contains five extracellular Ig-like domains, two variable and three constant domains (VVC2C2C2), and mediates both homotypic (ALCAM-ALCAM) and heterotypic (ALCAM-CD6) interactions. In fact, ALCAM was first identified as a ligand for CD6 (expressed on T lymphocytes, thymocytes and a subset of B cells) [71], and the affinity of ALCAM-ALCAM interactions is two orders of magnitude weaker than ALCAM-CD6 interactions [72]. ALCAM has been found to play a role in development of the central and peripheral nervous system, sensory organs, haematopoiesis and endothelial/epithelial lineage [73]. With respect to cellular expression, ALCAM has been shown to specifically localise at the intercellular junctions between endothelial cells, and also has a role in the machinery of diapedesis and extravasation of T cells [74].

ALCAM has been implicated as a marker for cancer metastasis in a wide range of malignancies, including cutaneous melanoma [75], pancreatic cancer [76], breast cancer [77], [78], and colorectal carcinoma [79], amongst others (for review see ref. [80], [81] and Figure 1.2). As a membrane protein expressed on a wide range of tumours, ALCAM targeted treatment strategies have been developed. For instance, liposomal nanocarriers containing a cytotoxic payload targeting ALCAM has been shown to selectively and effectively eradicate three different subtypes of prostate cancer cells *in vitro* [82], whilst single-chain antibodies targeting ALCAM were able to inhibit growth of breast cancer cells both *in vitro* and *in vivo* [83]. ALCAM

upregulation on cancer cells mostly represents poor prognosis and dismal outcome in patients, however, its contribution to metastasis is still unclear. All of these data support the presence of ALCAM on tumour cells and its role in tumour cell-tumour cell adhesion.

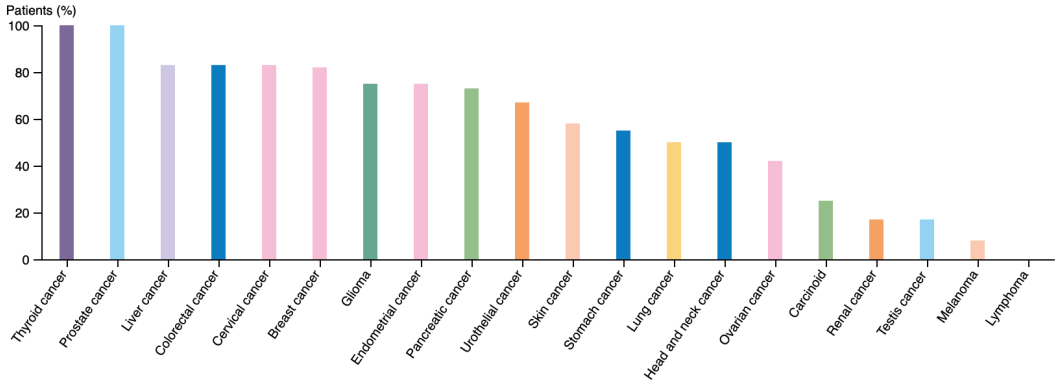


Figure 1.2: ALCAM protein expression in cancer tissues [84].[†]

Until recently, little was known of the role of ALCAM within the brain. However, very recently, the presence of ALCAM on endothelial cells during leukocyte trafficking in response to neuroinflammatory diseases such as multiple sclerosis (MS) has been demonstrated [85]–[87]. ALCAM has also been suggested to play a role in the integrity of the BBB; ALCAM knockout (KO) mice developed severe experimental autoimmune encephalomyelitis (EAE) owing to increased permeability of the BBB [87]. Further, previous results from our lab have shown the presence of ALCAM on tumour-associated vessels in breast cancer brain metastasis models [56]. Expression of ALCAM on the cerebral vasculature in response to inflammatory stimuli, and in particular the presence of brain metastasis, demonstrates it has the potential to be employed as a biomarker for detection or even treatment of inflammatory diseases and brain micrometastasis, and this premise forms the basis of Chapter 4 of this thesis.

[†] Courtesy of Human protein Atlas: v18.proteinatlas.org/ENSG00000170017-ALCAM/pathology.

1.5.4 E-selectin

Selectins represent a family of three type 1 membrane adhesion molecules: E-selectin (CD62E), P-selectin (CD62P) and L-selectin (CD62L). The term selectin highlights the presence of a lectin domain for all these molecules. E-selectin (previously referred to as endothelial leukocyte adhesion molecule-1 (ELAM-1)) is composed of an N-terminal, a C-type lectin domain, an EGF-like domain and a complement regulatory protein homology domain consisting of six consensus repeats [88]. The relative molecular weight of E-selectin ranges from 100 to 115 kDa for different glycosylated forms. E-selectin binds to α(2,3)sialyated and α(1,3)fucosyalted carbohydrates such as sialyl Lewis x (sLe^x) and sialyl Lewis a (sLe^a). Three principle E-selectin ligands have been found for human cells: (i) cutaneous lymphocyte antigen (CLA) (ii) hematopoietic cell E-selectin/L-selectin ligand (HCELL) and (3) CD43E, which are heavily sLe^x-decorated glycoforms of P-selectin glycoprotein ligand-1 (PSGL-1; CD162), CD44, and CD43, respectively [89].

E-selectin is restrictively expressed on the endothelial cells by *de novo* synthesis, triggered by inflammatory cytokines such as TNF, interleukin-1β (IL-1β), interferon-gamma (IF-γ), and lipopolysaccharide (LPS). The expression of E-selectin is temporally and spatially limited. Under shear-cytokine activation, naïve human endothelial cells showed peak activation for 8-12 hours, followed by a rapid downregulation of this marker [90]. Upregulation of E-selectin mediates slow and steady initial attachment (tethering) and subsequent rolling of the leukocyte on the surface of the inflamed endothelial cells, followed by firm adhesion, and eventually transmigration of monocytes, neutrophils and T cells to the inflammatory foci. E-selectin upregulation has been reported in acute and chronic inflammatory diseases [91]. It is perhaps not surprising, therefore, that E-selectin Velcro-like interactions under hydrodynamic shears stress plays an integral role in the metastatic process and homing of tumour cells. A role for E-selectin as a mediator of metastasis has been suggested from studies of breast, pancreatic and head and neck cancer cells *in vitro* [92]. Based on E-selectin expression in proximity to inflammation, infection, and cancer sites, this marker has raised interest as a target for several therapeutic and medical imaging

applications. Little is known about the function of E-selectin in brain metastases [56], [93], therefore, in Chapter 5 of this thesis, the role of this CAM is studied in mouse brain metastasis models.

1.5.5 Vascular Cell Adhesion Molecule (VCAM-1)

Vascular cell adhesion molecule-1 (VCAM-1, CD106; 90-110 kDa) is another transmembrane glycoprotein, and a member of the Ig-SF that plays an important role in vascular inflammation. Structurally, human VCAM-1 contains an extracellular domain with six or seven Ig-like domains, a transmembrane domain and a cytoplasmic domain [94]. VCAM-1 is not constitutively expressed and its upregulation is predominantly on the luminal surface of endothelial cells in response to the proinflammatory cytokines via NF-κB pathway [95]. It is a ligand for VLA-4 (also known as $\alpha_4\beta_1$ integrin) and binds weakly to $\alpha_4\beta_7$ integrin. Amongst adhesion molecules, VCAM-1 is a major regulator for firm adhesion and transmigration of leukocytes through interaction with VLA-4 integrin [94]. VCAM-1 is also involved in transmigration of monocytes and eosinophils. Its upregulation has been found in many inflammatory and immunological diseases such as rheumatoid arthritis, asthma, transplant rejection, and cancer [96]. Unlike the other two CAMs mentioned above (ALCAM and E-selectin), the contribution of VCAM-1 to metastasis, particularly brain metastasis, has been extensively explored [97]–[99]. Serres *et al.* [97] and Cheng *et al*. [98] demonstrated expression of VCAM-1 on the cerebral vasculature in the vicinity of brain metastases from breast, melanoma and lung in both preclinical models and human brain metastasis biopsies. Brain metastatic cells have also been shown to express significant amounts of VLA-4 on their surface, which suggests a role for VCAM-1/VLA-4 interactions in brain metastasis seeding [56]. Figure 1.3 shows the process of adhesion and transmigration of a cancer cell into the brain.

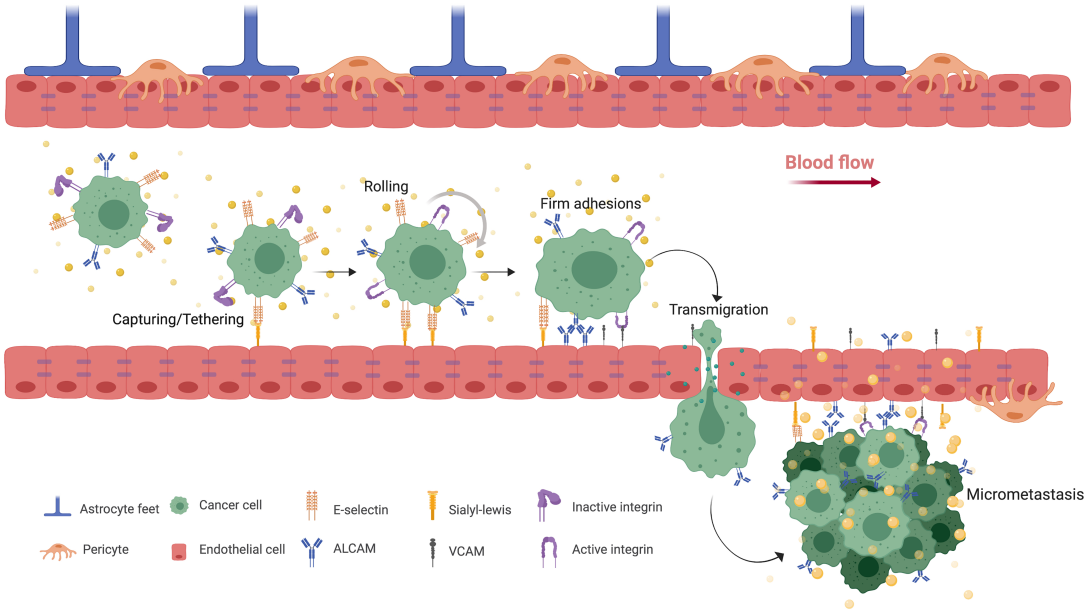


Figure 1.3: Cancer cell adhesion cascade and the representative adhesion molecules in brain. The cancer cell adhesion cascade is a multistep process that includes tethering, rolling, firm adhesions and transmigration steps. Different cell adhesion molecules are in involved in different phases by supporting cancer cell to cross the BBB. To achieve improved clarity the figure is limited to the adhesion molecules (ALCAM, E-selectin and VCAM-1) and their ligands introduced in Section 1.5**.**

1.6 Mouse Models of Brain Metastasis

The use of preclinical models to study brain metastasis is a powerful tool to investigate the intricacies of the metastatic process as seen in humans. These models provide insight into various stages of brain metastasis formation that is not possible in the clinic. In this thesis, patient-derived xenograft models, where human brain metastasis cancer cells were administrated into immune-compromised mice, were used. Although this approach lacks an efficient immune response, it allows for direct brain metastasis modeling that is applicable to human brain metastasis development.

To investigate the brain metastasis process, from extravasation to colonisation, cancer cells are commonly injected through the blood circulation. Two routes, intracardiac and intracarotid, allow cells to freely enter the circulation and disseminate to the brain [100]. To achieve brain specific cell lines, successive rounds of *in vivo* selections have been performed. Tumour cells from the

primary organ were injected into the circulation, and only a subset of tumour cells that were able to grow in the brain were collected and reinjected through the blood circulation again. After several rounds of selection, the result is an aggressive brain tropic subpopulation of metastatic cancer cells. For instance, to obtain the brain-seeking breast cancer brain metastasis cell line (MDA-MB-231-Br), cells were passaged six times *in vivo* and in culture [101]. This thesis employs intracardiac injections of MDA-MB-231-Br (human-derived breast cancer brain metastasis), H1_DL2 (human-derived melanoma brain metastasis), and SEBTA-001 (human-derived lung brain metastasis) cell lines to initiate experimental models of brain metastasis.

1.7 Cellular and Molecular Imaging

In 2007 the Society of Nuclear Medicine and Molecular Imaging (SNMMI) recommended the following definition for cellular and molecular imaging: "Molecular imaging is the visualisation, characterisation, and measurement of biological processes at the molecular and cellular levels in humans and other living systems. Molecular imaging typically consists of 2- or 3-dimensional imaging as well as quantification over time. The techniques used include radiotracer imaging/nuclear medicine, MR imaging, MR spectroscopy, optical imaging, ultrasound, and others" [102]. Molecular imaging is a multidisciplinary research field, which uses an arsenal of innovative methods spanning the fields of physics, chemistry, biology, biochemistry and others. One aim of molecular imaging is to develop probes to molecules that are upregulated early in disease progression. *In vivo* molecular imaging is analogous to immunohistochemistry or *in situ* hybridisation. The molecular imaging agent (imaging probe, tracer, contrast agent, radiolabelled probe) is key to molecular imaging studies and is typically composed of a high affinity component that interacts with the biological target, and a signaling component that is detected with the relevant imaging modality. With advances in the field of molecular imaging, there is a great potential to image molecular changes related to the pre-symptomatic state; this will allow earlier intervention and will potentially alter outcome significantly.

1.7.1 Targeted Molecular Imaging in CNS Diseases

Of all imaging modalities, molecular imaging has the strongest tie to nuclear medicine. Both PET (positron emission tomography) and SPECT (single-photon emission computed tomography) use tracers tagged with radioisotopes to image biomarkers. Both techniques are based on measurement of the radionuclide's decay, during which a positron or γ-ray will be emitted and captured by detectors, thus an image is generated. Neurological disorders such as Parkinson's disease (PD) targeting microglial activation (e.g. [11C]- PK1195 tracer) [103], Alzheimer's disease (AD) targeting amyloids (e.g. [18F]-FDDNP tracer) [104] and neuroinflammation targeting glial activation, translocator protein (TSPO) [105] have been studied extensively with such methods. These modalities have many advantages, such as high sensitivity and quantitative capabilities. However, these advantages are countered by the radiation risk, low spatial resolution and high cost [106]. In contrast, ultrasound is a non-invasive, portable, relatively inexpensive device. Contrast can be achieved using probes that increase acoustic reflection, thereby producing a detectable signal. Microbubbles (1-4 μm) are commonly used as ultrasound contrast agents. To date, the majority of studies have targeted VEGFR2 (receptor for vascular endothelial growth factor), followed by VCAM-1 and P-selectin markers. Targeted microbubbles have been used in atherosclerosis and inflammatory bowel disease models, however, their application for molecular neuroimaging is limited [107]. For optical molecular imaging, biomolecule dye conjugates or fluorescent nanoparticles, such as quantum dots are used for tumour detection and image guidance in surgery [108]. However, for *in vivo* diagnosis, this method suffers from low spatial resolution and attenuation by overlaying tissues. The final imaging modality that is extensively used in molecular neuroimaging is MRI. All of the molecular imaging modalities mentioned above own distinctive individual advantages, as well as limitations which need to be considered within the aim of molecular imaging studies. In the next section I will introduce molecular MRI in more detail.

1.7.2 Molecular Targeted MRI

Currently, MRI is an attractive modality for molecular imaging, owing to its non-invasive nature (no radiation exposure), reasonable signal-to-noise ratio (SNR), acceptable spatial resolution (up to ~ 50 μm isotropic resolution for preclinical high-field MRI), outstanding tissue contrast, unlimited depth penetration and acceptable imaging time. Molecular MRI yields information at the molecular and cellular level, thus extends our knowledge beyond the anatomical and physiological information obtained with conventional imaging. However, molecular MRI is sensitive primarily for the detection of receptors with high expression levels (higher than 10^6 receptors per cell), whilst molecular PET/SPECT are advantageous for targets with lower concentrations [109].

1.7.2.1 Molecular MRI Contrast Agents

MRI relies on the properties of hydrogen (^{1}H, protons) to generate an image. In MRI, protons within a subject experience a strong external magnetic field (B_0), which causes them to align, and create a net magnetisation vector in the same orientation as B_0. A radiofrequency (RF) excitation pulse is temporally applied, which changes the orientation of the net magnetisation vector away from alignment with B_0. Once the RF is turned off, the protons dephase and relax back into their equilibrium position precessing around the magnetic field. This precession produces signal in the RF coil which can be detected and translated into an image by advanced computer processing. Protons in different tissues, or different structures within tissues, dephase and realign with B_0 at different rates. Image contrast in MRI can be achieved by exploiting these different recovery rates and through changing pulse sequence timing parameters known as the repetition time[‡] (TR) and echo time[§] (TE) [110]. Although intrinsic contrast is enough for most MRI applications, the contrast of tissue is heightened by exogenous administration of contrast agents. Specific and sensitive MRI contrast agents are needed to visualise molecular epitopes and receptors by this imaging modality. These exogenous chemical contrast agents alter the relaxation times of water

[‡] TR: Time between each excitation pulse.
[§] TE: Time between application of RF pulse and when the signal is sampled.

protons at the sites they localise. MRI contrast agents can be categorised into T_1-based[**] contrast agents and T_2-based[††] contrast agents. T_1-based contrast agents are paramagnetic ion complexes that shorten the longitudinal relaxation time of surrounding water. Gd-DTPA (Gadolinium-diethylenetriaminepentaacetic acid) is an example of T_1-based contrast agent. Although Gd-DTPA [molecular weight: 547 D] is too large a molecule to cross the intact BBB, it can distribute evenly in the extracellular space of regions with a disrupted BBB, thus enhances those regions (shortens T_1) on a T_1-weighted image [111]. Gd-DTPA is widely used for MRI applications including angiography and perfusion imaging. One of the earliest molecular MRI studies, by Matsumura *et al.* [112], showed that monoclonal antibodies conjugated with Gd-DTPA were able to detect glioma tumour cells *in vivo*. However, often the receptor of interest is only present at low concentration (10^{-13}-10^{-9} mol/g), whereas local gadolinium concentration of 10^{-7} mol/g is needed to achieve sufficient MRI contrast [113]. Over the years, more complex paramagnetic contrast agents (largely gadolinium-based) and more specific pathological targets have been developed and identified. Incorporating Gd onto nanoparticles has enabled development of size and shape adjustable agents, with improved magnetic properties and increased blood half-life compared to traditional complexes [114], [115]. However, this subset of MRI contrast agents still suffers from low sensitivity even at high concentration, and challenging surface modification for the purpose of molecular imaging [116].

In contrast, T_2-based contrast agents decrease the detected water intensity signal locally by decreasing transverse relaxation time. These agents create a local magnetic field that efficiently dephase the transverse magnetisation. The efficacy of T_2 contrast agents[‡‡] is defined by their relaxivity, R_2 (= $1/T_2$), the transverse rate observed for 1 mM solution of contrast agent in water [110]. Currently, the majority of T_2-based contrast agents are iron oxide particles composed of a superparamagnetic core of nanocrystalline magnetite (Fe_3O_4) and/or maghemite (γ-Fe_2O_3) with

[**] T_1: Time constant for regrowth of longitudinal magnetisation (M_z).
[††] T_2: Time constant for dephasing/decay of transverse magnetisation (M_{xy}).
[‡‡] The term "T_2 contrast agent" has extensively been used for iron oxide particles in the literature and is followed in this thesis; however, it should be noted that these particles manifest greater T_2* properties.

a polymer shell of varying thickness and material. The surface coating (carboxylates, dextran, silicates, or other non-immunogenic polymers), plays a crucial role not only for biocompatibility of these agents, but also with respect to functionalisation for targeting and other applications [117]. In general, these particles are classified into three categories based on their hydrodynamic size: ultra-small superparamagnetic iron oxide (USPIO); superparamagnetic iron oxide (SPIO); and microparticles of iron oxide (MPIO)[§§] (Figure 1.4). These particles and their applications will be discussed in the next Section.

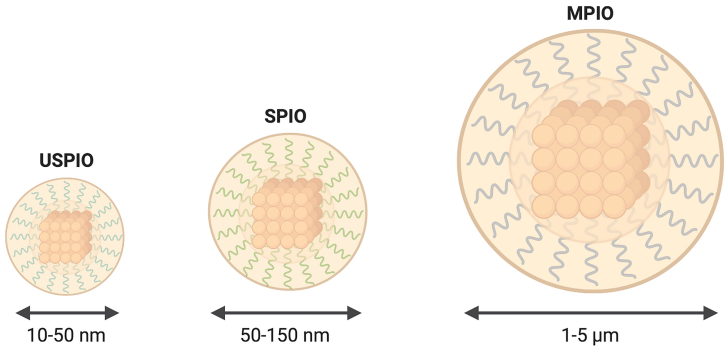


Figure 1.4: Iron oxide particles used for molecular MRI applications.

1.7.2.2 Iron Oxide Particles

USPIO, are nanoparticles with hydrodynamic diameter (including coating) of less than 50 nm. The magnetic core of these particles is generally less than 10 nm. USPIO shorten T_2 and T_2^*[***], but at low concentrations they are also able to shorten T_1 relaxivity owing to their small size [118]. The coating of these particles determines their fate *in vivo*. USPIO are generally able to avoid early uptake by spleen and liver macrophages and, hence, their long-circulating half-life can be used for blood pool imaging. Moreover, their ability to be taken up by inflammatory cells has allowed them to be used for detection of CNS pathologies, such as stroke, brain tumours and

[§§] Very small superparamagnetic iron oxide particles (VSOP), with hydrodynamic diameter < 10 nm are another category of iron oxide particles, which are not used for molecular imaging applications, therefore, will not be discussed in this Chapter.
[***] Dephasing caused by macroscopic and microscopic B_0 inhomogeneity; the observed or effective T_2.

MS [119]. Ferumoxytol (blood half-life; 9-15 hours; Feraheme®, AMAG Pharmaceuticals, US; Rienso®, Takeda Pharma, Denmark) is an FDA approved USPIO agent that is currently used in the clinic [119]–[121]. Finally, in some studies USPIO are used for *ex vivo* labelling of stem cells or even tumour cells, which can subsequently be tracked *in vivo* by MRI [122], [123].

SPIO, are nanoparticles with a hydrodynamic size of 50 nm-150 nm. These particles manifest shorter blood half-lives of 2-3 hours compared to USPIO. Ferumoxides (Feridex® IV, Berlex Laboratories, Endorem®, France) and ferucarbotran (Resovist®, Bayer Healthcare, Germany) are SPIO commercially used for intravenous injection in the clinic [120]. Oncological imaging such as liver tumour detection and lymph node metastasis evaluation are common applications of these nanoparticles [124], [125]. SPIO are entrapped in the reticulo-endothelial system (RES) cells in normal liver (Kupffer cells) and lymph nodes. However, malignant liver tumours do not have a substantial number of RES cells, which results in tumours presenting as hyperintense regions (less entrapped SPIO) in contrast to normal liver hypointense parenchyma. SPIO are also widely used in cell tracking studies for preclinical applications [126].

Finally, MPIO are the largest iron oxide particles, with a hydrodynamic size of 1-5 μm. MPIO have higher relaxivity than USPIO and SPIO per particle. The theory of the greater T_2* effect observed with larger iron oxide particles, has been tested by Shapiro *et al.* [127]. This work demonstrated that under optimal conditions, a single micron-sized MPIO is detectable *in vivo* in mouse embryos [128]. The contrast effect and magnetic field distortion of MPIO extends up to ~50 times their physical size. This phenomenon, known as the "blooming artefact" enables *in vivo* detection of MPIO at low concentrations [128], [129]. MPIO are also the preferred agent for cell tracking, as the label dilutes with each cell division, allowing long-term engraftment to be followed [127], [130]. MPIO show different clearance characteristics compared to USPIO and SPIO. In particular, MPIO exhibit very rapid blood clearance (< 2 minutes) [131], [132], which makes them a suitable carrier vehicle for molecular imaging *in vivo*, owing to reduction of background signal and clear detection of specific binding signal. Different surface chemistries such as p-toluene sulfhydryl- (tosyl-), amine and carboxylic acid groups can be functionalised

and allow conjugation of a diverse selection of targeting molecules, including peptides, carbohydrates and antibodies. However, these coatings prevent MPIO from breaking down *in vivo*, and instead they accumulate in RES [133]. On this basis and potential long-term toxicity in humans, MPIO are not approved for clinical studies and their application is limited to preclinical and experimental models. However, Perez-Balderas *et al.* have recently developed a new non-toxic, biodegradable generation of MPIO that allows clinical translation of MPIO targeted studies [134]. Biodegradable multimeric MPIO (mMPIO) are comprised of multiple colloidal iron nanoparticles (~ 65 nm) covalently linked together with protease cleavable peptides, which can be unlinked by cathepsins, the primary lysosomal proteases. Thus, once cleared from blood into the Kupffer cells of the liver these particles can be degraded inside and the iron is recycled in the body [134].

Collectively, selection of the appropriate USPIO, SPIO or MPIO contrast agents for imaging depends largely on the application and research or clinical question to be addressed.

1.7.3 Targeted Molecular MRI in CNS

The general concept of molecular MRI is to target the carrier vehicle (gadolinium or iron oxide) to the marker of interest (biomarker, surrogate) using a targeting moiety. Therefore, (i) a relevant target needs to be defined, (ii) an MRI contrast agent that can bind to the target needs to be designed, and (iii) an imaging method for detection of these contrast agents need to be developed. As discussed in Section 1.7.2.2, theoretically MPIO possess several desired attributes that make them suitable for molecular MRI application *in vivo*; MPIO convey a greater payload of iron compared to USPIO, whilst short blood half-life allows rapid molecular imaging of target-specific binding owing to minimal background levels. Finally, greater surface area of MPIO compared to USPIO enables for a higher number of targeting ligands, thereby increasing binding affinity. However, these hypotheses have not empirically been confirmed before. In Chapter 3 of this thesis, the sensitivity of targeted MPIO and USPIO are compared for the detection of activated endothelial cells in a neuroinflammation model.

The biomarker for molecular imaging also needs to meet the following criteria: (i) minimal and low basal expression; (ii) selective and rapid expression of the marker at site of pathology; (iii) continued high level of expression; and (iv) being accessible for the imaging probe. Although one desirable feature of MPIO compared to USPIO is that they are able to detect low levels of target molecule with great sensitivity, the density of target above threshold still contributes to the likelihood of particle binding and should, therefore, be considered in identifying targets [135]. Over the last 20 years, inflammation has been a particular area of interest for molecular imaging in the brain. Immune activation and inflammation within the brain is a classical feature of a spectrum of acute and chronic neurological diseases, including ischaemia, immune-mediated disorders (e.g. MS), neurodegenerative diseases (e.g. AD and PD), infection and trauma. As described in Section 1.5.1, in response to the inflammation, cytokines and chemokines are secreted that upregulate adhesion molecules on the BBB, and mediate recruitment of immune cells to the inflammatory foci. The location of adhesion molecules on the luminal surface of endothelial cells yields an accessible 'tag' for targeted MPIO to bind to at the site of inflammation. The endovascular expression of the target confers no size restriction for the MRI contrast agent and no requirement for the agent to cross the intact BBB. Commercially available MPIO (Promag™, Bangs Laboratories; Dynabeads, Invitrogen) can easily be functionalised and conjugated with monoclonal antibodies against these adhesion molecules, thus yielding molecularly targeted MRI contrast agents. Nevertheless, prior to developing antibody-based MPIO, inherent disadvantages of using antibodies should be considered. Firstly, antibodies are relatively expensive and a substantial quantity (40 μg antibody per 1 mg MPIO) is needed for *in vivo* studies. Secondly, non-human antibodies cannot be administered to humans owing to immune reactions, and an additional step of "humanising" antibodies is needed for translation of preclinical experiments to the clinic [136]. Alternatively, peptide (e.g. RGD; arginine-glycine-aspartic acid) or carbohydrate (e.g. sLe^x) based motifs can be coupled with MPIO for detection of integrins and adhesion molecules [132], [137], and are likely to be efficacious across species and could potentially to be used in humans without modification [138].

1.7.3.1 Targeted Molecular MRI for Neuroinflammation

From all adhesion molecules upregulated on endothelial cells in response to inflammation, VCAM-1 is an interesting biomarker that has been thoroughly studied. The use of MPIO to image inflammation *via* targeted binding to VCAM-1 has been described in a wide range of neuroinflammatory preclinical models [139], including AD [140], stroke [141], [142] and MS [143]. These studies were able to detect inflammatory events within the brain, and without the need for the contrast agent to cross the BBB or accumulate within the brain. Other adhesion molecules have been studied as potential MRI biomarkers for molecular imaging of neuroinflammation. Intercellular adhesion molecule-1 (ICAM-1), is a member of the Ig-super family that, unlike VCAM-1, is constitutively expressed on endothelial cells. However, ICAM-1 expression is amplified in the presence of inflammatory insults. An ICAM-1 targeted MPIO-based contrast agent has been used to detect overexpression of ICAM-1 in preclinical models of stroke [144], [145] and MS [146]. More recently, P-selectin targeted MPIO have been shown to be able to predict MS relapse and remission in both brain and spinal cord [147]. Apart from CAM targeted molecular imaging in neuroinflammation, activated platelets have been targeted with single-chain antibody-conjugated MPIO to diagnose cerebral malaria before pathology was visible by conventional MRI [148]. In all of these studies, MPIO were the chosen carrier vehicle for targeted MRI *in vivo*. An acknowledgement needs to be made to the use of targeted USPIO in neuroinflammation models. Although, USPIO have been tagged with VCAM-1 or selectins (E-selectin/ P-selectin) for molecular imaging of ischaemic stroke, the feasibility of *in vivo* USPIO-based molecular imaging remains elusive [149], [150]. This concept will be addressed in Chapter 3 of this thesis.

1.7.3.2 Targeted Molecular MRI for Brain Metastasis Diagnosis

Management of brain metastasis could be successful if diagnosed in the early stages (whilst the BBB is intact) when the metastasis is a sufficiently small size [151]. As discussed earlier, it appears the metastatic cancer cells employ the same machinery as immune cells to invade into a

secondary organ, and inflammation becomes a persistent and chronic process of cancer. One could speculate that the same principle for neuroinflammation molecular imaging could be applied for indirect detection of brain metastasis, targeting its inflammatory microenvironment. In fact, for the first time, Serres *et al.* were able to unmask breast cancer brain micrometastases by imaging inflammation present on the brain endothelial cells in close proximity to brain metastasis colonies [97]. Subsequently, Cheng *et al.* confirmed upregulation of VCAM-1 on brain metastasis-associated endothelial cells from all three main primaries, breast, melanoma and lung. This study demonstrated that the VCAM-MPIO MRI contrast agent is able to successfully detect brain micrometastasis prior to BBB breakdown [97], [98]. Nevertheless, other inflammatory adhesion molecules including ALCAM and E-selectin are present at early stages of brain metastasis formation and arguably to a greater degree than VCAM-1 [56]. Development of MRI contrast agents against these markers may therefore have the potential to detect brain micrometastases with even higher sensitivity and specificity. This concept is the premise of Chapters 4 and 5 of this thesis in which I explore the suitability of ALCAM and E-selectin for early detection of brain micrometastasis in preclinical models.

1.8 Purpose of This Thesis

This thesis describes optimisation of iron oxide particles, their visualisation and development of novel molecularly targeted contrast agents for molecular MRI applications in pathological preclinical models. The initial objectives of this work were to compare two types of targeted iron oxide particles, three magnetic field strengths and three MRI sequences for detection of neuroinflammation *in vivo*. Subsequently, the capacity for ALCAM and E-selectin surrogates for molecular imaging were assessed, and novel contrast agents developed and validated in mouse brain metastasis models.

1.8.1 Specific Hypotheses

Chapter 3:

I. Targeted MPIO are superior to targeted USPIO for detection of inflammation in a mouse model of neuroinflammation.

II. T_2*-weighted multiple-gradient-echo MRI is more sensitive than T_2*-weighted gradient-echo and balanced steady-state free precession (bSSFP) MRI for molecular imaging applications.

III. Higher magnetic field strength will improve detection and visualisation of iron oxide particles.

Chapter 4:

I. ALCAM is expressed on the endothelial cells in response to inflammatory stimuli, both *in vitro* and *in vivo.*

II. ALCAM is upregulated on brain metastasis-associated blood vessels.

III. The novel ALCAM-MPIO MRI contrast agent is able to detect brain metastases prior to BBB breakdown.

Chapter 5:

I. E-selectin is upregulated on endothelial cells in response to inflammatory stimuli, both *in vitro* and *in vivo.*

II. E-selectin is expressed on tumour-associated blood vessels.

III. E-selectin-MPIO have the ability to detect brain micrometastases *in vivo*.

IV. Targeting two adhesion molecules, VCAM-1 and E-selectin, concurrently will further improve the sensitivity detection of brain metastases detection *in vivo*.

CHAPTER 2

Materials and Methods

This Chapter describes the general materials and experimental methods used throughout this thesis. More specific and relevant methods are described in their corresponding experimental Chapters.

2.1 Buffers

IF-wash: 10 mM Na_2HPO_4 (cat. no. NIST2186II, SigmaAldrich, UK), 2 mM NaH_2PO_4 (cat. no. 71-500 SigmaAldrich), 137 mM NaCl (cat. no. BP358-212, Fisher Scientific, UK), 3.8 mM NaN_3 (cat. no. 71290, SigmaAldrich), 0.02% Triton X-100 (cat. no. X100, SigmaAldrich), 0.01% Tween-20 (cat. no. P9416, SigmaAldrich), pH 7.4.

MES Buffer: 15 mM 2-(N-morpholino)ethanesulfoci acid (cat. no. M5287, SigmaAldrich), pH 6.0.

Phosphate buffered saline (PBS): 10 mM Na_2HPO_4, pH 7.5, 150 mM NaCl.

Phosphate buffered saline with Tween-20 (PBST): 10 mM Na_2HPO_4, 150 mM NaCl, pH 7.5, and 0.01% Tween-20.

Periodate-lysine paraformaldehyde (PLP_{light}): 2% paraformaldehyde (PFA; cat. no. 158127 SigmaAldrich), 0.075 M L-lysin monohydrochloride (cat. no. L5626, SigmaAldrich), 0.37 M Na_3PO_4 (cat. no. 342483, SigmaAldrich), 0.01 M $NalO_4$ (cat. no. 27986.235, VWR), pH 7.2 and 0.1% glutaraldehyde (cat. no. G5882, SigmaAldrich).

Tris-NaCl buffer (TNB): 0.1 M Tris-Cl (cat. no. BPE153-1, Fisher Scientific, pH 7.5), 0.15 M NaCl, 0.5% (W/V) blocking reagent (cat. no. FP1020, PerkinElmer, UK).

PBS/Glycine: 10 mM Na_2HPO_4, 2 mM NaH_2PO_4, 137 mM NaCl, and 200 mM Glycine (cat. no. G8898, SigmaAldrich), pH 7.4.

0.1 M Phosphate buffer: 0.1 M Na_2HPO_4, 0.1 M NaH_2PO_4, pH 7.4.

*Sodium citrate buffer:*10 mM Trisodium (dehydrate; cat. no. 6132-04-3, SigmaAldrich), pH 6.0.

2.2 Injectable Agents

2.2.1 Antibody Conjugation to Carboxylic MPIO

Synthesis of antibody-MPIO was carried out as follows: For 1 mg MPIO, ProMag™ carboxylic acid MPIO (solid content: 2.5%, cat. no. PMC1N, lot. no. 10892, Bangs Laboratory Inc., USA) or Dynabeads® MyOne™ carboxylic acid (25.9 Fe mg/ml, cat. no. 65011, lot. no. 155367010,

Invitrogen, UK) were vortexed and transferred to a 2 ml plastic tube. MES buffer was added (15 mM, 1 ml, pH 6.0). MPIO were pelleted on a Dynal magnetic separator (Invitrogen) for 2 min, and the supernatant discarded. For the amine coupling reaction 100 µl MES buffer and 100 µl of a 10 mg/ml solution of EDC (N-(3-Dimethylaminoproyl)-N-ethylcarbodiimide hydrochloride, cat. no. E6383, SigmaAldrich) in 15 mM MES pH 6.0 were added to the pelleted MPIO and the solution was incubated for 30 min at 25°C on a shaker (1000 rpm, Eppendorf ThermoMixer®). The solution was washed twice with 1 ml of 15 mM MES buffer and incubated with 40 µg of the relevant antibody (Table 2.1), for 24 h at 25°C, shaking (1000 rpm). Conjugates were washed twice with PBS/0.01% Tween and the supernatant containing any unbound antibody discarded. The conjugated MPIO were diluted with sterile PBS to the desired concentration of antibody-MPIO. Figure 2.1 shows the syntheses of targeted MPIO used in this thesis.

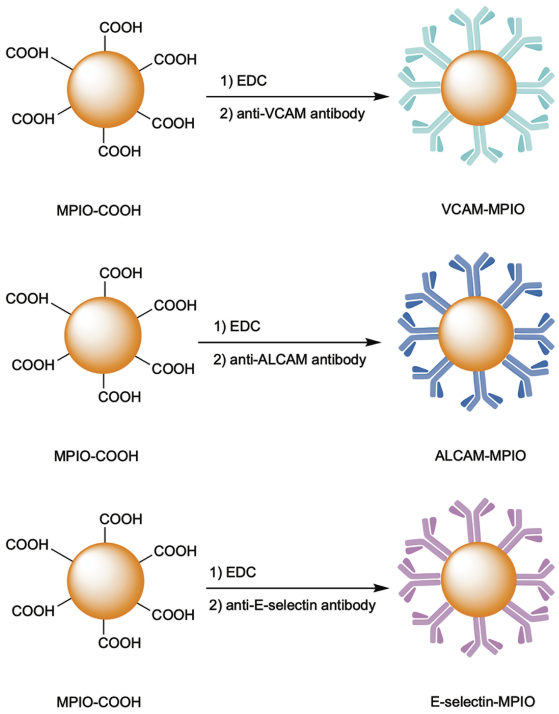


Figure 2.1: Synthesis of VCAM-/ALCAM-/E-selectin-MPIO.

Antibody	Host	Clonality	Reactivity	Manufacturer	cat. no.
IgG_1	Rat	Poly	Mouse	SouthernBiotech	0116-14
VCAM-1	Rat	Mono	Mouse	SouthernBiotech	1510-14
ALCAM	Rat	Mono	Mouse	R&D Systems	MAB1172
ALCAM	Rabbit	Poly	Mouse	LSBio	C292612-20
ALCAM	Rat	Mono	Mouse	eBioScience™	14-1661-82
E-selectin	Rat	Mono	Mouse	R&D Systems	MAB5751
E-selectin	Rat	Mono	Mouse	R&D Systems	MAB575

Table 2.1: List of the antibodies conjugated to MPIO.

2.2.2 Total Antibody Loading on MPIO

To measure the number of loaded antibodies on the MPIO, conjugated MPIO (10 µg) were diluted in 200 ml of PBS buffer with 2 µl of Alexa Fluor 647 goat anti-rat IgG (H+L) (cat. no. A21091, at a ratio of 5 fluorophores per antibody, Invitrogen) was added. Samples were shaken for 30 min (37°C, 1000 rpm), pelleted using a magnet, washed twice with PBS/0.01% Tween and resuspended in 400 µl of PBS. For Chapter 3, Qifikit calibration beads (cat. no. K0078, Agilent Dako, UK) were used as a reference. Beads were prepared according to the manufacturers protocol by substituting the provided fluorescently-conjugated antibody with Alexa Fluor 647 goat anti-mouse IgG (H+L) (cat. no. A21050, at a ratio of 5 fluorophores per antibody, Invitrogen). For Chapters 4 and 5, readily used Quantum Alexa Fluor 647 MESF (cat. no. 647, Bangs Laboratory Inc.) calibration beads were used as a reference. Flow cytometry experiments were performed on a BD FACSCalibur™ flow cytometer (BD Biosciences, UK), using channel FL4 (661/16 nm band pass filter). A calibration curve was generated, according to manufacturer protocol, by linear regression of the log-log plot of antibody loading versus fluorescence intensity. Figure 2.2 shows an example of calibration beads fluorescent intensities, and the intensity of antibody-MPIO tagged with fluorophores.

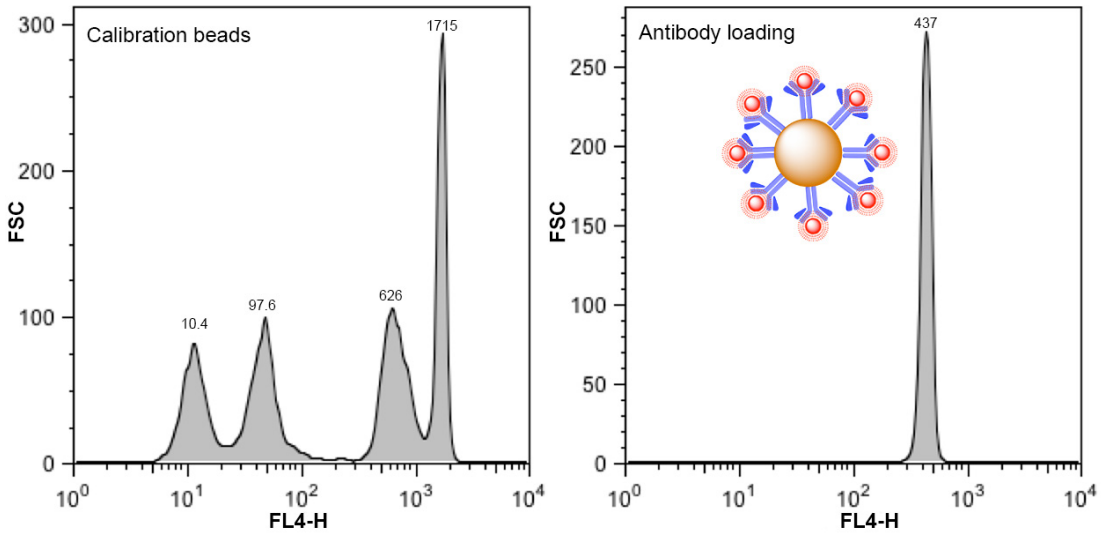


Figure 2.2: Quantification of antibody loading on MPIO.
A calibration curve was generated based on the known antibody loading provided by the manufacturer for each calibration population peak on the forward scatter (FSC) and fluorescent intensity (log) plot (left plot). The number of antibodies on MPIO was measured by fitting the intensity (right plot) into the calibration curve.

2.3 Cell Lines and Cell Culture

2.3.1 Brain Metastasis Cell Lines

- *MDA-MB-231-Br-GFP* cells: Subclone of human metastatic breast carcinoma that preferentially metastasises to the brain (kind gift from Prof. P. Steeg, USA); passage number (P#): 10. Culture: DMEM (high glucose; cat. no. E15-810, ThermoFisher, UK) containing 10% foetal bovine serum (FBS; heat inactivated, cat. no. FCS-SA, Labtech), and 1% L-glutamine (cat. no. 25030024, ThermoFisher).
- *H1_DL2* cells: Human brain metastasis-derived melanoma (kind gift from Prof. F. Thorsen, Norway); P#:8. Culture: ALT-DMEM (DMEM supplemented with 10% FBS, 2% L-glutamine and 4 times the prescribed concentration of non-essential amino acid (3.2% v/v, cat. no. 11140-035, lot. no. 1932100, Gibco)).
- *SEBTA-001* cells: Human brain metastasis-derived lung adenocarcinoma (kind gift from Prof. G. Pilkington, UK); P#:6. Culture: DMEM supplemented with 2% human serum (cat. no. H4522, SigmaAldrich).

2.3.2 Endothelial Cell lines

- *sEnd-1* cells: Murine skin-derived endothelial cells; P#:30. Culture: DMEM containing 10% FBS and 1% L-glutamine.
- *bEnd.3* cells: Murine (BALB/c) brain-derived endothelial cells. P#: unknown. Culture: DMEM ham Fl2 (cat. no. D8437, SigmaAldrich) containing 10% FBS and 1% L-glutamine.
- *hCMEC/D3* cells: Human brain microvascular endothelial cells (kind gift from Prof. I. Romero, UK); P#:25. Culture: medium (EGM-2) BulletKit (CC-3162, Lonza, UK) supplemented with the following components obtained from the manufacturer: 0.025% (v/v) recombinant human epidermal growth factor (rhEGF), 0.025% (v/v) vascular endothelial growth factor (VEGF), 0.025% (v/v) R3-insulin-like growth factor-1 (R3- IGF-1), 0.1% (v/v) recombinant human fibroblast growth factor-beta (rhFGF-b), 0.1% (v/v) gentamicin and amphotericin-B cocktail, 0.1% (v/v) ascorbic acid, 0.04% (v/v) hydrocortisone and 2.5% (v/v) FBS.

Human cell lines were authenticated annually using short tandem repeat (STR) profiling via the LGC standards (London, UK) cell line authentication service. STR markers were matched to the known American Type Culture Collection (ATCC) profiles or DNA fingerprints supplied by our collaborators.

2.3.3 Cell Handling

All aspects of cell handling, including preparation of cell culture reagents, were performed under sterile conditions within a laminar flow tissue culture hood (BioMat Class II, Medical Air Ltd, UK) that had been cleaned and sterilised with 70% v/v denatured ethanol in distilled water (dH_2O) purified by reverse osmosis. Prior to use in cell culture, the reagents were thawed in a 37°C water bath and allowed to equilibrate.

First cells were thawed, and the cell pellet was separated from the cell freezing medium (cat. no. C6295, SigmaAldrich) under centrifugation (1200 rpm, 5 min, 21°C, MEGAFUGE 40R, ThermoScientific) in a 10 ml falcon tube. Following aspiration of the freezing medium, cells

were resuspended in growth medium and transferred to a sterile uncoated polystyrene flask and allowed to culture in a 37°C incubator with a controlled atmosphere of 5% CO_2 and 95% humidified air.

Cultured cells were regularly inspected for morphology, confluence, adherence and absence of infection using an inverted light microscope. All cell lines underwent routine Mycoplasma testing before injection and freezing, according to the MycoAlert (Lonza) standardised protocol. At 70-80% confluence, the adherent cells were passaged by removing the culture medium, gently washing with PBS and enzymatically disassociated from the culture flask base by incubation at 37°C with 1 ml trypsin-EDTA (cat. no. T3924, SigmaAldrich) for 5-10 min. The trypsin-EDTA was inactivated by addition of 5 ml of growth medium.

2.3.4 Three-dimensional (3D) Cell Culture and Fluorescent Staining

To assess expression of cell adhesion molecules between endothelial cells and tumour cells *in vitro*, 3D-base co-culture of these cells was performed. First, frozen (-20°C) Matrigel (Matrigel© phenol red-free, cat. no. 356231, Corning©, UK) was placed in the fridge 3 h prior to the experiment. Millicell EZ slide-8-well glass chamber slide (cat. no. PEZGS0816, MerkMillipore, UK) and pipette tips were placed on ice. Then, the 8-well glass chamber slide was precoated with Matrigel as a basement membrane by adding 80 µl to each well. Slides were incubated at 37°C to let the Matrigel solidify. Meanwhile, mouse brain endothelial cells (bEnd-3) were trypsinised, counted, then added directly onto the Matrigel-precoated 8-well chamber slide (60,000 cell/ in 200 µl DMEM per well). Tubulation in this cell line was observed after 6-7 h. Subsequently, tumour cells were trypsinised, counted and added (50,000 cell/ in 200 µl medium per well) directly on top of the endothelial cells. After 14 h, the media was aspirated gently and washed 2 times with PBS. Cells were fixed at room temperature with 4% formaldehyde (Pierce™ 16% (w/v) formaldehyde, cat. no. 28908, ThermoFisher; Diluted in PBS) for 45 min. Cells were then washed 3 times, 10 min each with PBS: glycin. Cells were permeabilised using 0.5% Triton X-100 in PBS at room temperature for 5 min. Cells were rinsed 3 times, 10 min each with IF-wash.

Blocking was carried out using TNB for 1 h at room temperature. Then, the blocking buffer was aspirated, and cells were incubated with 150 µl of the primary antibody (CD31, ALCAM, E-selectin or tumour markers) diluted in TNB for 2 h at room temperature*. Subsequently, cells were washed 3 times, 20 min each with IF-wash, and then incubated for 1 h in 150 µl of secondary fluorophore diluted in TNB. Cells were then washed 3 times, 20 min each with IF-wash. Nuclei were stained with DAPI (4'-6-diamidino-2-phenylidole, cat. no. H-1200, Vector Laboratories, UK). Slides were mounted with anti-fade agent (cat. no. H-1000, Vector Laboratories) was added. Slides were stored in the dark at room temperature and fluorescent microscopy imaging using an inverted confocal microscope (LSM-780; Carl Zeiss Microimaging, Germany), was performed on the subsequent day.

2.4 Animal work

All animal experiments were approved by the University of Oxford Clinical Medicine Ethics Review Committee and the UK Home Office (Animals [Scientific Procedures] Act 1986), and conducted in accordance with the University of Oxford Policy on the Use of Animals in Scientific Research, the ARRIVE Guidelines and Guidelines for the Welfare and Use of Animals in Cancer Research [152]. All procedures in this body of work were performed under Procedure Project Licence (PPL) 30/3187 and Procedure Individual Licence (PIL) l466E0CA3.

2.4.1 Animal Husbandry

Animals were housed in environmentally enriched (activity wheel or crawl ball, nesting material and chew sticks) and individually ventilated polycarbonate solid-bottomed cages in groups of maximum 6 per cage, in a 12 h day-night cycle facility maintained at 21 ± 2°C in 55 ± 10% humidity. All mice had *ad libitum* access to certified food and tap water. All mice were acclimatised to their new environment at least 3 days prior to any experimental procedure. Mash food (loose diet powder) mixed with water was provided to animals after surgical procedures.

* Incubation at 4°C could liquefy the Matrigel resulting in loss of structures.

2.4.2 Mouse Brain Metastasis Model

2.4.2.1 Tumour Cells Preparation

Tumour cells (MDA-MB-231-Br, H1_DL2, SEBTA-001) were grown until 80-90% confluence in the culture flask. On the day of the experiment, tumour cells were washed and trypsinised, as previously described in Section 2.3.3. Cells were resuspended in sterile PBS and the number and viability of cells were checked with trypan blue using a Countess II automated cell counter (ThermoFisher). The final concentration of 1×10^{6} cells in 1 ml of sterile PBS was prepared for all the brain metastasis models. The cell suspensions were kept in an insulating cooling box (Eppendorf® IsoTherm-system, SigmaAldrich) for a maximum of 2 h.

2.4.2.2 Intracardiac Injection

Female SCID mice (7–8 weeks old) were purchased from Charles River, Kent, UK. Ultrasound image-guided intracardiac injection of tumour cells was performed using Vevo 3100 Imaging System (Fujifilm VisualSonics, Canada). General anaesthetic was administered with 2–3% (vol/vol) vaporised isoflurane (IsoFlo® Vet) in oxygen. The mouse was laid supine on an adjustable heated (37°C) imaging platform and the internal body temperature was monitored using a rectal probe connected to a homeothermic system (Harvard Instruments, Edenbridge, UK) and maintained at 37°C. The hair from chest and left armpit was removed using depilatory cream. Ultrasound gel (AQUASONIC®, cat. no. 01-02, Parker Laboratories, UK) was applied over the chest wall and the ultrasound probe was placed in and above the gel. The anatomical location of left ventricle was visually confirmed on the ultrasound screen. Prior to injection, cells were resuspended using a 23G needle to minimise the risk of clumping. Tumour cell suspension (100 µl) was loaded into a 27G needle and placed on an adjustable needle holder. Tumour cells were injected slowly into the left ventricle of the mouse heart. Confirmation of successful injection was assessed by a pulsating flashback of bright red blood into the syringe and blooming effect caused by tumour cells flowing out of the syringe. Following injection, the needle was withdrawn from the heart slowly and the animal was transferred to the recovery cage.

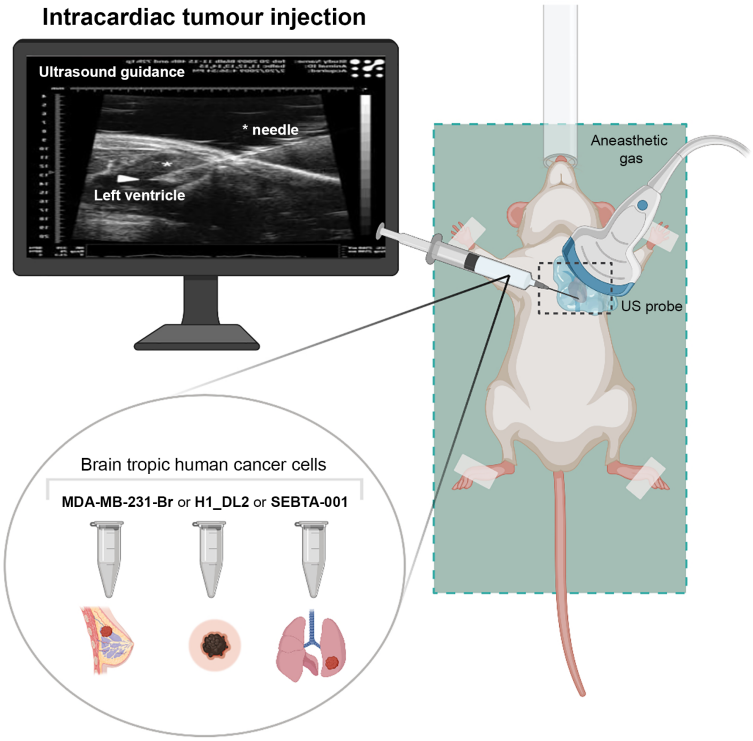


Figure 2.3: Ultrasound guided intracardiac injection of brain tropic tumour cells into the mouse left ventricle.

2.4.3 Mouse Neuroinflammation Model

Intracerebral surgery was performed following aseptic principles. Female BALB/c were purchased from Charles River, Kent, UK. The mouse was anaesthetised in an induction chamber with 2-3% v/v isoflurane vaporised in 30% O_2: 70% N_2O. Following confirmation of deep anaesthesia, the skull was shaved using hair clippers. The mouse was then transferred to a stereotaxic frame (cat. no. 502650, World Precision Instruments, UK) were the skull was fixed at three points using ear and teeth bars (Figure 2.4). Anaesthesia was maintained at 1.5-2% v/v isoflurane. Internal body temperature was monitored using a rectal probe connected to a homeothermic system (Harvard Instruments, Edenbridge, UK) and maintained at 37°C.The skull was cleaned with 4% w/v chlorhexidine gluconate, and an incision made along the scalp to expose bregma (the intersection between the coronal and the sagittal sutures). The following coordinates relative to bregma were identified: +0.5 mm (rostral-caudal), +2.5 mm (lateral). A

hole was drilled (powered drill 240 V, cat. no. 503599, World Precision Instruments) through the skull using a surgical light microscope at 40X magnification. A pulled glass microcapillary (tip diameter *ca.*, 50 µm) was filled with 1 µl of desired concentration of substrate in sterile PBS. The microcapillary was placed over the drilled hole and inserted to coordinates of -2.5 mm relative to the dura mater. The total volume was slowly injected over 2 min. The microcapillary was then removed and the incision was closed with non-absorbable suture (Mersilk 4-0 suture, Ethicon Inc., USA). Upon completion of surgery, the mouse was transferred to a recovery area.

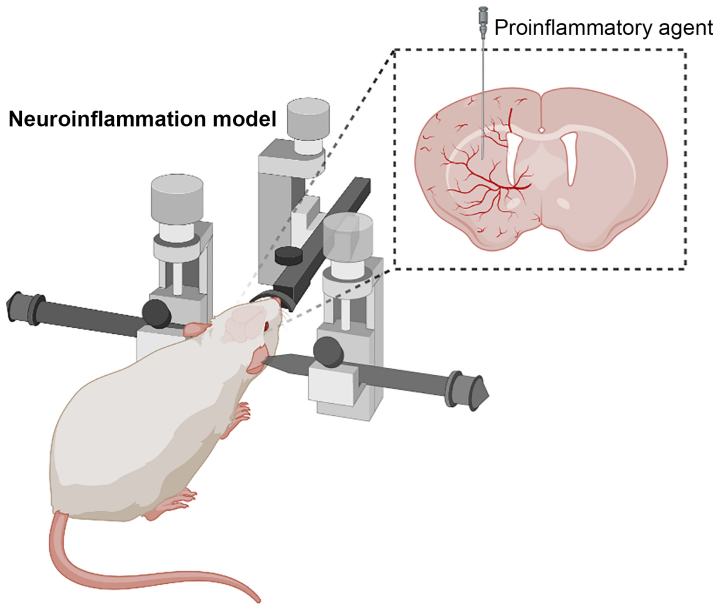


Figure 2.4: Intracerebral injection of the proinflammatory agent to the striatum.

2.4.4 Perfusion-Fixation and Tissue Handlings

At the relevant time-points of the studies, a 0.2 ml lethal dose of dilute pentobarbital (Vm.10347/4014, Animalcare Ltd, UK), diluted 1:5 in saline, was administrated intraperitoneally. Deep anaesthesia was confirmed by checking pedal and corneal reflexes. The chest cavity was opened, and an incision made into the right atrium of heart to create an outlet for drainage of blood and perfusate. Perfusions were performed using a perfusion pump (505 L, Watson Marlow, UK) with a slow flow rate of 4 ml/min. The needle for infusing the pre-chilled

saline containing 10 unit/ml heparin sodium (cat. no. 30170145, Wockhardt Ltd, UK) was inserted into the left ventricle. After approximately 2 min and clearance of blood (complete liver discolouration), the mouse was perfused with fixative PLP_{light} for approximately 2-3 min, the usual time which fixation tremors are observed. Following the perfusion, the brain was harvested and post-fixed in PLP_{light} for 4 h and then immersed in 30% v/v sucrose (cat. no. S9378, SigmaAldrich) in dH_2O until the specimen sank to the bottom of a 7 ml bijou tube (~24 - 48 h). For cryostorage of tissue, first, brains were dried on a paper towel in order to remove all the excess sucrose and avoid crystallisation. Then, pre-chilled isopentane (cat. no. 10030290, Fisher Scientific) was added to 7 ml bijou tubes and the tubes were placed in dry ice containing isopentane. Brains were immersed in the isopentane tubes for approximately 5 min, until the colour of the specimen changed. Samples were stored short-term in a -20°C freezer or long-term in a -80°C freezer.

2.5 Immunohistochemistry (IHC)

2.5.1 Mouse Tissue Preparation

Brains were cut using a cryostat (Leica CM1950. Leica Biosystems, Germany) in 10 µm or 20 µm thick sections, which were collected serially on super frost adhesion slides (cat. no. 10149870, Fisher Scientific). For the brain metastasis models, the whole brain was sectioned. For the inflammation model, sections were collected from the striatum. Slides were air dried for 24 h and then stored at -20°C.

2.5.2 Immunohistochemistry Protocol: Mouse Tissue

For the relevant antibodies shown in Table 2.2, a heat induced antigen retrieval step was applied. With the slides in sodium citrate buffer (0.1 M, pH 6.0), the heat was raised using a microwave for two rounds of 5 min each. The slides were cooled to room temperature (20 min), then washed with PBST for 5 min, followed by a 5 min wash in PBS. A blocking step, with 0.3% v/v hydrogen peroxide (cat. no. H1009, SigmaAldrich) in methanol (cat. no. 10675112,

SigmaAldrich), was then carried out for 20 min at room temperature to quench endogenous peroxidase. Afterwards, the slides were washed in PBS, followed by a PBST wash for 5 min each. Sections were then blocked by incubation with 10% v/v serum in PBS, corresponding to the animal in which the secondary antibody was raised, for 1 h at room temperature. Section were then incubated overnight with the primary antibody diluent using 1% v/v serum in PBS at 4°C. On the second day, slides were washed 3×5 min with PBS. Samples were then incubated with biotinylated secondary antibody diluted in PBS to the appropriate concentration at room temperature. After 1 h, the slides were washed 3×5 min in PBS. For immunodetection, an Avidin-Biotin Complex (ABC) kit was utilised (cat. no. PK-6100, lot. no. ZF0425, Vectastain® Elite ABC Kit, Vector Laboratories). The ABC mixture (A, B:1:100 µl PBS) was prepared at least 30 min prior to application. Sections were incubated in ABC for 45 min and washed 2×5 min with PBS. To visualise immunoreactivity, 125 µl of 30% v/v hydrogen peroxide was added to 5 ml of DAB (3,3'-Diaminobenzidine, cat. no. 11209, Acros Organics, USA) aliquot diluted in 300 ml PBS. The length of time required for the chromogenic development varied. The tissue sections were counterstained with 0.5% v/v cresyl violet acetate (cat. no. C5042, SigmaAldrich) in dH_2O for an appropriate time (varied between 20 sec to 5 min, depending on the freshness of the cresyl violet). Following dehydration in sequential rinses of ascending concentrations of ethanol (cat. no. 11994041, Fisher Scientific) (75% (dip), 95%(dip), 100% (5 min), 100% (5 min)), the tissue was cleared by 3×5 min washes in a xylene (cat. no. 10784001, Fisher Scientific) bath and then mounted with glass coverslips using DPX mounting medium (cat. no. 06522, SigmaAldrich). Once dry, the stained tissue sections were digitally scanned using the Aperio CS2 Brightfield scanner (Leica Biosystems) and the images were saved for future analysis.

2.5.3 Immunohistochemistry Protocol: Human Tissue

Paraffin-embedded human brain metastasis sections (6 µm thick) were de-paraffinised (3×5 min xylene), hydrated (graded alcohol series) and quenched using 1% hydrogen peroxide

in methanol (breast and lung). To bleach melanin in melanoma samples, slides were incubated in 10% hydrogen peroxide in PBS for 2.5 h at 60°C [153], [154]. Heat induced antigen retrieval was applied using sodium citrate buffer (0.1 M, pH 6.0) and heating in a for 10 min. Samples were then blocked with 10% of an appropriate blocking serum (goat serum for CD34, horse serum for ALCAM and goat serum for E-selectin). Sections were then incubated overnight with the primary antibody in 1% v/v serum in PBS at 4°C. After 16 h, biotinylated anti-rabbit or biotinylated anti-mouse or biotinylated anti-rat secondary antibodies were added to the sections and visualised by DAB (Table 2.2). Sections were counterstained with cresyl violet. Histological slides were digitally scanned on an Aperio CS2 Brightfield scanner at X20 or X40 magnification.

2.5.4 Perls' Prussian Blue Staining

Firstly, all glassware was cleaned with dilute (1 M) HCl, then rinsed with iron-free distilled water (Milli-Q® water) to remove any excess iron. Mouse brain sections were rinsed in PBS for 5 min, followed by distilled water for 5 min. While sections were in distilled water, Perls' *solutions A* and *B* were prepared separately in a cleaned glassware.

Perls' *solution A* was prepared by dissolving 4 g of potassium ferrocyanide (cat. no. 10205, AnalR) in 200 ml of Milli-Q® water. Perls' *solution B* was prepared by adding 4 ml of 37% HCl (12 M) to 196 ml of Milli-Q® water. *Solutions A* and *B* were mixed (1:1) just before the use. Follow the distilled water rinse, the sections were incubated in Perls' mixture for 15 min. The counterstain, nuclear fast red (cat. no. N8002, SigmaAldrich), which targets nucleic acids, was used as an alternative to cresyl violet counterstaining, owing to easier differentiation between Perls' blue staining and nuclei. Nuclear fast red solution was prepared by adding 0.2 g nuclear fast red dye to 100 ml dH_2O with 5 g of aluminium sulphate (cat. no. 202614, SigmaAldrich) as a mordant. The solution was boiled for 5 min, then filtered and allowed to cool before use. Following Prussian blue staining, sections were counterstained in nuclear fast red for 2 min. Sections were rinsed briefly in dH_2O before dehydration in increasing concentrations of ethanol, cleared in xylene, and mounted with coverslips using DPX.

2.5.5 Immunohistochemical Analyses

To measure CAMs (ALCAM or E-selectin) upregulation in metastasis or neuroinflammation models, mouse brain tissues were stained for the relevant markers and digitally scanned using the Aperio CS2 Brightfield scanner (Leica Biosystems). The digital images were visualised using Imagescope software and the region of interest (ROI; tumours or brain hemispheres) were manually annotated. The Imagescope built-in Positive Pixel Count v.9 algorithm was adjusted (tuned) on the ROI until the algorithm results were sufficiently accurate for the purpose of the study. The following parameters were used to define positive pixels (strong DAB) within the ROI: intensity threshold between 0 to 174, intensity threshold of negative pixels = -1, colour saturation threshold = 0.04, hue width = 0.5.

2.5.6 Fluorescent Immunohistochemistry Protocol

For immunofluorescent co-localisation staining, tissue sections were quenched with 0.3% v/v hydrogen peroxide in methanol for 20 min at room temperature. Afterwards, the slides were washed in PBS, followed by a PBST wash for 5 min each. Slides were sequentially streptavidin-and biotin-blocked (cat. no. SP-2002, Vector Laboratories) for 15 min each, followed by a 5 min PBS wash. Slides were incubated with image-iT™ FX signal enhancer (cat. no. 136933, Invitrogen) for 30 min. Blocking was done using TNB for 1 h at room temperature. Sections were then incubated overnight at 4°C with the desired combination of primary antibodies (e.g., ALCAM, CD31 and GFP) in TNB.

On the following day, slides were rinsed in PBS and incubated with a corresponding biotinylated IgG secondary antibody in TNB for 30 min, washed with PBS, incubated with streptavidin-HRP (1:200, TSA Biotin System, cat. no. NEL70000, PerkinElmer) in TNB for 30 min, washed, and incubated for 7 min in dark with tyramide signal amplification–biotin (TSA-BIO; 1:100) in dilution buffer provided by PerkinElmer. Slides were washed and incubated with relevant fluorophores (Table 2.2), mounted with anti-fade agent and stored at 4°C until microscopy. Fluorescent images were acquired using an inverted confocal microscope (LSM-780; Carl Zeiss

Microimaging, Germany) with constant imaging parameters and analysed using Zen software (Carl Zeiss).

2.5.7 Fluorescent Immunocytochemistry Protocol

For immunofluorescent detection of specific markers (i.e. ALCAM or E-selectin) on endothelial cells, cells were washed 2 times with PBS to remove traces of growth media. The cells were then fixed with pre-chilled 4% w/v formaldehyde for 10 min at 4°C. After 2 washes in PBS, the cell membranes were permeabilised by incubation in 0.1% v/v Triton X-100 in PBS for 5 min followed by 3 brief rinses in PBS. Cells were then incubated for 15 min in streptavidin, followed by 15 min in biotin and then 1 h with image-iT™ FX. A blocking step was performed with TNB for 1 h at room temperature. The primary antibody was diluted in TNB, added to the cells, which were then incubated at 37°C for 2 h in the mixture, followed by 3 brief PBS rinses. The cells were incubated with the biotinylated secondary for 1 h followed by 3 brief rinses in PBS and then a 30 min incubation with the relevant fluorophores diluted in TNB for 30 min at room temperature and shielded from light. Cell nuclei were counterstained with DAPI and were mounted with anti-fade agent onto glass microscope slides before imaging. Fluorescent images were acquired using a confocal microscope (Leica TCS SP8 Confocal platform; Leica Microsystems, Germany) and analysed using ImageJ (rsbweb.nih.gov) and Leica Application Suite X (Leica Microsystems) software.

1° Ab	Manufacturer	cat. no.	Application	Reactivity	Con	Ag ret	2° Ab	Company	cat. no.	Con
m α ALCAM	Novus bio	NBP2-37345	IHC, lF	m, h	1:100	Y	Biotin α m	Vector	BA-2001	1:100
g α ALCAM	R&D system	AF1172	IHC	m	1:500	Y	Biotin α g	Vector	BA-9401	1:1000
r α VCAM-1	Southern Biotech	1510-01	IHC, IF	m	1:200	N	Biotin α r	Vector	BA-4001	1:100
g α CD31	R&D system	AF3626	IF	m	1:100	Y/N	Alexa 594 α ch	Jackson	705-586-147	1:100
ch α GFP	abcam	ab13970	IF	m, h	1:100	Y	Alexa 488 α ch	Jackson	703-545-155	1:100
rb α Melan-a	abcam	ab210546	IF, IHC	m, h	1:200	Y/N	Biotin α rb Alexa 488	Vector Jackson	BA-1000 711-546-162	1:200 1:100
rb α cytokeratin	abcam	ab9377	IF	m, r, h	1:100	Y	Alexa 488 α rb	Jackson	711-546-162	1:100
rb α GLUT1	abcam	ab652	IF	m, r	1:100	Y	Alexa 594 α rb	Jackson	711-586-152	1:100
r α CLA	BD Pharmigen	550407	IHC	m, h	1:	Y	Biotin α r	Vector	BA-4001	1:100
rb α laminin	abcam	ab11575	IF	m, r	1:100	Y	Alexa 594 α rb	Jackson	711-586-152	1:100
r α E-selectin	LSBio	LS-C13903	IHC, IF	m, h	1:100	Y	Biotin α r	Vector	BA-4001	1:100
ch α E-selectin	R&D system	AF575	IHC	m	1:500	N	Biotin α ch	Vector	BA-9010	1:1000

Table 2.2: Immunohistochemistry antibodies.

2.6 Pre-clinical MRI

2.6.1 Mouse MRI Set-Up

On the day of imaging, mice (brain metastasis/inflammation model/naïve) were anaesthetised with 2-3% v/v vaporised isoflurane in a mixed 90% air:10% oxygen gas delivery. The mouse was placed on a heating pad on a bench and a heat lamp was used to induce tail vein vasodilation. Iron oxide contrast agent (4 mg Fe/kg body weight, 100 µl) was injected intravenously (iv) using ~ 1 m of tubing (0.28 mm ID, Smiths Medical™) attached to a butterfly cannula (30G insulin syringe). The mouse was then transferred to the magnet room and was positioned prone in a customised 3D printed cradle, with the head fixed using cheek pads. Respiration was monitored by placing a pressure balloon in contact with the chest, and the core temperature was monitored using an optical rectal temperature probe (OTP-M-X-62F2.5-1.5(PTFE/PVC)-XN-7GT-M1-PV0014a, Opsens Solutions, Canada) connected via a 10 m fiber optic extension to an AccuSens 4 channel Signal Conditioner (ACS-P4-N-62SC, Opsens Solutions) and maintained at 36-37°C [155], [156]. Once the animal was appropriately prepared, the cradle was inserted into a quadrature birdcage coil.

2.6.2 MRI Scanners Specifications

Specifications of MRI scanners used in this thesis can be found in Table 2.3.

Magnet	Bore size	Gradient size (OD/ID)	Gmax	Manufacturer	RF coil birdcage	Manufacturer
4.7 T	ID 310 mm	205/120 mm	40 G/cm	Agilent	ID 26 mm	RAPID
7.0 T	ID 210 mm	205/120 mm	40 G/cm	Agilent	ID 26 mm	RAPID
9.4 T	ID 160 mm	155/100 mm	40 G/cm	Agilent	ID 26 mm	RAPID

Table 2.3: MRI scanners specifications.

2.6.3 MRI Sequences

After mouse setup in the scanner, a scout image was acquired to position the brain in the middle of field-of-view (FoV). Prior to image acquisition for each animal, shimming was performed to correct inhomogeneities in the magnetic field (B_0).

◈ T_2*-weighted multi-gradient-echo 3D (MGE3D) Chapter 3*:

Excitation angle = 15°; repetition time (TR) = 65.1 ms; time of the 1st echo (TE_1) = 2.5 ms; echo separation time (TE_2) = 4 ms; FoV = 22.5×22.5×22.5 mm^3, SW = 100 kHz (acquisition time = 2.56 ms); acquisition matrix = 256×192×192 (final images zero-filled to 256×256×256; final isotropic resolution = 88 μm); number of echoes (NE) = 15; single average (NT) = 1; and total acquisition time ~ 40 min.

◈ T_2*-weighted multiple-gradient-echo 3D (MGE3D) Chapters 4 and 5:

Excitation angle = 15°; TR = 48.8 ms; TE_1 = 4 ms; TE_2 = 7 ms; NE = 6; SW = 50 kHz; FoV = 22.5×22.5×22.5 mm^3; acquisition matrix = 256×192×192 (final images zero-filled to 256×256×256; final isotropic resolution = 88 μm); NT = 1; and total acquisition time ~30 min. The same sequence with the above parameters was used to warm-up the scanner.

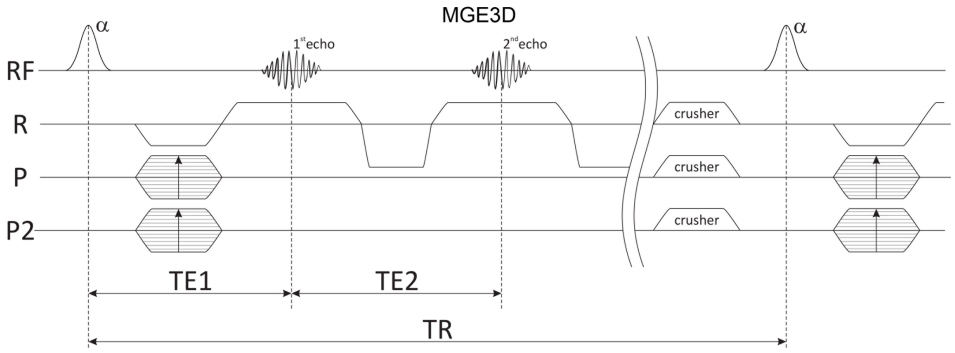


Figure 2.5: Pulse diagram of T_2*W-MGE3D sequence.

* This sequence was further optimised by Dr. Alexandre Khrapitchev for the subsequent Chapters.

◈T_2/T_1-weighted balanced steady-state free precession 3D (bSSFP3D)

Excitation angle = 20°; TR/TE = 8/4 ms; SW = 147 kHz (acquisition time = 1.74 ms); number of excitation frequency offsets = 8; FoV = 22.5 × 22.5 × 22.5 mm; acquisition matrix size = 256 × 192 × 192 mm (final images zero-filled to 256 × 256 × 256; final isotropic resolution = 88 µm) and the total acquisition time was ~ 40 min.

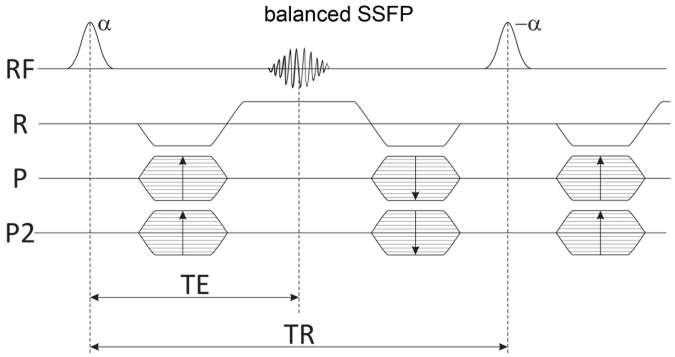


Figure 2.6: Pulse diagram of bSSFP3D sequence.

◈T_1-weighted spin-echo 2D (SEMS2D)

Excitation angle = 4°, TR = 500 ms; TE = 10 ms; NT = 1; FoV = 22.5×22.5 mm^2; acquisition matrix = 192×192 (zero-filled to 256×256); slice thickness = 0.7 mm and total acquisition time ~1.6 min. The same sequence was used for pre and post-gadolinium administration. Post-gadolinium images were obtained 5 min post intravenous injection of 30 µl (15 µmol, approximately 0.75 mmol/kg based on a 20 g mouse) Gadodiamide (Omniscan, GE Healthcare, USA).

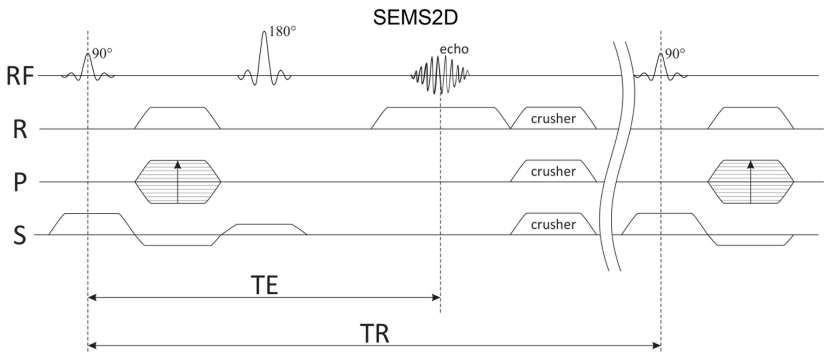


Figure 2.7: Pulse diagram of SEMS2D sequence.

2.6.4 MRI Data Processing

Each T_2*-weighted 3D image was reconstructed using home-built MATLAB (Mathworks, USA) program† based on the square root of the sum of squares (SqrtSOS) of individual echoes algorithm. In the neuroinflammation mouse model, each brain hemisphere was manually masked using ITK-SNAP (itksnap.org). MATLAB code was used to quantify number of hypointense voxels‡. True hypointense voxels rising from bound MPIO were defined in the script as a voxel value 0.68 times less than the mean value. Natural hypointense signals from ventricles and sinuses were excluded by using an upper threshold limit of 20 contiguous hypointense voxels (≥ 20), and single voxel (≤ 1) hypointensities were excluded as noise [97]. The number of hypointense voxels for each brain hemisphere was quantified and compared. In the brain metastasis model, a whole brain mask was generated, and the same algorithm was applied for the quantifications of number of hypointense voxels.

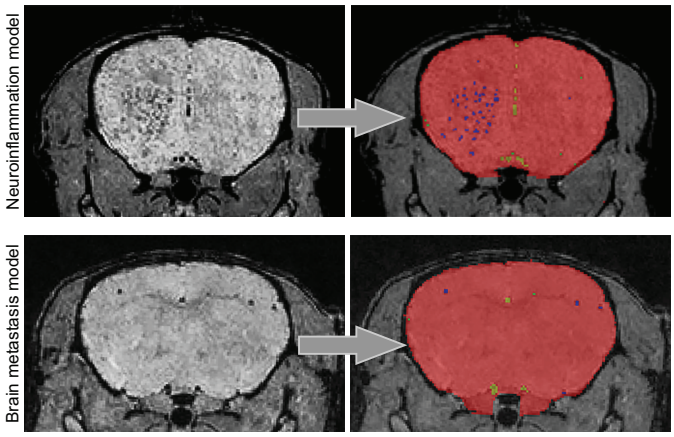


Figure 2.8: Automatic processing of iron oxide induced hypointensities.
Brains were manually masked (red) on T_2*W-MGE3D images. Hypointense voxels (blue) arising from bound MPIO in both inflammation and brain metastasis models were detected using a previously optimised in-house algorithm. Hypointensitites from natural structures of brain (≥ 20 voxels, green) and noise were excluded.

† The reconstruction MATLAB program was developed by Dr. Alexandre Khrapitchev.
‡ The quantification MATLAB code was provided by Dr. Alastair Hamilton.

2.6.5 MRI and Histology Co-Registration

Alternate histological sections (10 µm) were stained for tumour markers, and tumours were delineated manually using Imagscope software. Tumour volume (μm^3) of the missing sections was calculated by linear interpolation. Tumour volume was calculated by adding the tumour areas (μm^2) multiplied by slice thickness (10 µm). Based on this, histological volumetric and anatomical tumours maps of mouse whole brain were generated. All five alternated sections (fused thickness: ~ 88 µm, accounting 20% shrinkage during perfusion-fixation) were fused together to achieve similar spatial resolution as a single MRI slice (88 µm) as shown in Figure 2.9. The anatomical location of hypointensities on T_2*W-MGE3D MR images were visually matched with histological 3D brain tumour maps.

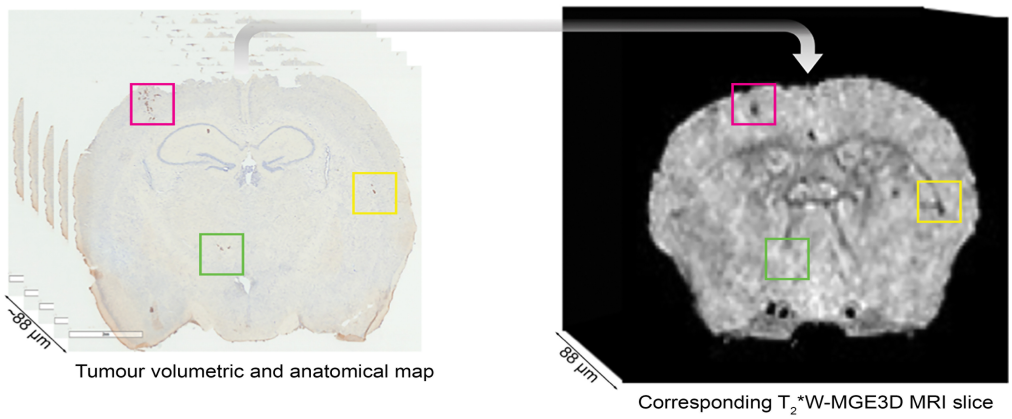


Figure 2.9: Volumetric histology and MRI co-registration.

CHAPTER 3

Optimisation of Molecularly Targeted MRI in the Brain: Empirical Comparison of MRI Sequences and Iron Oxide Particles

Parts of this Chapter have been published previously as N. Zarghami, A.A. Khrapitchev, F. Perez-Balderas, M. Sarmiento Soto, J.R. Larkin, L. Bau and N.R. Sibson as " Optimization of molecularly targeted MRI in the brain: empirical comparison of sequences and particles " in the International Journal of Nanomedicine, vol. 13, pp. 4345 - 4359, 2018. doi: 10.2147/IJN.S158071. Reproduction of this publication is permitted under the terms of the Creative Commons Attribution License (CC-BY).

3.1 Introduction

Preclinical molecular and cellular magnetic resonance imaging (MRI) is an evolving field of research with strong translational potential. Iron oxide particles are currently the preferred contrast platform for this application and have been thoroughly reviewed in the literature [157]–[160] and Introduction Chapter of this thesis. As discussed in Section 1.7.2.1, the magnetic core of these particles causes localised inhomogeneity of the local magnetic field, which leads to a reduction in the relaxation times of adjacent protons and the appearance of dark (hypointense) regions on T_2*/T_2 weighted MR images [161]. The degree of hypointense image contrast, or the susceptibility effect, is highly dependent on relaxivity values and the iron concentration of these agents [128], [162], as well as MRI parameters such as magnetic field strength [163], [164] and applied pulse sequence [163], [165], [166]. Two MRI sequences that are commonly used for the detection of iron oxide particles are T_2-weighted spin-echo (SE) and T_2*-weighted gradient-echo (GE) [167]. Balanced steady-state free precession (bSSFP) is another sequence used for MRI detection of iron oxide particles, which shows an interesting T_2/T_1 contrast, and offers very high SNR [168]. bSSFP has been used for *in vivo* tracking of iron loaded breast cancer brain metastasis cells and has shown high sensitivity for detection of these particles [123], [169]. However, this sequence is susceptible to an off-resonance field inhomogeneity "banding artifact", and an additional correction is needed [168] Although T_2*W-GE sequence is regarded as the gold standard for iron oxide-enhanced MRI [170]–[172], and 7.0 T is the most commonly used field strength preclinically, a robust comparison of other sequences (e.g. balanced steady-state free precession), and/or magnetic field strengths has yet to be demonstrated.

In Section 1.7.2.2 of the Introduction Chapter I introduced different types of iron oxide particles used in molecular imaging (USPIO, SPIO and MPIO) and their applications. Selection of the appropriate contrast agent for imaging depends largely on the research or clinical question to be addressed.

Over the last decade, molecular MRI of brain-immune system interactions has been the subject of numerous studies [97], [131], [140]–[143], [173], with iron oxide particles being conjugated to a variety of different ligands (including proteins, peptides, antibodies and carbohydrates) to target-specific molecular epitopes expressed in disease. MPIO are often the agent of choice for such targeted molecular imaging studies, having a number of postulated advantages over UPSIO. The micron size of these particles enables assessment of specific binding to the endovasculature, unlike USPIO that are susceptible to macrophage uptake and passive diffusion into the brain parenchyma across a leaky BBB [174], [175]. Moreover, the iron content of a single MPIO is 4.3 million times higher than that of a USPIO, yielding considerably greater contrast per particle, with the contrast effect extending up to 50 times the physical size of the particle [127]–[129], [176]. Finally, the increased surface area of MPIO greatly increases labelling valency and, hence, binding affinity to the molecule of interest, whilst their short blood half-life (< 2 minutes) compared to USPIO yields a high target-to-background ratio [131], [133], [177]. However, many of these advantages remain theoretical or have only been demonstrated *in vitro*, and a direct head-to-head *in vivo* comparison of molecularly targeted MPIO and USPIO has not previously been reported [140], [174].

In this Chapter the primary aims, therefore, are (i) to assess the relative sensitivities of three commonly used MRI sequences (single-gradient-echo 3D (GE3D), multiple-gradient-echo 3D (MGE3D), and balanced steady-state free precession 3D (bSSFP3D)) for the detection of iron oxide particles in mouse brain, (ii) to determine the effect of magnetic field strength (4.7 T-9.4 T) on the detection of iron oxide particles *in vivo*, and (iii) to compare the specificity and sensitivity of VCAM-MPIO and VCAM-USPIO for the detection of vascular cell adhesion molecule-1 (VCAM-1) in a mouse model of neuroinflammation.

3.2 Methods and Materials

3.2.1 MPIO Comparison

First, to identify the optimal commercially available MPIO for the *in vivo* molecular targeted studies, the aggregation potential, and physical properties (elemental analysis) of three different MPIO were compared: (1) Dynabeads MyOne tosylactivated MPIO (cat. no. 65501; lot. no. 138799150, Intvitrogen), (2) Dynabeads MyOne carboxylic acid (cat. no. 65011; lot. no. 155367010, Invitrogen, UK) and (3) ProMag 1 Series COOH (cat. no. PMC1N; lot. no. 10892, Bangs Laboratories Inc, USA).

3.2.1.1 MPIO Aggregation Assay; *In Vitro* and *In Vivo*

For the *in vitro* study, MPIO (MyOne tosylactivated, MyOne carboxylic acid and ProMag-COOH MPIO; 5 mg/ml) were diluted (1:50) in a solution of sucrose (39% w/w) in PBS to reduce Brownian motion. Samples were briefly vortexed, 20 µl of the solution was pipetted onto a glass slide, covered with a 2.5 cm glass coverslip and sealed to prevent solvent evaporation. Slides were scanned after preparation at 40X magnification on an Aperio Digital Pathology scanner (Leica Microsystems, UK). ImageJ (rsbweb.nih.gov) software was used for the aggregation analysis. A total surface of 100 mm^2 was cropped, flattened and transformed into binary.

To determine and visualise the degree of aggregation *in vivo*, naïve BALB/c mice (7-8 weeks old, n = 2/MPIO type; Charles River, UK) were injected via a tail vein with 4 mg Fe/kg of either (a) Dynabeads MyOne carboxylic or (b) ProMag-COOH MPIO. Dynabeads MyOne tosylactivated MPIO showed a high degree of aggregation in the previous *in vitro* study and were not included for the *in vivo* experiment. Mice were imaged on a 7.0 T MRI system (Agilent Technologies Inc., USA) using a T_2*W-MGE3D sequence (described in Section 2.6 of methods).

3.2.2 VCAM-MPIO Synthesis

Based on the aggregation study results, ProMag-COOH was chosen for the subsequent *in vivo* experiments. Conjugation protocol described in the Methods Chapter (Section 2.2.1) was followed for synthesis of VCAM-MPIO.

3.2.3 VCAM-USPIO Synthesis Steps*

VCAM-USPIO were generated using multi-step syntheses of different generations of USPIO as shown in Figure 3.1 and described below.

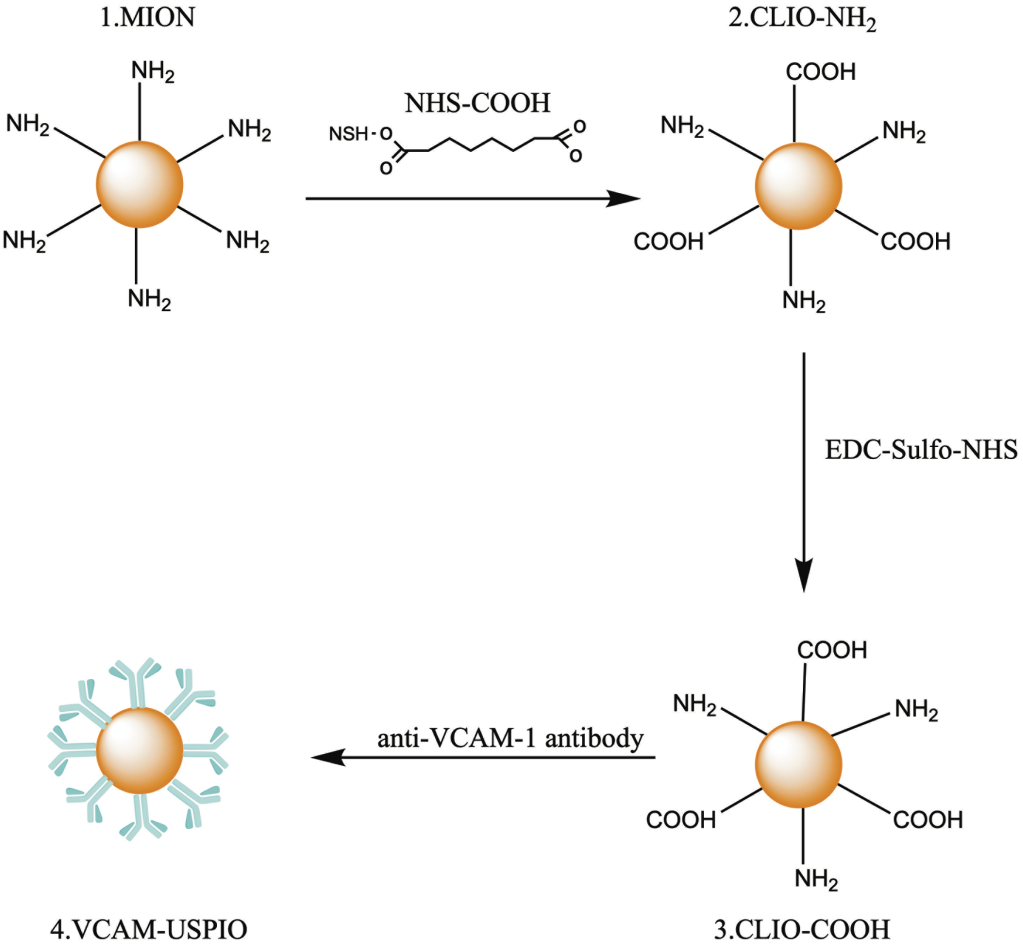


Figure 3.1: Multistep synthesis of VCAM-USPIO.

* Section 3.2.3 syntheses were performed by Dr. Francisco Perez-Balderas.

3.2.3.1 Monocrystalline Iron Oxide Nanocompounds

Monocrystalline iron oxide nanocompounds (MION) synthesis was performed according to the literature [178]. Briefly, 437.5 g of dextran T10 pharmaceutical quality (cat. no. 55100010, lot. no. HX 4271, Pharmacosmos, UK) were loaded into a 2 L 3 neck jacketed reactor equipped with a mechanical stirrer. Milli-Q® water (1000 ml) was added and the sample was stirred at 300 rpm until complete dissolution of the powder. Subsequently, 34.4 g of iron (III) chloride hexahydrate (mol; cat. no. 31232, SigmaAldrich, UK) and 12.4 g of iron (II) chloride tetrahydrate (mol; cat. no. 44939, SigmaAldrich) were added. The solution was stirred at 300 rpm and purged with Argon. The solution was cooled to 4ºC for 30 min; stirring rate was increased to 800 rpm and 200 ml of ammonium hydroxide 30% (cat. no. 221228, SigmaAldrich) was added using a peristaltic pump over 5 min. During ammonium hydroxide addition, the sample colour changed from orange to black. The solution was heated to 80ºC and kept at this temperature for 1 h. Subsequently, the solution was cooled to 25ºC, diluted with Milli-Q® water and transferred to a Tangential Flow Filtration (TFF) system (KR2 system, SpectrumLabs, USA) fitted with a 100 kDa mPES MidiKros filter module (cat. no. D02-E100-05-N, SpectrumLabs). The solution was concentrated to *ca.* 500 ml and dialfiltrated with Milli-Q® water to a conductivity less than 1 µS.

3.2.3.2 Crosslinked Iron Oxide (CLIO)-NH_2 Synthesis

Twenty ml of MION (10 mg Fe/ml) were placed into a 250 ml round flask equipped with a 30×16 mm oval stirrer bar. Whilst the solution was stirred at 500 rpm, 33.3 ml of NaOH 5 M was added at a rate of 168 ml/h. Subsequently, 13.3 ml of epichlorohydrin was added at a rate of 94 ml/h. The mixture was stirred at 1000 rpm for 8 h and then 20 ml of ammonium hydroxide (30%) was added at a rate of 168 ml/h. The mixture was transferred to a TFF system fitted with a 100 kDa mPES MidiKros filter module. The solution was dialfiltrated with Milli-Q® water to a conductivity less than 1 µS and further concentrated to 10 mg Fe/ml.

3.2.3.3 CLIO-COOH Synthesis

A freshly prepared solution of succinic anhydride (7.5 mg) in DMSO (0.5 ml) was added to a solution of CLIO-NH2 (8.2 mg Fe) in 1 ml NaHCO3 buffer 0.5 M. The sample was incubated for 6 h at 25°C on a shaker (1000 rpm) and additional succinic anhydride solution (0.5 ml) was added and incubated on the shaker for 17 h. The sample was purified on a Vivaspin 20 MWCO 30000 (cat. no. VS2022, Sartorius Ltd, UK), washed 3 times with 20 ml of Milli-Q® water and concentrated to 10 mg Fe/ml.

3.2.3.4 VCAM-USPIO Synthesis

For VCAM-USPIO synthesis, MES (0.2 M, 100 µl, pH 6.0) was added to the solution of CLIO-COOH (1 mg iron, 100 µl, 28.1 nm hydrodynamic diameter, 1.75×10^{14} particles/mg iron) and vortexed. Then, 10 µl of sulfoNHS (10 µmol; cat. no. 56485, SigmaAldrich) in MES buffer (1 M, pH 6.0) and 20 µl of EDC solution (10 µmol; cat. no. E6383, SigmaAldrich) in water were added. The mixture was incubated for 15 min at 25°C on a shaker (1000 rpm) and excess of EDC was quenched by addition of 50 mg of HL-COOH (Tentagel, cat. no. 86.333, SigmaAldrich) for 15 min. The sample was filtered and Tentagel was washed with 100 µl of MES buffer (0.2 M, pH 6.0). To this solution, 40 µg of anti-mouse VCAM-1 antibody (same antibody for MPIO) was added and the reaction was incubated for 24 h at 25°C on a shaker. Subsequently, to quench any remaining activated carboxylic acid, 100 µl of borate buffer (1 M, pH 8.5) was added and the solution incubated a further 24 h at 25°C on a shaker. The sample was centrifuged at 186000 g for 1.5 h, the supernatant discarded, and the pellet reconstituted in 1 ml of PBS. The sample was pelleted again (186000 g for 1.5 h), then reconstituted in 1 ml of PBS and pelleted as before. This final pellet was reconstituted in 100 µl of PBS.

3.2.4 Physicochemical Properties of VCAM-MPIO and VCAM-USPIO

The particle size of different generations of USPIO was measured by dynamic light scattering (DLS) on a Zetasizer Nano ZS (Malvern, UK), and reported as the z-average diameter. The polydispersity is reported as the coefficient of variation (CV) of the size distribution, which was

calculated as the square root of the mean of the polydispersity index (for USPIO) or provided by the manufacturer (for MPIO). The zeta potential was measured on a Zetasizer Nano ZS (Malvern, UK) in 0.1 M 4-(2-hydroxyethyl) piperazine-1-ethanesulfonic acid (HEPES) buffer at pH 7.0. The particle size of the MPIO was provided by the manufacturer as a volume-weighted mean diameter measured with a Coulter counter. The iron content of all three commercial MPIO and the USPIO was measured by ICP-OES on a Varian Vista MPX (Varian, UK) after acid digestion. The upper limit of COOH loading was estimated from the nitrogen content of a freeze-dried sample which was measured by combustion analysis. Results are reported as mean ± standard deviation of repeated measurements on the same sample.

3.2.5 Iron Content Per Particle and Estimation of Per Particle Properties

The mass of iron per particle was used as a conversion factor to relate intrinsic properties relative to the amount of iron (value per mmol of iron) to per particle properties (value for one particle). The mass of iron per particle was calculated as

$$\text{pg Fe/particle} = 10^9 \cdot \frac{\%\ \text{Fe}}{100} \cdot (\text{particles/mg})^{-1}$$

where % Fe is the weight/weight concentration of iron in a dry sample measured by ICP-OES and particles/mg is the number of particles per mg of dry sample. The latter is provided by the manufacturer for MPIO, whilst for USPIO it is calculated as

$$\text{particles/mg} = 10^{-3} \cdot \left[\frac{4}{3}\pi\left(\frac{d}{2}\right)^3 \left(\phi_{Fe_3O_4}\,\rho_{Fe_3O_4} + (1-\phi_{Fe_3O_4})\,\rho_{Dex}\right)\right]^{-1}$$

where d is the particle diameter, $\phi_{Fe_3O_4}$ is the volume fraction of magnetite in a dry sample, $\rho_{Fe_3O_4}$ is the density of magnetite, and ρ_{Dex} = 1.07 g/cm^3 is the density of hydrated crosslinked dextran [179]. The volume fraction of magnetite was calculated from the mass fraction of magnetite $\chi_{Fe_3O_4} = (\%Fe/100) \cdot [(3A_r(Fe) + 4A_r(O))/(3A_r(Fe))]$, where A_r(Fe) = 55.845 u and A_r(O) = 15.999 u are the atomic weights of iron and oxygen respectively, and the density ratio $\rho_{Fe_3O_4}/\rho_{Dex}$.

3.2.6 Assessment of VCAM Antibody Loading on MPIO and USPIO

VCAM-1 conjugated MPIO (ProMag-COOH, 10 μg) or USPIO (70 μg) were diluted in 200 of PBS buffer and 2 μl of Alexa Fluor 647 goat anti-rat IgG (H+L) (cat. no. A21091, 5 fluorophores per antibody, Invitrogen) was added. For MPIO, the number of VCAM-1 antibodies loaded on each MPIO was quantified as described in the Methods Chapter (Section 2.2.2). For USPIO, samples were centrifuged at 186000 g for 1.5 h, the supernatant discarded, and the pellet reconstituted in 1 ml of PBST. The samples were pelleted again (186000 g for 1.5 h) and reconstituted in 200 μl of PBS. Fluorescence intensity of the samples was measured and compared to a calibration curve composed of serial dilutions of Alexa Fluor 647 goat anti-rat IgG (H+L). Results are reported as mean ± standard deviation.

Previous experiments in our lab have suggested sonication of conjugated MPIO prior to *in vivo* administration in order to reduce aggregation [97], [132]. To assess the effect of sonication on antibody loading, MPIO were conjugated with rat anti-mouse IgG1 antibody (Table 2.1) as described in Section 2.2.1 of the Methods Chapter. IgG-MPIO were sonicated for 0, 2, 5, 10 and 15 minutes and the number of antibodies on the MPIO surface was quantified by FACS (Section 2.2.2).

3.2.7 Determination of MPIO and USPIO Relaxivity in Agarose Gel

MRI phantoms were prepared as described previously [134]. Unconjugated MPIO (ProMag-COOH) and USPIO were embedded in 2% w/v agarose gels at iron concentrations of 0.0025 – 0.2 mM. Gels were prepared in 15 ml tubes and heated at 95°C. MPIO and USPIO particles were added to the tubes and dispersed for a homogenous mixture. Samples were sonicated and kept undisturbed at room temperature until cool. MPIO and USPIO relaxitivities were measured using a spin-echo multi-slice sequence (SEMS) on a 7.0 T horizontal bore MRI system (Agilent Technologies, USA) with a 26 mm birdcage RF coil (Rapid Biomedical, Rimpar, Germany). Sequence parameters for the T_2 maps were: repetition time (TR) = 10 s, 12×echo time (TE) = [10 - 300] ms, spectral width (SW) = 100 kHz, matrix = 128×128, field-of-view

(FoV) = 72×72 mm, slice thickness = 2 mm, experimental time (Texp) = 4h 16 min. Sequence parameters for the T_1 maps were: TR = 10 s, TE = 10 ms, 12×Ti = [0.01 - 6.0] s, SW = 100 kHz, matrix = 128×128, FoV = 72×72 mm, slice thickness = 2 mm, Texp = 4h 16 min.

3.2.8 Mouse Neuroinflammation Model

Female BALB/c mice (7-8 weeks old, n = 24; Charles River, UK) were anaesthetised with isoflurane (1.5-2.0%) in 30% O_2: 70% N_2O, placed in a stereotaxic frame and a burr hole drilled above the injection site (co-ordinates from bregma: anterior +0.5 mm; left 2.0 mm; depth 2.5 mm). Using a glass microcannula (tip diameter *ca.* < 50 μm), 1 ng of mouse recombinant interleukin-1β (IL-1β; cat. no. 211-11B, Peprotech, UK) in 1 μl sterile PBS was injected into the left striatum to induce unilateral vascular activation [139] (more details in Section 2.4.3). Three hours after surgery [139], mice were injected via a tail vein with 4 mg Fe/kg of either (a) VCAM-MPIO (n = 12) or (b) VCAM-USPIO (n = 12).

3.2.9 MRI of Neuroinflammation Model

All MRI experiments were performed using horizontal, wide-bore superconductive 4.7, 7.0 or 9.4 T MRI systems (Agilent Technologies Inc., USA). The same size (ID = 26 mm) transmit/receive birdcage RF coils were used in all experiments. More specifications are provided in the Methods Chapter, Table 2.3.

Mice injected intravenously with VCAM-MPIO (n = 4 for each field strength) were imaged 1 hour after contrast agent administration, as previously reported. An imaging time-point of 13 hours post-injection was chosen based on the previous published data (i.e. *ca.* 5 × 2.5 h blood half-life for USPIO [132]) for mice injected with VCAM-USPIO (n = 4 for each field strength) to account for the longer circulation half-life [180], [181]. All mice were imaged with both T_2*W-MGE3D and bSSFP3D, respectively. MRI parameters and diagrams of these sequences are shown in the Methods Chapter Section 2.6.3.

3.2.10 Assessment of VCAM-MPIO and USPIO Binding

Following imaging, mice were transcardially perfusion-fixed under terminal anaesthesia and brains were removed, post-fixed and frozen down as described in Section 2.4.4 (Methods Chapter). Brains were cut at 10 μm and immunohistochemical staining for VCAM-1 and iron oxide particles (Perls' Prussian blue) was performed following the protocol in Section 2.5.2 and 2.5.3. Consecutive sections were also stained fluorescently for VCAM-1, as described in Section 2.5.6. Whole brain fluorescent images were taken at 20X magnification using an Aperio immunofluorescence slide scanner (Leica Biosystems, Germany).

3.2.11 Image Reconstruction

Images were reconstructed using an in-house MATLAB (MathWorks, USA) code*. The final MGE3D images were reconstructed as the square root of sum of squares (SqrtSOS) of individual echoes [182]–[184]. Based on previous data, the second single-echo (TE = 6.5 ms) was extracted from the MGE3D sequence to represent a single-echo gradient-echo (GE3D) dataset [97], [132]. For bSSFP3D, the final images were reconstructed by adding the individual frequency offsets using the same SqrtSOS algorithm as above [185], [186].

3.2.12 Image and Data Analysis

All MRI datasets were masked manually and the hypointensities were automatically quantified using an in-house MATLAB code (see Section 2.6.4 of Method Chapter for more details). The quantification of SNR was performed by measuring the signal intensity (SI_{brain}) within the mouse brain (excluding hypointensities) and standard deviation of background noise (SD_{noise}). For CNR I additionally measured the signal intensity as the effect of VCAM-MPIO or VCAM-USPIO (SI_{void}). Thus, SNR and CNR were estimated using the following calculations, respectively:

$$SNR = SI_{brain}/SD_{noise}$$

$$CNR = (SI_{brain} - SI_{void})/SD_{noise}$$

* The MATLAB reconstruction program was developed by Dr. Alexandre Khrapitchev.

3.2.13 Perls' Prussian Blue Staining Validation of Iron Oxide Particles

To assess whether Perls' Prussian blue staining is able to dye iron oxide particles, two carboxyl based MPIO, Dynabeads MyOne and ProMag-COOH (both with polymeric coating) were stained *in vitro* and *in vivo*.

For the *in vitro* assay: 1 mg Fe of carboxylic Dynabeads MyOne or ProMag, were added to a 1.5 ml Eppendorf tube. A mixture of solution A and B (described in Section 2.5.3) were added to the tubes. Images were taken at different time-points starting from 10 seconds to 20 minutes after the staining.

For the *in vivo* assay: Bilateral intracerebral injections of either 1 or 10 µg Fe/µl of Dynabeads MyOne carboxylic acid, to the right striatum and 1 or 10 µg Fe/µl of ProMag-COOH, to the left striatum were performed as described in Section 3.2.9, in female BALB/c mice (n = 1 per concentration). A control naïve mouse was injected bilaterally with PBS. Mice underwent MRI immediately using the T_2*W-MGE3D sequence to confirm successful injection and to assist with correlation of injection site and histology. Brains were taken for histological assessment of Prussian blue staining. For USPIO, positive control liver and spleen samples from mice previously injected with USPIO were included for the Prussian blue staining.

3.2.14 Blood Circulatory Half-Life: VCAM-MPIO, VCAM-USPIO and Untagged USPIO

To determine the blood half-life of VCAM-MPIO (ProMag-COOH), VCAM-USPIO and different generations of USPIO, particles were injected via a tail vein into female BALB/c mice (6-7 weeks old, n = 2/time-point, Charles River, UK) at a constant dose of 4 mg Fe/kg in 100 µl sterile PBS. At 0, 0.8, 1, 2, 2.5, 3, 5, and 10 minutes after injection for VCAM-MPIO and 1, 6, 13, 24, 48, 72 and 96 h after VCAM-USPIO injection, mice underwent anaesthesia with 2-3% isoflurane in 30% O_2 with 70% N_2 followed by thoracotomy. Blood was collected from the left ventricle using a 1 ml syringe with a 23G needle containing 1 µl of heparin sodium (25,000 I.U./ml, Wockhardt Ltd, UK). Blood samples (up to 1 ml) were oxygenated by placing in 15 ml tubes with a 100% O_2 atmosphere and inverting gently for 5 min until the colour changed

to bright red. Final blood volume (100 µl) was mixed with 1% agarose solution in PBS (100 µl), at 41°C and placed in a 500 µl microcentrifuge tube. T_2 relaxivities of samples were immediately measured using a 7.0 T MRI system. For T_2 relaxometery a simple 90° and 180° pulse sequence were used with a long TR (10 sec) and an adjusted array of TE for best fitting. Circulatory blood half-life was determined from the fitted one phase decay curve, constrained to a plateau at the average naïve blood sample value (n = 6, baseline).

3.2.15 Statistical Analyses

Statistical analyses were performed using Prism software (GraphPad, USA). The normality of the measured variables was tested using the Shapiro-Wilk test. For multiple comparisons, analysis of variance (ANOVA) followed by Tukey post-hoc tests were used.

3.3 Results

3.3.1 MPIO Comparison

Sizes and elemental analyses of the three different types of MPIO (MyOne tosylactivated, MyOne carboxylic acid and ProMag-COOH) are shown in Table 3.1. The aggregation potential of MPIO plays a critical role in the detection of true positive MRI signals *vs.* non-specific retention in preclinical experimental models. Therefore, first I looked at aggregation of these beads *in vitro*. Results shown in Figure 3.2 suggest the degree of aggregation to be: MyOne tosylactivated > MyOne carboxylic acid > ProMag-COOH. These results are in line with previous work (unpublished data) in our lab that suggests lower aggregation for MPIO with carboxylic acid functional groups. Therefore, for the *in vivo* study I visually compared aggregation of just the two types of carboxylic beads (MyOne *vs.* ProMag) in naïve mice. MRI data from mice injected with MyOne carboxylic MPIO showed significant retention of beads, whilst minimal hypointensities were detected in mice injected with ProMag-COOH (Figure 3.3). For this reason, from this point forwards, only ProMag-COOH were used for all molecular MRI *in vivo* experiments.

MPIO	Diameter[a]	C (%)	H (%)	N (%)	Fe (%)[b]	Functional group
MyOne tosylactivated	1.05	40.57	3.71	5.28	19.93	p-Toluen sulfonyl
MyOne carboxylic acid	1.05	38.13	4.16	3.58	23.04	carboxylic acid
ProMag-COOH	0.88	37.27	3.95	2.38	27.76	carboxylic acid

Table 3.1: Summary of different commercially available MPIO.

[a]According to manufacturer data in µm. [b]Elemental analyses were measured by ICP-OES.

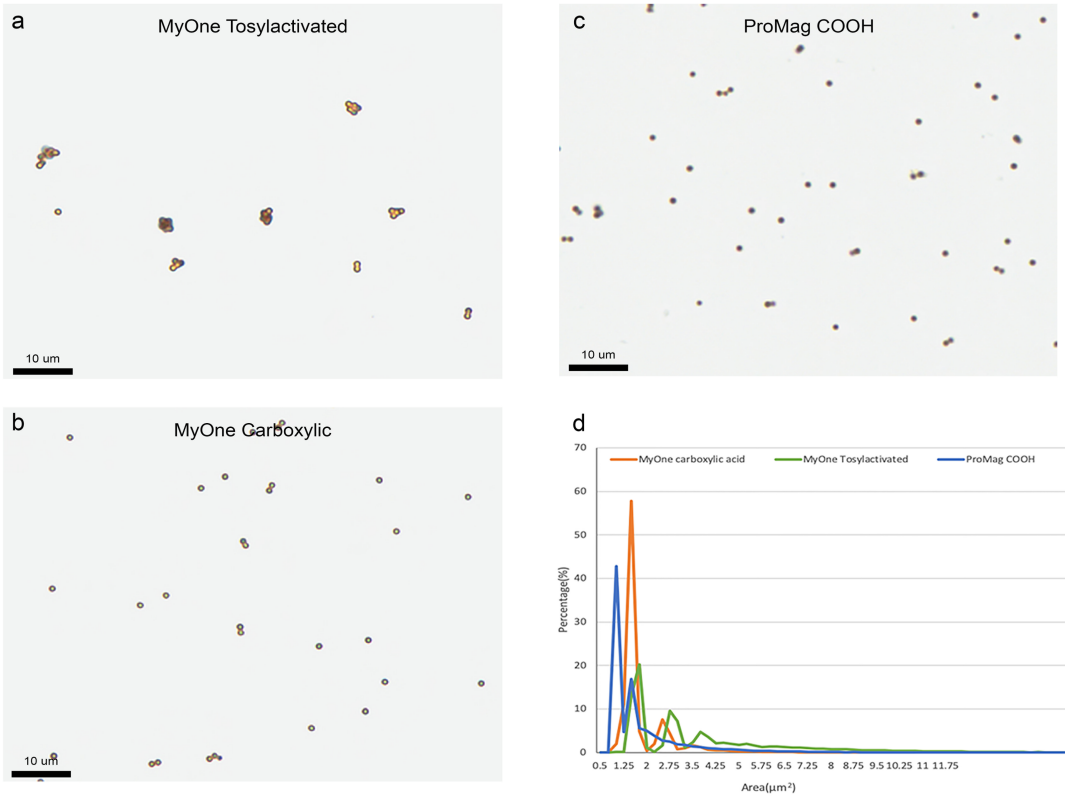


Figure 3.2: Aggregation analysis of MPIO *in vitro*.

Representative images illustrating degree of aggregation for **(a)** MyOne Tosylactivated, **(b)** MyOne carboxylic acid and, **(c)** ProMag-COOH MPIO. **(d)** Size distribution plots from the analysed microscopy images indicate highest degree of aggregation for MyOne tosylactivated (monomer is 1 µm) and lowest aggregation for Promag-COOH MPIO (~43% as monomers; 0.88 µm – blue line).

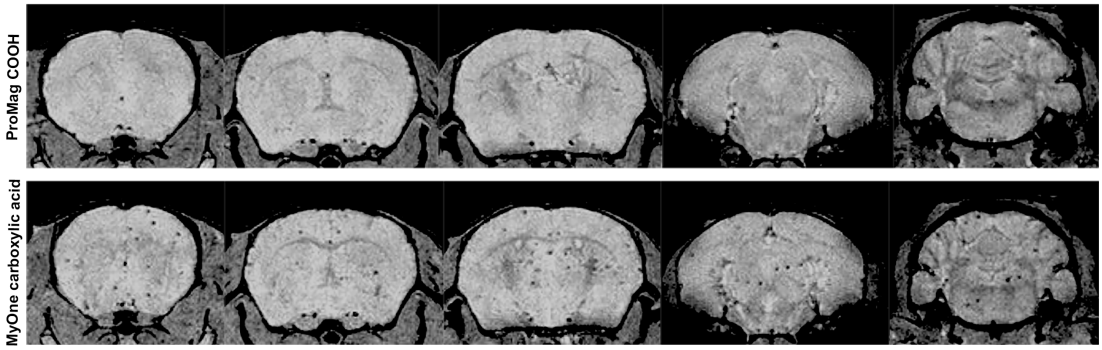


Figure 3.3: Aggregation of carboxylic MPIO *in vivo*.
Representative brain images (in rows, 5 images per brain) from a T_2*W-MGE3D dataset acquired from naïve mice injected with either ProMag-COOH or MyOne carboxylic acid MPIO. Hypointensities were observed in the mouse injected with MyOne carboxylic acid, whilst minimal hypointensities were found in the mouse injected with ProMag-COOH.

3.3.2 Physicochemical Properties of VCAM-MPIO and VCAM-USPIO

The z-average hydrodynamic sizes of different generations of USPIO measured by DLS were as follows: MION = 21.08 nm, CLIO-NH_2 = 27.66 nm, CLIO-COOH = 27.62 nm and VCAM-USPIO = 28.1 nm.

For VCAM-USPIO, the particle size distribution was moderately polydispersed, with a coefficient of variation of 36%. The particle size distribution of Promag-COOH MPIO was narrower, with a coefficient of variation of 15% and a mean diameter of 880 nm. Both USPIO and MPIO were negatively charged, with a zeta potential of -9.3 ± 0.9 mV and -25.6 ± 1.3 mV, respectively. The iron content of USPIO and MPIO was 30.6% w/w and 27.8% w/w, respectively, as measured by ICP-OES.

Quantitation of antibody loading showed the density of VCAM antibody to be 10490 ± 450 molecules per particle (n = 4) on MPIO, and 7.4 ± 3.1 molecules per particle on USPIO (n = 3). Although the number of antibodies per particle differs by three orders of magnitude, the surface density (number of antibodies per unit area) is comparable, with 4320 ± 200 molecules/μm^2 on MPIO and 3000 ± 1300 molecules/μm^2 on USPIO. The zeta potential of each agent did not change significantly after conjugation to the antibody (-10.3 ± 1.1 for VCAM-USPIO and

- 26.4 ± 1.4 mV for VCAM-MPIO), which is not entirely unexpected as the measurement pH falls within the isoelectric point range of rat IgG [187].The R_2 relaxivity of MPIO and USPIO, measured in agarose phantoms, was found to be 500 Hz·L/mmol Fe and 126 Hz·L/mmol Fe, respectively (Figure 3.4). Both values are consistent with previous literature reports [134], [140], [188], [189] and correspond to average relaxivity per particle of 1.18×10^{-9} Hz·L/particle for MPIO and the much lower value of 1.29×10^{-14} Hz·L/particle for USPIO. Properties of MPIO and USPIO are summarised in Table 3.2.

To determine the optimum duration of sonication prior to *in vivo* imaging, the number of conjugated IgG antibodies were measured on MPIO after various sonication times. Results showed that the sonication process decreased the number of loaded antibodies on MPIO. This reduction was more evident after 5 minutes (Figure 3.5). For this reason, for all *in vivo* imaging experiments in this thesis 2 minutes sonication before administration of contrast agent is chosen.

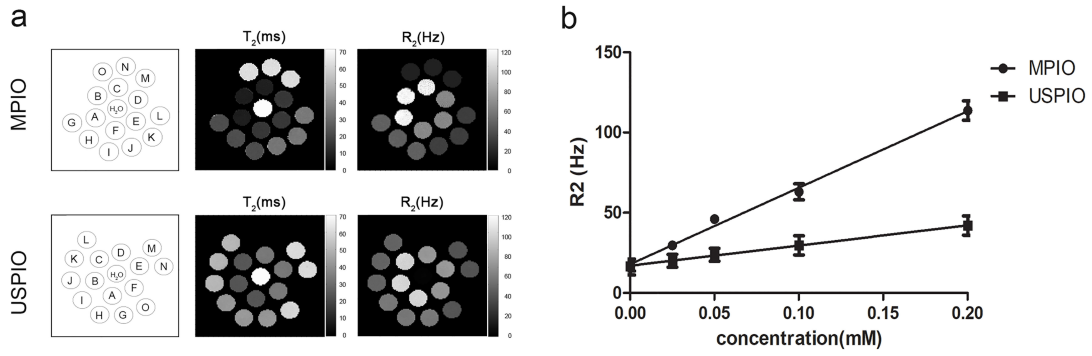


Figure 3.4: Relaxivity measurements of MPIO and USPIO in agarose gel.

(a) MPIO (top row) and USPIO (bottom row) were embedded in 2% agarose gel at the same iron concentrations (triplicates). [A-C]: 0.2 mM, [D-F]: 0.1 mM, [G-I]: 0.05 mM, [J-L]: 0.024 mM, [M-O]: PBS. T_2 (ms) and R_2 (Hz) maps generated at 7.0 T are shown. **(b)** T_2 relaxivity was measured for both particles; MPIO showed significantly greater relaxivity (steeper slope; $p < 0.0001$) than USPIO. Error bars are expressed as mean ± SD for n = 3.

	MPIO	USPIO
Mean diameter (nm)	880[a]	28.1
Coefficient of variation[b] (%)	15[a]	36
Iron content (% w/w)	27.8	30.6
Core diameter (nm)	5.1[c]	9-14[d]
Saturation magnetization (emu/g Fe)	115[c]	62[e]
Zeta potential (mV)	-26.4 ± 1.4[f]	-10.3 ± 1.1[g]
COOH loading (µmol/mg Fe)	122[a]	<1.24
Surface area of one particle[e] (μm^2)	2.4	0.0025
Iron content per particle (pg Fe/particle)	0.13	5.7×10^{-6}
Antibody density per particle (Ab/particle)	10490 ± 450[g]	7.4 ± 3.1[g]
Antibody density per unit area (Ab/μm^2)	4320 ± 200[g]	3000 ± 1300[g]
Bulk relaxivity (Hz·L/mmol Fe)	500	126
Particle relaxivity (Hz·L/particle)	1.18×10^{-9}	1.29×10^{-14}

Table 3.2: Physiochemical properties of MPIO and USPIO.
[a]Data provided by the manufacturer. [b]Relative standard deviation of particle diameters within a sample. [c]From ref. [188]. [d]From ref. [134]. [e]From ref. [187]. [f]Calculated from diameter assuming spherical particles. [g]Data are reported as mean ± SD of repeated measurements of the same sample.

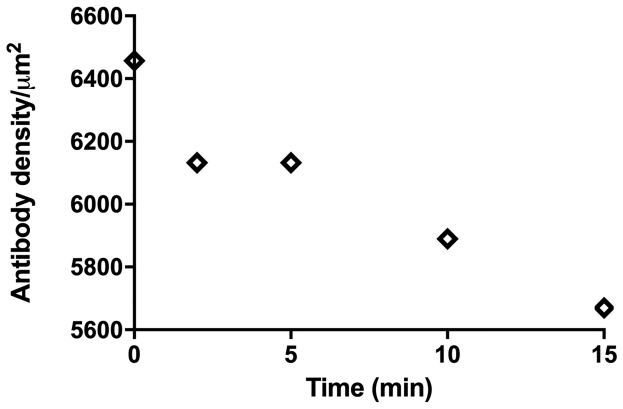


Figure 3.5: Effect of sonication on antibody loading.
IgG-MPIO were sonicated for 2, 5, 10 and 15 minutes. Graphs shows that the number of IgG conjugated antibodies per unit area (μm^2) decreases with longer sonication time. Two minutes sonication time was chosen for all *in vivo* experiments in this thesis.

3.3.3 Comparison of MRI Sequences and Field Strengths for Detection of Iron Oxide Particles

Representative images obtained using each of the three sequences (MGE3D, GE3D and bSSFP3D) at 4.7 T, 7.0 T and 9.4 T, with the same resolution and scan time, are shown in Figure **3.6**a and Figure 3.7a. Qualitatively, all three sequences enabled visualisation of hypointense foci in the brains of mice injected with either VCAM-MPIO (Figure 3.6a) or VCAM-USPIO (Figure 3.7a). However, the T_2*W-MGE3D sequence appeared to reveal hypointensities more prominently than either the T_2*W-GE3D or the T_2/T_1 weighted bSSFP3D sequence. Quantitative assessment of SNR (Figure 3.8a, c) and CNR (Figure 3.8b, d) for all sequences at each magnetic field confirmed that the highest SNR was conferred by the MGE3D sequence compared to both of the other sequences for both MPIO and USPIO (in all cases, ANOVA; $p < 0.001$, followed by Tukey's post-hoc tests; Figure 3.8). The T_2/T_1 weighted bSSFP3D sequence also showed significantly greater CNR than the standard GE3D sequence for the USPIO (Figure 3.8d). When comparing SNR and CNR of the optimal MGE3D sequence at different magnetic field strengths, a significant increase in both SNR and CNR was evident from 4.7 T to 7.0 T (in all cases, ANOVA; $p < 0.05$, followed by Tukey's post-hoc tests). However, no additional increase in either signal or contrast was gained by increasing field strength from 7.0 to 9.4 T.

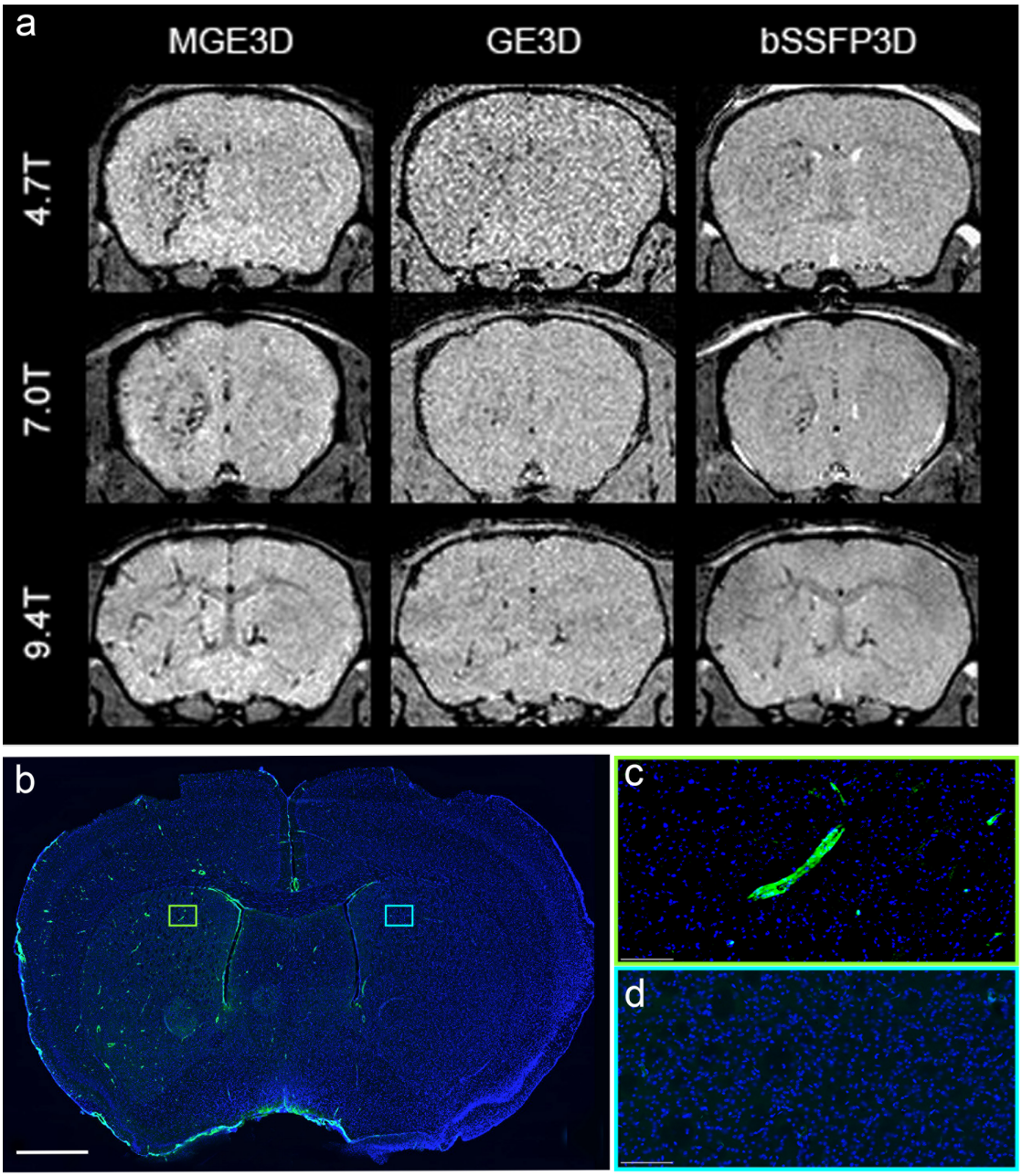


Figure 3.6: Representative *in vivo* images from mice 1 hour post VCAM-MPIO injection at different magnetic fields.

(a) Images acquired with three sequences of MGE3D, GE3D and bSSFP3D at three different scanners are shown. Intense low signal areas on the left side of the brain reflect the specific retention of MPIO on acutely activated vascular endothelium with visually absent contrast effects in the contralateral control hemisphere. MGE3D demonstrates better visualisation of hypointensities compared to other sequences. **(b-d)** Histological assessment of VCAM-1 upregulation at the injection side. Green vessels show unilateral upregulation of VCAM-1. Nuclei: DAPI; blue. Scale bars: b = 1 mm; c, d = 50 µm.

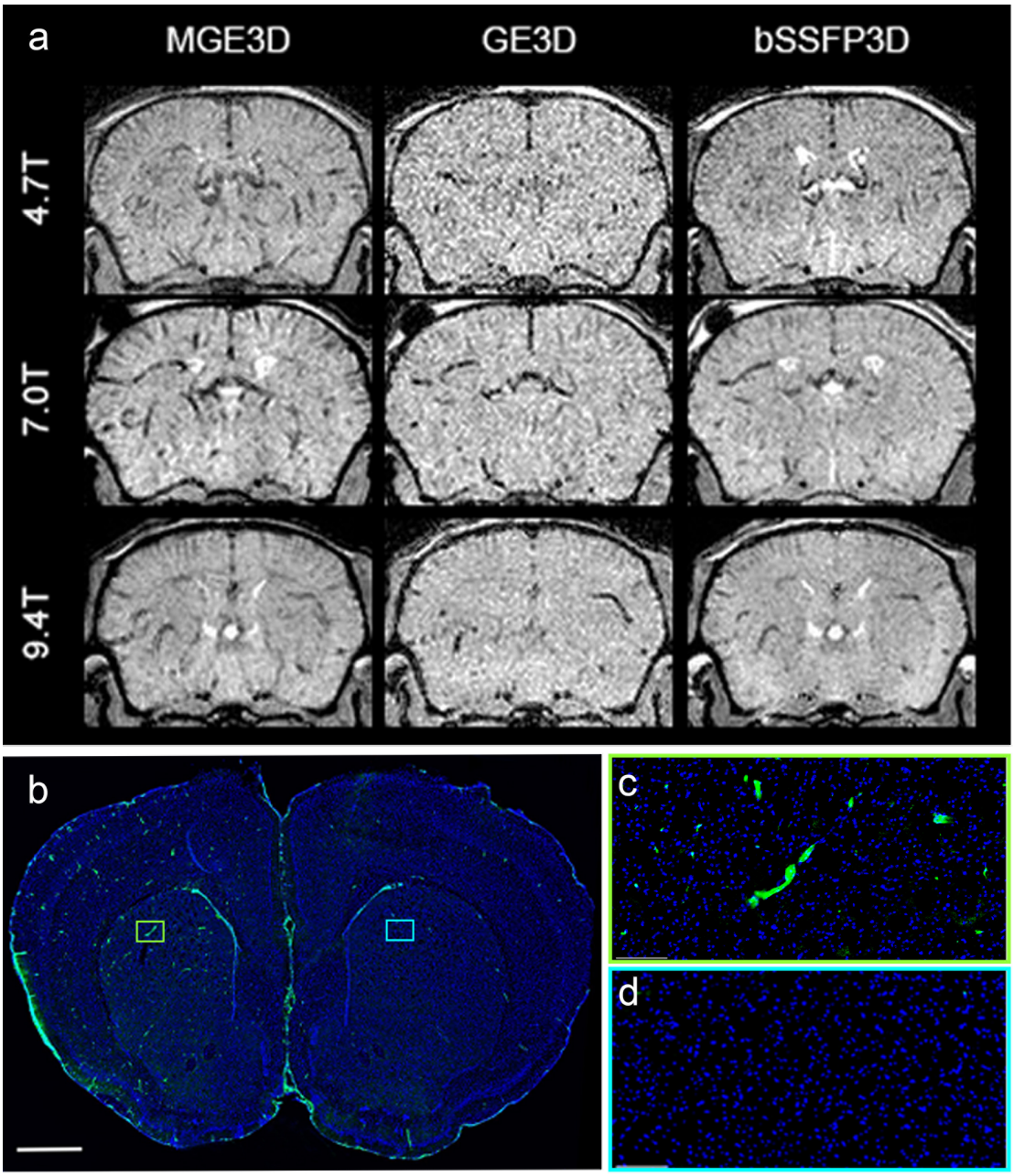


Figure 3.7: Representative *in vivo* images from mice 13 hours post VCAM-USPIO injection at different magnetic fields.

(a) Images acquired with three sequences of MGE3D, GE3D and bSSFP3D at three different scanners are shown. Hypointensities were detected in both hemispheres of the brains from VCAM-USPIO injected mice, indicating non-specific retention or presence of these particles. **(b-d)** Histological assessment of VCAM-1 upregulation at the injection side. Green vessels show unilateral upregulation of VCAM-1. Nuclei: DAPI; blue. Scale bars: b = 1 mm; c, d = 50 µm.

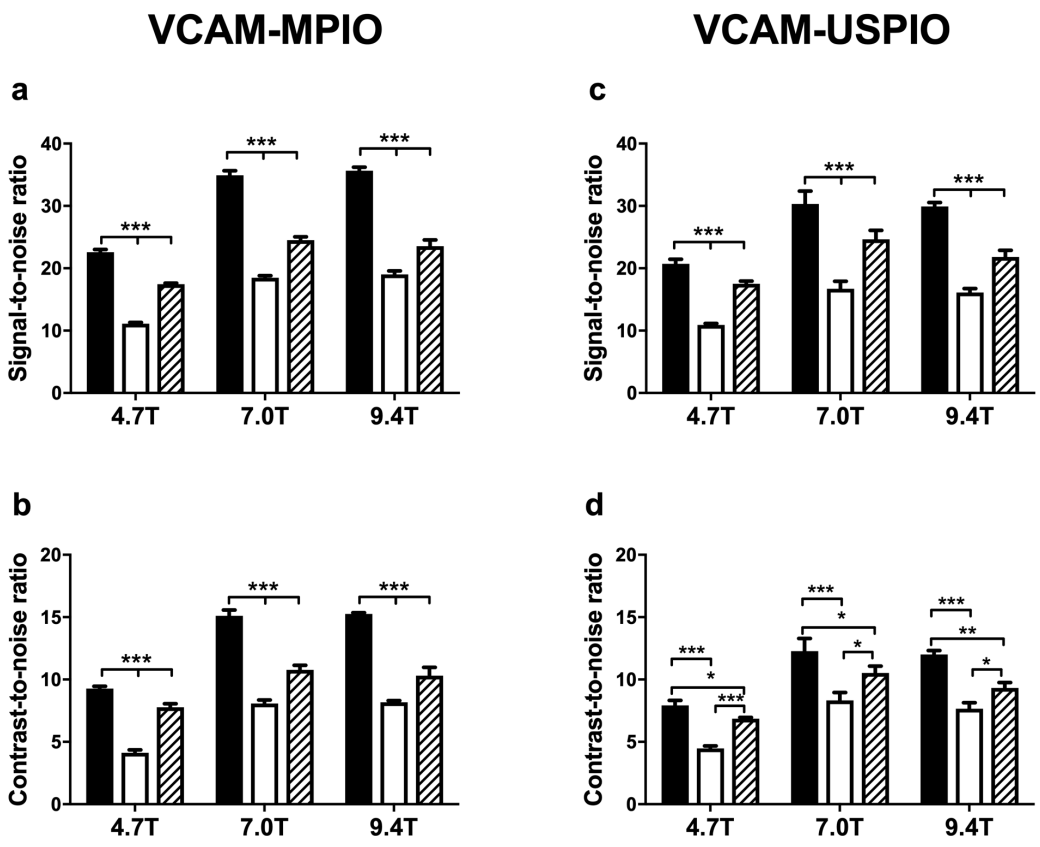


Figure 3.8: Quantitative comparison of MRI sequences for detection of VCAM-MPIO/-USPIO. Graphs showing comparison of SNR and CNR of MGE3D (black), GE3D (white) and bSSFP3D (hashed) sequences for detection of MPIO and USPIO at different magnetic field strengths. MGE3D yielded significantly higher SNR **(a, c)** and CNR **(b, d)** compared to the other sequences at all field strengths for both MPIO and USPIO detection. Error bars = SEM, *$p < 0.05$, **$p < 0.01$, ***$p < 0.001$.

3.3.4 Comparing Sensitivity and Specificity of VCAM-MPIO and VCAM-USPIO

Immunohistochemically, unilateral upregulation of VCAM-1 was evident in mice injected intracerebrally with IL-1β and intravenously with VCAM-MPIO (Figure 3.6 b-d). In accord with this unilateral upregulation, a marked unilateral contrast effect was evident in brain images at all field strengths and with all three sequences (Figure 3.6a). In contrast, in mice injected intracerebrally with IL-1β and intravenously with VCAM-USPIO, bilateral contrast effects were evident in all animals, with no apparent differences between the hemispheres (Figure 3.7a). Immunohistochemistry confirmed unilateral VCAM-1 upregulation (Figure 3.7 b-d).

Quantitative analysis of hypointense voxels (mean ± SEM) for all three field strengths showed a significant difference between the number of hypointense voxels in the injected and contralateral hemispheres for mice injected with VCAM-MPIO (4.7 T: 446 ± 119 vs. 229 ± 30; 7.0 T: 430 ± 47 *vs.* 253 ± 47; 9.4 T: 425 ± 98 *vs.* 214 ± 58; n = 4 per group, $p < 0.05$, Figure 3.9a), but no significant difference for VCAM-USPIO induced hypointensities (4.7 T: 1444 ± 75 *vs.* 1213 ± 125; 7.0 T: 1244 ± 90 *vs.* 1138 ± 36; 9.4 T: 1058 ± 28 *vs.* 933 ± 95; n = 4 per group). Immunohistochemically, VCAM-1 and Perls' Prussian blue staining revealed the presence of VCAM-MPIO in the lumen of VCAM-1-positive vessels following MRI. However, despite intense bilateral contrast effects observed by MRI, no VCAM-USPIO were detected on VCAM-1 positive vessels or within the brain parenchyma following MRI (Figure 3.9b).

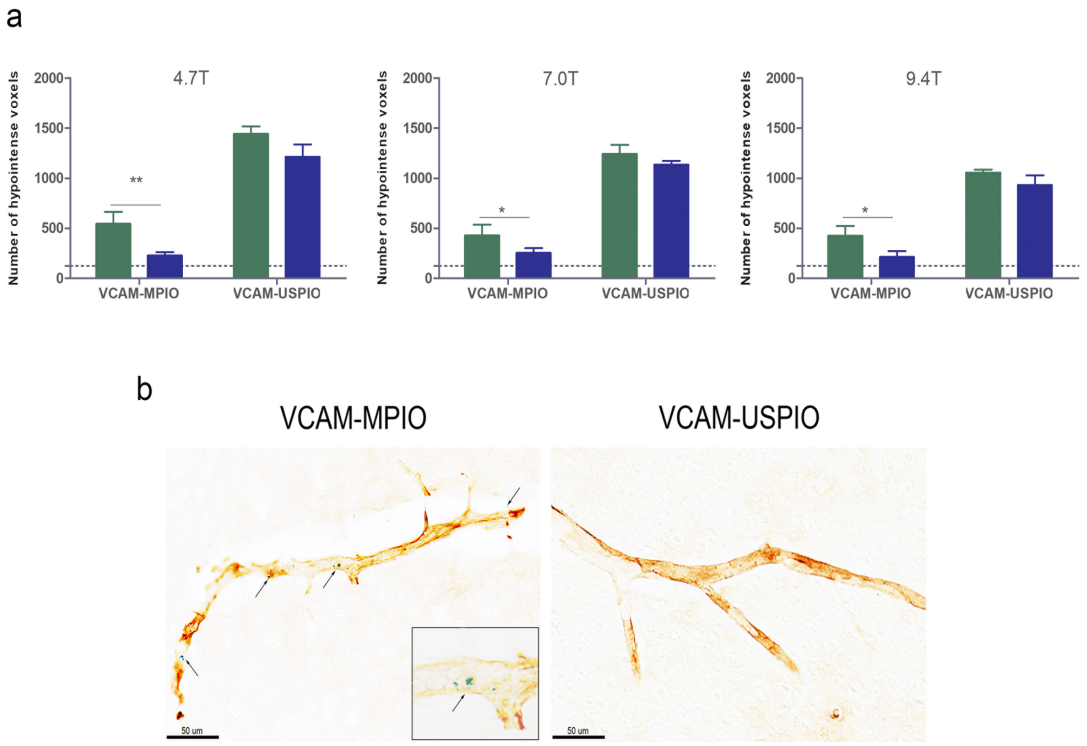


Figure 3.9: **Comparison of VCAM-MPIO and VCAM-USPIO sensitivity and specificity.** **(a)** Graphs showing quantitation of MPIO and USPIO induced hypointensities in injected (green bars) and contralateral (blue bars) hemispheres of mice injected intracerebrally with IL-1β and intravenously with VCAM-MPIO or VCAM-USPIO using the T_2*W-MGE3D sequence. The baseline level of endogenous hypointensities is shown with the dotted line (n = 2 naïve mice). A significant difference in the number of hypointensities was evident between the two hemispheres for VCAM-MPIO injected mice at all field strengths. In contrast no significant difference between hemispheres was found for VCAM-USPIO injected mice. n = 4/group; error bars = SEM, $*p < 0.05$, $**p < 0.01$. **(b)** Histological staining for VCAM-1 (brown) and iron beads (Prussian Blue) demonstrated upregulation of VCAM-1 on endothelial cells together with VCAM-MPIO binding (arrows); but not detectable VCAM-USPIO.

3.3.5 Blood Circulatory Half-Life: VCAM-MPIO, VCAM-USPIO and Untagged USPIO

Given the long half-life observed in VCAM-USPIO injected mice *in vivo*, the actual biological clearance of VCAM-USPIO and VCAM-MPIO were then measured and compared empirically. To this end, blood samples were collected from naïve mice injected with VCAM-MPIO or VCAM-USPIO at different time-points. The half-life of particle clearance was determined from the T_2 relaxivity of blood samples obtained at intervals after intravenous injection (Section

3.2.14). The half-life of VCAM-MPIO in the circulation was measured to be 1.2 min, in comparison to 16.5 h for VCAM-USPIO (Figure 3.10a, b). Furthermore, in order to compare these findings for VCAM-USPIO to previously published data [132], the blood clearance of different generations of USPIO was measured. The blood half-life of MION shown to be the shortest at 4.5 h, followed by 5.8 h for CLIO-NH_2. CLIO-COOH exhibited to have the longest half-life of 18 h compared to the other generations of USPIO (Figure 3.10c).

The pharmacokinetics and differences in blood clearance of iron oxide particles depend largely on their physiochemical properties, such as size, charge, surface nature, and composition [134]. It has been shown that increasing mean diameter of iron oxide particles increases the liver uptake, thus shorten the blood clearance (MPIO:1.2 min *vs*. USPIO:16.5 h) [134].

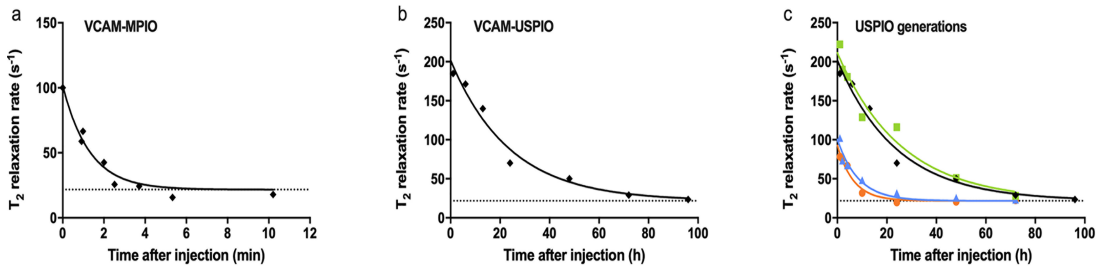


Figure 3.10: Blood clearance half-life of VCAM-MPIO, VCAM-USPIO and USPIO generations. Graphs showing T_2 relaxivity values of blood samples from mice injected at a constant dose of 4 mg Fe/kg of body weight with either **(a)** ProMag-COOH conjugated with VCAM antibody (0.88 µm diameter), or **(b)** VCAM-USPIO (28.1 nm diameter), or **(c)** different generations of USPIO: MION (orange line), CLIO-NH_2 (blue line), CLIO-COOH (green line) and VCAM-USPIO (black line), over time. The clearance half-lives were calculated to be: 1.2 min, 16.5 h, 4.5 h, 5.8 h and 18 h for VCAM-MPIO, VCAM-USPIO, MION, CLIO-NH_2, CLIO-COOH, respectively. Curves are fitted as a single-phase exponential decay constrained to a plateau at the average naïve blood sample values (n = 6, baseline; dotted lines).

Consequently, to determine whether contrast effects could be rising from unbound VCAM-USPIO within the blood, the bilateral contrast effects arising from VCAM-USPIO administration was further investigated in both naïve mice and mice injected intracerebrally with IL-1β. Mice were injected intravenously with VCAM-USPIO and imaged at different time-points

(1, 13 and 80 h) after injection (Figure 3.11). Results showed bilateral contrast effects and, hence, presence of VCAM-USPIO, in both cohorts at 1 and 13 h after injection. In both naïve and IL-1β injected mice, contrast effects arising from VCAM-USPIO were no longer evident 80 h after injection (i.e. *ca.* 5 × blood half-life (16.5 h) of VCAM-USPIO).

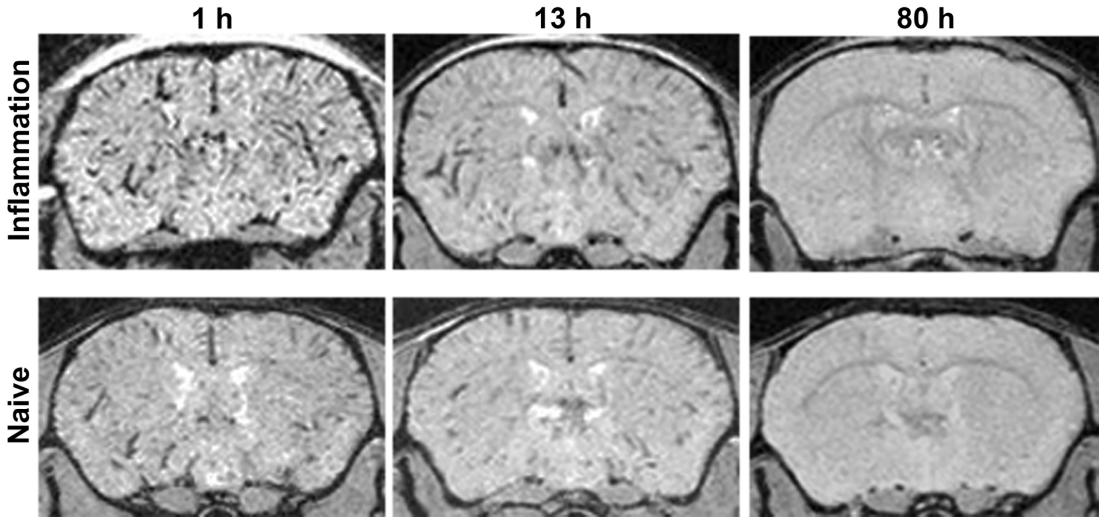


Figure 3.11: VCAM-USPIO blood circulation in an inflammation model and naïve mouse.
T_2*W-MGE3D image of mice injected with VCAM-USPIO at different time-points at 7.0 T – images show the bilateral presence of VCAM-USPIO in an inflammation model (top row) and naïve mouse (bottom row) at 1 and 13 hours after contrast agent administration. No signal was detected 80 hours after injection in both cohorts.

3.3.6 Perls' Prussian Blue Staining for Detection of Iron Oxide Particles

Finally, to test whether Prussian blue stains carboxylic MPIO, 1 mg Fe of Promag-COOH or MyOne carboxylic acid MPIO were stained directly in Eppendorf tubes. Results showed that the dye is able to penetrate through the coating of these beads and after 5 min their colour changed to different shades of blue (Figure 3.12).The same effect was also observed for histological samples from naïve mice injected intracerebrally with either 1 or 10 µg Fe/µl of each type of beads. No evidence of hypointensities or positive blue staining was found on MRI or histology for the control mouse injected bilaterally with PBS (Figure 3.12b).

Furthermore, to verify that Prussian blue can stain and detect USPIO (due to their small size), positive control samples (liver and spleen) from mice previously injected with USPIO were stained. The results indicate that it is possible to detect USPIO histologically (Figure 3.12c).

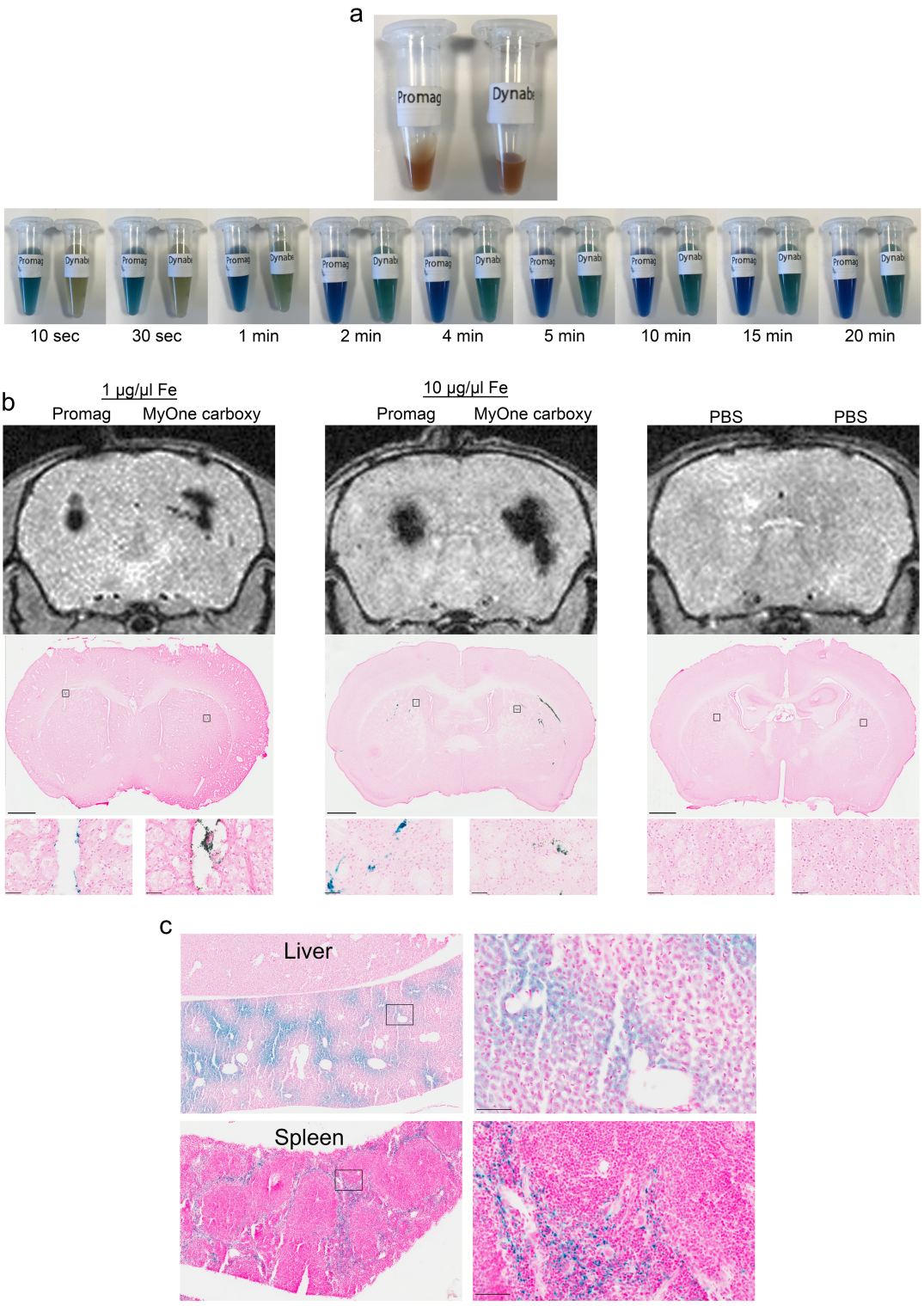


Figure 3.12: Perls' Prussian blue staining validation for detection of MPIO and USPIO.
(a) Colour spectrum of 1 mg Fe of ProMag or MyOne COOH MPIO after Prussian blue staining. **(b)** MRI and histological results from mice injected intracerebrally with either 1 or 10 µg Fe/µl of ProMag and Myone COOH MPIO. Positive Perls' staining (blue) demonstrated detection of beads on histology; counter staining Nuclear Fast Red. Scale bars = 1 mm (whole brain) and 50 µm (insets). **(c)** Positive control Prussian blue staining for USPIO and Nuclear Fast Red in liver and spleen. Scale bars = 50 µm.

3.4 Discussion

The overall goal of this Chapter was to identify the optimal pulse sequence, magnetic field strength and particle size for molecular MRI in mice. It has been demonstrated that the T_2* weighted multiple-gradient-echo sequence provides the highest signal-to-noise and contrast-to-noise ratios for detection of targeted iron oxide particles in mouse brain. All sequences showed an improvement in both SNR and CNR on increasing field strength from 4.7 to 7.0 T, but no further improvements in these parameters were observed on going to higher field. Finally, it has been shown that whilst targeted MPIO enable selective and specific detection of target expression on the cerebral vasculature, the long half-life and lower relaxivity, and hence CNR, per particle of the targeted USPIO will likely render these particles impractical for most applications of molecular MRI targeting endovascular ligands.

Several different MRI approaches have been used previously for mouse neuroimaging of iron oxide contrast effects. As the transverse magnetization decays with T_2*, it distorts the gradient-echo and, therefore, induces geometrical distortions [190]. Hence, conventional T_2* weighted gradient-echo (GE3D) is the most commonly used sequence for imaging such particles [142]. This sequence uses a single-echo sampled per line in k-space. Whereas, for T_2* weighted multiple gradient-echo (MGE3D), the recovery time (TR) is used to acquire additional echoes without increasing the total experimental time. Thus, a series of echoes at different TE are recorded for each line in k-space. This additional information can be used in a number of different ways, such as applying a SqrtSOS algorithm on the magnitude images from each echo to obtain MGE3D images [191]. The bSSFP3D sequence has also been used previously for tracking cells labelled with iron oxide particles and has shown advantages over conventional T_2 and T_2* weighted sequences [129], [169], [192].

The results of the current study suggest that by combining echoes in the MGE3D dataset, both SNR and CNR show significant improvements. Thus, T_2*W-MGE3D provides better depiction of both VCAM-MPIO and VCAM-USPIO contrast effects and greater overall image quality and

sharpness compared to conventional GE3D and bSSFP3D. Consequently, quantitation of contrast effects will be improved significantly through the use of the T_2*W-MGE3D sequence.

With regards to field strength, theoretically an improvement in SNR would be anticipated with increasing field strength. However, many factors can limit the results observed in practice. In this Chapter, improvements in both SNR and CNR were achieved for all sequences between 4.7 and 7.0/9.4 T, in accord with other rodent neuroimaging studies [193], [194]. Although a significant improvement was observed between 4.7 and 7.0 T, no significant gain was obtained by increasing field strength further to 9.4 T in the current study. One possible reason for this lack of further SNR benefit is that magnetic susceptibilities inherent in mouse brain produce field dependent perturbations in B_0 homogeneity, which result in degradation of SNR at 9.4 T. However, direct comparison of different magnetic field strengths suffers from a number of practical limitations [193]. For example, one consideration is the effect of different bore sizes. For the systems used in this study, the 9.4 T scanner had the smallest bore size (ID 160 mm), only allowing the use of a gradient coil with lower performance (gradient coil dimensions: OD 156 mm, ID 100 mm) than the 210 mm bore 7.0 T and 310 mm bore 4.7 T systems (gradient coil dimensions in both cases: OD 205 mm, ID 120 mm). Although it is not possible to generalise these results to all MRI scanners, given the vast array of different set-ups, our findings suggest that improved detection of iron oxide particles will be obtained by working at 7.0 T compared to lower field strengths. Beyond this field strength, the negative impact of field inhomogeneities and system constraints may counteract the benefits of higher field.

Moreover, it should be noted that the spatial resolution achievable in mice presented in this Chapter is considerably higher than the spatial resolution possible clinically (e.g. 3.0 T scanner). Thus, as voxel size increases, the number of MPIO per voxel should increase to induce detectable contrast. However, Shapiro *et al*. indicated that only 20% reduction in signal within a voxel is required to detect MPIO-induced contrast effects [128]. Another factor to consider is whether the SNR that is achievable at clinical field strength is sufficient to detect 20% signal reduction. The SNR required to achieve this reduction has been corresponded to be 15:1 [97]. Datasets from

human brain acquired with GE3D sequence on 3.0 T clinical scanner (~1 mm isotropic resolution; 9.5 minutes acquisition time) has shown to provide SNR of 21:1 for grey matter and 27:1 for white matter, which is more than sufficient SNR for detection of 20% signal change owing to specific binding of MPIO [97]. Furthermore, lower clinical imaging resolutions has an important outcome with regards to the very low false-positive rate. The average number of pixels encompass non-specific MPIO has calculated to be ~3.5, thus, the false-positive rate from non-specific MPIO retention should be zero at clinical imaging resolution [97].

It has been shown that in response to disease, injury and inflammation VCAM-1 upregulates rapidly on activated endothelial cells of the brain [195]. VCAM-1 targeted MPIO have been widely studied by a number of groups for detection of VCAM-1 in preclinical models of disease, and have shown high sensitivity and specificity for detecting this biomarker *in vivo* [97], [139]–[141], [173], [196]–[199]. As a simple model for inducing endothelial activation, it has been demonstrated that a focal unilateral injection of IL-1β causes unilateral hemispheric upregulation of adhesion molecules on the endovascular surface, including VCAM-1 [139], [196]. Therefore, this model was used to determine the relative sensitivity and specificity of VCAM-MPIO and VCAM-USPIO for detection of target expression *in vivo* and found dramatically different results. For VCAM-MPIO, a combination of high valency targeted delivery of a high payload of iron oxide to sites of inflammation and rapid clearance of MPIO from the blood conferred a high degree of specificity and sensitivity for target detection, as reported previously [97], [134], [139], [174]. These properties are crucial in detecting biomarkers such as VCAM-1, that have relatively low abundance on endothelial cells [135] and may only be detectable using particles with higher contrast owing to their greater iron payload.

In contrast to VCAM-MPIO, no target-specific binding was detected by either MRI or histology (using Perls' Prussian blue staining) in mice injected with VCAM-USPIO. Moreover, our data show that VCAM-USPIO were still present in the blood circulation 13 h post-administration, in both naïve and IL-1β injected mice. As a consequence of this long circulation time, marked background contrast effects were evident, which preclude detection of target-specific binding in

the injected hemisphere. This is not to say that target-specific binding is entirely absent in the case of VCAM-USPIO, but rather that it is undetectable owing to the continuing presence of circulating agent and the low relaxivity, and hence CNR, of the particles that are bound. Although, theoretically, it may be possible to identify an imaging window at which point all circulating USPIO have been eliminated, it is unlikely that specific binding will still be present and detectable at that time-point. Moreover, the necessity for a long-time window between contrast administration and imaging would also be less favourable for downstream clinical use, than an agent that allowed administration and rapid imaging within a short time-frame thereafter. In practice, I was unable to detection of any VCAM-USPIO binding on the activated endothelium 13 hours after injection histologically, and no specific VCAM-USPIO contrast effects were visible by MRI at 80 hours after injection when the blood pool has cleared.

Collectively, these findings demonstrate empirically that MPIO provide significant benefits for molecularly targeted MRI in brain and exhibit higher sensitivity than USPIO. Whilst for USPIO many effective applications have been reported, the small size of these particles is likely to be limiting for their application in molecular MRI studies, particularly of endovascular targets. One of the drawbacks of MPIO that is often discussed, is their limited translational capacity to the clinic. However, with the new generation of degradable biocompatible particles [134], this platform now has realisable translational potential.

3.5 Summary of Chapter 3

In this Chapter I have shown:

- ProMag-COOH MPIO aggregate less both i*n vitro* and *in vivo* compared to other commercially available MPIO.
- T_2*W-MGE3D sequence has higher SNR and CNR compared to GE3D and bSSFP3D for detection of iron oxide particles.
- Increasing field strength from 4.7 to 7.0 T improves both SNR and CNR.

CHAPTER 4

Activated Leukocyte Cell Adhesion Molecule (ALCAM) as an MRI Biomarker for Early Detection of Brain Metastases

Parts of this Chapter have been submitted as N. Zarghami, M. Sarmiento Soto, F. Perez-Balderas, A.A. Khrapitchev, C. Simoglou Karali, V.A. Johanssen, O. Ansorge and N.R. Sibson as "Activated Leukocyte Cell Adhesion Molecule (ALCAM) as an MRI biomarker for early detection of brain metastases" in the Journal of Neuro-Oncology. Reproduction of this publication is permitted under the terms of the Creative Commons Attribution License (CC-BY).

4.1 Introduction

In the previous Chapter I focused on optimisation of targeted iron oxide particles for molecular imaging and identifying the optimal MRI sequence and magnetic field strength to enhance their detection. These optimisations are of particular importance for further development of molecular imaging in mouse brain tumour models.

As discussed in the Introduction Chapter, the poor survival of patients with brain metastases is attributed, in part, to our incomplete understanding of the biological and molecular processes involved in their formation and, in part, to our inability to diagnose them in the early stages of onset. The presence of an intact blood-brain barrier (BBB) in the early stages of tumour formation limits accessibility of imaging contrast agents and, hence, detection at the micrometastatic stage. Thus, diagnosis of brain metastases currently relies on BBB breakdown, which occurs only in the later stages of tumour growth, and extravasation of gadolinium in order to make these tumours visible. The need to uncover brain metastases at the microscopic level when the BBB is still intact is urgent, enabling the potential benefit of early treatment in these patients to be assessed and, ultimately, improving prognosis.

The role of cell adhesion molecules (CAMs) on the vasculature in brain metastasis has been extensively discussed in Section 1.5 of the Introduction Chapter. Our lab has previously demonstrated that by targeting MRI contrast agents to the endothelial cell adhesion molecule vascular cell adhesion molecule-1 (VCAM-1), it is possible to detect the presence of brain metastases at the micrometastatic stage and significantly earlier than by conventional gadolinium-enhanced MRI [97], [98]. VCAM-1, however, is not the only CAM that is upregulated in the early stages of brain metastasis formation. As discussed earlier, activated leukocyte cell adhesion molecule (ALCAM) upregulation on cerebrovascular endothelial cells has previously been demonstrated in response to both inflammation and cytokine secretion [85], [200]. Moreover, previous work in our lab has shown that ALCAM is also specifically upregulated on cerebral vessels closely associated with breast cancer brain metastases, and to a greater extent than VCAM-1 [56]. On this basis, in this Chapter, I hypothesised that targeting

ALCAM might improve the sensitivity and specificity of brain metastasis detection to an even greater extent than has previously been achieved with VCAM-1-targeted MRI *in vivo*.

The aims of this Chapter, therefore, are (i) to determine whether ALCAM is upregulated in mouse models of brain metastasis not only from breast carcinoma, but also from melanoma and lung adenocarcinoma in the early stages of tumour establishment, (ii) to develop a novel MRI contrast agent using anti-ALCAM antibodies conjugated to micro particles of iron oxide (MPIO), and (iii) to assess whether ALCAM targeted MRI enables detection of brain metastases prior to BBB breakdown.

4.2 Methods

4.2.1 Cell Lines

For the mouse brain metastasis models, three brain tropic human-derived cell lines, MDA-MB-231-Br (breast), H1_DL2 (melanoma) and SEBTA-001 (lung adenocarcinoma) were used. Mouse endothelial cells (sEnd-1 or bEnd-3) and human brain microvascular endothelial cells (hCMEC/D3) were cultured for the *in vitro* experiments of this Chapter.

4.2.2 ALCAM Response to Cytokines; *In Vitro*

Mouse endothelial cells (sEnd-1, 50,000 cells/ml) and human brain endothelial cells (hCMEC/D3, 100,000 cells/ml) were seeded onto a 24-well plate. sEnd-1 cells were treated with recombinant murine interleukin-1β (IL-1β; cat. no. 211-11B, Peprotech, UK) or recombinant murine tumour necrosis factor (TNF; cat. no. 315-01A, Peprotech) at a concentration of 10 ng/ml or 50 ng/ml. hCMEC/D3 cells were treated with recombinant human IL-1β (cat. no. 200-01B, Peprotech) or recombinant human TNF (cat. no. 300-01A, Peprotech) at a concentration of 10 ng/ml or 50 ng/ml. Cells were stimulated for 20 hours. Normal medium (DMEM) was used for the control untreated group.

4.2.3 Endothelial ALCAM Response to Proinflammatory Agents; *In Vivo*

Female BALB/c mice (7-8 weeks old, n = 24; Charles River, UK) were intracerebrally injected with 1 µl of one of the following proinflammatory agents into the left striatum, to induce unilateral endothelial activation: (i) recombinant murine IL-1β (1 ng/µl); (ii) recombinant murine TNF (100 ng/µl); (iii) recombinant murine interferon-gamma (IF-γ; 10 ng/µl, cat. no. 315-05, Peprotech); (iv) recombinant murine tumour growth factor beta-1 (TGF-1β; 10 ng/µl, cat. no. 7666-MB-005, R&D systems, UK); (v) vascular endothelial growth factor (VEGF; 100 ng/µl, cat. no. 450-32, Peprotech); or lipopolysaccharide (LPS; 2 ng/µl, cat. no. L3755, SigmaAldrich). Brains were collected at two different time-points post-injection, to determine the kinetics of the ALCAM response on the vessels (6,18 hr; n = 2 per time-point).

4.2.4 Endothelial ALCAM Response in Presence of Tumour Cells; *In Vitro*

First, mouse endothelial cells (sEnd-1, 50,000 cells/ml) cells were seeded onto a 24-well plate and treated for 24 or 48 hours with tumour-conditioned medium (TCM) collected from MDA-MB-231-Br cells. TCM was collected at 90% of tumour cell confluency in T-175 tissue culture flask (Sarstedt, UK) and filtered using Filtropur syringe filter membranes (0.2 µm pore size, Sarstedt) to obtain cell-free medium. Medium was then centrifuged at 1200 rpm for 5 minutes. Experiments were performed in triplicates and medium (DMEM) was used for the control untreated group.

Subsequently, to simulate the *in vivo* scenario, mouse brain endothelial cells (bEnd-3) were co-cultured with MDA-MB-231-Br cells. bEnd-3 cells (300,000 cell/ml) were seeded onto Matrigel™ coated Millicell Slides for 6 hours, and until micro-tubules were formed. Then, tumour cells (MDA-MB-231-Br; 250,000 cell/ml) were added to top of the bEnd-3 cells and cells were fixed after 14 hours. Baseline levels of ALCAM was assessed in the wells seeded with either endothelial or tumour cells alone. Details of the 3D co-culture technique can be found in Section 2.3.4 of the Methods Chapter.

4.2.5 Mouse Brain Metastasis Models

Tumour cells (1×10^5 MDA-MB-231-Br, H1_DL2 or SEBTA-001 cells in 100 μl of sterile PBS) were injected into the left ventricle of female SCID mice (7–8 weeks old; Charles River, Kent, UK), under ultrasound guidance, as described in Section 2.4.2 .To measure ALCAM upregulation on metastasis-associated vessels during the early phases of tumour growth, mice (n = 4 per time-point) were perfused on day 7, 14, 21 or 28 after tumour injection for the breast cancer and melanoma brain metastasis models. Two later time-points were assessed for the lung cancer brain metastasis model, day 35 and 42, owing to the slower doubling time and, hence, tumour growth rate of the SEBTA-001 cell line [93], [98]. All experimental mice in this Chapter were transcardially perfusion-fixed under terminal anaesthesia, using 0.9% heparinised saline followed by PLP_{light}.

4.2.6 Immunohistochemistry and Immunofluorescence; Mouse Tissue

Mouse brain sections (inflammation and metastasis models), were immunohistochemically stained (ALCAM or VCAM-1) using the same protocol, as described in Section 2.5.2 and using the antibodies in Table 2.2.

For temporal measurement of ALCAM in the brain metastasis models, tumour bearing brain sections (10 μm) were stained for the ALCAM marker. The tumours were then outlined, and the number of strong positive pixels were calculated using built-in Positive Pixel Count v.9 algorithm on Imagescope (dark brown; ALCAM+) as described in Section 2.5.5 of the Methods Chapter. This measurement was reported as the percentage of positive pixels per tumour area. Over 30 tumour sections were analysed for each model at each time-point.

For immunofluorescent co-localisation of ALCAM and endothelial cells, three different endothelial markers were assessed: (i) anti-CD31; (ii) anti-glucose transporter-1 (GLUT-1); and (iii) anti-laminin (specifications of these antibodies can be found in Table 2.2). Images were acquired using an inverted confocal microscope (LSM-780; Carl Zeiss Microimaging) with constant imaging parameters and analysed using Zen software (Carl Zeiss). Co-localisation

analysis between ALCAM and endothelial markers was performed using an in-house plugin* for Fiji open-source software. The background fluorescent intensity was first measured in non-tumoural regions, and the signal was set as threshold. The plugin measured the percentage of overlapped area for each pair of markers, above a user set threshold for each signal. More than 20 tumour sections were analysed for each model at each time-point.

4.2.7 Immunohistochemistry; Human Tissue

Expression of ALCAM was assessed in human brain metastasis biopsies from breast, melanoma and lung adenocarcinoma. All human samples were obtained from the Oxford Brain Bank, licensed by the Human Tissue Authority and operating under generic Research Ethics Committee approval (Reference 15/SC/0639). A Melanin bleaching method was used for melanoma brain metastasis samples. Details of this technique can be found in the Methods Chapter (Section 2.5.4). Biopsies were stained for ALCAM and CD34 following the protocol in Section 2.5.4. All histological slides were digitally scanned on an Aperio CS2 Brightfield scanner (Leica Biosystems) at X20 or X40 magnification and analysed using Imagescope (v.12.3.2; Leica Biosystems) software.

4.2.8 ALCAM-MPIO Synthesis

Three different primary antibodies against mouse ALCAM were evaluated: (1) R&D systems; (2) LifeSpan Biosciences, Inc.; and (3) eBioscience™ Fisher Scientific. To construct ALCAM-MPIO, antibodies were conjugated to ProMag-COOH MPIO, using the protocol as described in detail in Section 2.2.1. As a control, MPIO were conjugated with a rat anti-mouse IgG1 antibody. The number of antibodies (ALCAM or IgG1) loaded on the MPIO was measured using a BD FACS-Calibur flow cytometer, on channel FL4 (661/16 nm band pass filter), as described previously [134], [201]. Antibody loading was determined against a standard calibration curve using Quantum Alexa Fluor 647 MESF (Bangs Laboratory Inc., USA).

* Fiji co-localisation plugin was developed by Dr. Vasiliki Economopoulos.

4.2.9 ALCAM-MPIO Binding Assay under Static and Flow Conditions

For the static *in vitro* binding assay, sEnd-1 cells (125,000 cells/ml) were seeded onto a 24-well plate. Cells were stimulated with mouse TNF at a concentration of 10 ng/ml. After 20 h, 6.25 μg MPIO/ml, conjugated with either ALCAM (R&D, LSBio or eBio) or IgG were added to the wells. Plates were then placed on a bench-top rocker for 5 minutes at room temperature. Cells were thoroughly washed with PBS for 3×10 minutes on a shaker (300 Mot/min), then fixed with 4% formaldehyde (Pierce™ 16% Formaldehyde (w/v), cat. no. 28906) for 10 minutes at 4°C, washed with PBS and stored in the cold-room (4°C). sEnd-1 cells were fluorescently stained for ALCAM, and MPIO were visualised using either a Texas Red anti-rat antibody (1:100, cat. no. TI-9400, Vector Laboratories) or a Texas Red anti-rabbit antibody (1:100, cat. no. TI-5000, Vector Laboratories) for cells treated with LifeSpan Biosciences ALCAM-MPIO. Confocal fluorescent images were taken at X20 magnification, using Leica SP8 (Germany) and the percentage of co-localised red (MPIO) and green (ALCAM) pixels was calculated for each field-of-view (FoV). The ALCAM antibody showing the highest MPIO loading and static binding was chosen for the subsequent *in vitro* flow experiment and *in vivo* studies.

To measure the binding capacity of antibody-conjugated MPIO under flow conditions, glass capillaries (ID 0.2 mm, cat. no. cv-2033-b-100, CM Scientific, UK) were glued to syringe needles (blunt 22G, cat. no. FIS5601078, Intertronics, UK) and dried for 12 hours. The capillaries were then dried in a closed chamber containing phosphorous pentoxide (cat. no. P/2960/50, Fisher Scientific) for at least 6 hours. To functionalise the capillaries, they were filled and incubated for 16 h at 80°C with a mixture of o-xylene anhydrous (cat. no. 294780, SigmaAldrich), TEGOPS (triethoxy-(3-glycidyloxypropyl) saline cat. no. T2675, TCI chemicals, UK) and DIPEA (N, N-Diisopropylethylamine, cat. no. 496219, SigmaAldrich); ratio 1000:320:10, respectively. The capillaries were next washed with 1 ml methanol and dried by flushing with air. After 4 hours in a closed chamber containing phosphorous pentoxide (to remove the moisture), capillaries were filled using a micro-syringe with recombinant mouse ALCAM protein (cat. no. 1172-AL-050, R&D Systems) at a concentration of 100 μg/ml in PBS and incubated for 24 hours at room

temperature. Subsequently, capillaries were washed with PBS and incubated for 24 hours with 10 mM ethanolamine (cat. no. 8.00849.0100, Merck, USA) to quench the remaining functional groups. Capillaries were washed with PBST followed by PBS and stored at 4°C in PBS.

For the flow experiment, ALCAM-MPIO or IgG-MPIO were fluorescently labelled using 2 μg of a goat anti-rat FITC (cat. no. ab6840, Abcam, UK) fluorophore. To mimic the blood viscosity, fluorescently labelled ALCAM-MPIO or IgG-MPIO were diluted with 30% sucrose in PBS to a final concentration of 0.1 mg MPIO/ml. A custom-built capillary holder was mounted on a Nikon TE 2000-U fluorescent microscope. The capillaries were attached to a peristaltic pump (Dial 10 (20-25 μl/min); 120U Bench-top multi-channel, Watson Marlow, UK) and ALCAM-MPIO or IgG-MPIO were pumped through the capillaries. After 2 minutes, images were acquired across 10 separate FoV along the capillaries using X40 magnification and the FITC channel. The number of bound ALCAM-MPIO or IgG-MPIO per FoV was counted manually.

4.2.10 *In vivo* Brain Imaging

For the *in vivo* imaging experiment, two time-points, day 21 and 28 after tumour cell injection, were chosen for the breast and melanoma brain metastasis models. These time-points were selected based on previous studies, which have shown that, for these models, tumours are still at the micrometastatic stage and the BBB is intact up to at least day 28 [97], [98]. A single time-point, day 42, was used for the lung brain metastasis model, owing to the slower growth rate. On the day of imaging, tumour bearing mice were injected intravenously with either ALCAM-MPIO or control IgG-MPIO. Mice were placed in a 7.0 T MRI spectrometer (Agilent Technologies Inc., USA). After a 30 minutes warm-up scan to bring the gradient coils to constant temperature, mice were imaged with a 3D T_2*W-MGE3D, followed by acquisition of pre- and post-gadolinium-DTPA T_1W images, to assess the BBB permeability [201]. ALCAM imaging experimental plan is shown in Figure 4.1. Details of MRI sequences and mouse setup are described in detail in the Methods Chapter (Section 2.6).

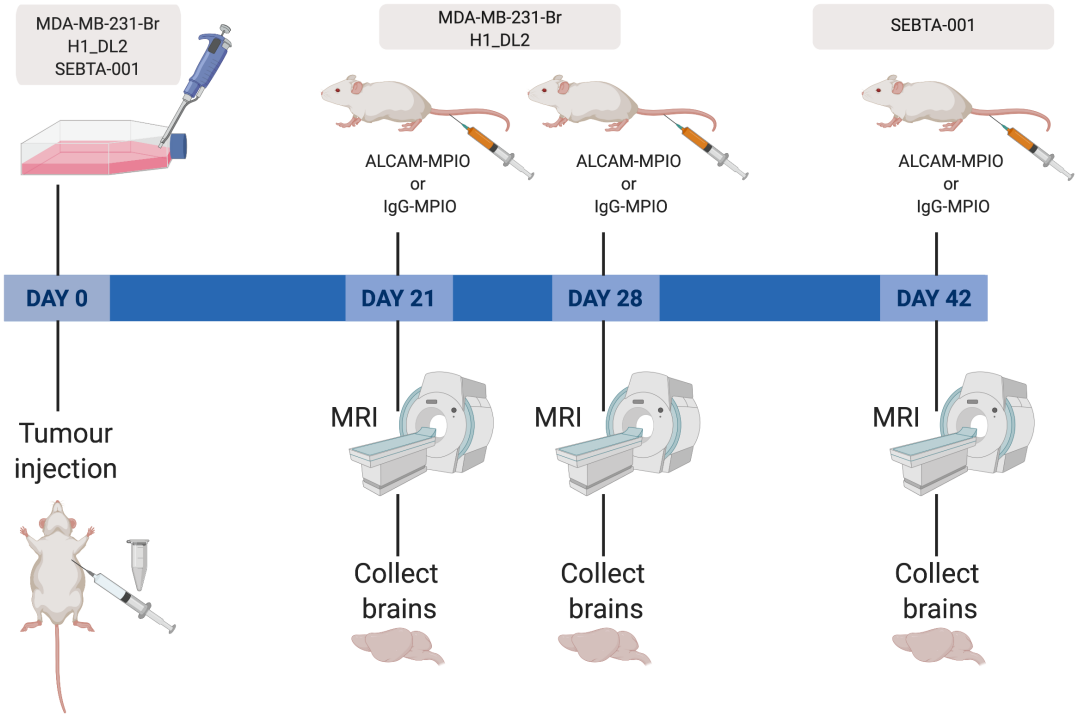


Figure 4.1: ALCAM imaging experimental plan in the brain metastasis models.

4.2.11 MRI and Histology Co-Registration

To determine the sensitivity of ALCAM-MPIO imaging, every other section (10 µm) of whole mouse brain was immunostained for ALCAM and tumour volume (μm^3) calculated for cohorts imaged on day 21 after tumour cell injection for MDA-MB-231-Br and H1_DL2 models, and day 42 for SEBTA-001 model. Volumetric and anatomical maps of tumours based on histology were generated and visually compared with the anatomical location of hypointensities on T_2*W-MGE3D MR images. Spatial correlation between histology and MRI was assessed blind, by an independent observer[†].

4.2.12 Statistical Analysis

Statistical analyses were performed using Prism (GraphPad Software, USA). Parametric analyses of variance (ANOVA) was applied after assessing normality of variables using the Shapiro-Wilk test. Tukey post-hoc tests were conducted to identify significant ($p < 0.05$)

[†] Dr. Vanessa Johanssen assisted with MRI and histology co-registration.

differences between groups. All error bars on graphs are shown as standard error of the mean (SEM) and the level of significance is shown with asterisks; *$p < 0.05$, **$p < 0.01$, ***$p < 0.001$.

4.3 Results

4.3.1 Evaluating Endothelial ALCAM Upregulation in Response to Cytokines

The role of ALCAM as a mediator involved in leukocyte migration into the CNS and its upregulation in response to proinflammatory cytokines has been demonstrated previously *in vitro* [202], [203]. To confirm these findings, mouse endothelial (sEnd-1) and human brain endothelial cells (hCMEC/D3) were treated with IL-1β or TNF for 20 hours (10 ng/ml and 50 ng/ml). ALCAM immunocytochemistry showed upregulation of this marker in both mouse and human endothelial cell lines, treated with both cytokines and doses (Figure 4.2). Low expression of ALCAM was detected on un-treated endothelial cells, and no signal was detected for the ALCAM negative control staining (Figure 4.2).

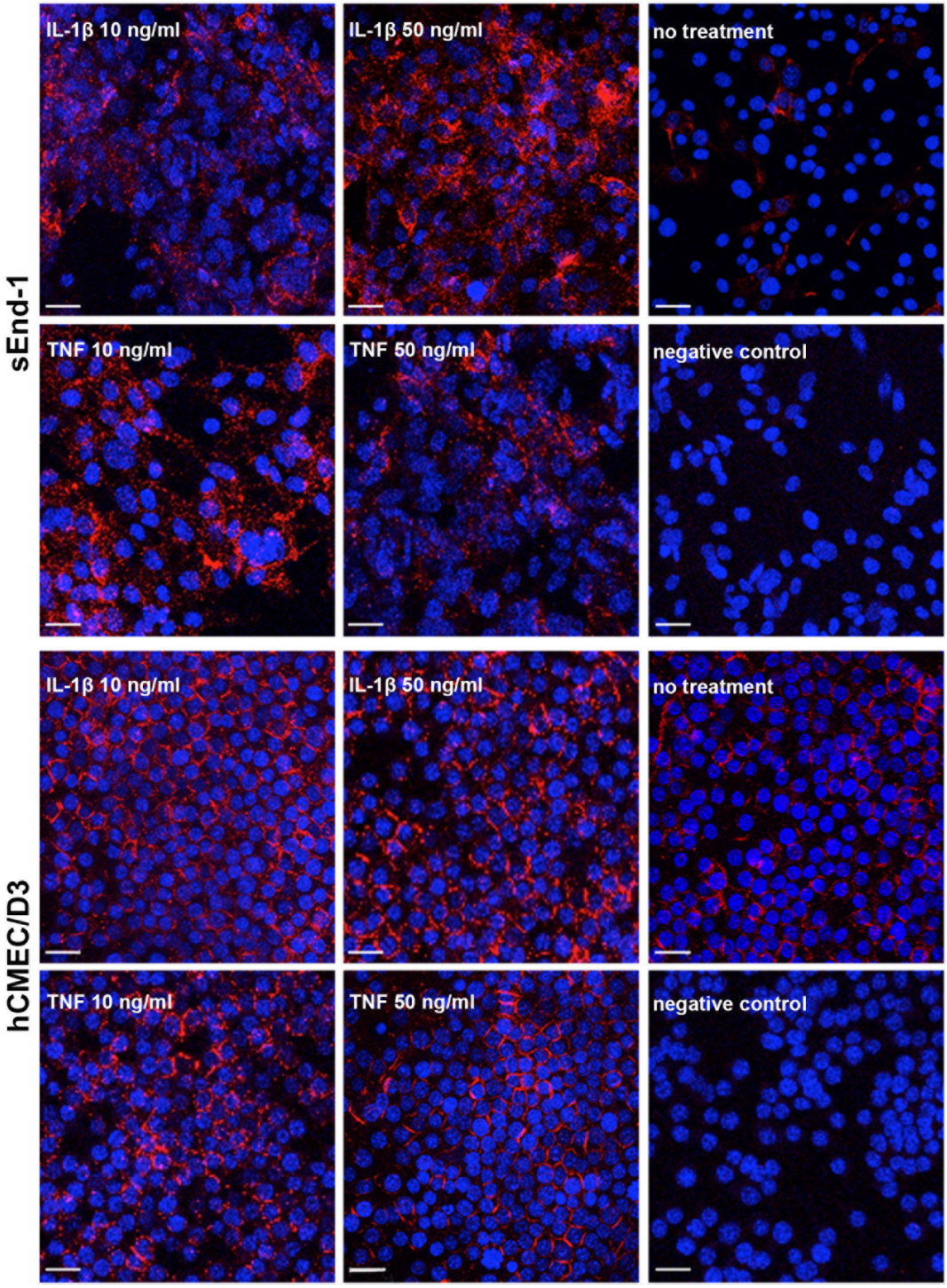


Figure 4.2: ALCAM response to cytokines on mouse and human endothelial cells.
Mouse endothelial cells (sEnd-1) and human brain endothelial cells (hCMEC/D3) treated with different concentration of IL-1β and TNF (10 and 50 ng/ml). ALCAM (red) is upregulated in response to these cytokines after 20 hours of stimulation. Baseline levels of ALCAM cultured in normal media are shown. No signal was detected in the red channel for ALCAM negative control staining. Nuclei: DAPI; blue. Scale bars = 20 μm.

In contrast, *in vivo* models of ALCAM upregulation, in brain specifically, are lacking. Therefore, with the aim of developing a robust acute mouse inflammation model, that could be used as a proof-of-principle model to test ALCAM-MPIO binding *in vivo*, mice were intracerebrally injected with an array of proinflammatory agents (IL-1β, TNF, IF-γ, TGF-β, VEGF or LPS). Mice were euthanised either 6 or 18 hours after injection. Histological samples were stained for both ALCAM and VCAM-1 (as a positive control for vessel activation and a successful intracerebral surgical procedure). The contralateral hemisphere was used as the negative control for the injected hemisphere (ipsilateral). Surprisingly, histological assessment of ALCAM expression showed no positive vessels in the stimulated hemisphere even 18 hours after injection of any proinflammatory agents (Figure 4.3). This finding is in contrast to the above *in vitro* findings, which showed upregulation of ALCAM on mouse and human endothelial cells in response to both IL-1β and TNF, as has also been shown previously [202], [204], [205]. Histological assessment of the same injected mice showed VCAM-1 upregulation in the stimulated hemisphere with minimal expression in the contralateral side for all the proinflammatory agents (Figure 4.4).

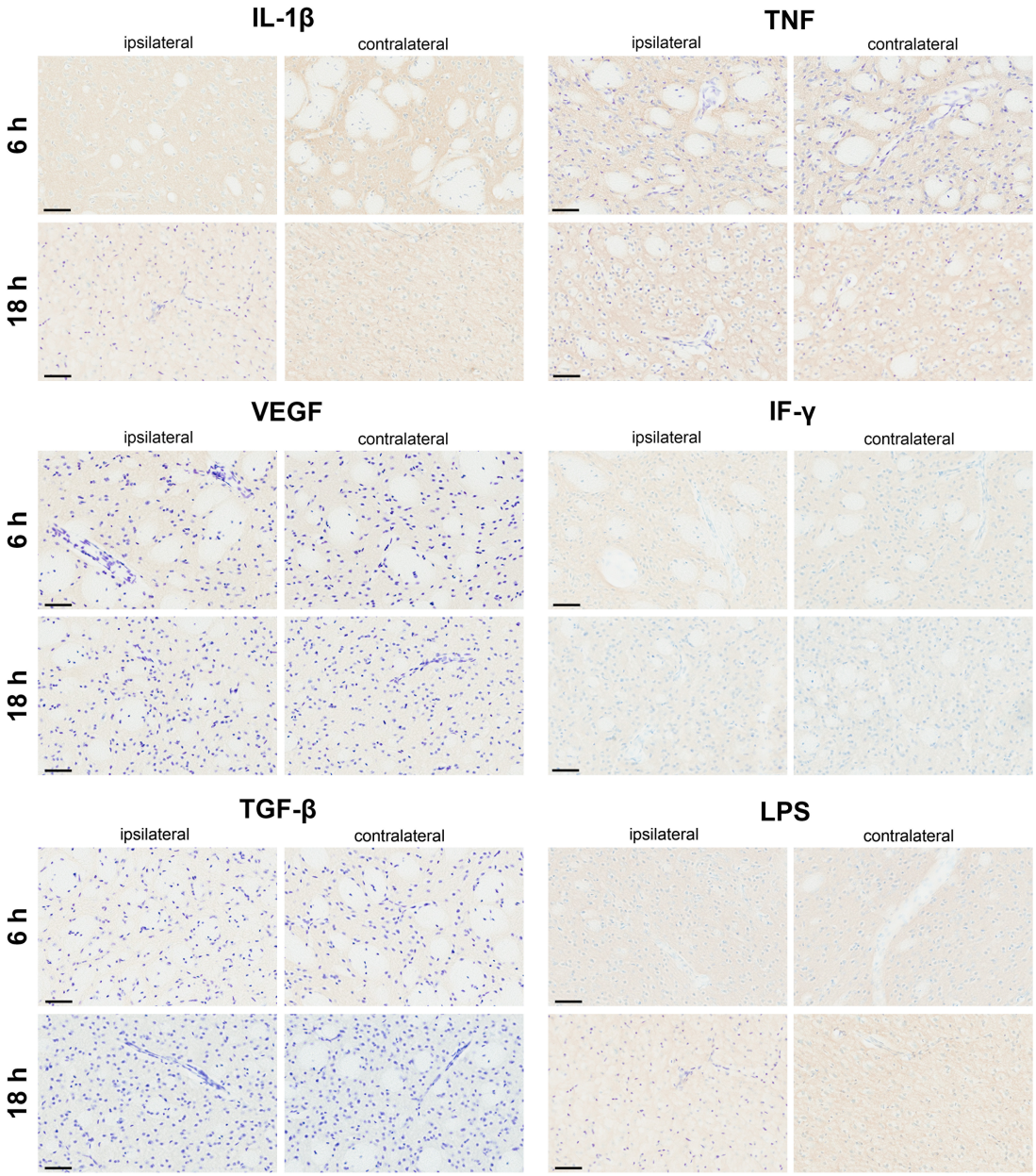


Figure 4.3: ALCAM response to proinflammatory agents *in vivo*.
ALCAM (brown) immunohistochemistry results of mouse brain sections stimulated with TNF, IL-1β, IF-γ, TGF-β, VEGF and LPS. No ALCAM was visually detected on the brain vessels from the ipsilateral and contralateral hemispheres. Counterstain: cresyl violet; blue. Scale bars = 50 μm.

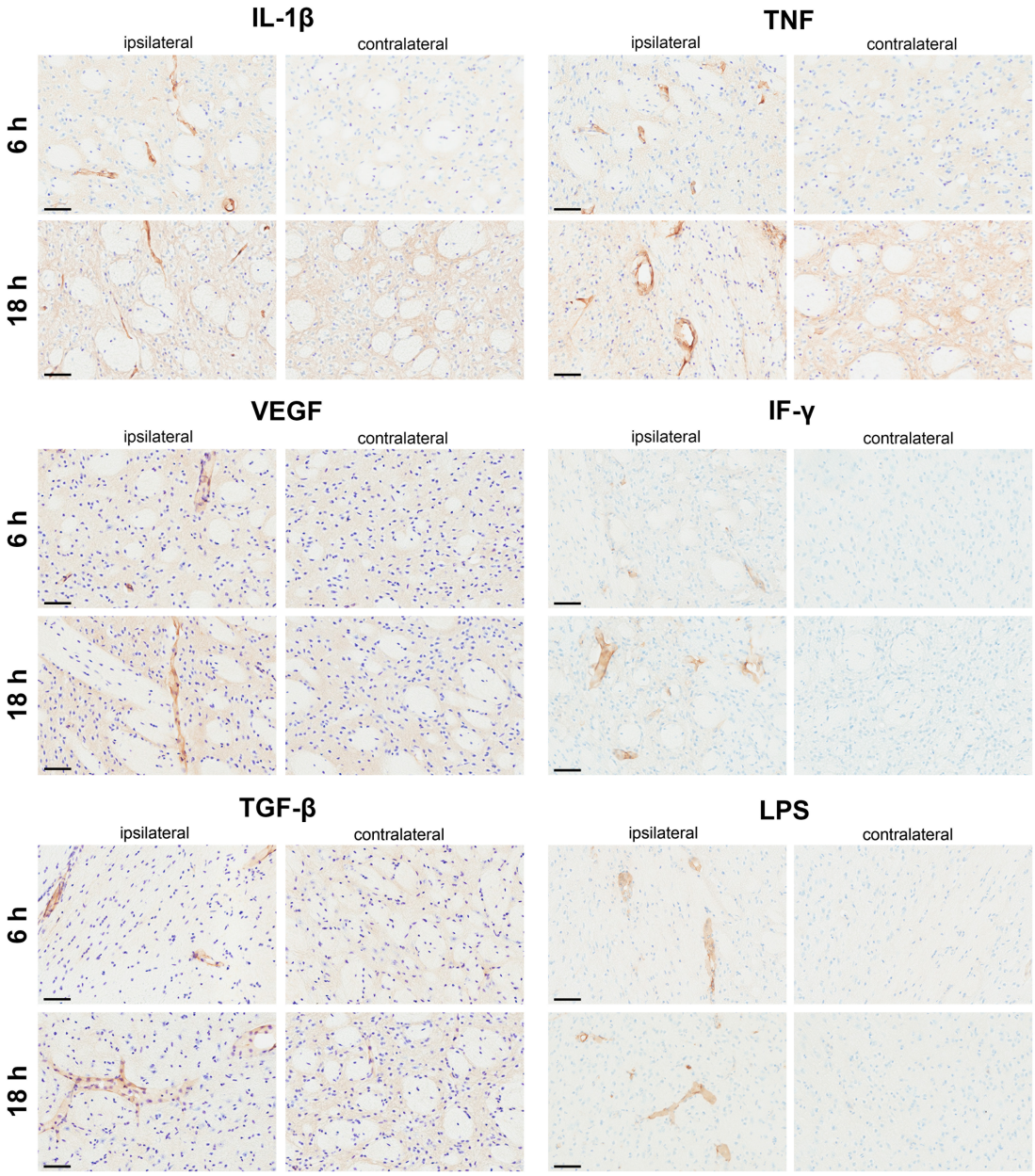


Figure 4.4: VCAM-1 response to proinflammatory agents *in vivo*.

VCAM-1 (brown) immunohistochemistry results of mouse brain sections stimulated with TNF, IL-1β, IF-γ, TGF-β, VEGF and LPS. Activated VCAM-1 was detected on the vessels of the ipsilateral (injected) hemisphere. Minimal VCAM-1 expression was found on the vessels of contralateral side. Counterstain: cresyl violet; blue. Scale bars = 50 μm.

4.3.2 Endothelial ALCAM Response in Presence of TCM and Tumour Cells

To determine whether tumour cells secrete proinflammatory cytokines that could stimulate ALCAM upregulation on vessels, mouse endothelial cells (sEnd-31) were first treated for 24 or 48 hours with tumour-conditioned medium (TCM) obtained from MDA-MB-231-Br cells. ALCAM immunocytochemistry and quantification showed significantly greater ($p < 0.001$) ALCAM expression on treated cells compared to cells cultured in DMEM, at both 24 and 48 hours (Figure 4.5). Moreover, 48 hours of incubation with TCM induced significantly greater ($p < 0.05$) ALCAM upregulation than to 24 hours (Figure 4.5b).

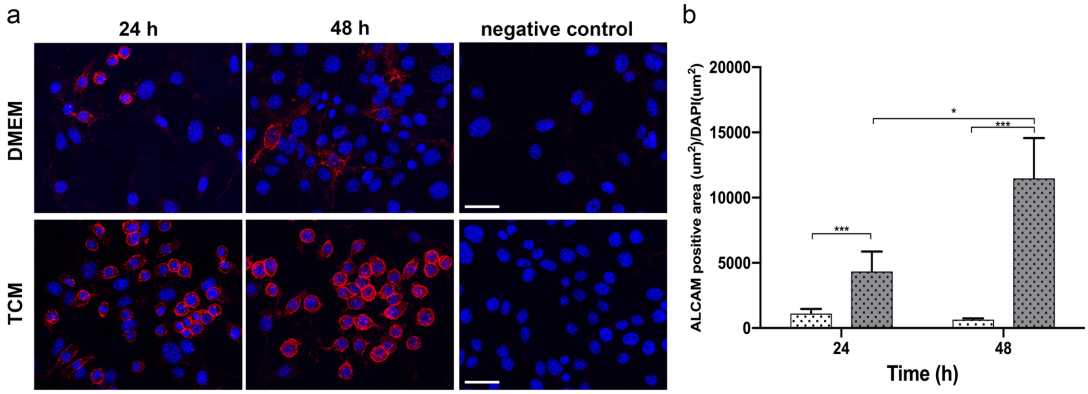


Figure 4.5: ALCAM response to tumour-conditioned medium (TCM).
(a) Mouse endothelial cells (sEnd-1) were cultured either in normal medium (DMEM) or treated with TCM collected from MDA-MB-231-Br tumour cells. ALCAM (red) is upregulated in response to TCM 24 and 48 hours after stimulation. Negative control staining showed no signal in the red channel. Nuclei: DAPI; blue. Scale bars = 20 μm. **(b)** A significant difference was found in the amount of ALCAM upregulation between treated and untreated cells at both 24 and 48 hours. Between stimulated cells, a longer incubation time (48 h) resulted in a higher ALCAM response compared to the shorter treatment duration (24 h). Error bars = SEM, *$p < 0.05$, ***$p < 0.001$.

Next, mouse brain endothelial cells (bEnd-3) were co-cultured with tumour cells (MDA-MB-231-Br) in 3D. Negligible ALCAM expression was evident on the membrane of mouse endothelial cells when cultured alone (Figure 4.6, top row). In contrast, tumour cells cultured alone showed high levels of endogenous ALCAM on their membranes (Figure 4.6, middle row), suggesting an adhesive role of ALCAM in tumour-tumour contact. Finally,

co-culture of endothelial and tumour cells for 14 hours, showed ALCAM expression at the contact points between some of the endothelial and tumour cells (Figure 4.6, bottom row), indicating that tumour cells promote ALCAM expression on endothelial cells, which assists with their binding.

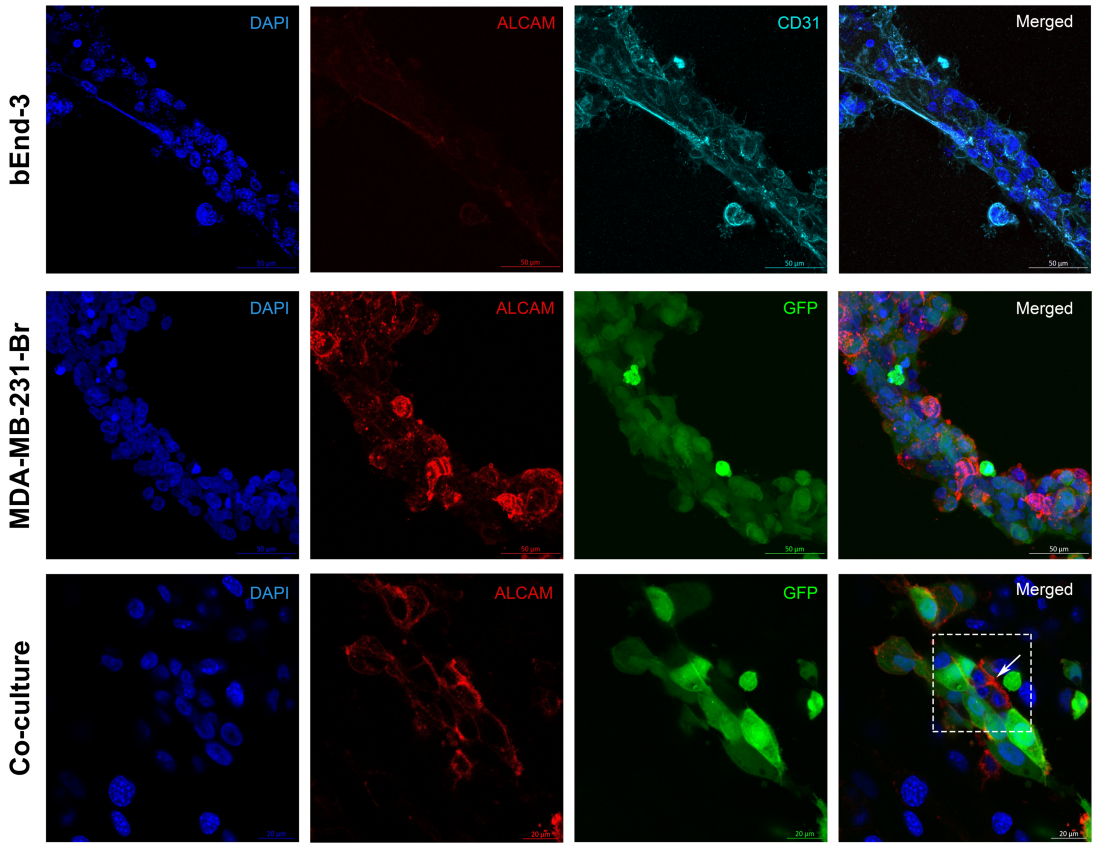


Figure 4.6: Three-dimensional culture of mouse brain endothelial cells and tumour cells.
(Top row) Minimum ALCAM (red) was detected on mouse brain endothelial cells (bEnd-3) cultured alone in Matrigel-coated wells. Endothelial marker: CD31, turquoise. **(Middle row)** ALCAM (red) was present on the membrane of tumour (MDA-MB-231-Br) cells cultured alone. Tumour marker: GFP; green. **(Bottom row)** co-culture of bEnd-3 and MDA-MB-231-Br cells in Matrigel-coated wells. ALCAM (red) was present on mouse endothelial cells (GFP negative cells) in the close proximity of tumour cells (dashed box, white arrow pointing at the ALCAM on endothelial cells). Nuclei: DAPI; blue. Scale bars = 50 µm (Top two rows), 20 µm (bottom row).

4.3.3 ALCAM Expression in Breast, Melanoma and Lung Brain Metastasis Models

Brain metastases were detected histologically in all mice following successful intracardiac tumour cell injection. For models of both breast and melanoma brain metastasis, mice were culled at weekly time-points up to 4 weeks post-intracardiac injection to enable assessment of the time-course of ALCAM upregulation. For the lung brain metastasis model, mice were culled on days 35 and 42 after intracardiac tumour cell injection. In both MDA-MB-231-Br and H1_DL2 models, ALCAM expression was evident from the earliest stages of tumour formation (Figure 4.7a, b). Similarly, ALCAM expression was evident in mice injected with SEBTA-001 cells at both time-points studied (Figure 4.7c). The number of ALCAM positive pixels normalised by tumour area (%ALCAM+) showed consistent expression throughout the time-course for all three brain metastasis models. No significant differences were found between time-points for each model. On average, for the MDA-MB-231-Br model, 33-41% of the tumour area showed positive ALCAM expression across the time-course (Figure 4.7d). Similarly, the H1_DL2 and SEBTA-001 models showed on average 34-37% and 33-36% ALCAM staining across the time-course, respectively (Figure 4.7d).

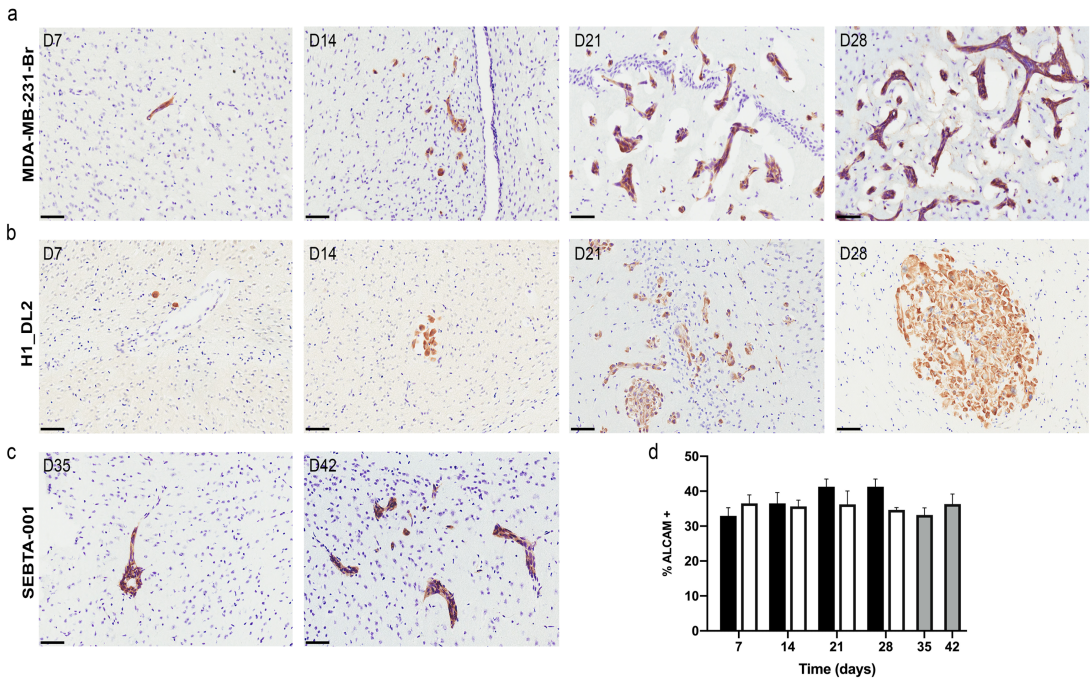


Figure 4.7: ALCAM upregulation in mouse brain metastases from breast, melanoma and lung. **(a-c)** ALCAM (brown) expression associated with brain metastases was evident at all time-points studied in all models: **(a)** MDA-MB-231-Br, **(b)** H1_DL2 and **(c)** SEBTA-001, Scale bars = 100 µm. **(d)** Graph showing ALCAM positive staining as a percentage of tumour area for MDA-MB-231-Br (black), H1_DL2 (white) and SEBTA-001 (grey) models; no significant differences were observed between time-points for each model.

The above immunohistochemistry results reflect total expression of ALCAM at different time-points, irrespective of cell origin. However, for the purpose of developing an ACLAM targeted MRI agent, presence of this biomarker on the vessels associated with tumours is crucial for agent accessibility when the BBB is still intact. To this end, co-localisation of ALCAM with three widely used BBB endothelial markers was assessed: (i) laminin; (ii) GLUT-1; and (iii) CD31. Laminin is a major protein expressed on the basal lamina and is one of the four extracellular matrix proteins that forms the basal membrane of the BBB [206]. GLUT-1 is a transporter protein that facilitates the transport of glucose across the cell membranes, and is highly expressed on the BBB endothelium to maintain the high glucose and energy intake of the brain [207]. CD31 or PECAM-1 (platelet/endothelial cell adhesion molecule-1) is a member of immunoglobin superfamily and is a glycosylated transmembrane protein highly expressed on

endothelial cells [208]. CD31 plays a major role in the adhesion cascade between endothelial and inflammatory cells.

Fluorescently stained sections from the MDA-MB-231-Br brain metastasis model showed co-localisation of ALCAM with all these three markers, expressed on the brain vasculature (Figure 4.8). Based on the universal application of CD31 as an endothelial cell marker in the literature [209], this antibody was chosen as a marker for mouse brain endothelial cells in this thesis.

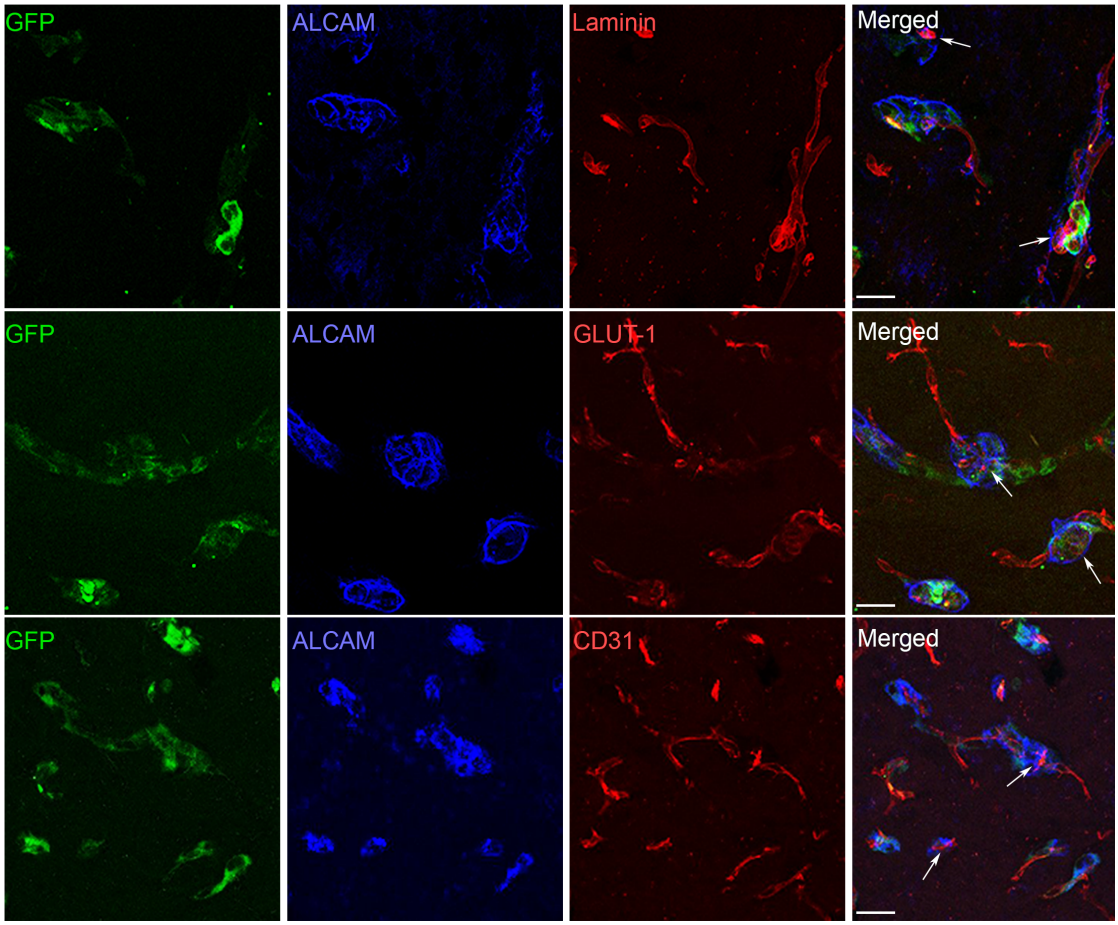


Figure 4.8: ALCAM co-localisation with three different BBB endothelial markers.
Co-localisation of ALCAM (blue) with laminin, GLUT-1 and CD31 (red) in the mouse MDA-MB-231-Br (GFP; green) brain metastasis model (day 21) are shown (pink colour, white arrows). Scale bars = 25 µm.

To explore the presence of ALCAM on endothelial cells further, the temporal expression of endothelial ALCAM was assessed immunofluorescently. Two subsets of vessels were defined for these analyses: (i) intratumoral vessels - vessels in close association with tumour cells; and (ii) peritumoural vessels - vessels 20-100 µm away from tumour cells (Figure 4.9).

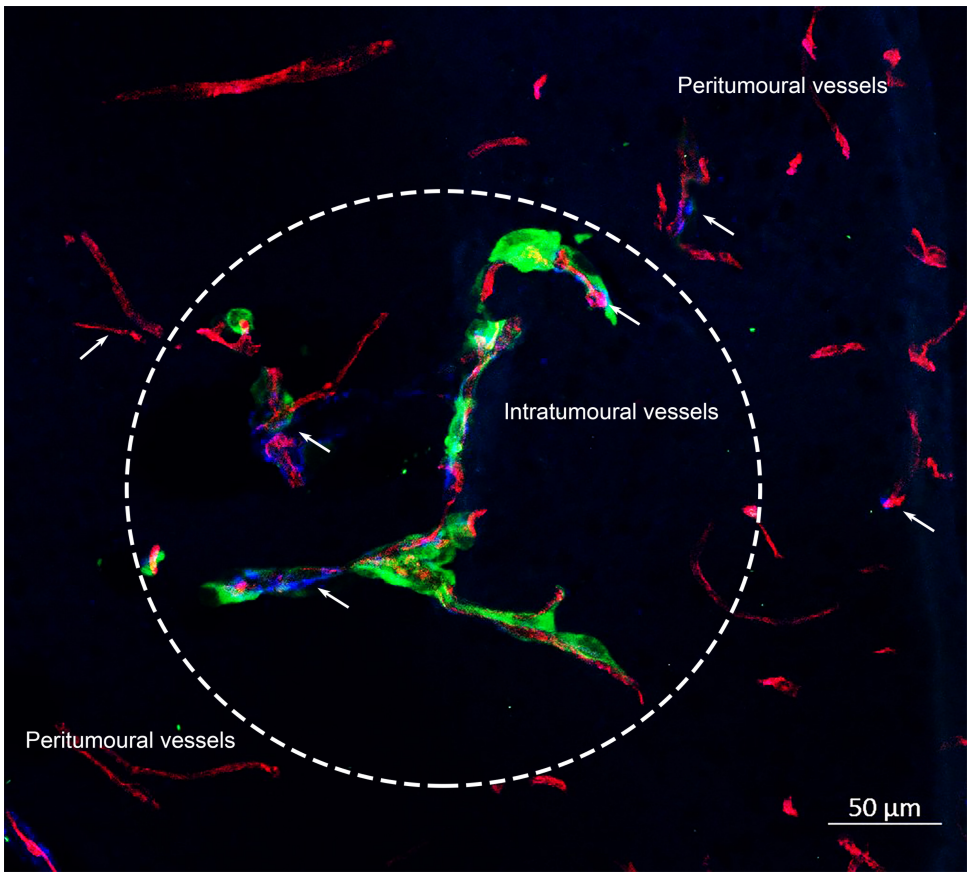


Figure 4.9: Classification of intratumoural and peritumoural vessels.
Example of vessel classification for the ALCAM and endothelial cells co-localisation study: (1) Intratumoural vessels are in association with tumour cells (vessels inside of the dashed circle); and (2) Peritumoural vessels are 20-100 µm away from the tumour (vessels outside of the dashed circle). Tumour: GFP; green. ALCAM: blue. Endothelial marker: CD31; red.

Representative fluorescence images for breast brain metastasis models are shown in Figure 4.10. Co-localisation in the MDA-MB-231-Br model showed that intratumoural vessels were positive for ALCAM, with the percentage of positive vessels increasing significantly from day 7 to 21

($p < 0.01$; Figure 4.10b). In contrast, ALCAM expression on peritumoural vessels remained at baseline levels up to day 14 (Figure 4.10c; dotted line = ALCAM positive vessels in contralateral hemisphere of brain), but then increased significantly at days 21 and 28 ($p < 0.05$; Figure 4.10c). As the H1_DL2 metastases grow slower than the MDA-MB-231-Br metastases and only a few tumours were detectable at day 7, ALCAM and CD31 co-localisation was assessed from day 14 in this model (Figure 4.11). Intratumoural vessels showed elevated and stable ALCAM expression across the time-course, with no significant differences being evident between time-points (Figure 4.11b). However, in this model, no significant difference was found in ALCAM expression on peritumoural vessels at any time-point compared to baseline levels from contralateral non-tumoural areas (Figure 4.11b). A similar pattern was observed in the SEBTA-001 model, with ALCAM positive intratumoural vessels at both days 35 and day 42 after tumour cell injection, but no significant increase in ALCAM expression on peritumoural vessels compared to baseline (Figure 4.12a, b, c).

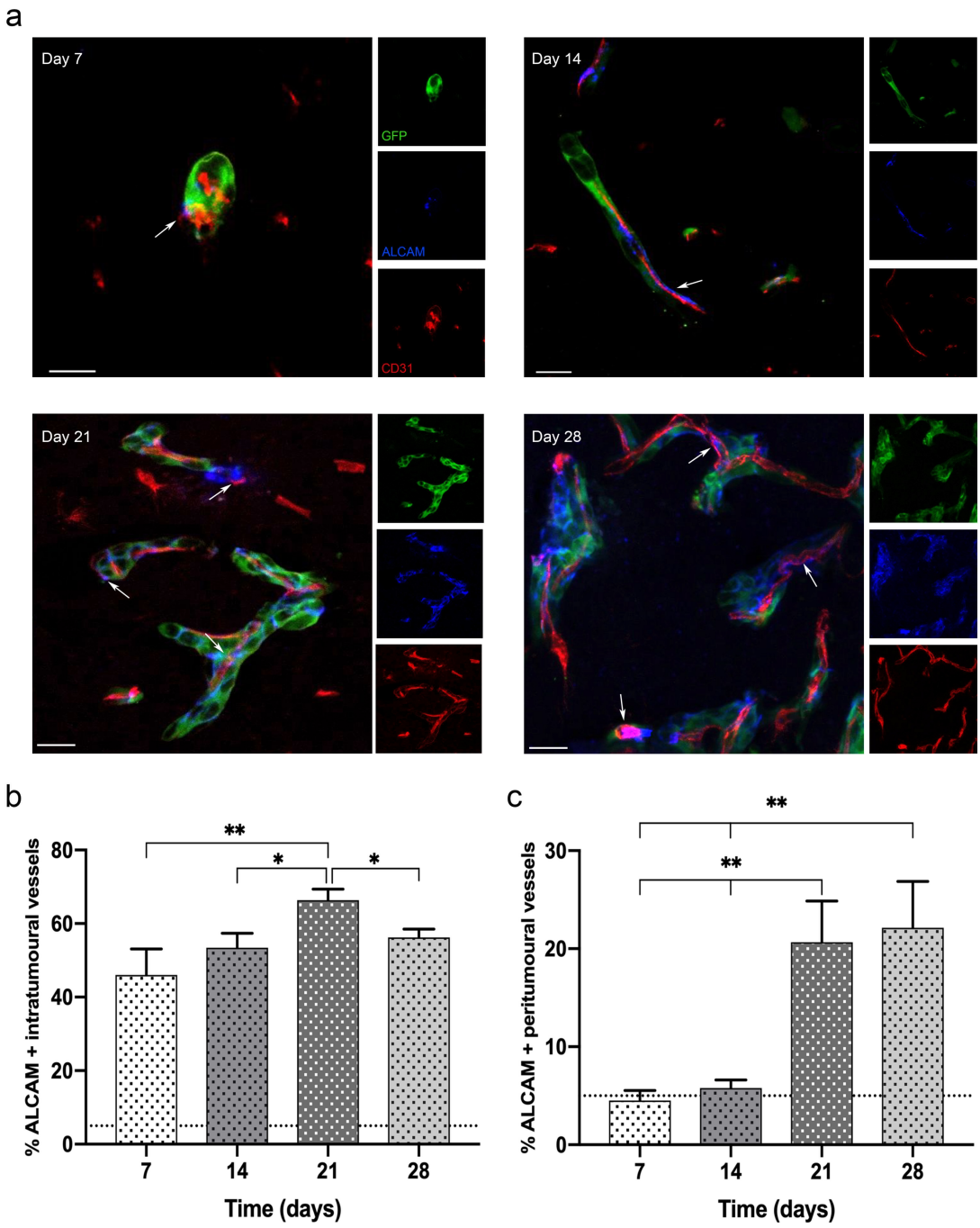


Figure 4.10: ALCAM and CD31 co-localisation in the breast cancer brain metastases model.

(a) Representative immunofluorescence images from the MDA-MB-231-Br brain metastasis model (GFP; green) from days 7, 14, 21, and 28 post-injection. White arrows pointing at ALCAM (blue) positive vessels. Endothelial marker: CD31; red. Scale bars = 25 μm. **(b, c)** Graphs showing quantitative analysis of the percentage of ALCAM positive intratumoral and peritumoural vessels. Dotted line = Averaged baseline level of ALCAM on normal brain vessels of contralateral hemisphere for each cohort. *$p < 0.05$, **$p < 0.01$; n > 15 tumours per group.

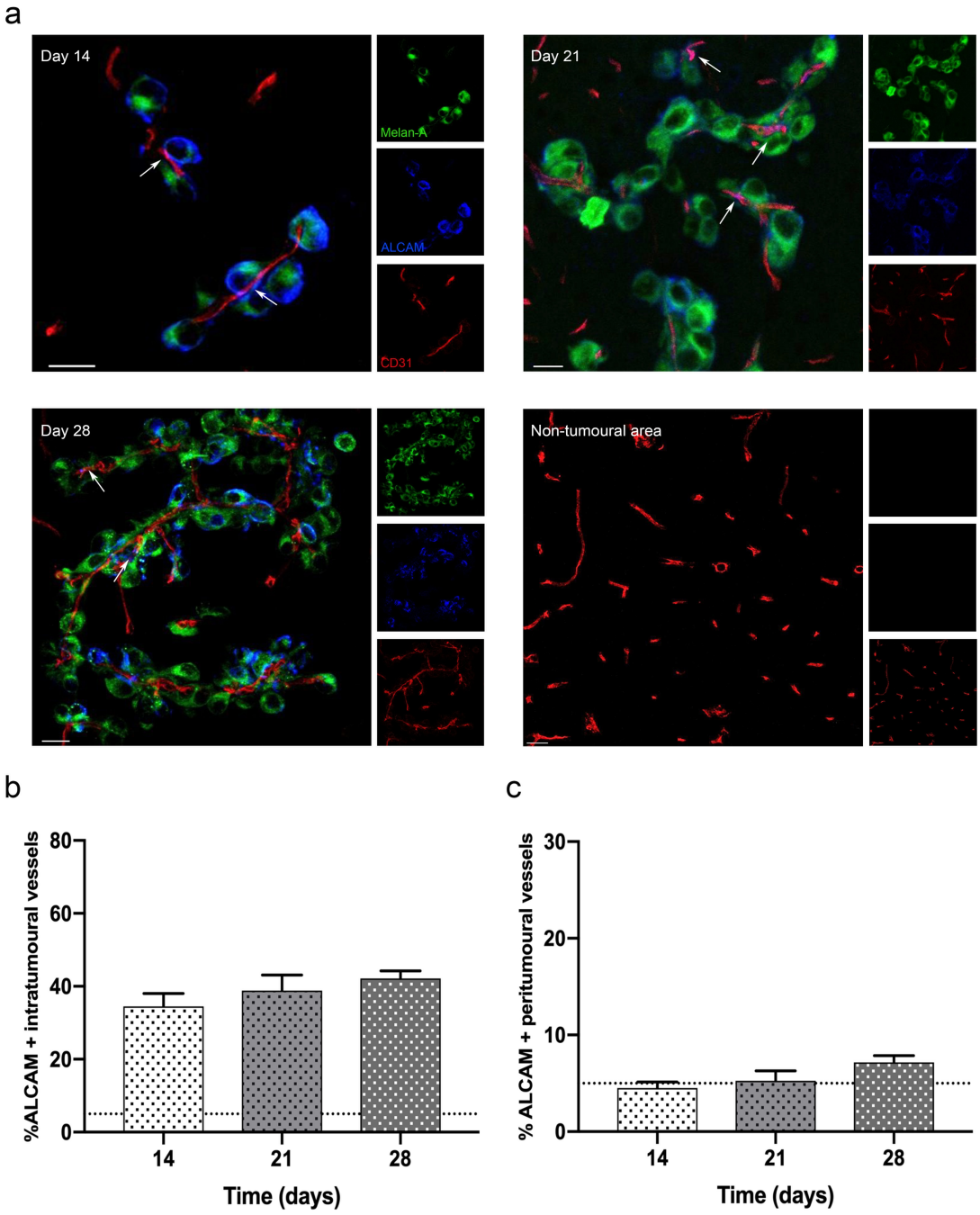


Figure 4.11: ALCAM and CD31 co-localisation in the melanoma brain metastases model.
(a) Representative immunofluorescence images from the H1_DL2 brain metastasis model (Melan-A; green) from days 14, 21, and 28 post-injection. White arrows pointing at ALCAM (blue) positive vessels. Vessels from non-tumour bearing areas showed no ALCAM upregulation. Endothelial marker: CD31; red. Scale bars = 20 μm. **(b, c)** Graphs showing quantitative analysis of the percentage of ALCAM positive intratumoral and peritumoural vessels. Dotted line = Averaged baseline level of ALCAM on normal brain vessels of contralateral hemisphere for each cohort, as shown in the bottom right panel. n > 15 tumours per group.

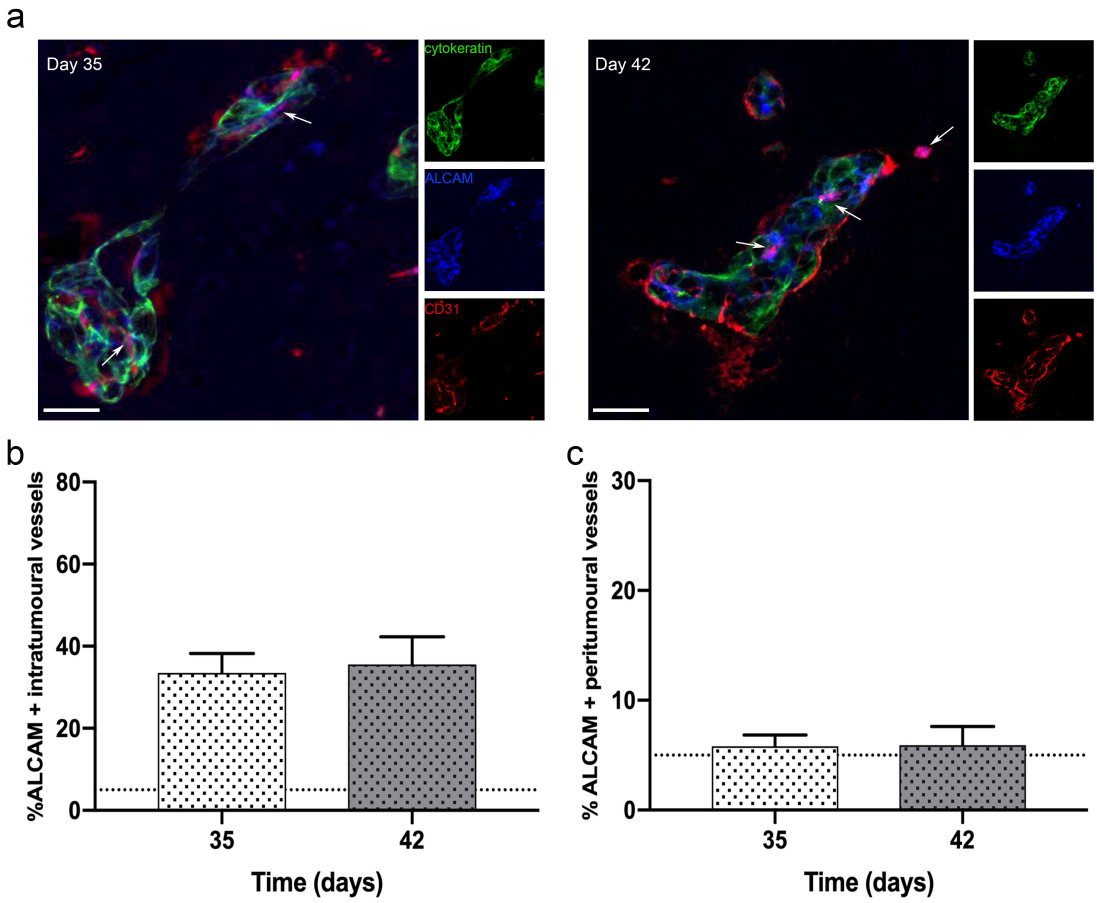


Figure 4.12: ALCAM and CD31 co-localisation in the lung brain metastases model.
(a) Representative immunofluorescence images from the SEBTA-001 brain metastasis model (cytokeratin; green) from days 35 and 42 post-injection. White arrows pointing at ALCAM (blue) positive vessels. Endothelial marker: CD31; red. Scale bars = 20 μm. **(b, c)** Graphs showing quantitative analysis of the percentage of ALCAM positive intratumoral and peritumoural vessels. Dotted line = Averaged baseline level of ALCAM on normal brain vessels of contralateral hemisphere for each cohort. n > 15 tumours per group.

4.3.4 Assessment of ALCAM Expression in Human Brain metastasis Biopsies

Human brain metastasis biopsies from breast, melanoma and lung adenocarcinoma patients were stained for ALCAM (n ≥ 3 cases for each primary). ALCAM was prominently expressed on most of tumour cells and associated vessels in all cases assessed (Figure 4.13a, c, e). Due to the strong presence of tumour cell ALCAM staining in the samples studied, distinguishing vascular morphology from the rest of the stained features was challenging. To overcome this issue, the consecutive sections were stained for CD34, an endothelial marker. Registering

ALCAM and CD34 immunostained sections showed that tumour-associated vessels are positive for ALCAM in brain metastases from all primary tumours studied‡ (Figure 4.13a-d). ALCAM negative control staining showed no positive signal, and no positive vessels were detected in normal human brain tissue stained for ALCAM (n = 1) (Figure 4.13g, h).

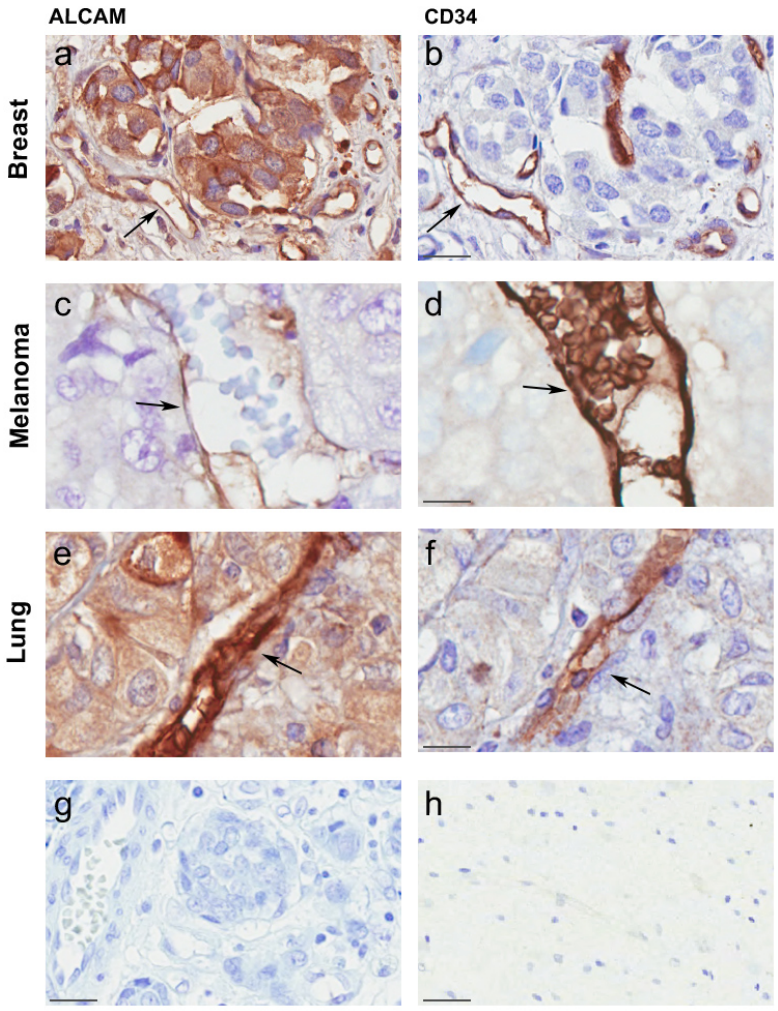


Figure 4.13: ALCAM positive vessels in human brain metastasis biopsies.
(a, c, e) showing ALCAM staining (brown) for brain metastases from breast, melanoma and lung cancer. **(b, d, f)** showing endothelial staining (CD34, brown) of consecutive sections. Arrows indicate positive staining for both ALCAM and CD34. **(g)** Negative control staining of a breast cancer brain metastasis section. **(h)** ALCAM staining of normal brain tissue. Scale bars = 15 µm.

‡ These results were confirmed by Dr. Olaf Ansorge, Clinical Neuropathologist.

4.3.5 Optimisation and Binding Assessment of ALCAM-MPIO Conjugate

To find the optimal ALCAM antibody for an MRI contrast agent, total antibody loading on MPIO and *in vitro* binding ability were initially assessed for three commercially available primary ALCAM antibodies (Figure 4.14a). Peak intensities from histograms generated from flow cytometry were compared to a calibration curve, and densities calculated to be 23,650 ± 3,128 ALCAM (R&D systems), 17,735 ± 1,429 ALCAM (LSBio), 18,263 ± 5,181 ALCAM (eBio) and 18,985 ± 4,230 IgG antibodies per MPIO (mean ± SD, n = 10 per group). These densities are equivalent to 13,000, 9,700, 10,000 ALCAM (R&D systems, LSBio, and eBio, respectively) and 10,500 IgG antibodies per μm^2 surface of MPIO (diameter: 0.76 μm). Subsequently, the binding capacities of conjugates were assessed under static conditions. TNF stimulated sEnd-1 cells showed marked transmembrane ALCAM expression (Figure 4.14c), and the percentage of MPIO (red) that were attached to ALCAM (green) for each FoV was quantified (Figure 4.14b). The R&D antibody conjugate was found to have significantly higher ($p < 0.05$) binding to ALCAM upregulated on endothelial cells compared to LSBio, eBio and IgG antibody conjugates (Figure 4.14b, c). Based on the above results, all subsequent experiments were carried out using the monoclonal rat anti-mouse ALCAM antibody purchased from R&D systems.

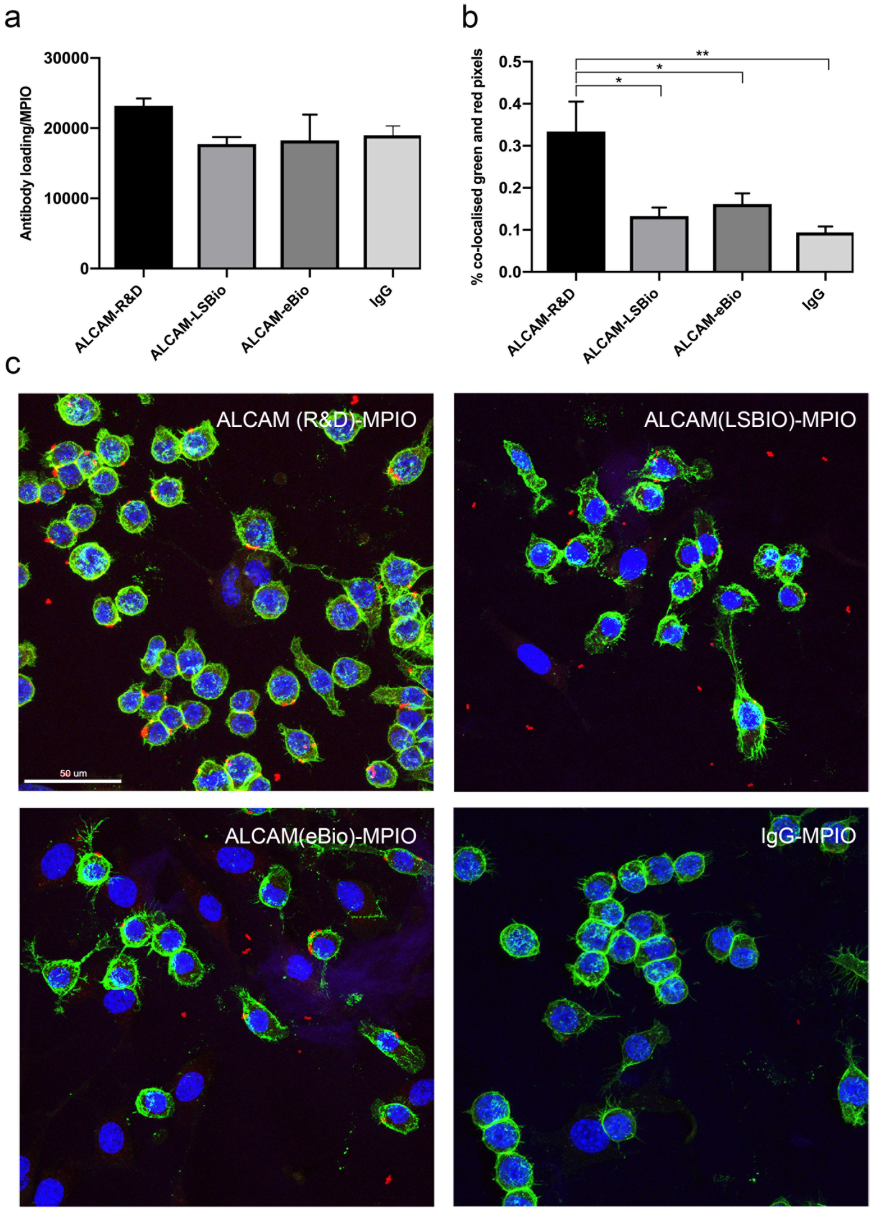


Figure 4.14: ALCAM-MPIO static binding ability *in vitro*.

(a) Total antibody loading of three commercially purchased ALCAM antibodies and IgG on MPIO. R&D showed to have highest amount of antibody loading on MPIO (mean = 23,657) compared to LSBio (mean = 17,735), eBio (mean = 18,263) and IgG (mean = 18,985); more than three samples measured per conjugate. **(b, c)** Binding capacity of ALCAM-MPIO (red) conjugates with R&D, LSBio, eBio and IgG antibodies was measured on mouse TNF stimulated endothelial cells. ALCAM: Green. Nuclei: DAPI; blue. Percentage of co-localised red (MPIO) and green (ALCAM) pixels was quantified for each FoV. ALCAM-MPIO with antibodies from R&D showed significantly higher binding to ALCAM upregulated on endothelial cells compared to LSBio, eBio and IgG antibody conjugates; $*p < 0.05$, $**p < 0.01$.

Finally, antibody-MPIO binding was evaluated under flow conditions. Fluorescently labelled ALCAM-MPIO (R&D systems) or IgG-MPIO were pumped into glass capillaries pre-coated with mouse recombinant ALCAM protein. The shear stress induced by the flow of 20-25 μl/min in these capillaries would be comparable to the shear stress experienced within arterioles *in vivo* [135]. Notable binding of ALCAM-MPIO was evident on the capillary walls, whilst minimal binding was detected for IgG-MPIO (Figure 4.15). Quantitative analyses showed a significantly greater ($p < 0.0001$) number of bound ALCAM-MPIO than IgG-MPIO under flow (n = 10 FoV; Figure 4.15).

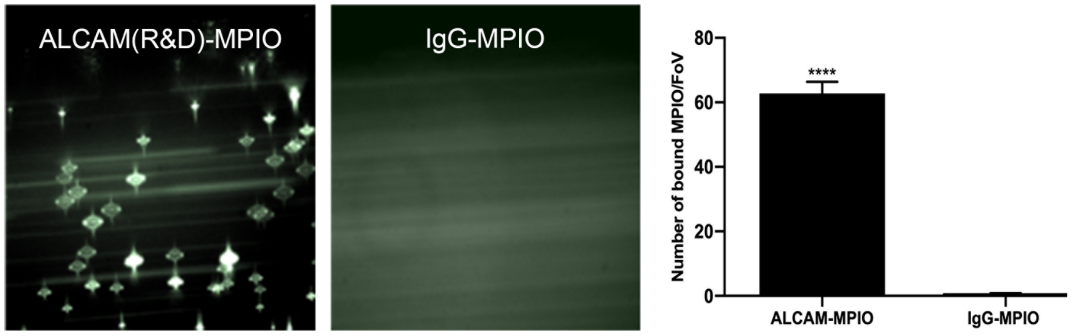


Figure 4.15: ALCAM-MPIO flow binding ability *in vitro*.
Fluorescently labelled ALCAM-MPIO or IgG-MPIO were pumped through glass capillaries coated with ALCAM protein. The number of bound ALCAM-MPIO to the capillary wall was manually counted and found to be significantly higher than IgG-MPIO; ****$p < 0.0001$.

4.3.6 *In Vivo* Detection of Micrometastases Using ALCAM-MPIO

Mice bearing breast, melanoma and lung brain metastases were injected intravenously with either ALCAM-MPIO or control IgG-MPIO on either day 21 and 28 (breast and melanoma), or day 42 (lung) post-tumour cell injection. These time-points were chosen based on the immunohistochemistry and co-localisation results for these models (see Section 4.3.3). In all cases, T_2^*W-MGE3D images showed marked hypointensities arising from bound ALCAM-MPIO. Focal hypointense areas were evident throughout the brain (olfactory bulb, forebrain and cerebellum) for all three models (Figure 4.16a; white arrows). Negligible hypointense foci were detected in the tumour bearing cohorts injected intravenously with IgG-MPIO (Figure 4.17). For all tumour bearing mice, no signal enhancement owing to BBB breakdown was found on T_1W post-gadolinium images (Figure 4.18). Only one mouse from the SEBTA-001 cohort (injected with IgG-MPIO), showed BBB breakdown on day 42. Owing to the leakiness of the vessels, this tumour manifested itself as a hyperintense region on T_1W post-gadolinium image (Figure 4.18; last row)[§]. Quantitation of the number of hypointense voxels in each brain showed a significant difference between mice injected with ALCAM-MPIO and IgG-MPIO for all tumour models and all time-points studied (Figure 4.16b). Dashed line denotes background hypointense voxels detected in naïve mice (n = 2) injected with ALCAM-MPIO (Figure 4.16b).

[§] This mouse was excluded from the study, since the aim was to evaluate ALCAM targeted detection of metastases prior to BBB breakdown.

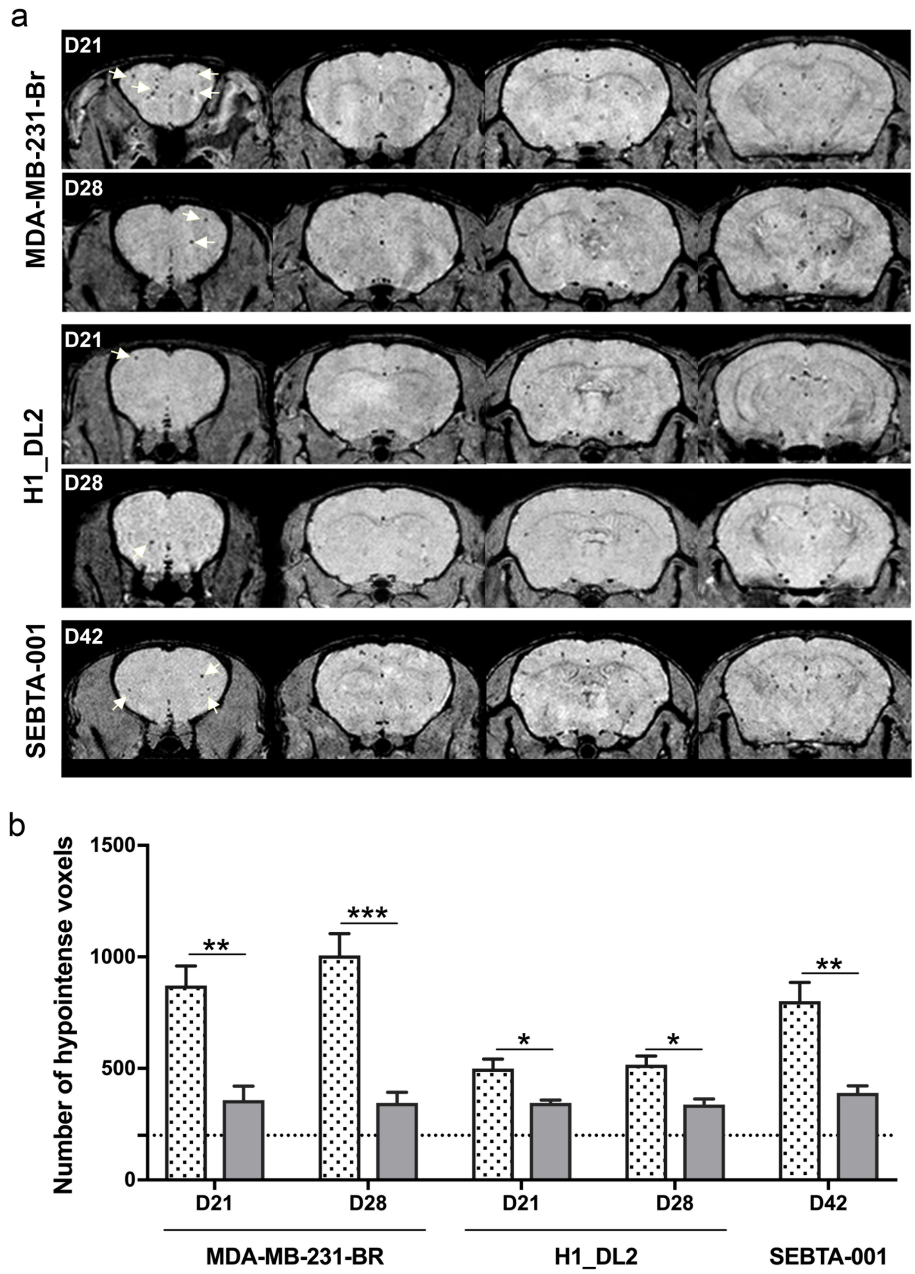


Figure 4.16: Detection of brain micrometastases using ALCAM-MPIO.

(a) Representative T_2*W coronal images from MGE3D datasets. Prominent focal hypointense (black) foci corresponding to retention of ALCAM-MPIO were evident in mice injected with MDA-MB-231-Br or H1_DL2 cells at both days 21 and 28, and SEBTA-001 cells at day 42 after tumour cell injection. Examples of hypointense foci are indicated with white arrows in the first column. **(b)** Graph showing quantitation of the number of hypointense voxels for each tumour model (n = 5-6 per group). A significant difference was evident between tumour bearing mice injected with ALCAM-MPIO (dotted bars) and IgG-MPIO (grey bars) for all time-points in all three models; *$p < 0.05$, **$p < 0.01$, ***$p < 0.001$. Dashed line denotes background hypointense voxels detected in naïve mice injected with ALCAM-MPIO (n = 2).

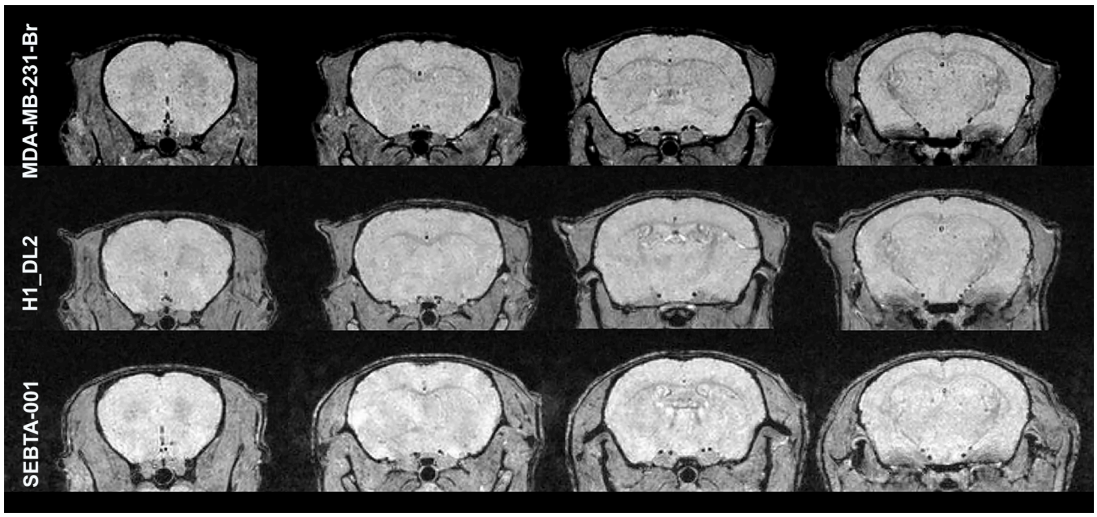


Figure 4.17: Tumour bearing mice injected with IgG-MPIO.
Representative T_2*W-MGE3D coronal images from tumour bearing mice injected with non-specific IgG-MPIO on day 21 (MDA-MB-231-Br, H1_DL2) or day 42 (SEBTA-001). Negligible amount of hypointense voxels were found in these mice.

Histological examination of mice injected with either ALCAM-MPIO or IgG-MPIO showed the presence of widespread brain metastases for all models. The majority of hypointensities on T_2*W-MGE3D images corresponded spatially with micrometastases detected histologically for all three brain metastases models (purple arrow, Figure 4.19a-i). To confirm that the hypointensities reflect bound ALCAM-MPIO, samples were stained for ALCAM and iron, using Perls' Prussian blue (black arrows, Figure 4.19j). Presence of both MPIO and endothelial ALCAM on vessels in close proximity to brain metastases was evident (Figure 4.19k, l).

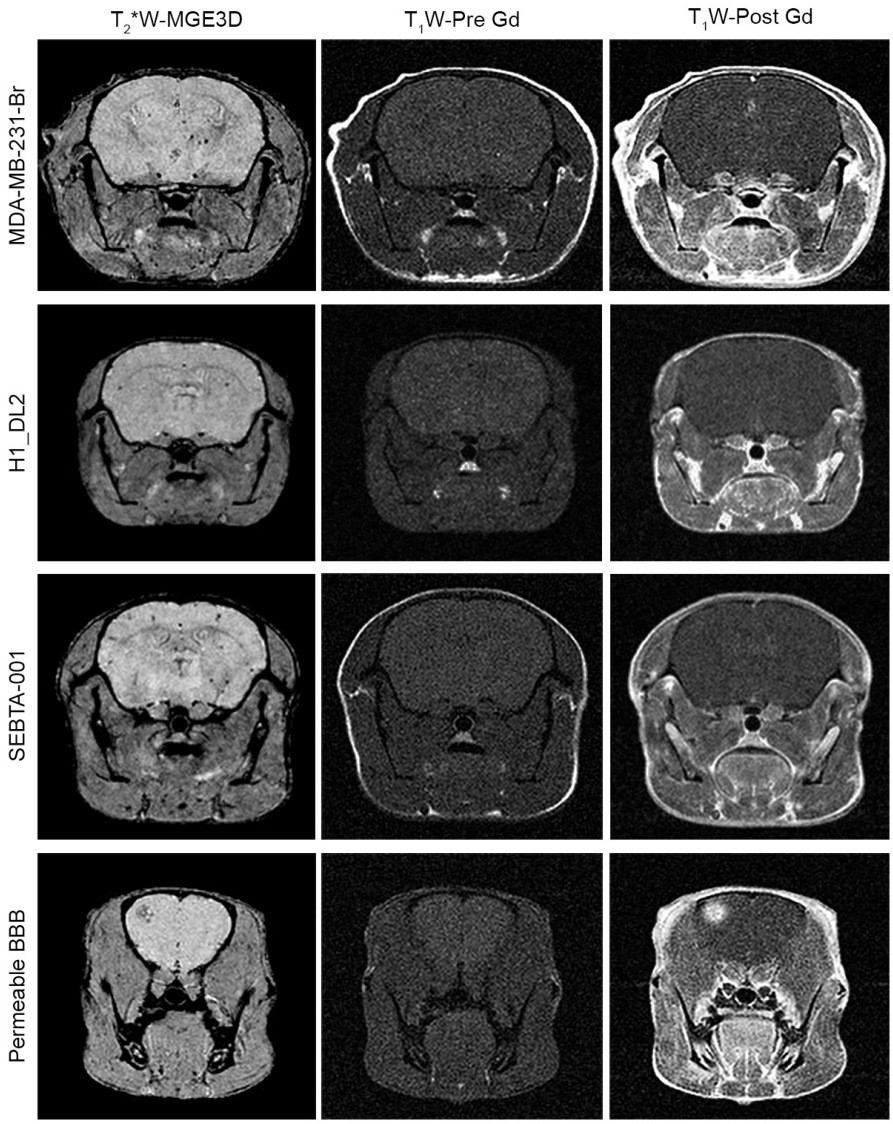


Figure 4.18: MRI BBB permeability assessment in the brain metastasis models.

(Top three rows) Representative T_2*W-MGE3D images and corresponding T_1W pre- and post-gadolinium images for mice injected intracardially with MDA-MB-231-Br, H1_DL2 or SEBTA-001 cells. No gadolinium enhancement (bright regions) was detected in T_1W-post Gd images, indicating an intact BBB. The presence of hypointense foci on the T_2*W-MGE3D correspond to the bound ALCAM-MPIO and micrometastases, which are not detected on the post-contrast T_1W image. Images are from the latest time-point of the study (day 28 post-injection for MDA-MB-231-Br, H1_DL2 and day 42 for SEBTA-001). **(Bottom row)** Example of a mouse with a permeable BBB. Only one mouse from the SEBTA-001 cohort, injected with IgG-MPIO, showed BBB breakdown on day 42 post-tumour cell injection. Note the presence of MPIO (dark) on T_2*W-MGE3D and Gd (bright) on post-gadolinium T_1W image.

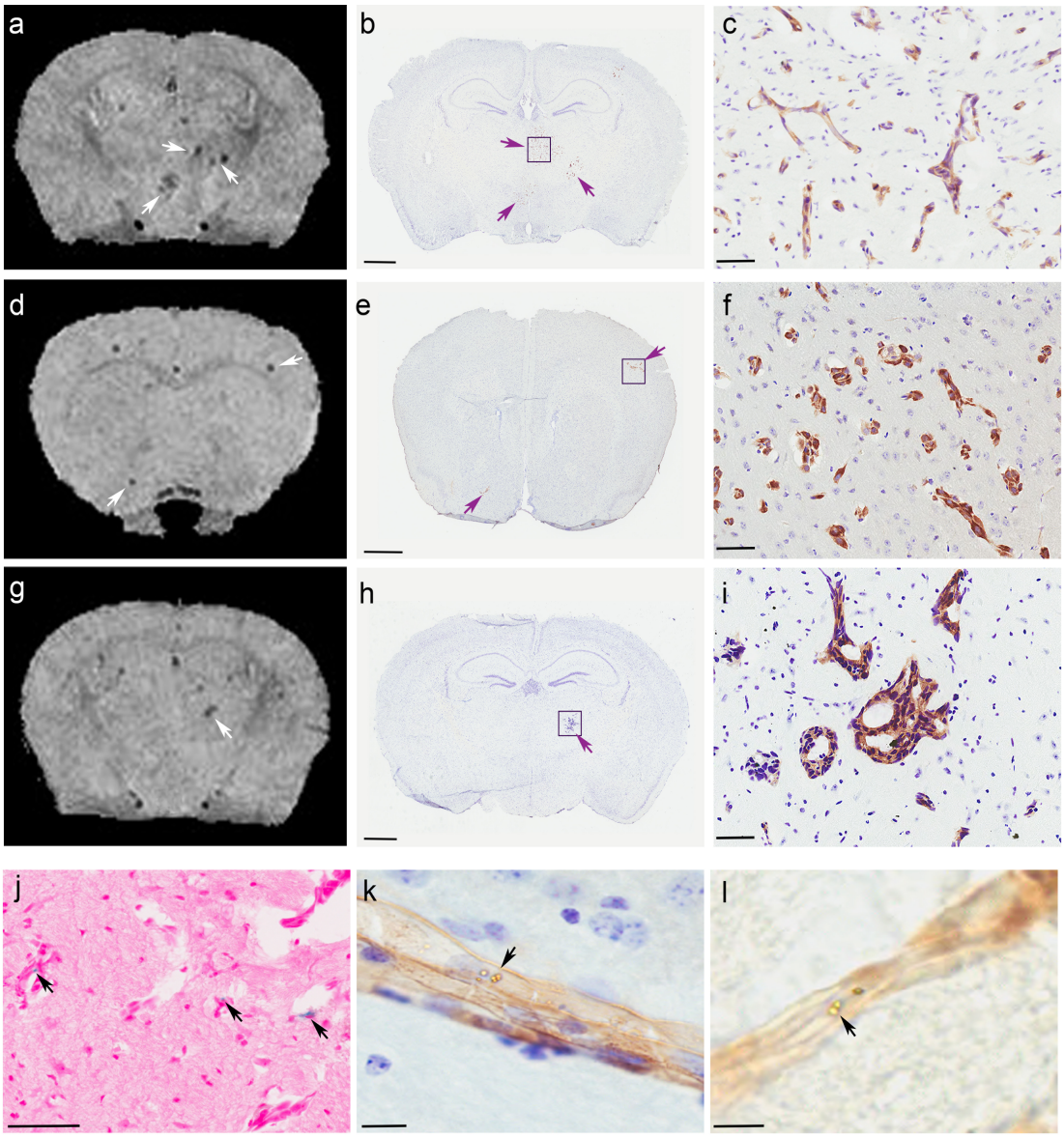


Figure 4.19: ALCAM-MPIO *in vivo* binding and detection of brain metastases.

(a-c) Representative T_2*W-MGE3D image from MDA-MB-231-Br brain metastasis model and the corresponding histological sections **(b)** showing co-localisation of hypointensities on the T_2*W image (white arrows) with brain metastases (purple arrows) and **(c)** the higher magnification photomicrograph from ALCAM (brown) stained tumour. Counterstain = cresyl violet; blue. **(d-e)** Representative T_2*W-MGE3D image from the H1_DL2 brain metastasis model and the corresponding histological sections. **(g-i)** Representative T_2*W-MGE3D image from SEBTA-001 brain metastasis model and the corresponding histological sections. **(j)** Perls' Prussian blue staining of tumour showing presence of MPIO (blue; arrows), counterstain = Nuclear Fast Red. **(k-l)** MPIO (black arrows) were found in ALCAM activated vessels (brown). Scale bars: (b, e, h) = 1 mm; (c, f, I, j) = 30 µm; (e, f) = 5 µm.

4.3.7 Sensitivity Assessment of ALCAM-MPIO Imaging in Tumour Models

To assess the sensitivity of ALCAM-MPIO imaging, both the number of metastases associated with vascular ALCAM positivity, and the number of brain metastases detected by ALCAM-MPIO imaging were determined histologically. First, tumour volumes were calculated manually. Then, ALCAM upregulation on tumour-associated vessels was assessed visually and each tumour was scored as either ALCAM endothelial positive (Endo ALCAM +) or ALCAM endothelial negative (Endo ALCAM -). For the MDA-MB-231-Br model, 88.5% of all tumours had ALCAM positive vessels (n = 3 mice). For tumours above and below the median volume (0.893×10^{-3} µl), 94% and 83%, respectively, were ALCAM positive (Figure 4.20a). For the H1_DL2 model, 50.6% of all tumours were associated with ALCAM positive vessels (n = 4 mice). For tumours above and below the median volume (0.304×10^{-3} µl), 59% and 42%, respectively, were ALCAM positive (Figure 4.20b). For the SEBTA-001 model, 79% of all tumours were associated with ALCAM positive vessels (n= 3 mice). For tumours above and below the median volume (0.405×10^{-3} µl), 89% and 68%, respectively, were ALCAM positive (Figure 4.20c).

Comparing the anatomical location of brain metastases on histology with the corresponding hypointensities on T_2*W images, revealed 82% of tumours were detected by ALCAM-MPIO MRI for the MDA-MB-231-Br model. For tumours above and below the median volume, 88.5% and 75.5%, respectively, were detected (Figure 4.20d). For the H1_DL2 model, 54% of all brain metastases being detected by ALCAM-MPIO MRI; for tumours above and below the median volume, 59.4% and 50%, respectively, were detected (Figure 4.20e). Finally, for the SEBTA-001 model, ALCAM-MPIO detected 68% of all brain metastases; for tumours above and below the median volume, 70% and 66%, respectively, were detected (Figure 4.20f). All metastases with a volume greater than 3.3×10^{-3} µl, 6.8×10^{-3} µl and 9.5×10^{-3} µl for MDA-MB-231-Br, H1_DL2 and SEBTA-001 models, respectively, were detected with ALCAM imaging (Figure 4.20g-i), showing higher sensitivity for detection of smaller brain metastases in the MDA-MB-231-Br model, compared to the other models.

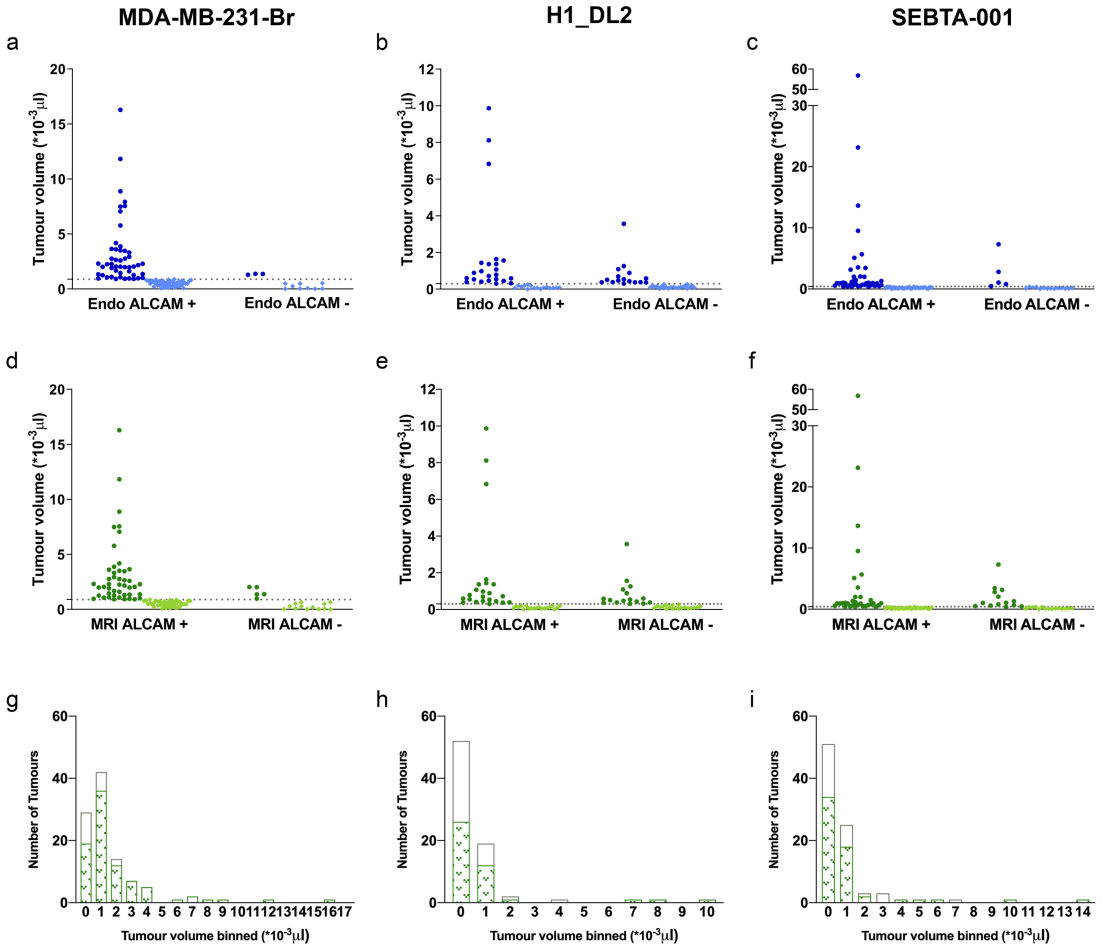


Figure 4.20: Graphs indicating volume of metastases from breast, melanoma and lung that were endothelial ALCAM +/- and MRI hypointense +/-.

(a-c) Scatter plots for presence of endothelial ALCAM (Endo ALCAM +) or absence of endothelial ALCAM (Endo ALCAM -) on tumour-associated vessels for individual brain metastases in **(a)** MDA-MB-231-Br, **(b)** H1_DL2 and **(c)** SEBTA-001 models based on immunohistochemistry. Dark blue circles show tumours above the median volume (dashed line) and light blue diamonds show tumours below the median volume for each model. **(d-f)** Corresponding scatter plots showing numbers of MRI hypointensity positive or negative micrometastases. Dark green circles show tumours above the median volume and light green diamonds show tumours below the median volume for each model. **(g-i)** Frequency distributions showing the number of tumours detected by ALCAM-MPIO on MRI (green doted bars) stacked with undetected tumours (clear bars) for each tumour volume ($*10^{-3}$ µl) bin. Two outlier tumours (volume: 23.1×10^{-3} µl and 56.7×10^{-3} µl) were excluded for the SEBTA-001 frequency plot. Data are shown from day 21 after induction of brain metastases for MDA-MB-231-Br and H1_DL2 models, and day 42 for the SEBTA-001 model.

4.3.8 Growth Pattern of Melanoma Brain Metastases

Distinctive growth patterns for the H1_DL2 melanoma model (day 21) were observed on the histological samples. Tumours were found to either grow in a more diffuse co-optive pattern alongside the vessels (Figure 4.21a, b) or to form solid cluster shapes with a low vascular density (Figure 4.21c, d). The sensitivity of ALCAM-MPIO for brain metastasis detection is highly dependent on the number of ALCAM positive vessels. Through MRI and histological co-registration, I observed that ALCAM targeted MRI was mostly able to detect melanoma brain metastases with a more co-optive growth pattern and, hence, more tumour-associated vessels.

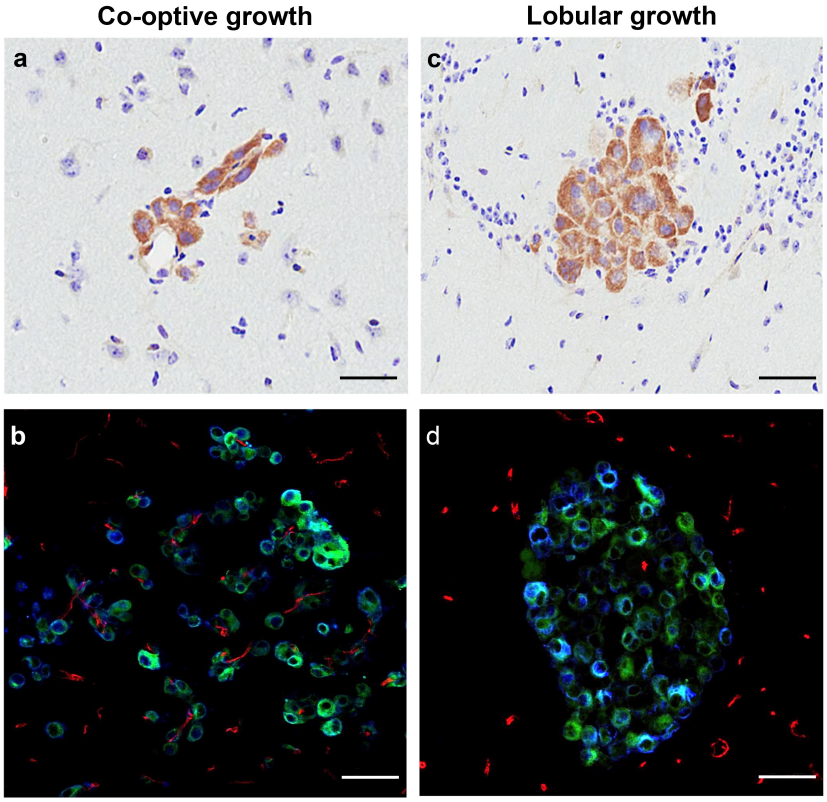


Figure 4.21: Histological comparison of two growth patterns in melanoma brain metastasis. **(a)** ALCAM (brown) staining of melanoma brain metastasis showing co-optive growth of tumour cells along the ALCAM positive vessel on day 21. **(b)** Fluorescent staining of ALCAM (blue) and CD31 (red) shows co-localisation of ACLAM and endothelial cells in the co-optive growth pattern. **(c)** Lobular growth of melanoma brain metastases showing no ALCAM activated vessels. **(d)** Fluorescent staining of ALCAM and CD31 showing negligible co-localisation of ACLAM and endothelial cells in the lobular growth pattern. Tumour marker: Melan-A; green. Scale bars: (a, c) = 20 µm; (b, d) = 50 µm.

4.4 Discussion

In this Chapter, a novel molecular MRI contrast agent targeting ALCAM, one of the endothelial adhesion molecules that is upregulated in the early stages of brain metastasis formation, was developed, validated and implemented. I demonstrated that this agent enables detection of brain micrometastases in mouse models originating from breast, melanoma and lung primary cancers. The agent showed high selectivity and sensitivity for ALCAM-targeting both *in vitro* and *in vivo*. Whilst detection of brain metastases at the micrometastatic stage was very high for breast cancer brain metastases, ALCAM appeared to be a less sensitive biomarker for melanoma and lung brain metastases in the very early stages of growth. Nevertheless, ALCAM targeted MRI still enabled detection of a substantial fraction of melanoma and lung brain metastases considerably earlier than conventional contrast-enhanced MRI.

First, upregulation of endothelial ALCAM in response to proinflammatory cytokines was assessed both *in vitro* and *in vivo*. Although marked ALCAM upregulation was evident on both human and mouse endothelial cells in response to the proinflammatory stimuli, no ALCAM expression was observed when these stimuli were injected intracerebrally *in vivo*. Our results showed that *in vitro* findings for ALCAM upregulation in response to stimuli cannot replicate the *in vivo* conditions. The latest time-point that the reactivity was assessed *in vivo* was 18 hours after intracerebral injection. A possible explanation for the lack of ALCAM upregulation on brain vessels could be the dose of the cytokines injected and/or the treatment duration. Longer stimulation time or higher doses of proinflammatory agents may induce endothelial ALCAM upregulation *in vivo*.

Subsequently, ALCAM expression in mouse models of human-derived brain metastases from breast carcinoma, melanoma and lung adenocarcinoma was assessed. Immunohistochemistry results showed ALCAM upregulation on tumour-associated vasculature and tumour cells. ALCAM was not detected on either parenchymal brain cells or blood vessels in normal, non-tumour bearing areas of the brain. Temporally, ALCAM expression as a percentage of tumour area appeared to be stable across the time-courses of micrometastatic growth studied in

all three brain metastasis models. However, the focus of this study was to identify endothelial ALCAM expression specifically, whilst the tumours are microscopic, as a target for diagnosis prior to BBB disruption. To this end, immunofluorescent staining for ALCAM and endothelial cells indicated presence of ALCAM positive vessels for breast, melanoma and lung brain metastasis models. Moreover, in breast cancer brain metastasis model, progressive upregulation of ALCAM expression on vessels in close proximity to tumour cells was observed over time. Also, at later time-points, weeks 3 and 4 after tumour cell injections, upregulation of ALCAM was also found on vessels peripheral to the tumour (up to *ca.*100 μm away from metastatic cells) in this model. For the melanoma brain metastasis model upregulation of endothelial ALCAM on intra-tumoral vessels appeared to be stable across all time-points studied and peripheral ALCAM positive vessels were not detected. Although the slower growth rate of the lung cancer brain metastases precluded a full time-course study here, upregulation of endothelial ALCAM was clearly evident at the two time-points studied (35 and 42 days after tumour cell injection), and this still preceded BBB breakdown. Thus, in all three models our data suggest that endothelial ALCAM expression could provide a sensitive biomarker for early detection of micrometastases, and in the case of breast cancer brain metastases this signal may be amplified by the broader upregulation observed.

Next, ALCAM was assessed in post-mortem human brain metastasis biopsies from breast, melanoma and lung. ALCAM expression in humans has been explored previously in several malignancies [80], [81], however, no data currently exists with respect to ALCAM upregulation in human brain metastasis of any origin. Immunohistochemistry results from the human brain metastasis biopsies showed that ALCAM is expressed on tumour-associated blood vessels, and its upregulation is independent of the primary origin. ALCAM levels in healthy brain tissue were negligible and no ALCAM upregulation was found in human brain tissue distant from tumours, indicating specificity of this marker to the tumour site. These results were consistent with ALCAM expression in the preclinical brain metastasis models.

On the basis of the above findings, an ALCAM targeted MPIO construct for molecular imaging was developed. The binding ability of this imaging compound under static and flow conditions *in vitro* was verified, and subsequently its capacity to reveal the presence of brain micrometastases *in vivo* was assessed. Based on the histological data above, two time-points, days 21 and 28, were chosen for *in vivo* imaging of the breast and melanoma models using ALCAM-MPIO and a single time-point of day 42 for the lung brain metastasis model. No brain metastases were visible with conventional gadolinium-enhanced T_1W MRI for any of the models, indicating that the BBB was intact at these time-points. However, after intravenous administration of ALCAM-MPIO, numerous hypointensities were visible on T_2*W images, whilst few were evident in either tumour bearing mice injected with IgG-MPIO or naïve mice injected with ALCAM-MPIO. In the breast cancer brain metastasis model, at day 21, a significant proportion (82%) of brain metastases found histologically co-registered with hypointensities on T_2*W images. This finding was in accord with the percentage of tumours that showed endothelial ALCAM positivity (88.5%). Sensitivity analysis indicated high sensitivity of ALCAM-MPIO detection across the range of tumour volumes observed. From all tumours detected, the smallest breast cancer brain metastasis that was detected by ALCAM-MPIO was approximately 7.8e-05 µl in volume. In the melanoma model, ALCAM-MPIO appeared to show lower sensitivity (54%) for detection of micrometastases. However, the histological results also showed that endothelial ALCAM upregulation was present in a lower percentage of tumours (50.6%) than for the breast cancer brain metastasis model, in support of the *in vivo* findings. Similarly, the time-course study showed lower endothelial ALCAM expression in the melanoma brain metastases than the breast cancer brain metastases, and this model did not show peritumoural ALCAM upregulation. In the lung cancer brain metastasis model, ALCAM-MRI enabled detection of 68% of all tumours, with 79% showing endothelial ALCAM expression. These results demonstrate that ALCAM imaging is sensitive to presence of endothelial ALCAM and it is able to provide biological insight *in vivo* that matches the underlying histology. The lower sensitivity of ALCAM-MPIO for *in vivo* detection of brain micrometastases from melanoma and

lung primaries compared to breast can largely be attributed to the differential expression of ALCAM in the metastasis-associated vessels across the models studied. In addition, a lack of peritumoural spread of the ALCAM signal in the melanoma and lung brain metastasis models used in this study will also yield a more restricted ALCAM-target for the *in vivo* imaging. A possible explanation for both these differences between lung/melanoma and breast brain metastasis models could lie in differences in the growth patterns, vascular density and angiogenic properties of the models. Co-registration of histology and MRI indicated that ALCAM-MPIO were able to detect the subset of micrometastases that were highly vascular and co-optive in growth pattern, but not those exhibiting a lobular, non co-optive growth pattern. The same explanation can be applied to the lung brain metastases model (SEBTA-001), as slower growth rate of this cell line together with lower microvessel density may contribute to less sensitivity of ALCAM-MPIO imaging for detection of these lesions *in vivo*. In accord with this notion, different phenotypes of growth and interaction with the BBB have been shown previously, depending on the primary origin of brain metastasis cells [54], [55]. It should also be noted that different time-points between breast, melanoma (day 21) and lung (day 42) brain metastasis models were compared for these analyses. Based on different doubling time of these cell lines, the median tumour volume for MDA-MB-231-Br and H1_DL2 even at the same time-point post-tumour cells injection were found to be substantially different, 0.893×10^{-3} µl *vs*. 0.304×10^{-3} µl, respectively. Nevertheless, with all the caveats mentioned above ALCAM-MPIO contrast agent was able to detect more than 50% of all brain micrometastases (with intact BBB) regardless of their primary origin. This is significantly higher that what is currently achievable in the clinic where tumours need reach to a minimum size of 2-5 mm in diameter and have a permeable BBB before they become visible on MRI [21].

Taken together, the findings of this Chapter indicate that the ALCAM-MPIO agent is highly sensitive for detection of ALCAM expression on the cerebral vasculature.

4.5 Summary of Chapter 4

In this Chapter I have shown:

- Upregulation of endothelial ALCAM at early stages of brain metastasis formation.
- Low endogenous expression of ALCAM on the healthy brain vessels in normal brain.
- Successful detection of brain micrometastases from breast, melanoma and lung, using a novel ALCAM targeted MRI contrast agent.

CHAPTER 5

Targeting E-selectin for Early Detection of Brain Metastases

5.1 Introduction

The previous Chapter confirmed the presence of ALCAM on tumour-associated vessels in brain metastasis tissue from all three main primary tumour types (breast, melanoma and lung), both in human brain metastasis biopsies and mouse brain metastasis models. ALCAM targeted MRI was then shown to provide biological insight *in vivo* that closely reflects the underlying biology. This novel MRI agent was able to diagnose brain micrometastases from all three primary mouse models, but to a greater extent (84%) for breast cancer brain metastases, as the number of ALCAM positive vessels was fewer in the melanoma and lung brain metastasis models.

A further adhesion molecule that has been shown to be one of the most highly expressed on vessels associated with breast cancer brain metastases, is E-selectin [56]. E-selectin is predominantly expressed on the luminal surface of blood vessels in response to inflammatory stimuli [210], and is implicated in many health issues including inflammatory diseases, cardiovascular disorders, cancer and metastasis. During the heamatogenous metastasis process, E-selectin provides shear-resistance adhesion on the vessel surface that mediates capturing of circulating cancer cells under dynamic blood flow (please see Section 1.5.3 for more details about E-selectin and its role). In brain metastasis, it has been shown that E-selectin and its ligand CD15s (sialyl Lewis^X (sLe^x)) mediate adhesion of non-small cell lung cancer to human endothelial cells *in vitro* [93]. Nevertheless, the presence of E-selectin on cerebral vessels in brain metastasis models other than breast primary, has not yet been confirmed.

Over the last two decades, there has been a growing interest in targeting E-selectin as a pharmacological biomarker, as a result of its expression in the vicinity of neuroinflammatory diseases. Most research in the field is concentrated on using E-selectin as a target for anti-inflammatory and anti-cancer therapies [211]. Although *in vivo* mapping of E-selectin with SPECT [212], [213], optical imaging [214] and ultrasound [215] has been reported previously, molecular MRI studies for rodent pathological brain models are scarce. Various strategies to exploit E-selectin and its ligands for molecular MRI applications in neuroinflammation models have been developed. Initial E-selectin targeted MRI studies, used diethylenetriaminepentaacetic

acid (DTPA) coupled with gadolinium (Gd) as a carrier vehicle for development of molecular imaging contrast agents. Sibson *et al.* showed that the Gd-DTPA-B(sLe^x) MRI contrast agent, which contains an sLe^x mimetic moiety, enabled detection of IL-1β or TNF induced endothelial activation *in vivo* in the rat brain [196]. A similar contrast agent (Gd-DTPA-sLe^x A) showed *in vivo* binding to activated vessels in a focal stroke mouse model [216]. Despite these encouraging results, as discussed in the Introduction Section 1.7.2.1, it is known that Gd-based contrast agents generally have low sensitivity, and a high concentration of gadolinium is often needed to obtain adequate contrast on MRI. On the other hand, iron oxide particles have higher relaxation properties and allow detection at very low concentrations, thereby providing increased contrast for the purpose of molecular imaging. On this basis, subsequent E-selectin molecular MRI studies from our group employed iron oxide particles as the carrier vehicle for contrast agent development. Van Kasteren *et al.* chemically synthesised the sLe^x natural glycan ligand to be grafted onto iron oxide microparticles [217]. These sLe^x-MPIO were able to successfully map activated vessels and lesions in rat models of stroke and multiple sclerosis (MS) [137], [217]. However, targeting E-selectin through its natural ligand, sLe^x, may not be the optimal approach for *in vivo* imaging of this surrogate. Carbohydrate-MPIO contrast agents bring possible disadvantages of low avidity and sensitivity. As mentioned earlier, the E-selectin/sLe^x interaction is transient, and occurs during the "rolling" stage of the leukocyte adhesion cascade. As a result, E-selectin imaging using sLe^x relies highly on the physiological time-window. Moreover, sLe^x is also a carbohydrate ligand for P-selectin, thus specific and sensitive detection of E-selectin alone may not be feasible with this technique [137]. Jefferson *et al.* provided an alternative strategy by developing an antibody-based E-selectin targeted MRI contrast agent [135]. They targeted E-selectin expression on stimulated human umbilical vein endothelial cells (HUVEC) *via* an E-selectin antibody (mouse anti-human E-selectin monoclonal antibody) coupled with MPIO [135]. High binding efficacy of this compound was confirmed under physiologically relevant shear stresses *in vitro*. In light of these results and developments in the production of high-affinity antibodies, in this Chapter I advance *in vivo* E-selectin imaging by developing a novel E-selectin

antibody-conjugated MPIO. I validate binding capacity and sensitivity of this compound both *in vitro* and *in vivo* in neuropathological mouse models and assess sensitivity for detection of brain micrometastases.

It has also become clear that there is a dynamic cross-talk between metastatic tumour cells and brain endothelial cells, such that up or downregulation of adhesion molecules is highly influenced by tumour stage, phenotype and microenvironment. As mentioned in the Introduction (Section 1.5.1), the adhesion cascade during metastasis is a multi-step process including tethering, rolling, firm adhesion and finally extravasation of tumour cells. It is suggested that the initial rolling of circulating cancer cells on the endothelium is selectin-mediated, whilst firm adhesion is supported by integrin binding to VCAM-1 and ALCAM amongst others [65]. It is still not clear whether distinctive classes of CAMs are involved at each step of the adhesion process or whether there is an active synergy between CAMs for these sequential steps. The outcome of brain metastasis detection by targeting a single adhesion molecule depends highly on the binding specificity, pharmacokinetics, target biodistribution and stage of brain metastasis formation. Consequently, owing to complex nature of brain metastasis process, I hypothesised that combination of targeted adhesion molecules (e.g. VCAM-1+E-selectin) may yield even more sensitive and robust detection of brain micrometastasis. I speculate that dual targeted molecular imaging agents may increase the efficacy of detection by effectively enhancing binding affinity and embracing a broader window of opportunity during the metastasis multi-step process.

On this basis, the aims of this Chapter are as follows: (i) to assess the suitability of E-selectin as an imaging biomarker in a model of neuroinflammation; (ii) to develop E-selectin targeted MPIO, and test their binding capacity both *in vitro* and *in vivo*; (iii) to assess E-selectin upregulation in mouse brain metastasis models from breast, melanoma and lung; (iv) to detect brain micrometastases using E-selectin-MPIO *in vivo*; and, finally, (v) to assess whether dual CAMs targeting (VCAM-1+E-selectin) increases sensitivity for early detection of brain micrometastases compared to single targeting.

5.2 Methods

5.2.1 Cell Lines

For the mouse brain metastasis models, three brain tropic human-derived cell lines, MDA-MB-231-Br (breast), H1_DL2 (melanoma) and SEBTA-001 (lung adenocarcinoma) were used. Mouse brain endothelial cells (bEnd-3) were cultured for the *in vitro* experiments of this Chapter.

5.2.2 E-selectin Response to Cytokines; *In Vitro*

Mouse endothelial cells (bEnd-3, 50,000 cells/ml) cells were seeded onto a 24-well plate. Cells were stimulated with recombinant murine IL-1β or recombinant murine TNF at a concentration of 10 ng/ml for 8 or 16 hours. Normal medium (DMEM) was used for the control unstimulated group.

5.2.3 E-selectin Response to Proinflammatory Agents; *In Vivo*

To assess E-selectin upregulation in response to proinflammatory stimuli, brain histological sections from mice previously injected intrastriatally with an array of proinflammatory cytokines (see Section 4.2.3) were immunohistochemically stained for E-selectin.

5.2.4 E-selectin-MPIO Synthesis

Two different primary monoclonal antibodies against mouse E-selectin were purchased from R&D systems: (1) Monoclonal rat IgG_{2A} anti mouse E-selectin (cat. no. MAB5751, R&D systems); and (2) Monoclonal rat IgG_1 anti mouse E-selectin (cat. no. MAB575, R&D systems). E-selectin antibodies were conjugated to ProMag-COOH MPIO, using the protocol described in detail in the Methods Chapter (Section 2.2.1). Subsequently, the number of E-selectin loaded on the MPIO were measured using BD FACSCalibur flow cytometer, details of this protocol can be found in the Methods Chapter (Section 2.2.2)[*].

[*] Antibody loading on MPIO was measured and confirmed prior to all *in vivo* experiments of this Chapter.

5.2.5 E-selectin-MPIO and Control IgG-MPIO Binding Assay; *In Vitro*

The binding capacity of E-selectin-MPIO to the mouse brain endothelial cells (bEnd-3) under static and shear stress conditions was measured using channel slides (μ-Slide $VI^{0.4}$, cat. no. 8066, ibidi, Germany). Channels were filled with medium (90 μl) and placed in an incubator 24 hours prior to the experiment. bEnd-3 cells (20,000 cells/ 30 μl in each reservoir) were seeded onto the chambers. After 24 hours, the medium was removed and cells treated with recombinant murine IL-1β (10 ng/ml) for 6 hours [218]. Untreated cells were used as the baseline of the experiment. Cells were washed with PBS, and the chambers were connected to a syringe pump (model 44, Harvard Apparatus, UK) using tube adapters (Figure 5.1).To fluorescently tag the MPIO, E-selectin-MPIO or IgG-MPIO were incubated with 10 μl Alexa Fluor® 594 (Donkey anti-rat, cat. no. 712-586-150, Jackson ImmunoResearch, UK) for 30 minutes on a shaker (1000 Mot/min) at room temperature, then thoroughly washed with PBS to remove the unbound fluorophores. For the static condition (0 dyne[†]/cm^2), fluorescently tagged antibody-MPIO (6.25 μg MPIO/ml) were added to the chambers for 5 minutes. For the flow experiment, to simulate the range of physiological shear stresses that are found in the circulatory systems, flow chambers were exposed to 1, 5, 10 and 15 dyne/cm^2 (E-selectin-/IgG-MPIO). The mean shear stress has shown to be lower in large veins (1-6 dyne/cm^2), and higher (15-90 dyne/cm^2) in small venules given the high flow rate and small diameters of these vessels [219], [220] The shear stress for each chamber was calculated based on the equation provided by the manufacturer:

$$\tau = \eta \times 171.1 \times \phi$$

where τ is the shear stress (dyne/cm^2), η is the dynamic viscosity (dyne·s/cm^2, PBS was used) and ϕ is the flow rate (ml/min). After 5 minutes of flow, cells were washed with PBS and fixed with 4% paraformaldehyde. Experiments were performed in triplicate. Chambers were then fluorescently stained for E-selectin and images were acquired using an inverted confocal microscope (LSM-780; Carl Zeiss Microimaging) at X20 magnification. The number of bound

[†] Dyne: The force required to accelerate a mass of one gram at a rate of one centimeter per second square.

E-selectin-/IgG-MPIO to the E-selectin expressed on cells were counted manually for each FoV (n = 6 per flow rate).

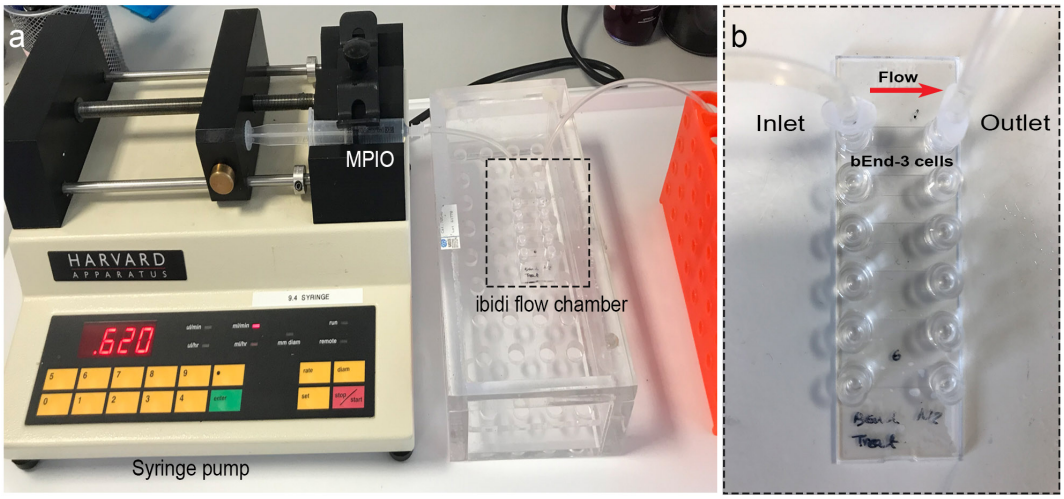


Figure 5.1: Flow chamber setup for binding assessment of E-selectin-MPIO.
(a) Syringe (20 ml, I.D: 20.18 mm, Terumo) was filled with fluorescently-tagged E-selectin-MPIO or IgG-MPIO and placed on the syringe pump. Syringe was then connected to the inlet tube of the ibidi chamber and the desired flowrate was set on the pump. **(b)** zoomed picture of ibidi chamber showing the inlet and outlet tubing connections, and the flow direction of fluorescently-tagged-MPIO on treated un-fixed bEnd-3 cells.

5.2.6 E-selectin Imaging in an Acute Neuroinflammation Model

To assess E-selectin-MPIO binding to a model of acute neuroinflammation, an imaging time-point post-cytokine injection had to first be identified. Female BALB/c mice (7-8 weeks old, n = 9; Charles River, UK) were injected intrastriatally with 1 ng of recombinant murine IL-1β in 1 µl of sterile PBS as described in detail in the Methods Chapter (Section 2.4.3). Brains were collected at 4, 6 and 8 hours after injection (n = 3 per time-point). Histological brain sections were stained for E-selectin as describe in Section 2.5.2, and based on these results, the optimal E-selectin MRI window was determined.

For the in vivo E-selectin imaging, female BALB/c mice (7-8 weeks old, n = 12; Charles River, UK) were injected intracerebrally with either (i) 1 ng/µl of recombinant murine IL-1β (n = 8) or (ii) 1 µl sterile PBS (n = 4). Three hours after surgery, mice were intravenously injected with

either 100 µl of E-selectin-MPIO (n = 4 per cohort, IL-1β or PBS injected; 4 mg Fe/kg mouse weight) or 100 µl of control IgG-MPIO (n = 4, IL-1β injected cohort; 4 mg Fe/kg mouse weight). The sample size (n = 4 per group) was computed using G*Power tool. Based on the previous data by McAteer et.al. [139], in order to observe statistically significant MPIO contrast effect in the IL-1β injected neuroinflammation model, minimum three mice per group is needed ($n_1 = n_2$, effect size d= 2.85, α error = 0.05 and power (1- β error) = 0.95). For the purpose of this study an extra mouse was added per group to account for any error during the procedures (e.g. failed cytokine injection).

Subsequently, mice were imaged on the 7.0 T preclinical scanner using the T_2*W-MGE3D sequence described in the Methods Chapter (Section 2.6). All experimental mice in this Chapter were transcardially perfusion-fixed immediately after imaging under terminal anaesthesia, using 0.9% heparinised saline followed by PLP_{light} as described in Section 2.4.4. Experimental plan for E-selectin-MPIO imaging in the neuroinflammation model is shown below (Figure 5.2).

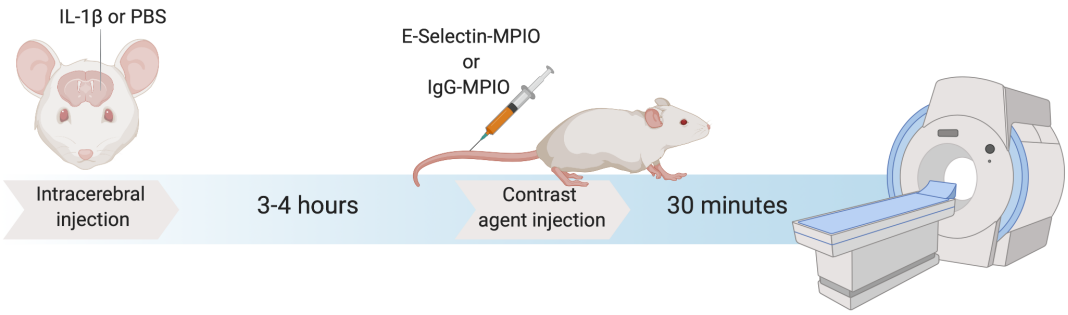


Figure 5.2: Experimental plan for E-selectin imaging in the neuroinflammation model.

5.2.7 E-selectin Expression on Endothelial Cells in the Presence of Tumours

Mouse brain endothelial cells (bEnd-3, 300,000 cell/ml) were seeded onto Matrigel™-coated Millicell wells for 6 hours. Tumour cells (MDA-MB-231-Br or H1_DL2 or SEBTA-001; 250,000 cell/ml) were then added on top of the mouse endothelial cells. After 14 hours, wells were washed with PBS and fixed with 4% paraformaldehyde. Wells were then fluorescently

stained for E-selectin. Details of 3D endothelial and tumour cell co-culture, and staining can be found in the Methods Chapter (Section 2.3.4).

5.2.8 Mouse Brain Metastasis Models

Tumour cells (1×10^5 MDA-MB-231-Br, H1_DL2 or SEBTA-001 cells in 100 μl of sterile PBS) were injected into the left ventricle of female SCID mice as described in Section 2.4.2. To measure E-selectin upregulation on metastasis-associated vessels, mice (n = 4 per time-point) were perfused on day 7, 14, 21 or 28 after tumour cell injection for the breast and melanoma brain metastasis models, and day 35 and 42 for the lung brain metastasis model.

5.2.9 Immunohistochemistry and Immunofluorescence; Mouse Tissue

Mouse brain sections (inflammation and metastasis models), were immunohistochemically stained for E-selectin, or fluorescently stained for E-selectin, the tumour-specific markers (GFP, Melan-A and cytokeratin) and CD31, following the same staining protocols, as described in Sections 2.5.2 and 2.5.5, using the antibodies in Table 2.2. To detect iron oxide particles, Perls' Prussian staining was performed using the protocol described in Section 2.5.3. Immunohistochemical sections were scanned on an Aperio CS2 Brightfield scanner (Leica Biosystems) at X20 or X40 magnification and analysed using Imagescope (v.12.3.2; Leica Biosystems) software. Immunofluorescent images were acquired using an inverted confocal microscope (LSM-780; Carl Zeiss Microimaging) with constant imaging parameters and analysed using Zen software (Carl Zeiss). Whole brain fluorescent images were taken at X20 magnification using an Aperio immunofluorescence slide scanner (Leica Biosystems).

5.2.10 Immunohistochemical Analyses

To measure E-selectin upregulation in the neuroinflammation model, brain sections (10 μm) were collected from the striatum and stained for E-selectin. Ipsilateral and contralateral hemispheres were outlined manually. The built-in Positive Pixel Count v.9 algorithm on Imagescope was used to quantify the strong positive staining (dark brown; E-selectin +) as

described is Section 2.5.5. The positivity area was then normalised by the outlined hemisphere (μm^2) and reported as the activated E-selectin area per hemisphere. More than 10 sections were analysed for each time-point.

For temporal measurement of E-selectin in the brain metastasis models, tumour bearing brain sections (10 μm) were stained for E-selectin. The entire brain section was outlined, and the number of strong positive pixels calculated using the same algorithm as above. This measurement was reported as the number of positive pixels per mm^2 of mouse brain. In both analyses, choroid plexus and ventricles were excluded from the segmentations owing to false-positive staining of these areas. More than 30 tumour sections were analysed for each tumour model and time-point.

5.2.11 Immunohistochemistry; Human Tissue

Human brain metastasis biopsies from breast, melanoma and lung adenocarcinoma were stained for E-selectin (n = 2 patients for each primary). Melanin bleaching technique was used for melanoma samples. Details of human tissue staining, E-selectin antibody, and melanin bleaching technique can be found in the Methods Chapter (Section 2.5.4).

5.2.12 E-selectin Imaging in the Brain Metastasis Models

For the *in vivo* imaging experiment, two time-points, days 21 and 28 after tumour cell injection, for the breast and melanoma brain metastasis models, and two time-points, days 35 and 42, for the lung brain metastasis model were chosen. On the day of imaging, tumour bearing mice were injected intravenously with either E-selectin-MPIO or control IgG-MPIO (100 μl; 4 mg Fe/kg mouse weight). Mice were imaged using 3D T_2*W-MGE3D, followed by acquisition of pre- and post-gadolinium-DTPA T_1W (SEMS) sequences on the 7.0 T MRI spectrometer. Experimental plan for this study is shown in Figure 5.3. More details regarding the MRI sequences used for this study can be found in the Methods Chapter (Section 2.6).

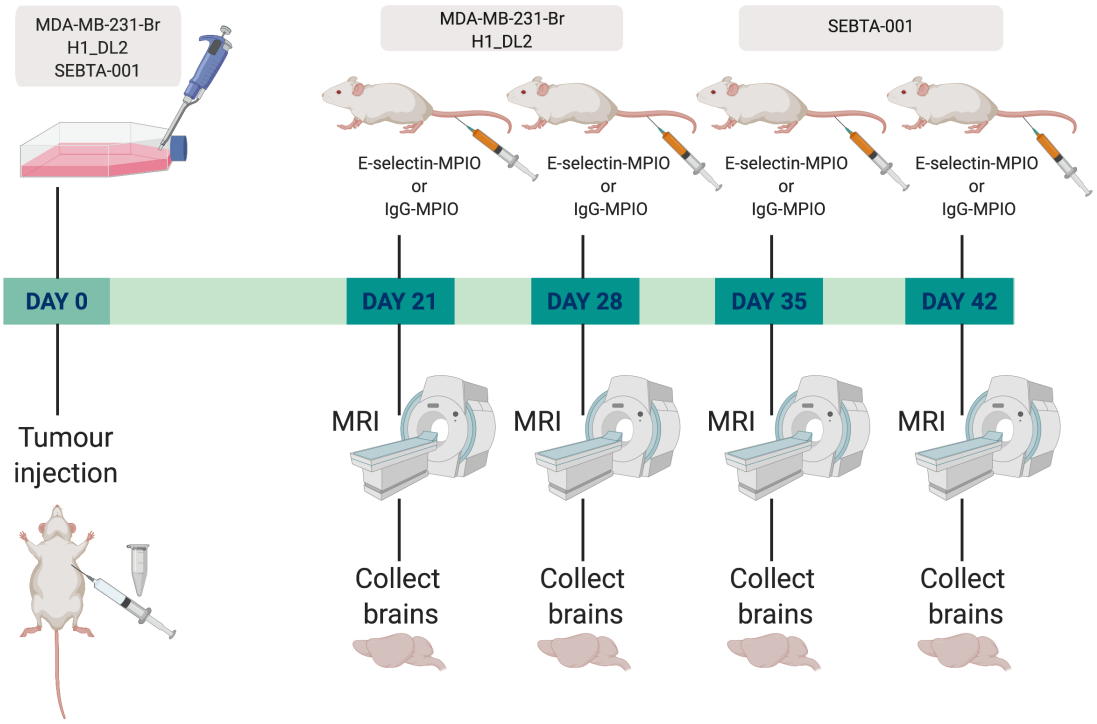


Figure 5.3: Experimental plan for E-selectin imaging in the brain metastasis models.

5.2.13 MRI and Histology Co-Registration

To determine the sensitivity of E-selectin-MPIO imaging, alternate sections (10 µm) of whole mouse brain were stained for tumour-specific markers (breast, GFP; melanoma, Melan-A; and lung, cytokeratin). Tumour volume (μm^3) was calculated for cohorts imaged on day 21 after tumour cell injection for MDA-MB-231-Br and H1_DL2 models and day 42 for SEBTA-001 model as described in detail in Section 2.6.5. Subsequently, alternate brain sections were stained for E-selectin marker and tumours were assessed for endothelial E-selectin positivity or negativity. Histology anatomical maps were visually compared with the anatomical location of hypointensities on T_2*W-MGE3D MR images. Spatial correlation between histology and MRI was assessed blind, by an independent observer[‡].

[‡] Claire Bristow assisted with histology and MRI co-registration.

5.2.14 Dual Targeted Imaging in the Brain Metastasis Models

Single imaging time-point post-tumour injection was chosen per tumour model (day 21 breast/ melanoma and day 42 lung). On the day of imaging, mice were administrated via a tail vein with 2 mg Fe/kg mouse weight of VCAM-MPIO (in 50 µl PBS) followed by 2 mg Fe/kg mouse weight of E-selectin-MPIO (in 50 µl PBS). Approximately 30 minutes later, mice were imaged using T_2*W-MGE3D sequence followed by acquisition of pre-and post-gadolinium-DTPA T_1W (SEMS). To co-register MRI results with the histology, alternate brain sections (20 µm[§] thickness, 5 histological section per MRI slice) were stained for the tumour-specific marker (breast, GFP; melanoma, Melan-A; and lung, cytokeratin). The anatomical location of each tumour was outlined on the histology and correlated with the spatial position of hypointensities on T_2*W-MGE3D imaging dataset (Section 2.6.5).

5.2.15 Statistical Analysis

Statistical analyses were performed using Prism (GraphPad Software, USA). Parametric analyses of variance (ANOVA) was applied after assessing normality of variables using the Shapiro-Wilk test. Tukey post-hoc tests were conducted to identify significant ($p < 0.05$) differences between groups. All error bars on graphs are shown as standard error of the mean (SEM) and the level of significance is shown with asterisks; *$p < 0.05$, **$p < 0.01$, ***$p < 0.001$.

5.3 Results

5.3.1 E-selectin Upregulation in Response to Cytokines; *In Vitro* and *In Vivo*

The expression of E-selectin on endothelial cells in response to the proinflammatory cytokines (IL-1β and TNF) is shown below (Figure 5.4). E-selectin was present on the mouse brain endothelial cells (bEnd-3) treated with either cytokine after both 8 and 16 hours of incubation. Baseline levels of E-selectin on unstimulated endothelial cells was found to be negligible. No

[§] Volumetric tumour quantifications were not performed in this study. Histological samples were only used to register anatomical location of MRI hypointense voxels with tumours, hence 20 µm slice thickness was chosen.

signal was detected in the green channel for the negative control immunofluorescent staining (Figure 5.4). The microscopy settings (exposure and offset) were kept constant across samples.

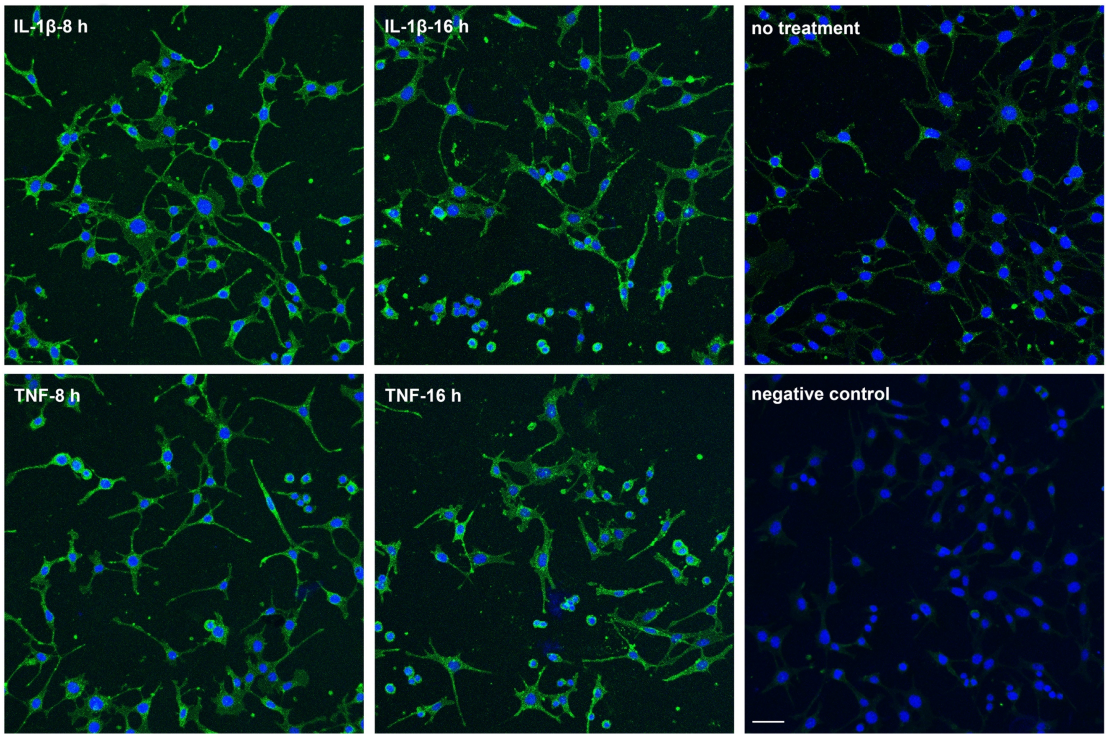


Figure 5.4: E-selectin response to the inflammatory cytokines on mouse brain endothelial cells. Mouse brain endothelial cells (bEnd3) were treated with 10 ng/ml of either IL-1β or TNF for 8 or 16 hours. Marked E-selectin expression was evident on the membrane of the endothelial cells for both cytokines and time-points studied. Minimum background levels of E-selectin was shown for the untreated cells. E-selectin negative control staining showed no signal in the green channel. E-selectin: green. Nuclei: DAPI; blue. Scale bar = 50 μm.

In line with the *in vitro* findings, E-selectin immunohistochemistry of brain tissues previously intrastriatally injected with the array of proinflammatory agents, showed prominent expression of E-selectin on vessels in the injected (ipsilateral) side (Figure 5.5). This upregulation was evident for both time-points (6 and 18 hours) and for all agents. No upregulation was found on the vessels of the contralateral hemisphere. Together these *in vitro* and *in vivo* results demonstrated that proinflammatory agents induce E-selectin expression on cerebral vessels. On the basis of these results a subsequent study to determine the optimal imaging time-point was performed from 4-8 hours after IL-1β intracerebral injection.

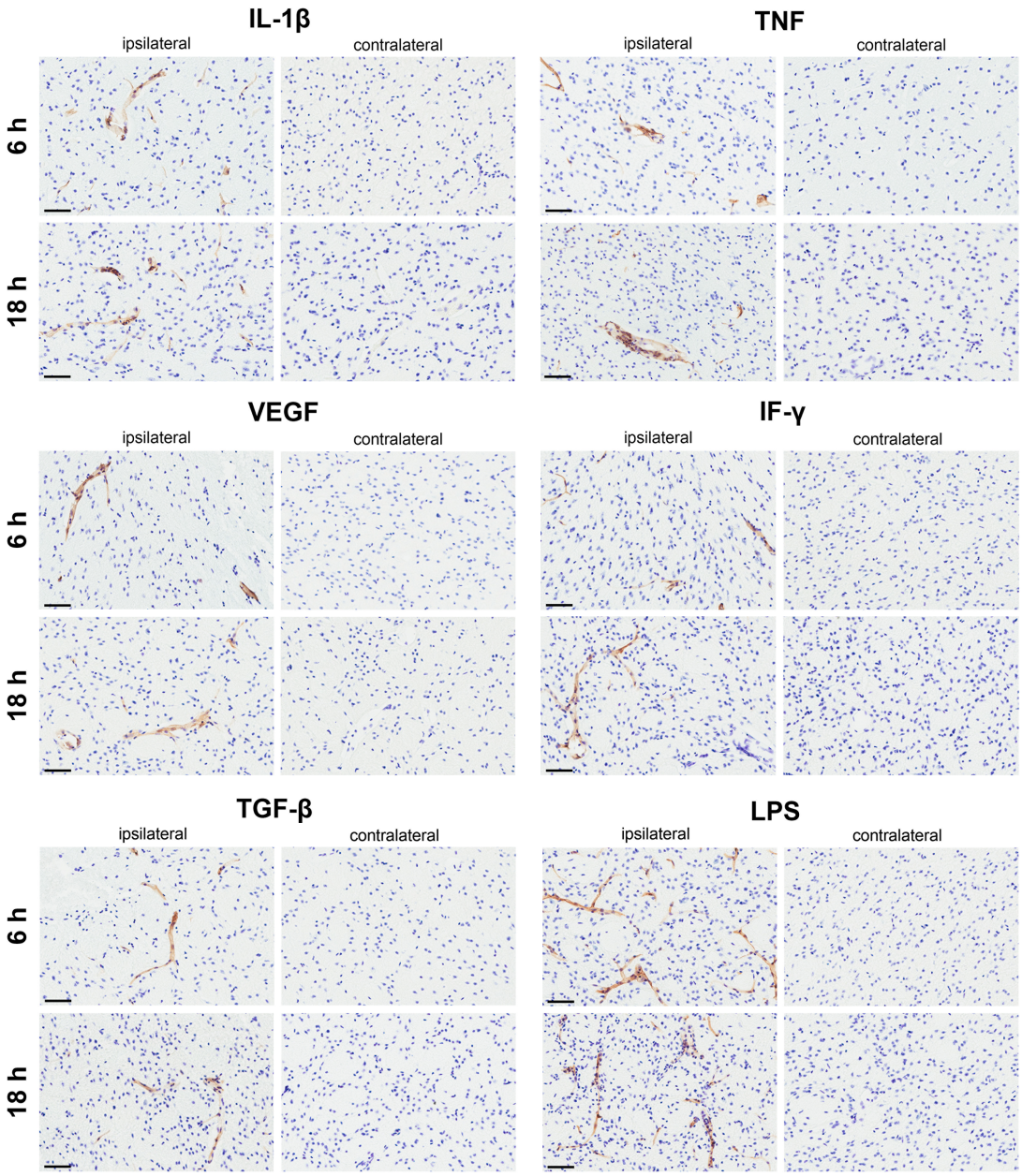


Figure 5.5: E-selectin response to proinflammatory agents *in vivo*.

E-selectin (brown) immunohistochemistry of mouse brain sections stimulated with TNF, IL-1β, IF-γ, TGF- β, VEGF or LPS. E-selectin was expressed on the vessels of the ipsilateral hemisphere at 6 and 18 hours after intracerebral injection. Minimum upregulation was observed on the vessels of the contralateral hemispheres. Counterstain = cresyl violet; blue. Scale bars = 50 μm.

5.3.2 Optimisation and Binding Assessment of E-selectin-MPIO Conjugate

E-selectin antibody loading on MPIO was assessed for two commercially available antibodies. Monoclonal rat IgG_{2A} anti-mouse E-selectin (cat. no. MAB5751) showed higher antibody loading 21,523±3,000 (mean ± SD, n = 3; 11,861 antibodies per μm^2) compared to monoclonal rat IgG_1 anti-mouse E-selectin (cat. no. MAB575) 17,400±4,230 (mean ± SD, n = 3; 9,600 antibodies per μm^2). On this basis, the monoclonal rat IgG_{2A} anti-mouse E-selectin was used for the following experiments in this Chapter.

The capacity of E-selectin-MPIO for specific and quantitative binding was first assessed under static and shear stress conditions *in vitro*. IgG-MPIO were used for the control setting. Mouse brain endothelial cells (bEnd-3) were stimulated with IL-1β to provoke surface expression of E-selectin, as shown in Section 5.3.1, and exposed to fluorescently labelled E-selectin or IgG-MPIO. Substantial binding of E-selectin-MPIO (red) to E-selectin (green), expressed on the endothelial cells was evident (Figure 5.6a) at different flow rates. In contrast, IgG-MPIO (red) showed only low levels of binding to the activated endothelial cells (Figure 5.6b). E-selectin-MPIO were retained only sparsely on unstimulated cells, reflecting low level of basal E-selectin (Figure 5.6c). Quantitative binding analyses for each shear stress condition showed a greater number of bound E-selectin-MPIO (black circles) compared to IgG-MPIO (black squares) (Figure 5.6e) for all flow rates. The number of bound E-selectin-MPIO decreased with increasing in shear stress; nevertheless, even at the highest shear stress (15 dyne/cm^2), bound E-selectin-MPIO were present on the activated endothelial cells.

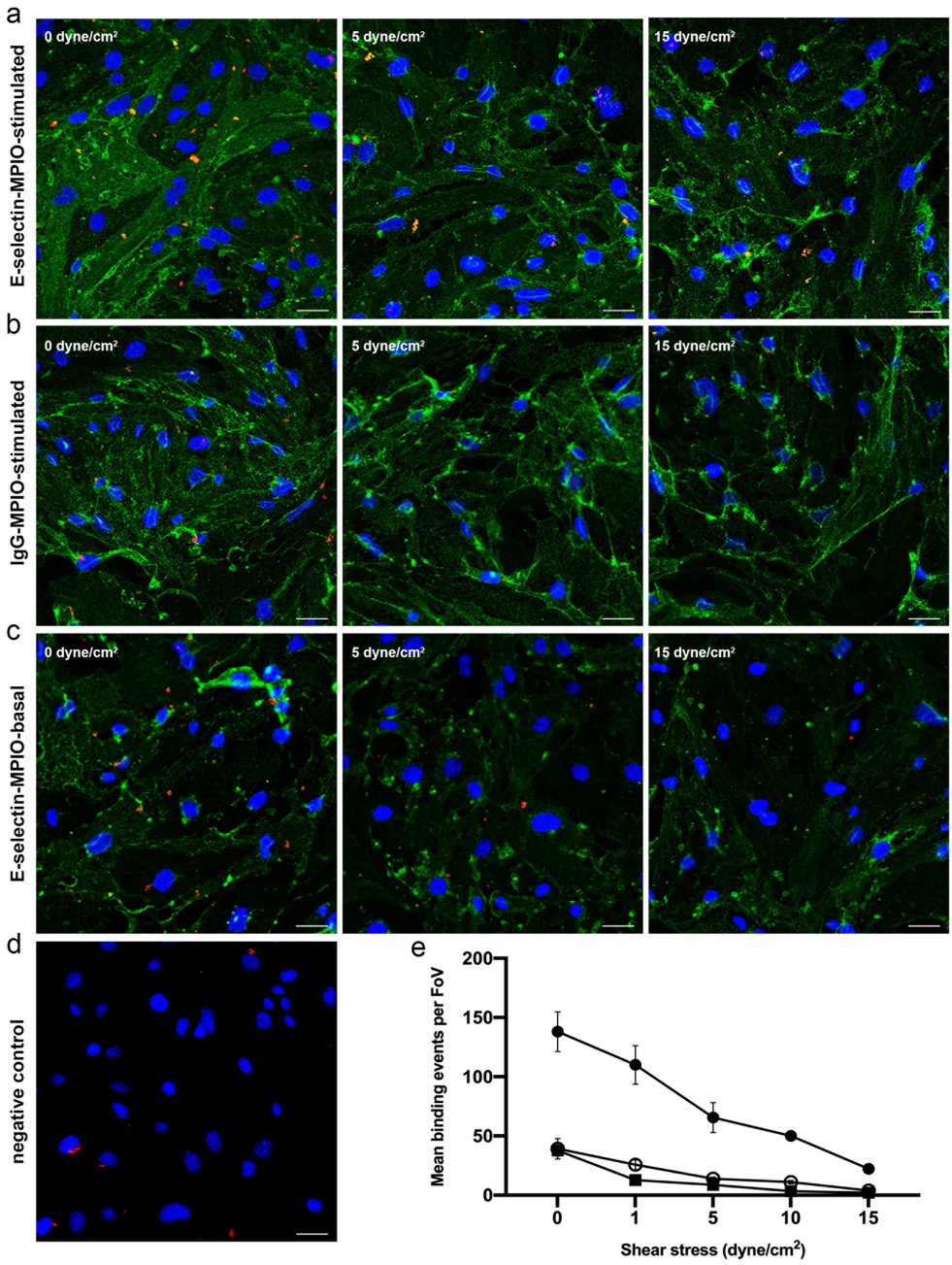


Figure 5.6: E-selectin-MPIO binding ability *in vitro*.

(a) Representative images showing binding ability of E-selectin-MPIO (red) to E-selectin (green) on activated mouse brain endothelial cells (bEnd-3), under static and flow conditions. **(b)** Representative images showing minimum binding of IgG-MPIO to stimulated bEnd-3 cells under static and flow conditions. **(c)** Sparse retention of E-selectin-MPIO on unstimulated cells reflects low E-selectin upregulation. **(d)** No green signal was detected for E-selectin negative control staining. **(e)** Graph showing data points expressed as mean ± SEM of bound MPIO per FoV under static (0 dyne/cm^2) and different shear stress conditions for E-selectin-MPIO (black circles), IgG-MPIO (black squares) and basal cells treated with E-selectin-MPIO (empty circles). MPIO: red. E-selectin: Green. Nuclei: blue. Scale bars = 25 μm.

5.3.3 Binding Assessment of E-selectin Conjugate; *In Vivo*

To induce E-selectin endothelial activation *in vivo*, and determine the optimal imaging window, mice were given IL-1β by stereotactic injection to the left striatum. Brains were collected at 4, 6, and 8 hours after injection. Histological staining showed a direct correlation between the amount of E-selectin activation on the ipsilateral hemisphere and the time post-cytokine injection (Figure 5.7a, b, c). Quantitative histological analyses showed a significant difference ($p < 0.0001$) between E-selectin expression in the ipsilateral (dotted bar) and contralateral (black bar) hemispheres for all time-points studied, and a significant difference ($p < 0.0001$) between ipsilateral hemispheres (Figure 5.7 d) across the time-course studied.

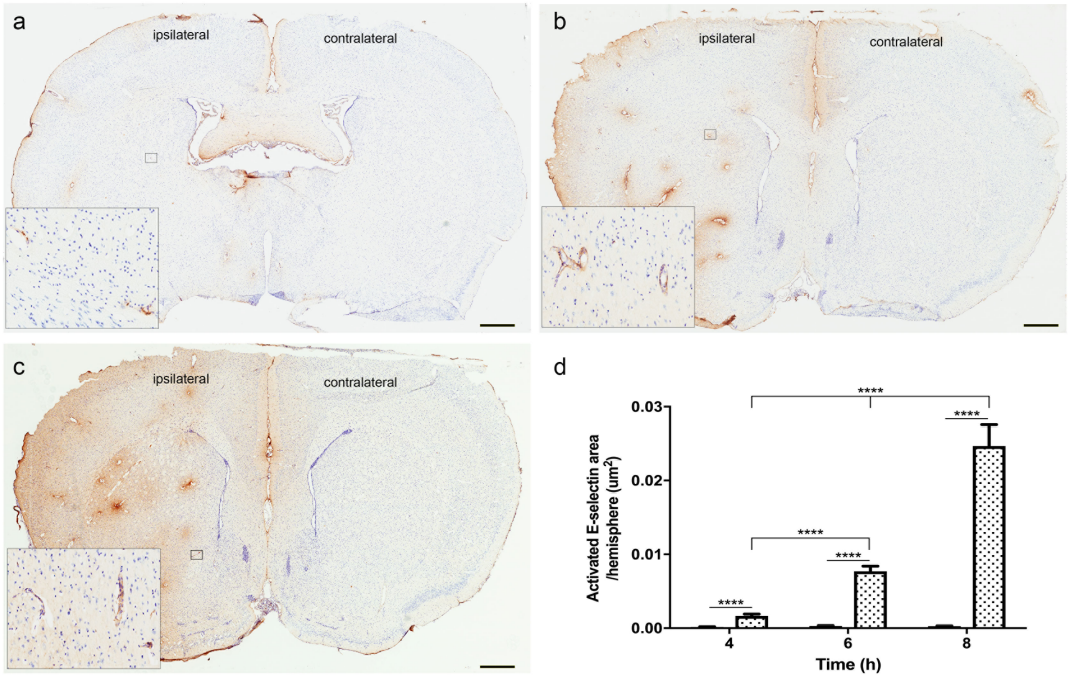


Figure 5.7: Temporal upregulation of E-selectin in the mouse neuroinflammation model. E-selectin (brown) staining of mouse brain injected with IL-1β (1 ng/μl) after 4 **(a)**, 6 **(b)** and 8 hours **(c)**. E-selectin upregulation on the ipsilateral side was evident for all time-points. Counterstain: cresyl violet; blue. Scale bars = 0.5 mm. **(d)** Quantitative analysis of E-selectin activation over time showed significant difference between the amount of E-selectin expression on the ipsilateral side (dotted bars) compared to contralateral side (black bars) and a significant difference between ipsilateral hemispheres after 4, 6 and 8 hours. ****$p < 0.0001$, error bars = SEM.

Although E-selectin expression showed to be higher at later time-points (4 *vs.*8 hours), in order to reflect the degree of E-selectin upregulation in brain metastasis model, 4 hours post stimulus injection was chosen for the E-selectin imaging in the neuroinflammation model.

To test the binding ability of E-selectin-MPIO *in vivo*, the compound was administrated systemically *via* a tail vein 3 hours[**] after IL-1β intracerebral injection. E-selectin-MPIO caused MRI contrast effects in the IL-1β injected hemisphere. Minimal non-specific retention was evident in the contralateral hemisphere (n = 4, Figure 5.8a). Negligible contrast effects were evident in IL-1β injected mice administrated with IgG-MPIO (n = 4, Figure 4.8b). Moreover, almost no hypointensities were found in the PBS-injected mice, administrated with E-selectin-MPIO (n = 4, Figure 5.8c). Quantification of the number of hypointense signal for each brain hemisphere showed a significant difference ($p < 0.001$) between ipsilateral (purple bar) and contralateral (blues bar) for IL-1β + E-selectin-MPIO mice (Figure 5.8d). No significant differences were found between hemispheres for either IL-1β + IgG-MPIO or PBS + E-selectin-MPIO injected mice. E-selectin immunofluorescent results confirmed unilateral presence of E-selectin after IL-1β injection (Figure 5.8e). Although no hypointensities were detected in IgG-MPIO injected mice, immunohistochemistry results confirmed unilateral upregulation of E-selectin as for other cohort injected with IL-1β (Figure 5.8).

[**] This time-point was chosen to account for the mouse set-up time in the scanner (~30 minutes) and the warm-up sequence (30 minutes).

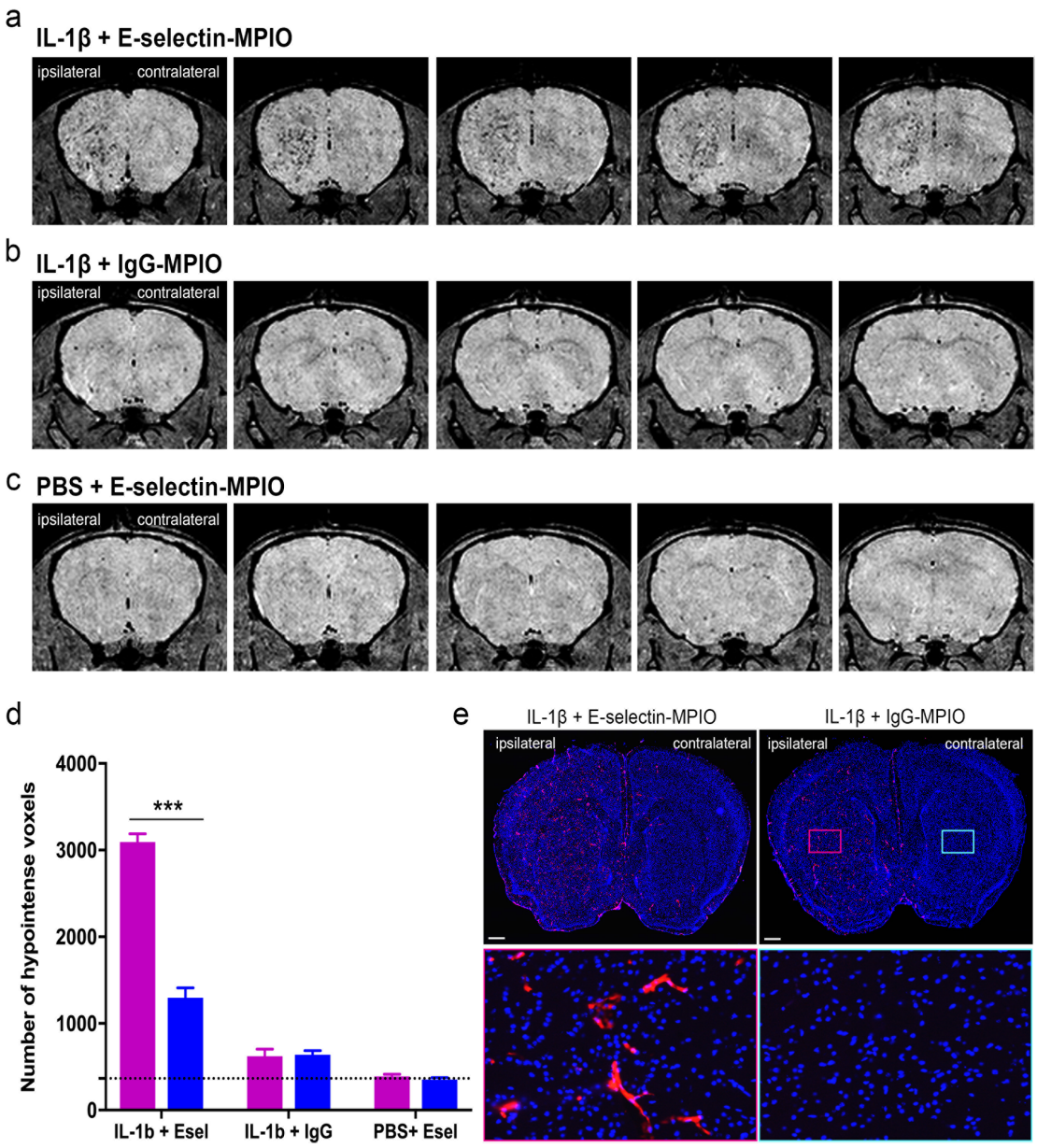


Figure 5.8: E-selectin binding in the neuroinflammation model.

(a-c) Representative T_2*W-MGE3D images (in rows, 5 images per brain) of mice injected intrastriatally with either IL-1β or PBS, 4 hours prior to intravenous of E-selectin-/IgG-MPIO imaging. **(a)** Unilateral hypointensities on the ipsilateral side of the brain reflect the specific binding of E-selectin-MPIO to the activated vessels with visually absent effect on the contralateral side. **(b)** Absence of unilateral specific binding in mouse injected with IgG-MPIO. **(c)** Minimal contrast effects were evident in the PBS injected group. **(d)** Graph showing quantitation of MPIO induced hypointensities in ipsilateral (purple bar) and contralateral (blue bar) hemispheres. Baseline level of endogenous hypointensities in naïve mice is shown by dotted line, n = 2. ***$p < 0.001$, error bars = SEM. **(e)** Corresponding histological sections of IL-1β injected mice imaged with either E-selectin-MPIO or IgG-MPIO. E-selectin: red. Nuclei: blue; DAPI. Scale bar = 0.5 mm.

5.3.4 E-selectin Expression in Breast, Melanoma and Lung Brain Metastasis Models

Findings so far have shown that E-selectin is upregulated on inflamed brain vessels in response to the proinflammatory agents, and that the novel targeted E-selectin-MPIO compound is able to detect this phenomenon in an acute neuroinflammation mouse model. These results are in line with the role of E-selectin as a mediator in leukocyte trafficking. In the following section the expression of E-selectin on vessels in the vicinity of brain metastases is assessed.

First, tumour cells (MDA-MB-231-Br, H1_DL2 and SEBTA-001) were 3D co-cultured with mouse brain endothelial cells (bEnd-3). After 14 hours[††], E-selectin (red) was exclusively present on the endothelial cells in close proximity to cancer cells for all three brain metastasis cell lines (Figure 5.9).

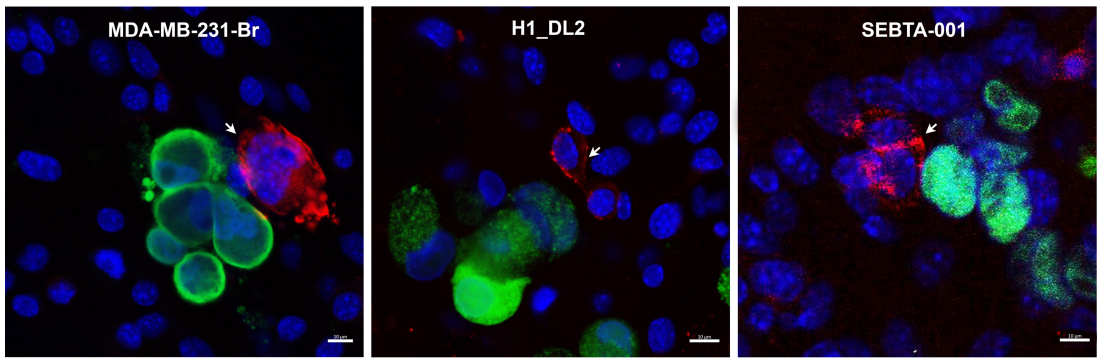


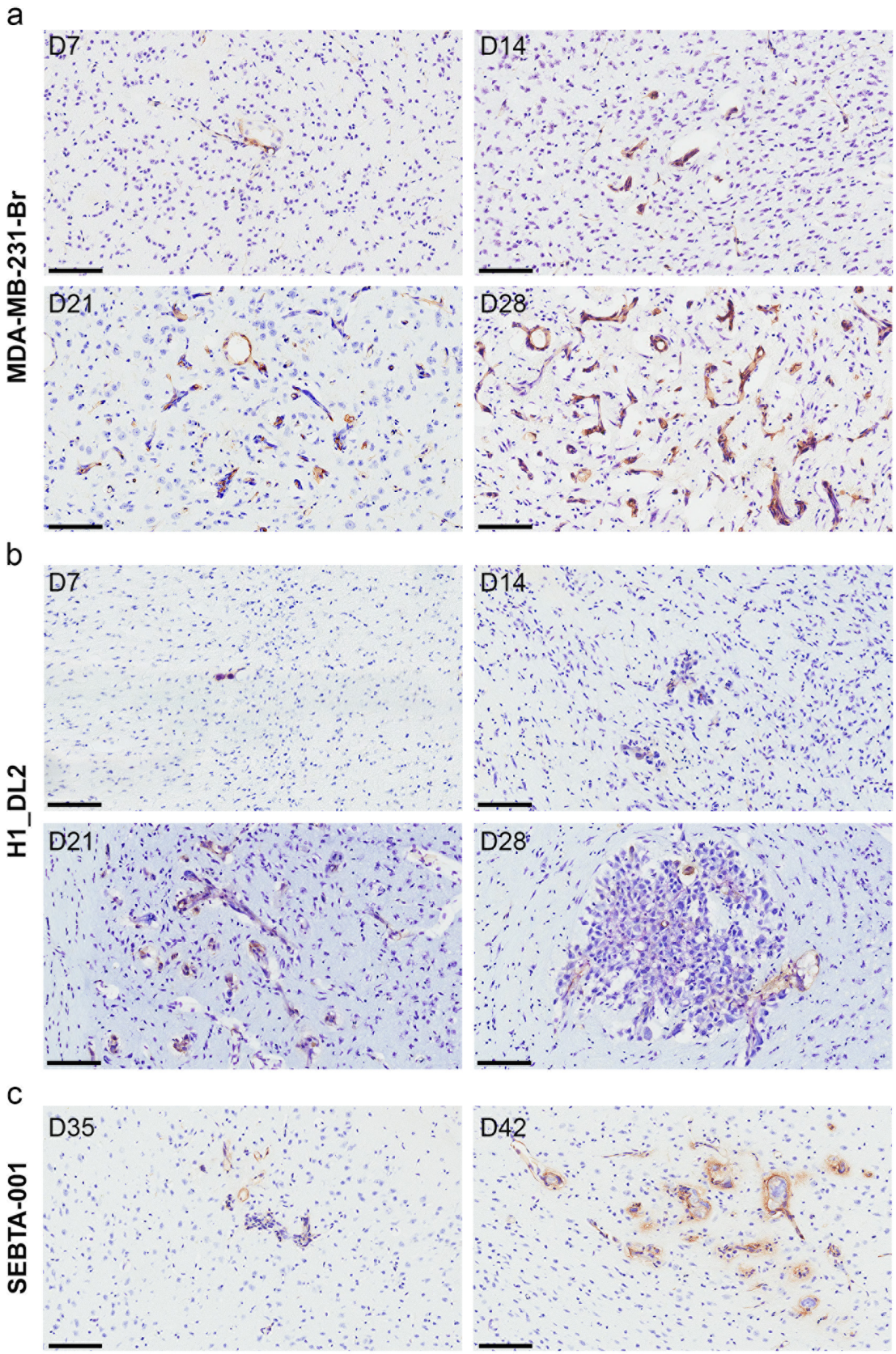
Figure 5.9: E-selectin expression on endothelial cells in presence of cancer cells *in vitro*.
E-selectin (red; white arrow) was expressed on the membrane of mouse brain endothelial cells (bEnd-3) that were in close proximity to tumour cells (green). Tumour markers: GFP; Melan-A; cytokeratin= green. Nuclei: DAPI = blue. Scale bars = 10 μm.

Subsequently, E-selectin expression was evaluated on histological samples of breast, lung and melanoma brain metastasis models. Samples from weekly time-points up to 4 weeks post-intracardiac injection of tumour cells for the breast and melanoma models, and on days 35 and 42 for the lung model were stained for E-selectin. The presence of E-selectin on the vessels close to the tumour colonies was evident from early time-points for all three brain metastasis

[††] It was not possible to study later time-points owing to the structure of endothelial cells being deformed by cancer cells.

models (Figure 5.10a, b, c). E-selectin immunohistochemical quantification showed for the MDA-MB-231-Br model, expression of E-selectin significantly increased as the tumours developed (n = 3 tumour model per time-point; n = 2 naïve mouse). Significantly higher E-selectin expression was evident at days 21 and 28 compared to earlier time-points, days 7 and 14 ($p < 0.05$ and $p < 0.01$, respectively; Figure 5.10d). For the H1_DL2 model, only low levels of E-selectin were detected at day 7, but this increased over-time; significant difference ($p < 0.05$) in E-selectin upregulation was found between days 7 and both 21 and 28 post-intracardiac tumour cell injection (Figure 5.10d). Finally, for the SEBTA-001 model, greater E-selectin expression compared to baseline was evident at both days 35 and 42 after tumour cell injection (Figure 5.10d). Overall, comparing E-selectin expression between tumour models, H1_DL2 appeared to show less E-selectin expression than the other two models. In all models, E-selectin upregulation was confined to tumour-associated vessels, with minimal upregulation on distant vessels and in non-tumour bearing areas.

Based on immunohistochemistry results, E-selectin appeared to be predominantly expressed on the cerebral endothelium and this observation was confirmed by fluorescent co-localisation staining of E-selectin and the endothelial marker, CD31, for breast, melanoma and lung brain metastasis models (Figure 5.11). Interestingly, assessment of fluorescent staining indicated that E-selectin expression is not continuous along blood vessels, as seen for VCAM-1 [98], but rather shows a more discontinuous expression pattern that is segmented along the vessels. I speculate that this pattern of expression likely reflects the role of E-selectin for initial tethering and rolling of leukocytes/circulating cancer cells on the endothelial cells, and that continuous expression may not be favourable for this step.


a
MDA-MB-231-Br
D7
D14
D21
D28
b
H1_DL2
D7
D14
D21
D28
c
SEBTA-001
D35
D42

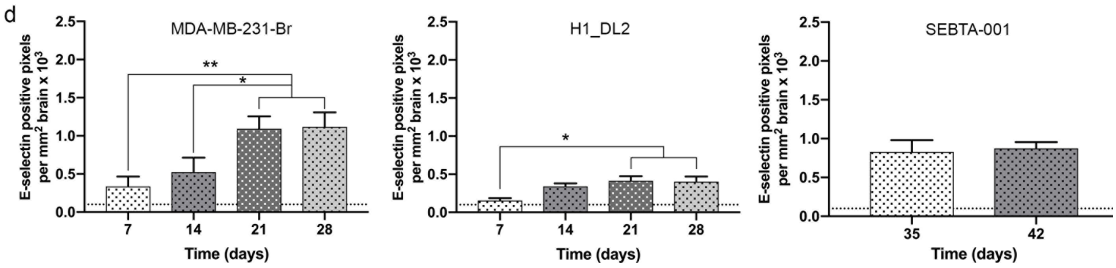


Figure 5.10: E-selectin expression in brain metastasis models.

(a-c) E-selectin (brown) expression associated with brain metastases was evident at all time-points studied in all models: **(a)** MDA-MB-231-Br, **(b)** H1_DL2 and **(c)** SEBTA-001. Scale bars = 100 µm. (d) Graphs showing time-course of E-selectin upregulation for MDA-MB-231-Br, H1_DL2 and SEBTA-001 models (n > 20 tumours per time-point). Dashed line denotes baseline expression of E-selectin in brains of naïve mice (n = 2). *$p < 0.05$, **$p < 0.01$, error bars = SEM.

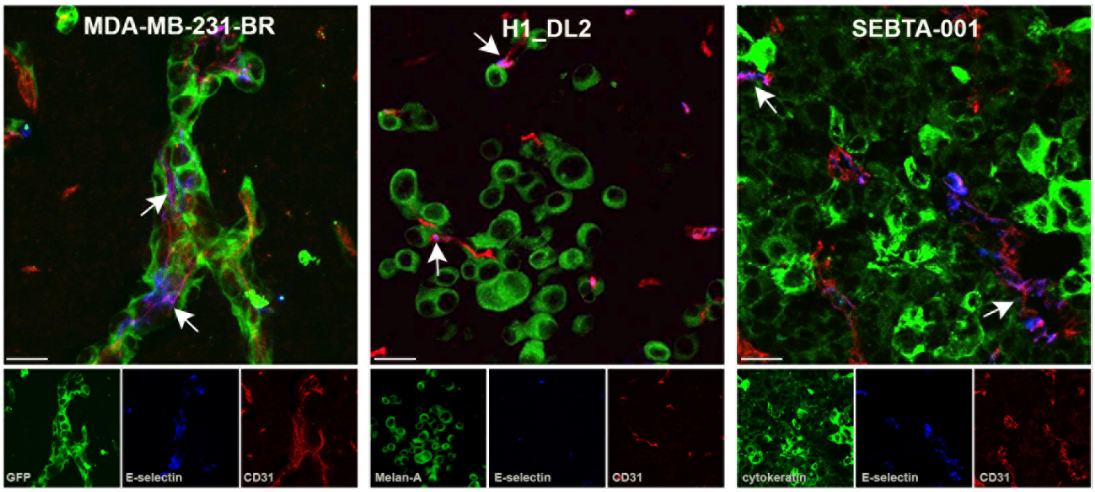


Figure 5.11: E-selectin and CD31 co-localisation in brain metastasis models.

Representative immunofluorescence images from brain metastasis models showing co-localisation (white arrows) of E-selectin (blue) with vascular endothelium (CD31; red) in close vicinity to metastatic tumours (green) for all three models; MDA-MB-231-Br (day 21), H1_DL2 (day 21) and SEBTA-001 (day 42). Note the discontinues pattern of E-selectin on the vessels. Tumour markers: GFP, Melan-A and cytokeratin = green. Scale bars = 25 µm.

5.3.5 E-selectin Expression in Human Brain Metastasis Biopsies

Brain metastasis biopsies from human brain showed prominent E-selectin expression on vessels adjacent to brain metastases from breast, lung adenocarcinoma and melanoma in all samples studied (Figure 5.12). Activated E-selectin vessels were not detected in the normal human brain tissue.

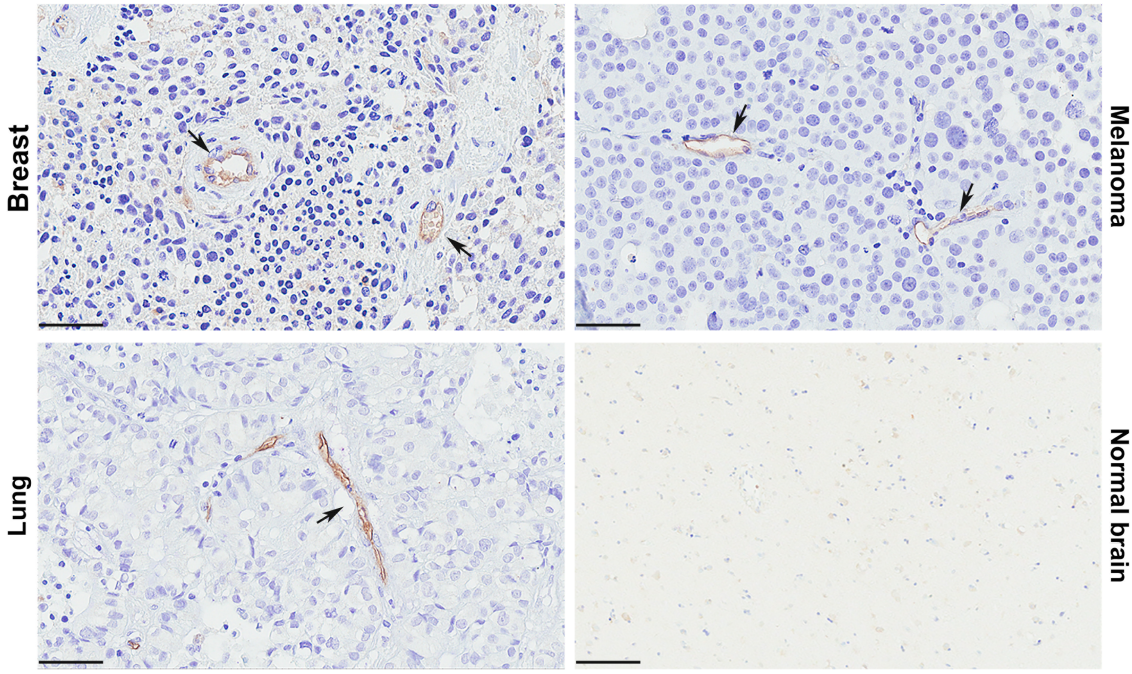


Figure 5.12: Representative E-selectin staining for human brain metastasis biopsies.
E-selectin staining (brown) for brain metastases from breast, melanoma, and lung cancer. E-selectin expression on cerebral vessels (black arrows) in close proximity to tumour cells was evident for all cases studied (n = 2 patients for each primary, n = 2 sections each patient). No E-selectin activated vessels was detected in the normal human brain tissue (black arrow, n = 2 sections). Counterstain= cresyl violet; blue. Scale bars = 50 μm.

Taken together, presence of E-selectin on brain endothelial cells in the early stages of brain metastasis formation in all three mouse models, and evidence of this marker in all human brain metastasis biopsies regardless of their origin, suggests that E-selectin could be a suitable biomarker for early diagnosis of brain metastasis *in vivo*.

5.3.6 *In Vivo* Detection of Micrometastases Using E-selectin-MPIO

Mice bearing breast, melanoma and lung brain metastases were injected intravenously with either E-selectin-MPIO or control IgG-MPIO at days 21 and 28 (breast and melanoma), or day 35 and 42 (lung) post-tumour cell injection. These time-points were chosen based on the maximum expression of E-selectin histologically on the tumour-associated vessels. In all three models, T_2*W-MGE3D images showed prominent hypointensities arising from bound E-selectin-MPIO. Focal hypointense areas were evident throughout the brain (olfactory bulb, forebrain, cerebellum) for all cases (Figure 5.13). Minor hypointense foci were detected in the tumour bearing cohort injected intravenously with IgG-MPIO (Figure 5.14).Quantitation of the number of hypointense voxels in each brain showed a significant difference between mice injected with E-selectin-MPIO and IgG-MPIO for all tumour models and at all time-points studied (Figure 5.13b). Dashed line denotes background hypointense voxels detected in naïve mice (n = 2) injected with E-selectin-MPIO (Figure 5.13b).

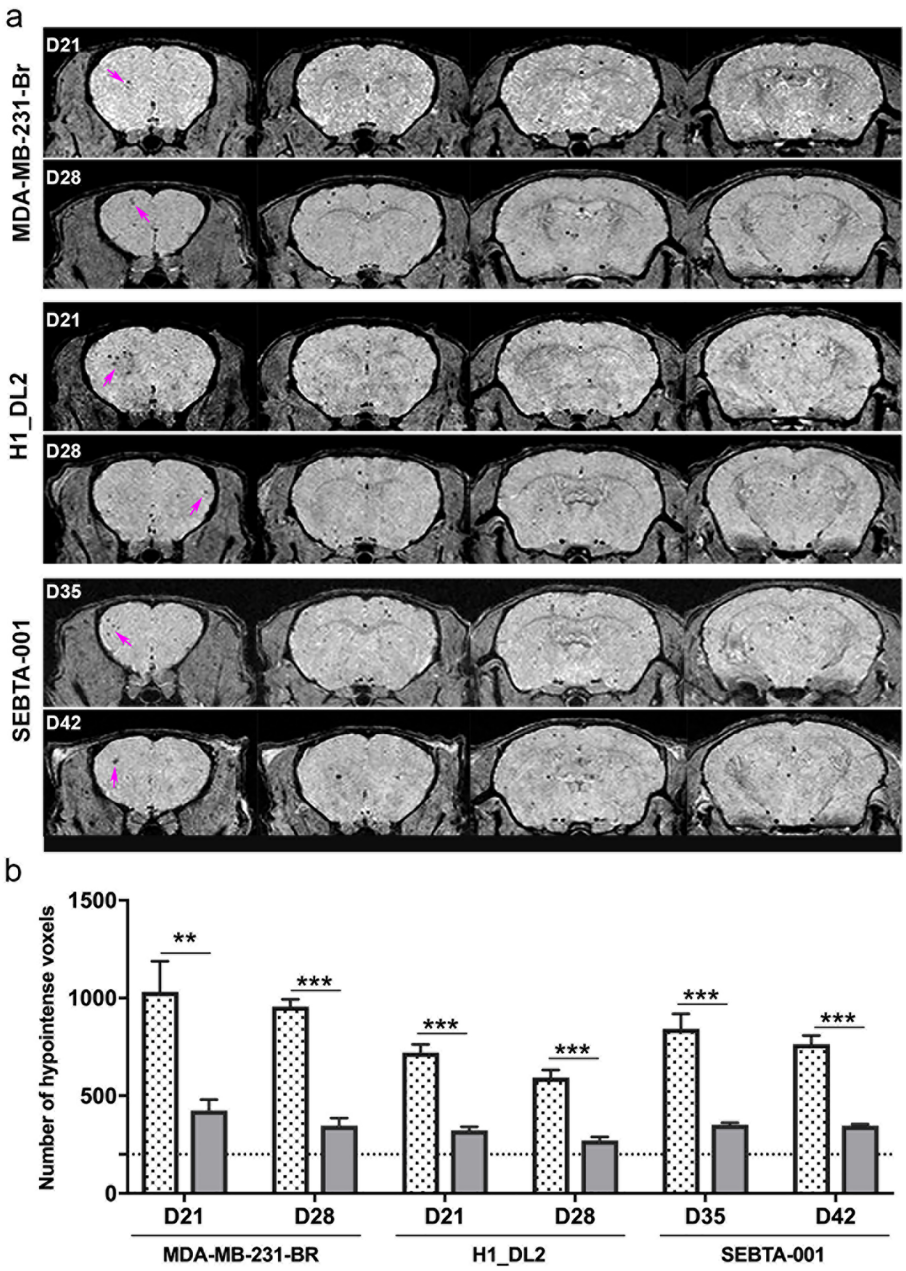


Figure 5.13: Detection of brain micrometastases using E-selectin-MPIO.

(a) Representative T_2*W coronal images from MGE3D datasets. Prominent focal hypointense (black) foci corresponding to retention of E-selectin-MPIO were evident in mice injected with MDA-MB-231-Br or H1_DL2 cells at both days 21 and 28, and SEBTA-001 cells at both days 35 and 42 after tumour cell injection. Examples of hypointense foci are indicated with pink arrows in the first column. **(b)** Graph showing quantitation of the number of hypointense voxels for each tumour model (n=5-per group). A significant difference was evident between tumour bearing mice injected with E-selectin-MPIO (dotted bars) and IgG-MPIO (grey bars) for all time-points in all three models; $^{**}p < 0.01$, $^{***}p < 0.001$. Dashed line denotes background hypointense voxels detected in naïve mice injected with E-selectin-MPIO (n=2).

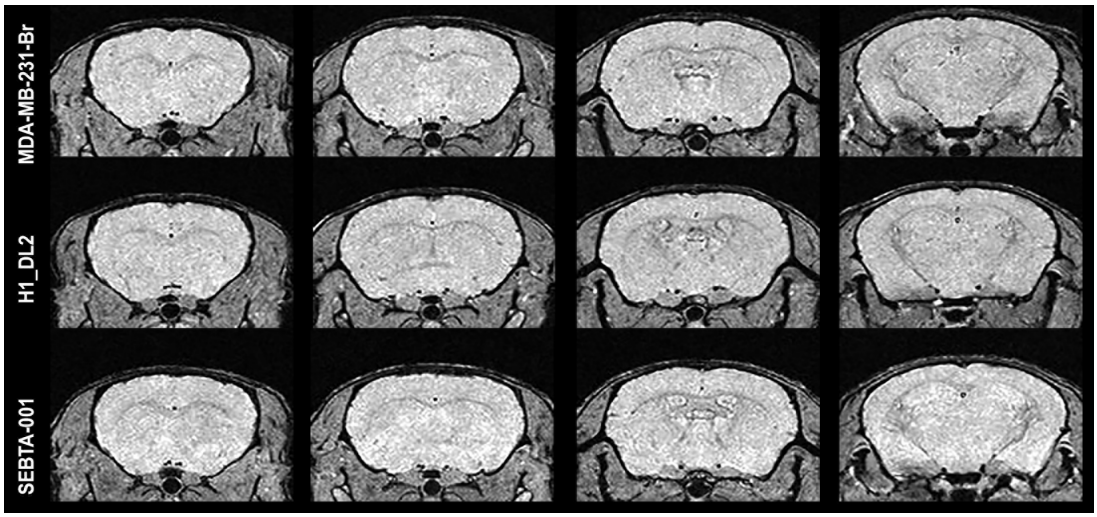


Figure 5.14: Brain metastasis tumour bearing mice injected with IgG-MPIO.
Representative T_2*W-MGE3D coronal images from tumour bearing mice injected with non-specific IgG-MPIO on day 21 (MDA-MB-231-Br, H1_DL2) and day 42 (SEBTA-001). Minimum hypointense foci arising from circulating IgG-MPIO were detected in this cohort.

No gadolinium signal enhancement was detected in tumour bearing mice, suggesting that the BBB was intact in mice at the time-points studied (Figure 5.15).

Histological assessment of mice injected with either E-selectin-MPIO or IgG-MPIO showed the presence of widespread brain metastases for all models. The majority of hypointensities on T_2*W-MGE3D images corresponded spatially with micrometastases detected histologically for all three brain metastasis models (purple arrows, Figure 5.16a-i). To confirm that the hypointensities reflect bound E-selectin-MPIO, samples were stained for iron, using Perls' Prussian blue (black arrow, Figure 5.16j). Presence of both MPIO and E-selectin on vessels in close proximity to brain metastases was evident (Figure 5.16k, l).

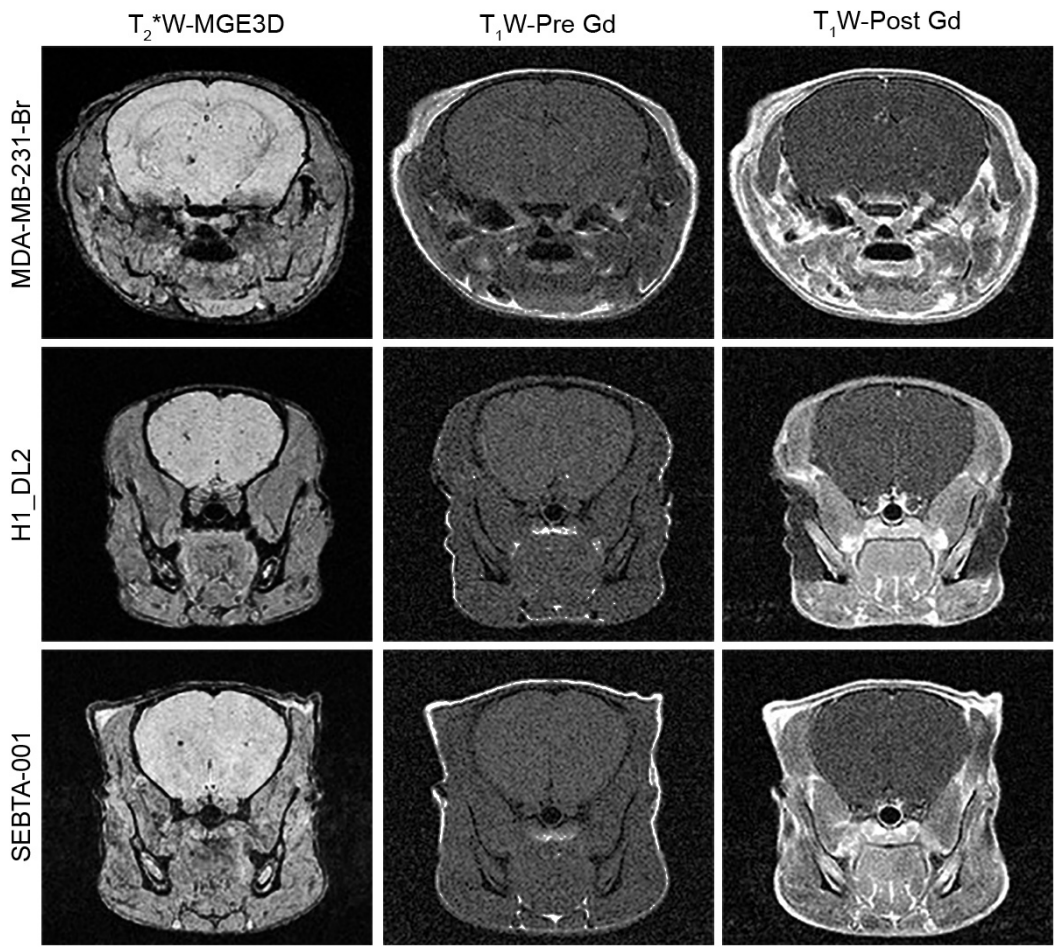


Figure 5.15: MRI BBB permeability assessment in the brain metastases models.

Representative T_2*W-MGE3D images and corresponding T_1W pre-and post-gadolinium images for mice injected intracardially with MDA-MB-231-Br, H1_DL2 and SEBTA-001 cells. No gadolinium enhancement (bright regions) was detected in T_1W-post Gd images, indicating an intact BBB. The presence of hypointense foci on the T_2*W-MGE3D correspond to the bound E-selectin-MPIO and micrometastases, which are not detected on the post-contrast T_1W image. Images are from the latest time-point of the study (Day 28 post-injection for MDA-MB-231-Br, H1_DL2 and day 42 for SEBTA-001).

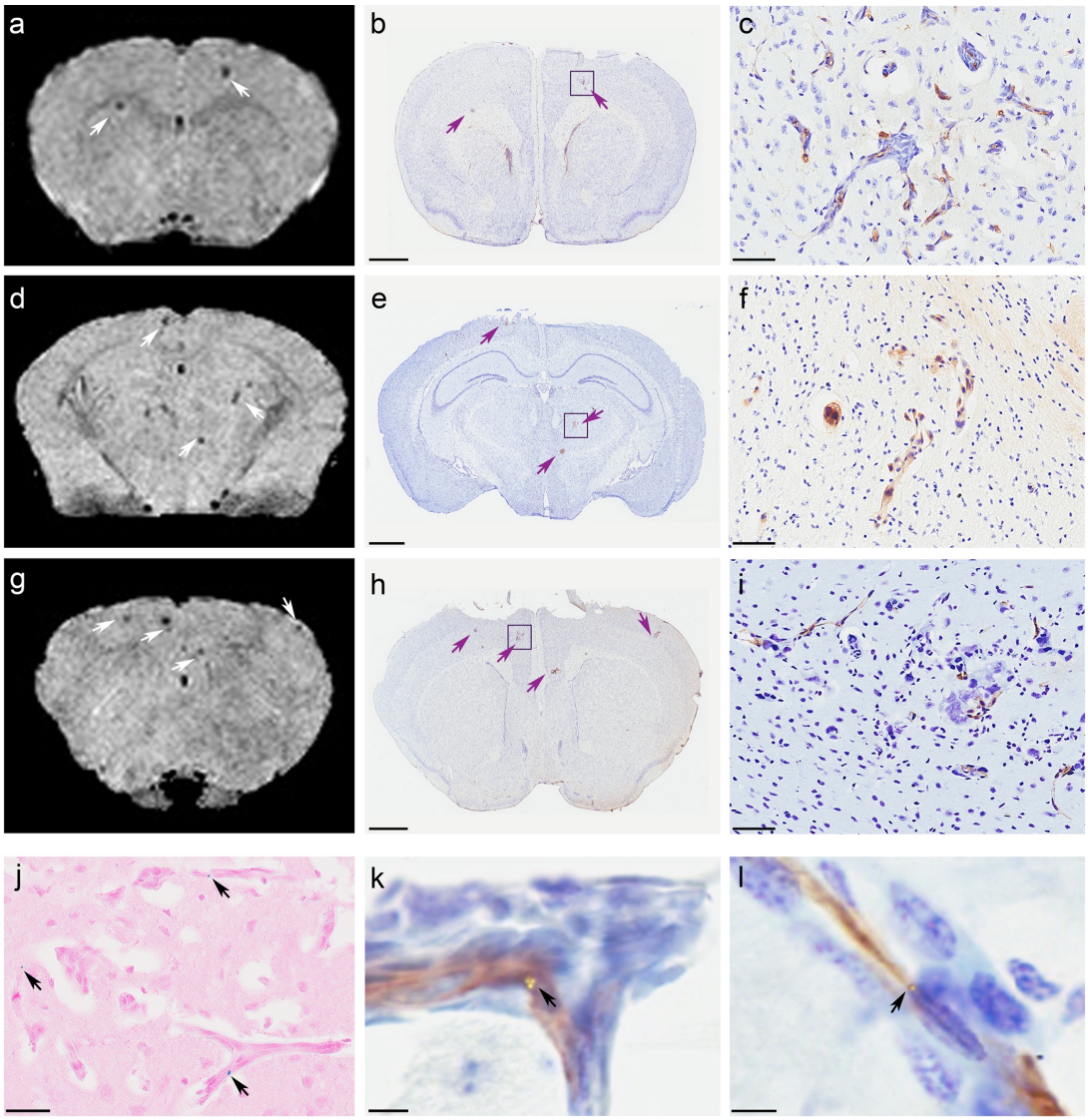


Figure 5.16: E-selectin-MPIO *in vivo* binding and detection of brain metastases.
(a-c) Representative T_2*W-MGE3D image **(a)** from the MDA-MB-231-Br model and the corresponding histological section **(b)** showing co-localisation of hypointensities on the T_2*W image (white arrows) with brain metastases (GFP, purple arrows) and the higher magnification photomicrograph **(c)** from E-selectin (brown) stained tumour, counterstain = cresyl violet; blue. **(d-e)** Representative T_2*W-MGE3D image **(d)** from H1_DL2 model and the corresponding histological sections (e; Melan-A, f; E-selectin). **(g-i)** Representative T_2*W-MGE3D image **(g)** from SEBTA-001 model and the corresponding histological sections (h; cytokeratin, i; E-selectin). **(j)** Perls' Prussian blue staining of tumour showing presence of MPIO (blue; arrows), counterstain = Nuclear Fast Red. **(k-l)** MPIO (black arrows) were found in E-selectin activated vessels (brown). Scale bars: (b, e, h) = 1 mm; (c, f, I, j) = 30 µm; (e, f) = 5 µm.

5.3.7 Sensitivity Assessment of E-selectin-MPIO Imaging in Tumour Models

To assess the sensitivity of E-selectin-MPIO imaging, both the number of metastases associated with E-selectin positivity, and the number of brain metastases detected by E-selectin-MPIO imaging were determined histologically. First, every other histological section was stained for the specific tumour marker (breast, GFP; melanoma, Melan-A; and SEBTA-001, cytokeratin). Tumours were segmented manually, and their volumes calculated. Next, the sequential slides were stained for E-selectin and each tumour-associated vessel was scored visually as either E-selectin positive or E-selectin negative. For the MDA-MB-231-Br model, 91% of all tumours had E-selectin positive vessels (n = 3 mice). For tumours above and below the median volume (0.886×10^{-3} µl), 96.5% and 85%, respectively, were E-selectin positive (Figure 5.17a). For the H1_DL2 model, 70% of all tumours were associated with E-selectin positive vessels (n = 3 mice). For tumours above and below the median volume (0.619×10^{-3} µl), 78% and 61%, respectively, were E-selectin positive (Figure 5.17b). For the SEBTA-001 model, 79% of all tumours were associated with E-selectin positive vessels (n = 3 mice). For tumours above and below the median volume (0.683×10^{-3} µl), 89% and 64%, respectively, were E-selectin positive (Figure 5.17c). Comparing the anatomical location of brain metastases on histology with the corresponding hypointensities on T_2*W-MGE3D images, revealed that 83% of tumours were detected by E-selectin-MPIO MRI for the MDA-MB-231-Br model. For tumours above and below the median volume, 93% and 74%, respectively, were detected (Figure 5.17d). For the H1_DL2 model, 66% of all brain metastases being detected by E-selectin-MPIO MRI; for tumours above and below the median volume, 75% and 59%, respectively, were detected (Figure 5.17e). Finally, for the SEBTA-001 model, E-selectin-MPIO detected 72% of all brain metastases; for tumours above and below the median volume, 87% and 57%, respectively, were detected (Figure 5.17f). All metastases with a volume greater than 1.9×10^{-3} µl, 4.6×10^{-3} µl, 6.7×10^{-3} µl for MDA-MB-231-Br, H1_DL2 and SEBTA-001, respectively, were detected with E-selectin imaging (Figure 5.17g-i), showing higher sensitivity for detection of smaller brain metastases in the MDA-MB-231-Br model, compared to the other models.

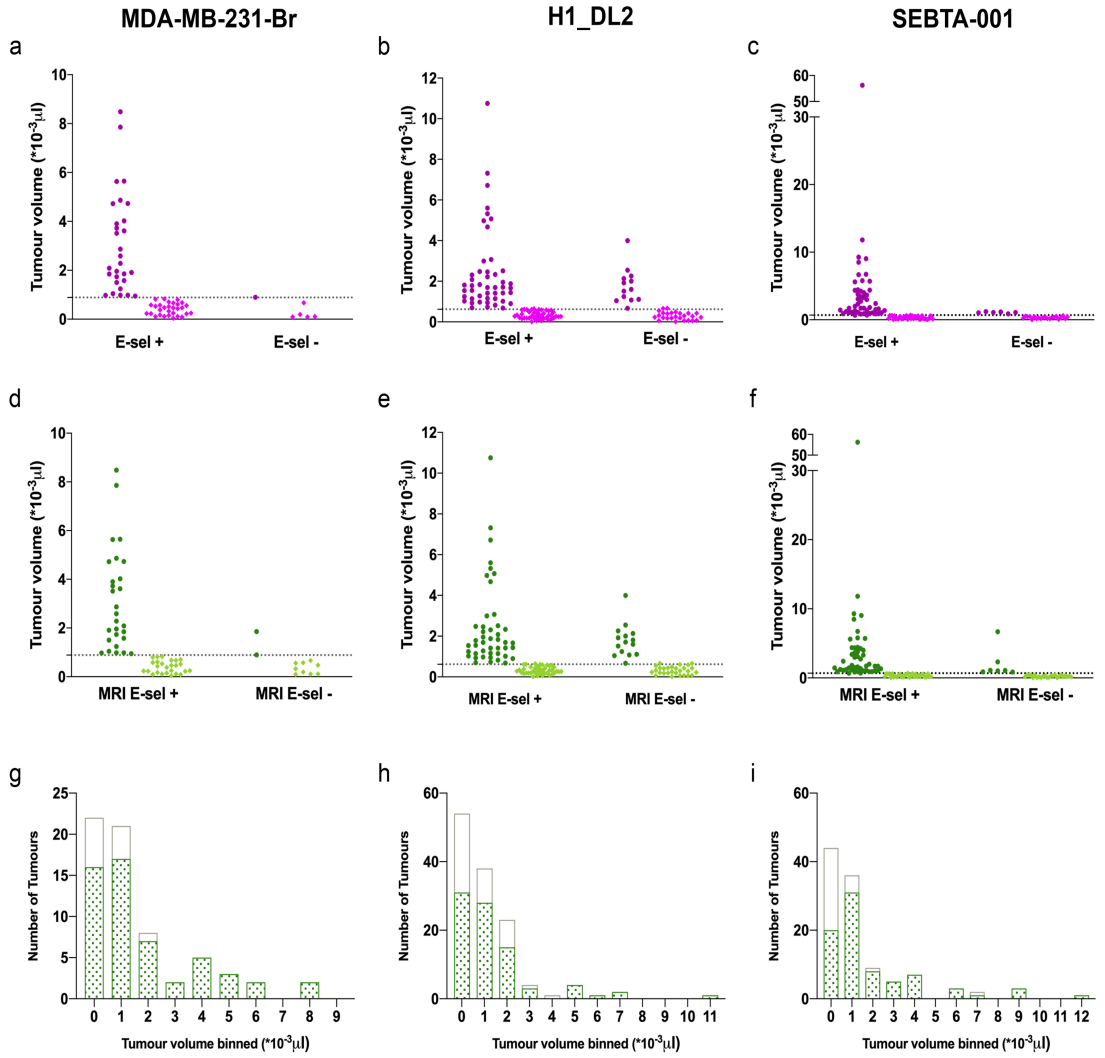


Figure 5.17: Graphs indicating volume of metastases from breast, melanoma and lung that were endothelial E-selectin +/- and MRI hypointense +/-.

(a-c) Scatter plots for presence of E-selectin (E-selectin +) or absence of E-selectin (E-selectin -) on tumour-associated vessels for individual brain metastases in **(a)** MDA-MB-231-Br, (b) H1_DL2 and **(c)** SEBTA-001 models based on immunohistochemistry. Dark pink circles show tumours above the median volume (dashed line) and light pink diamonds show tumours below the median volume for each model. **(d-f)** Corresponding scatter plots showing numbers of MRI hypointensity positive or negative micrometastases. Dark green circles show tumours above the median volume and light green diamonds show tumours below the median volume for each model. **(g-i)** Frequency distributions showing the number of tumours detected by E-selectin-MPIO on MRI (green doted bars) stacked with undetected tumours (clear bars) for each tumour volume (*10^{-3} µl) bin. One outlier tumour volume (56.2 × 10^{-3} µl) was excluded for the SEBTA-001 frequency plot. Data are shown from day 21 after induction of brain metastases for MDA-MB-231-Br and H1_DL2 models, and day 42 for the SEBTA-001 model.

5.3.8 Targeting Dual Adhesion Molecules for Detection of Brain Micrometastases

As discussed earlier, there is a constant transition in the expression of adhesion molecules on tumour-associated vessels. Although singly targeted imaging probes are very sensitive for brain micrometastasis detection (as shown previously and in this thesis), molecular imaging strategies using bispecific agents may further improve visualisation of brain micrometastases by increasing their likelihood of binding at each time-point with dynamic change in CAMs profile. To test this hypothesis, the two molecular targeted MRI agents with the highest sensitivity for brain metastases detection (1) VCAM-1 and (2) E-selectin were chosen (Table 5.1 and Figure 5.18).

Adhesion molecule target	Brain metastasis model	%Tumours detected
VCAM-1	MDA-MB-231-Br	82%
ALCAM	MDA-MB-231-Br	82%
E-selectin	MDA-MB-231-Br	83%
VCAM-1	H1_DL2	72%
ALCAM	H1_DL2	54%
E-selectin	H1_DL2	66%
VCAM-1	SEBTA-001	89%
ALCAM	SEBTA-001	68%
E-selectin	SEBTA-001	72%

Table 5.1: Sensitivity of targeted adhesion molecule MRI contrast agents in detection of brain micrometastases.

Mice bearing breast, melanoma and lung brain metastases were injected concurrently with VCAM-MPIO and E-selectin-MPIO (2 mg Fe/kg body weight for each agent; iv total volume of 100 μl) on either day 21 (breast and melanoma), or day 35 (lung) post-tumour cell injection (n = 4-5 per model). T_2*W-MGE3D images in all three models, showed marked hypointensities arising from bound VCAM-/E-selectin-MPIO. The hypointensities were evident throughout the brain for all cases (Figure 5.19a). No hyperintense regions were found on the corresponding post-gadolinium T_1W images (white arrows, Figure 5.19a), indicating an intact BBB. Higher number of hypointense voxels were detected in tumour bearing mice injected with

VCAM-/E-selectin-MPIO agent compared to the number of hypointense voxels in naïve mice (n = 2, dashed line, Figure 5.19b).

To determine the sensitivity of dual targeting for detection of brain micrometastases, histological sections were stained for the tumour specific markers (breast, GFP; melanoma, Melan-A; and SEBTA, cytokeratin; n = 3 per model). As previously, the anatomical location of brain metastases was manually marked on histological sections and their spatial co-localisation with the hypointensities on T_2*W-MGE3D images assessed. For MDA-MB-231-Br, H1_DL2 and SEBTA-001 models, 91% (n = 128 tumours), 75% (n = 104 tumours) and 90% (n = 45) of all brain metastases were detected by VCAM-/E-selectin-MPIO, respectively. These results demonstrated that a higher percentage of tumours was detected with dual targeting than with either agent alone (Table 5.1). The greatest improvement in detection was observed for the breast cancer brain metastasis model.

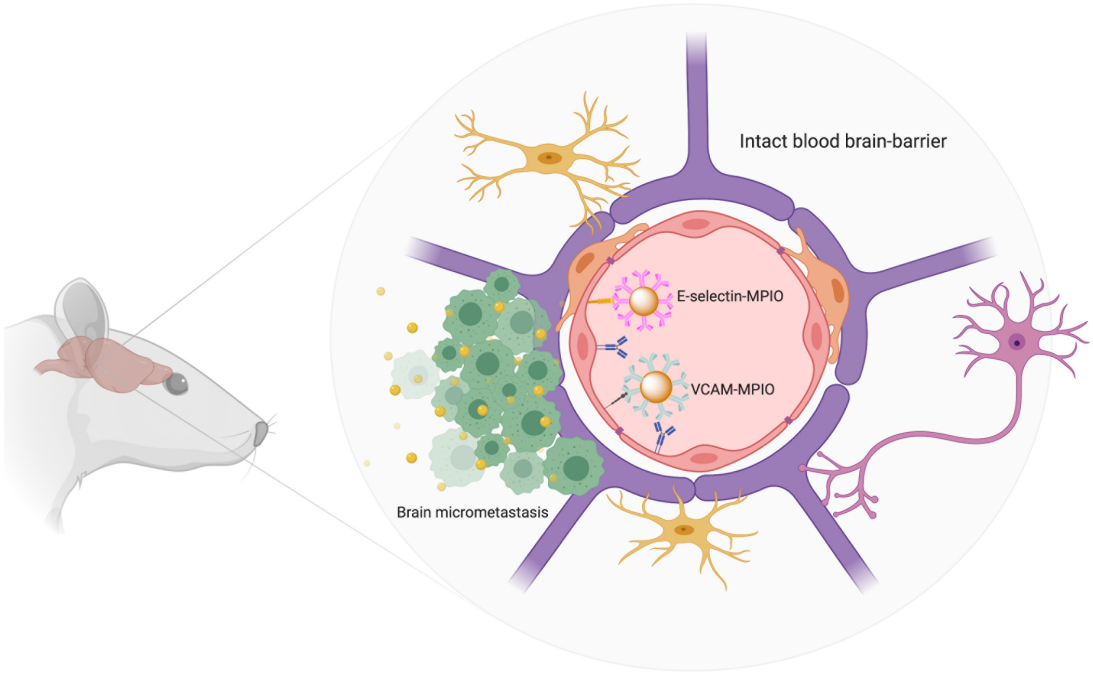


Figure 5.18: Targeting E-selectin and VCAM-1 adhesion molecules for early detection of brain micrometastases [221].

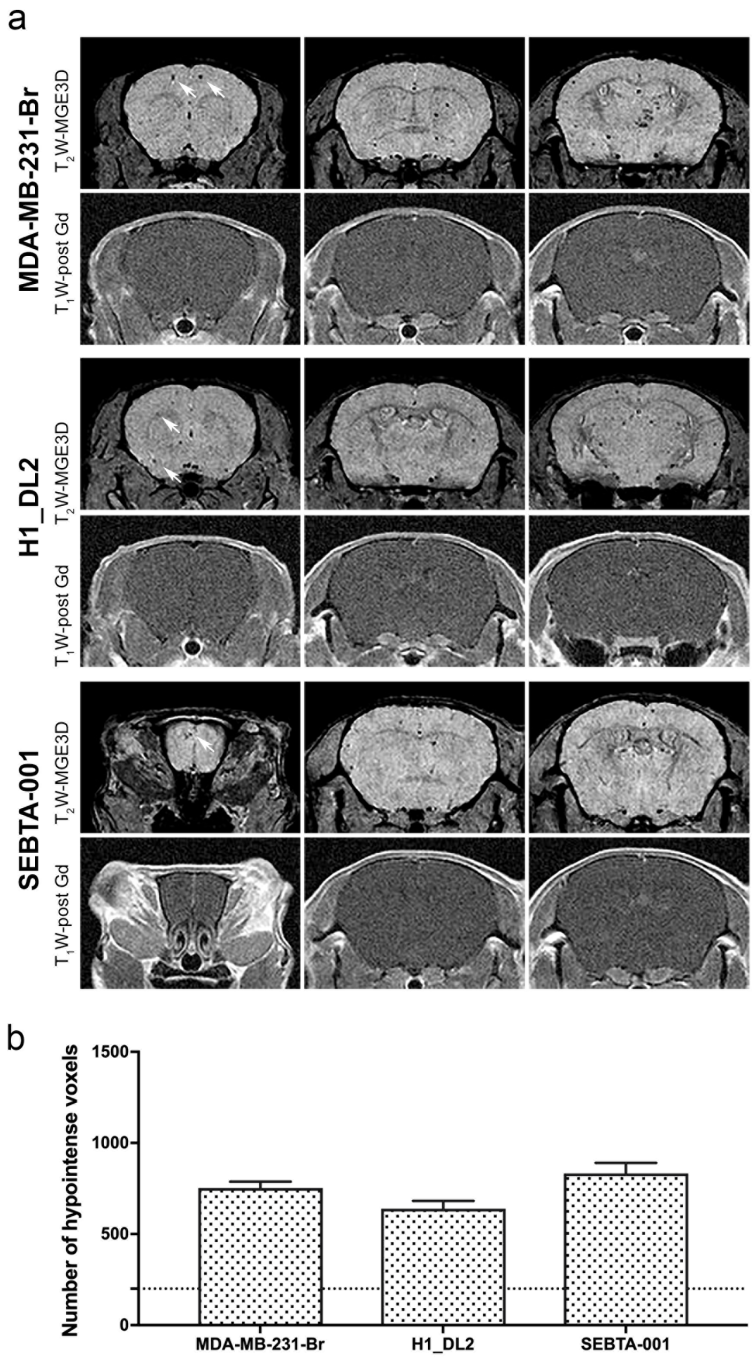


Figure 5.19: Detection of brain metastases using dual target (VCAM-/E-selectin-MPIO) MRI agent.

(a) Representative T_2*W coronal images from MGE3D datasets and the corresponding post-gadolinium T_1W images. Hypointense (black) foci corresponding to retention of VCAM-/E-selectin-MPIO were evident in mice injected with MDA-MB-231-Br or H1_DL2 cells at day 21; and SEBTA-001 cells at day 42 after tumour cell injection. Examples of hypointense foci are indicated with white arrows in the first column. **(b)** Graph showing quantitation of the number of hypointense voxels for each tumour model (n = 4-5 per group; mean ± SEM). Dashed line denotes background hypointense voxels detected in naïve mice injected with VCAM-/E-selectin-MPIO (n = 2).

5.4 Discussion

In this Chapter, a second novel molecular MRI probe has been developed, validated and implemented. This new probe targets E-selectin, one of the adhesion molecules that is exclusively expressed on the endothelial cells in response to inflammation and metastasis. The results of this Chapter have demonstrated that E-selectin targeted MPIO can be used not only for the *in vivo* detection of inflamed vessels in a model of acute neuroinflammation, but also as a tool for detection of brain micrometastases originating from breast, melanoma and lung primary cancers. This novel agent was shown to be highly selective and sensitive for E-selectin targeting both *in vitro* and *in vivo*. Similar to the ALCAM targeted agent, E-selectin was also more sensitive for the detection of breast cancer brain metastases than either melanoma or lung brain metastases in the very early stages of growth. Nevertheless, E-selectin targeted MRI was slightly more sensitive than ALCAM targeted MRI for the detection of melanoma (66% *vs.* 54%) and lung (72% *vs.* 68%) brain micrometastases. Finally, detection of brain micrometastases was enhanced in all three brain metastasis models once two different adhesion molecules, VCAM-1 and E-selectin, were targeted simultaneously. These results support the hypothesis that the interaction of molecular imaging agents with two different targets increases binding at target sites.

First, the E-selectin response to proinflammatory agents was assessed both *in vitro* and *in vivo*. In the presence of inflammatory stimuli, E-selectin was significantly upregulated on brain endothelial cells compared to unstimulated cells *in vitro*. E-selectin was also upregulated on blood vessels in the ipsilateral hemisphere of mice intracerebrally injected with an array of proinflammatory agents. As a result of this demonstrated expression of E-selectin in the vicinity of an inflammatory stimulus and minimal baseline expression of this marker, an E-selectin targeted MRI probe for *in vivo* applications was developed. The binding capacity of the E-selectin-MPIO agent was first tested *in vitro* under static and shear stress conditions, and subsequently assessed *in vivo*, via intravenous injection to mice 3 hours after intrastriatal IL-1β injection. The E-selectin targeted probe was found to be highly sensitive for the detection of inflammation *in vivo.* Neuroinflammation is a pathological feature in many neurodegenerative

diseases, including Alzheimer's disease (AD), Parkinson's disease (PD), frontotemporal dementia, multiple sclerosis (MS), Huntington's disease (HD), stroke, infection and seizures [222]. The CNS response to these insults involves biosynthesis and release of pro- and anti-inflammatory molecules from brain resident cells, which evoke responses in the CNS microenvironment [223], [224]. Thus, the appeals of E-selectin targeted imaging are multiple. This technique enables imaging of processes that occur early in the pathogenesis of numerous neuroinflammatory diseases and does not require BBB destruction. Over the last decade, E-selectin has gained a lot of attention as a target for therapeutic interventions, and many studies have developed liposomes or nanoparticles attached to either E-selectin or its ligand sLe^X, for the treatment of inflammation [211]. As for E-selectin targeted neuroimaging, various ligands (mimetic sLe^X , natural sLe^X glycan) have been coupled with different types of MRI contrast vehicles (gadolinium and iron oxide-based) to detect upregulation in preclinical models [137], [196], [216], [217]. The limitations of these approaches for *in vivo* molecular MRI have been discussed previously (5.1). Although E-selectin antibody-based targeted MPIO have been developed and validated *in vitro* [135], this is the first study that has shown successful detection of E-selectin expression in a mouse neuroinflammation model using an antibody-conjugated MPIO agent.

Evidence from liver, lung and bone metastasis has suggested the importance of E-selectin interactions for the adhesion of circulating cancer cells to the endothelium and subsequent metastasis formation [69], [70], [225]–[227]. However, little is known about the role of E-selectin in brain metastasis. Previous data have shown the presence of E-selectin on vessels adjacent to breast cancer brain metastasis models *in vivo* [56] and on endothelial cells cultured with lung brain metastatic cancer cells *in vitro* [93]. In the current study, E-selectin expression in mouse models of human-derived brain metastases from breast carcinoma, melanoma and lung adenocarcinoma was assessed. Immunohistochemistry and immunofluorescent staining showed E-selectin upregulation on tumour-associated vasculature for brain metastases from breast, melanoma and lung. E-selectin was not detected on blood vessels in normal, non-tumour bearing

areas of the brain. Temporally, in the breast cancer brain metastasis model, total E-selectin expression quantified by immunohistochemistry, significantly increased with tumour growth from day 7 to days 21 and 28 after tumour cell injection. The same expression pattern was observed in the melanoma brain metastasis model; total E-selection expression was low (baseline) at day 7 and had increased significantly by day 21 after tumour cell injection. In the lung brain metastasis model, a high level of E-selectin expression was again evident at both time-points (days 35 and 42 after tumour cell injection) studied. Elevated levels of E-selectin in the later stages of tumour establishment is contradictory to the general concept of transient E-selectin expression in the early stages of tumour seeding, as seen in lung and liver metastasis [69], [225]. Data presented here suggest the continued presence of E-selectin positive vessels throughout micrometastasis formation. This phenomenon could be explained by the various and dynamic roles of E-selectin. I speculate that E-selectin expression on the cerebral blood vessels primarily assists with rolling and extravasation of circulating cancer cells in the early stages in agreement with previous studies on other cell types [228], and that its expression subsequently remains elevated in response to proinflammatory cytokines originating from the microscopic tumours as they grow. Another possible explanation for the elevated E-selectin level could be the interaction of E-selectin with brain cells including astrocytes and microglia in the tumour microenvironment, as their co-registrations have been shown previously [56]. This would add to the 'total' E-selectin signal quantified by immunohistochemistry. However, immunofluorescent results in this Chapter showed most of E-selectin signal is co-localised with the endothelial cells. Collectively, the data presented here suggest that E-selectin could provide a sensitive biomarker for the early detection of micrometastases.

Subsequently, E-selectin was assessed in post-mortem human brain metastasis biopsies from breast, melanoma and lung. The results were consistent with E-selectin expression in the preclinical brain metastasis models. E-selectin was expressed on tumour-associated blood vessels, and its upregulation was independent of the primary origin. E-selectin levels on healthy

brain tissue were negligible and no E-selectin upregulation was found in human brain tissue distant from tumours, indicating specificity of this marker to the tumour site.

On the basis of the above data, subsequent *in vivo* studies were performed to assess the potential of E-selectin targeted MRI for detection of micrometastases in the brain. At all time-points studied, the BBB remained intact and no gadolinium enhancement was visible on T_1W images for any of the models of brain metastasis. T_2*W-MGE3D images showed marked hypointense regions after intravenous administration of E-selectin-MPIO, whilst minimal hypointense voxels were evident in the brains of tumour bearing mice injected with IgG-MPIO. In the breast cancer brain metastasis model, at day 21, a significant proportion (83%) of brain metastases found histologically co-registered with hypointensities on T_2*W-MGE3D images and 91% of these tumours were shown to be E-selectin positive. The smallest brain metastasis detected with E-selectin-MPIO was from the breast cancer brain metastasis model and had a volume of 4.7e- 05 μl. In the melanoma model, E-selectin expression was lower (70%) than in the breast cancer brain metastasis model, and in support of the histological findings, 66% of all melanoma metastases were detected *in vivo* using E-selectin-MPIO. In the lung cancer brain metastasis model, E-selectin imaging enabled detection of 72% of all tumours, with 79% showing E-selectin expression. Thus, the lower sensitivity of E-selectin-MPIO for the *in vivo* detection of brain micrometastases from melanoma and lung primaries, compared to breast, may be attributed, largely, to the lower E-selectin expression on metastasis-associated vessels. As discussed in Section 4.4, the growth pattern, tumour cell doubling time, vascular density and angiogenic pattern of these different models are distinctive. Nevertheless, the E-selectin targeted imaging probe was found to be more sensitive than the previous ALCAM imaging agent for the detection of brain metastases from all three primaries at the same time-points.

Dual targeted strategies have previously been shown to be promising for both imaging and therapy [229]. Moreover, it has become clear that the heterogeneity of cancer needs to be addressed for diagnostic applications. Within a single anatomical site, biomarker expression can vary widely. This concept is supported by the current body of work in which brain metastases

from different origins show distinctive phenotypes. Thus, dual or multiple targeted imaging agents may enable enhanced detection by providing a greater number of potential binding sites and accounting for heterogeneity in expression of each individual target. Data presented so far have suggested that E-selectin and VCAM-1 have the highest sensitivity for detection of brain micrometastases from all three primary tumours. Interestingly, MPIO dual targeted with anti-VCAM-1 and anti-E-selectin antibodies have shown enhanced particle binding under shear stress compared with the constituent single targeted MPIO *in vitro* [135]. I, therefore, tested the hypothesis that targeting more than one CAM will improve detection of brain micrometastasis by concurrent intravenous administration of both VCAM-MPIO and E-selectin-MPIO to brain metastasis bearing mice. Results showed that 91%, 75% and 90% of all tumours were detected with the dual agent for breast, melanoma and lung brain metastases, respectively. Thus, the sensitivity for detection of brain micrometastases increased for all brain metastasis models, with the greatest improvement being evident in the breast brain metastasis model (82% - 83% single agent *vs.* 91% dual agent). Slight improvements were also evident for lung cancer brain metastases (72% - 89% single agent *vs.* 90% dual agent) and melanoma brain metastases (66% - 72% single agent *vs.* 75% dual agent) (Table 5.1). However, with co-injection of VCAM-/E-selectin-MPIO, it is not possible to determine that the hypointensities visible on MRI are due to binding of which compound. Further studies to assess binding capacities of VCAM-/E-selectin-MPIO *in vitro* on pre-treated cells and development of MPIO tagged with both VCAM and E-selectin antibodies is needed.

To conclude, findings in this Chapter indicated that the novel E-selectin-MPIO agent is highly sensitive for the detection of E-selectin expression on the cerebral vasculature and that this agent enables accurate visualisation and characterisation of biological process *in vivo*.

5.5 Summary of Chapter 5

In this Chapter I have shown:

- Abundance of E-selectin on the brain vasculature in response to inflammation and in the early stages of brain metastasis formation.
- Low endogenous expression of E-selectin on healthy brain vessels in normal brain.
- Successful mapping of neuroinflammation and brain micrometastases from breast, melanoma and lung, using a novel E-selectin targeted MRI contrast agent

CHAPTER 6

Discussion and Future Directions

Brain metastases are described as rare and late complications in patients with metastatic cancer, however, recent epidemiologic studies have shown that the incidence of brain metastases has increased over the last decade [14]. Upon brain metastasis diagnosis, there are limited therapeutic options available, and their impact on prognosis is low. A major issue for treatment of brain metastases is the late stage of diagnosis. Detection of brain metastases using the gold standard gadolinium-enhanced MRI, relies on passive extravasation of the contrast agent, which only occurs if the BBB is disrupted (macrometastasis). Therefore, conventional MRI techniques currently used in the clinics are unable to identify tumours with an intact BBB (micrometastases). Earlier detection, at the micrometastatic stage, could radically alter prognosis for patients suffering brain metastasis. Therefore, the primary goal of this thesis was to identify new imaging targets and drive the development of diagnostic imaging tools for early detection of brain micrometastases. Thus, first the type of MRI-detectable iron oxide particles (MPIO or USPIO) and MRI sequences and field strengths were optimised for targeted molecular imaging application in preclinical models. Subsequently, these findings were extended by developing novel molecular MRI agents, targeting specific endothelial adhesion molecules for detection of brain micrometastases. In the following sections, I discuss the significance of each experimental Chapter presented in this body of work:

6.1 Optimisation of Targeted Molecular Imaging in a Mouse Neuroinflammation Model

The optimisation of iron oxide particles for molecular MRI alongside assessing relevant MRI sequences and magnetic fields, is crucial for enhancing their detection and visualisation. USPIO (e.g. Ferumoxytol) are generally non-toxic *in vivo,* and are routinely used in humans as a positive contrast agent for angiography applications or even brain tumour imaging [119], [172]. On this basis, novel molecular targeted USPIO based agents would be easily translatable to the clinical setting. On the other hand, over the last few years, biocompatible and biodegradable (i.e. non-toxic) MPIO have been developed, which address the most significant issue for clinical translation of MPIO [134]. Theoretically, MPIO are superior to USPIO for molecularly targeted MRI, owing to their increased surface area for antibody binding, greater payload of iron oxide,

and rapid clearance from the circulation. Nevertheless, an empirical head-to-head comparison of targeted USPIO and MPIO has not been shown before. In Chapter 3 of this work, VCAM-1, a robust endothelial marker was chosen as a target for antibody-conjugated MPIO and USPIO for the detection of neuroinflammation in a mouse model. Physiochemical analyses of VCAM-MPIO and VCAM-USPIO showed higher VCAM-1 antibody density per particle for MPIO (10490 ± 450 antibody/particle) *vs.* USPIO (7.4 ± 3.1 antibody/particle). Moreover, MPIO showed higher relaxivity per particle (1.18×10^{-9} Hz·L/particle) compared to USPIO (1.29×10^{-14} Hz·L/particle), hence providing potent contrast on MRI. Finally, the long blood half-life of USPIO (16.5 h) precluded detection of target-specific binding *in vivo* compared to VCAM-MPIO (blood half-life: 1.2 min); the latter would provide a clinically practical time window for molecular imaging application. These finding showed empirically that MPIO based targeted MRI contrast agents provide significant benefits over targeted USPIO for molecular imaging applications in mouse brain. Subsequently, three different MRI sequences were used to optimise detection of these particles. T_2*W-MGE3D showed the highest SNR and CNR for iron oxide detection compared to both T_2*W-GE3D and T_2/T_1W-bSSFP. Finally, differences in SNR and CNR at three different magnetic field strengths, 4.7 T, 7.0 T and 9.4 T, were assessed. Although this comparison suffers from a number of limitations mentioned in Section 3.4, results showed that, for our studies, the 7.0 T magnetic field is suitable for molecular imaging application in mouse brain. Collectively, optimisations in this Chapter set the ground work for the subsequent studies in this thesis.

6.2 ALCAM Targeted MRI

In Chapter 4, ALCAM was assessed as a potential target for detection of brain micrometastases. It is well established that tumours promote inflammation that triggers activation of endothelial cells in their vicinity. This activation involves upregulation of a series of adhesion molecules that support tumour growth from the earliest stages [55]. On this basis, MPIO targeting activated adhesion molecules on the luminal surface of blood vessels can detect brain micrometastases, without the need to cross the BBB. VCAM-1 was the first adhesion molecule that was identified

as a target for molecular imaging of brain micrometastases. Serres *et al.* [97] and Cheng *et al.* [98] have demonstrated the sensitivity and feasibility of VCAM-MPIO MRI for detection of brain micrometastases using intracardiac syngeneic and xenograft brain metastasis models from breast, melanoma and lung primaries. However, VCAM-1 is just one of many adhesion molecules that are expressed on the brain vasculature in response to the presence of metastases. Sarmiento Soto *et al.* [56] demonstrated that a subset of adhesion molecules is upregulated on the cerebral endothelium in the early stages of brain metastasis formation. Of these, ALCAM was shown to be upregulated on the tumour-associated vessels to an even greater extent than VCAM-1. Consequently, with a view to improving the sensitivity of brain micrometastases detection, the suitability of ALCAM as a molecular imaging target was assessed.

To determine the potential of a new molecular target for brain metastasis imaging, the surrogate needs to meet the following criteria: (1) expressed on the luminal surface of the brain endothelium, which allows accessibility of agent; (2) absent or minimum basal expression; (3) expression in the early stages of brain metastasis formation; and (4) consistent expression over the course of tumour establishment [230]. The results of this Chapter indicated that ALCAM possesses all of the desired attributes for a potential molecular target. Endothelial cells (human and mouse) showed ALCAM upregulation in response to proinflammatory cytokines and the presence of endothelial ALCAM was confirmed in co-localisation analyses of ALCAM and an endothelial marker (CD31) in brain metastasis sections from breast, melanoma and lung (both in mouse and human). Whilst negligible ALCAM expression was evident constitutively on distant and normal brain vessels, marked endothelial ALCAM expression was evident from the early stages of tumour formation and was consistent throughout the course of study. As a result, a novel ALCAM-MPIO conjugate was developed and its binding capacity tested *in vitro*. Although the development of a proof-of-principle neuroinflammation model was not achieved in this work, the extensive presence of endothelial ALCAM in all three brain metastasis models (breast, melanoma and lung) supported the advance of ALCAM imaging to the brain metastasis models. The novel ALCAM-MPIO compound was shown to be sensitive for detection of brain

micrometastases from all three primary tumours prior to BBB disruption and any conventional imaging technique.

In this Chapter, for the first time, I demonstrated the presence of ALCAM on both tumour and endothelial cells in brain metastases from various origins. Although the aim of this Chapter was to identify endothelial ALCAM for early detection, the striking presence of ALCAM on the membrane of brain metastasis tumour cells from all primaries, also makes it an attractive marker for therapeutic options. ALCAM targeted therapies could be developed for delivering drugs and radioactive substances to brain micrometastases, whilst selective opening of the BBB using new technologies such as focused ultrasound using microbubbles [231] or TNF receptor 1[60] is applied.

6.3 E-selectin Targeted MRI

Another adhesion molecule that has been shown to be highly upregulated on brain endothelial cells in close proximity to brain metastases is E-selectin [56]. The results of Chapter 4 showed that ALCAM as an imaging surrogate is more sensitive to detect breast cancer brain metastases, than either melanoma or lung cancer brain metastases. As a consequence, to investigate any further improvement in detection of brain micrometastases, particularly with melanoma and lung origin, E-selectin properties as a target for molecular imaging was assessed in Chapter 5. E-selectin was found to be highly expressed on endothelial cells in response to proinflammatory agents both *in vitro* and *in vivo*. Negligible levels of endogenous E-selectin were found on unstimulated cells *in vitro,* and on contralateral vessels of the mouse neuroinflammation model, suggesting rapid and specific upregulation of this marker to the stimuli. Therefore, a novel E-selectin targeted MPIO agent was developed and demonstrated successful binding capability to E-selectin both *in vitro* and *in vivo.*

It has been suggested, during the metastatic process, that circulating cancer cells “hijack” the inflammatory system. E-selectin facilitates attachment of leukocytes and their transmigration at sites of inflammatory foci. Thus, it is easily imaginable that E-selectin is used in a similar fashion to mediate rolling and extravasation of circulating cancer cells [232]. Ligands on the cancer cells

bind to E-selectin on the surface of the endothelial cells, which allows them to roll and develop bindings. The role of E-selectin for the initial binding of metastatic cancer cells has been shown in different cancer types and also for metastatic brain cancer cells *in vitro* [93], [233]. Moreover, in preclinical models, it has been demonstrated that the number of lung metastatic foci from colon cancer decreases in E-selectin-deficient mice compared to wild-type [234]. In line with these previous studies, in Chapter 5 I showed E-selectin upregulation on mouse endothelial cells co-cultured with metastatic cell lines (breast, melanoma and lung primaries) after 12 hours. Observation of "primary response" of E-selectin for capturing metastatic cancer cells *in vivo,* was outside the scope of this thesis, as this phenomenon occurs at the extravasation stage of tumours after intracardiac injection [54]. However, I speculate that there is a "secondary response" of E-selectin expression following a successful extravasation stage during the subsequent micrometastatic colonisation. The presence of E-selectin activated vessels in the vicinity of brain metastases, which increased over-time, implies that the response could be at least partly due to secretion of proinflammatory cytokines in the tumour microenvironment. The role of E-selectin after tumour extravasation step is not clear, however, its upregulation has been suggested to act as a double-edge sword [233]. The presence of E-selectin allows lymphocyte infiltration into tumours, which could have both anti- and pro-tumorigenic effects. As an example of anti-tumorigenic effect, squamous cell carcinoma recruit nitric oxide (NO)-producing myeloid-derived suppressor cells to reduce E-selectin expression and evade immune detection [235]. In this case lower E-selectin expression correlates with higher survival. On the other hand, many cancer cells including leukaemia cells benefit from E-selectin upregulation in various ways [233], [236]. Nevertheless, further investigation is needed to understand the role of this adhesion molecule in brain metastasis.

Finally, E-selectin positive vessels in close proximity to tumour cells allowed this marker to be targeted for molecular imaging of brain micrometastases. The novel E-selectin-MPIO agent enabled detection of brain micrometastases to a greater extent than ALCAM-MPIO in all brain metastasis models.

6.4 Comparing VCAM-1, ALCAM and E-selectin for Brain Micrometastases Detection

So, what is the optimal adhesion molecule for brain micrometastases detection? To answer this question, I have summarised the findings of this work in the tables below (Table 6.1 and Table 6.2). Comparing the overall expression of endothelial VCAM-1[*], ALCAM and E-selectin in histological sections of brain metastasis models, shows that breast cancer brain metastasis (MDA-MB-231-Br) has the highest expression of all three adhesion molecules together, followed by lung brain metastasis (SEBTA-001) (Table 6.1). In melanoma brain metastasis (H1_DL2), expression of adhesion molecules is lower than for the other two cell lines, but still above 50% of vessels are positive for all markers. Nevertheless, comparing CAMs expression between different brain metastatic cell lines suffers from a number of limitations. It should be noted that different time-points post-tumour cell injection were compared for MDA-MB-231-Br, H1_DL2 at day 21 *vs.* SEBTA-001 at day 42. Moreover, owing to different growth rates of these tumours, the average median volume for MDA-MB-231-Br was found to be higher (0.88×10^{-3} µl) at day 21 compared to H1_DL2 (0.46×10^{-3} µl) at a same time-point, and SEBTA-001 (0.5×10^{-3} µl) at day 42. However, in general, greater expression of adhesion molecules was detected for tumours with volumes above the median for each cohort (Table 6.1).

Target	Cell line	Overall + vessels	+ above median	+ below median
VCAM-1	MDA-MB-231-Br	89%	98%	80%
ALCAM	MDA-MB-231-Br	88.5%	94%	83%
E-selectin	MDA-MB-231-Br	91%	96.5%	85%
VCAM-1	H1_DL2	72%	84%	60%
ALCAM	H1_DL2	50.6%	59%	42%
E-selectin	H1_DL2	70%	78%	61%
VCAM-1	SEBTA-001	93%	96%	89%
ALCAM	SEBTA-001	79%	89%	68%
E-selectin	SEBTA-001	79%	89%	64%

Table 6.1: Expression of VCAM-1, ALCAM and E-selectin adhesion molecules on tumour-associated vessels.[†]

[*] Data extracted from the previous work of Cheng *et al*. [98].
[†] Day 21 for breast and melanoma brain metastasis models, and day 42 for the lung brain metastases model.

As for the sensitivity of each adhesion molecule for the detection of brain micrometastases *in vivo*, VCAM-MPIO and E-selectin-MPIO enabled detection of a greater percentage of brain tumours than ALCAM-MPIO (Table 6.2). All three compounds were able to detect a higher percentage of brain micrometastases from breast cancer compared to melanoma and lung primaries (Table 6.2) withstanding the same caveats of different time-points and growth rates. Overall, the MRI results are in keeping with the underlying biology, and provide insight into the temporal and spatial expression of CAMs in brain metastases from distinctive primaries.

Target	Cell line	%Tumour detected	+ above median	+ below median
VCAM-1	MDA-MB-231-Br	82%	94%	69%
ALCAM	MDA-MB-231-Br	82%	88.5%	75.5%
E-selectin	MDA-MB-231-Br	83%	93%	74%
VCAM+E-sel	MDA-MB-231-Br	91%	-	-
VCAM-1	H1_DL2	72%	92%	52%
ALCAM	H1_DL2	54%	59.5%	50%
E-selectin	H1_DL2	66%	75%	59%
VCAM+E-sel	H1_DL2	75%	-	-
VCAM-1	SEBTA-001	89%	100%	78%
ALCAM	SEBTA-001	68%	70%	66%
E-selectin	SEBTA-001	72%	87%	57%
VCAM+E-sel	SEBTA-001	90%	-	-

Table 6.2: Sensitivity of cell adhesion molecules targeted MRI compounds in detection of brain metastases.

There is no definite answer for the optimal target for detection of brain micrometastases. The microenvironment of tumours is complex and there is a dynamic interplay between metastatic cancer cells and endothelial cells. Based on the work presented here and literature, I have generated a general schematic pattern of VCAM-1, ALCAM and E-selectin expression in brain metastasis over time (Figure 6.1). Understandably, the degree of expression may be altered for different cell lines. Figure 6.1 illustrates, VCAM-1, ALCAM and E-selectin are expressed to a different degree on cerebral vessels across micrometastatic development. Based on the literature,

E-selectin assists with the initial attachment of circulating cancer cells (Figure 6.1; first dashed pink line, grey area) [237], and remains upregulated during brain metastasis formation (second dashed pink line; based on results of Chapter 5). Subsequently, VCAM-1 (green line) and ALCAM (blue line) are expressed on endothelial cells for further adhesion and extravasation of metastatic cancer cells [67], [200]. The data obtained in this thesis do not demonstrate exactly when upregulation of each these CAMs begins (Figure 6.1; grey area), however both VCAM-1 and ALCAM were evident on the tumour-associated endothelial cells by day 7. Based on immunohistochemistry analyses, VCAM-1 expression was shown to be higher than ALCAM and E-selectin, and this could partly be explained by the continuous pattern of expression along vessels, and, partly, by its role in maintaining firm binding of tumour cancer cells with their microenvironment [98].

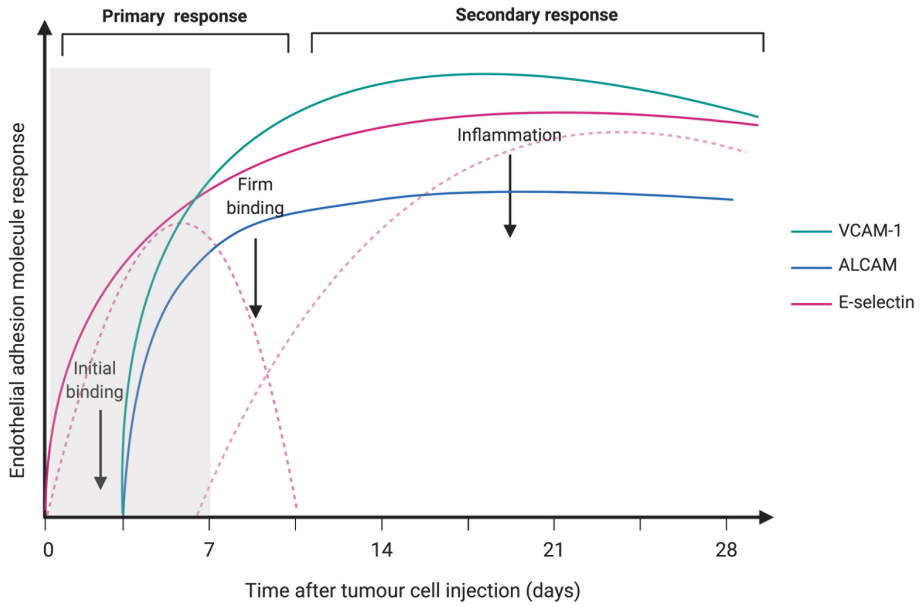


Figure 6.1: Schematic of endothelial VCAM-1, ALCAM and E-selectin upregulation in brain metastasis.

E-selectin (primary response; first dashed pink line) primary role is to mediate the initial attachment and rolling of circulatory cancer cells on blood vessels. Subsequently, firm bindings are developed between cancer cells and endothelial cells through VCAM-1 (green line) and ALCAM (blue line) expression. The initial steps of attachment and intravasation of cancer cells were not investigated in this thesis, and the "unknown delay" or "grey area" is based on the literature. However, immunohistochemical analyses of brain metastasis from day 7 after tumour cell injection have confirmed the presence of all three adhesion molecules, at varying degrees, on the tumour-associated vessel (secondary response; second dashed pink line for E-selectin). Further roles of these cell adhesion molecules after the extravasation step are not clear.

Owing to the different degree of upregulation of CAMs at different stages, targeting more than one adhesion molecule may improve sensitivity of detection. In Chapter 5, two adhesion molecules, VCAM-1 and E-selectin were targeted for combined detection of brain micrometastases. Results showed that the highest improvement achieved by concurrent targeting of two CAMs for breast cancer brain metastasis (↑9.5%), followed by melanoma (↑4%) and lung (↑1%) brain metastases (Table 6.2). To conclude this section, developing MRI contrast agents that can target multiple adhesion molecules could improve the sensitivity of detection of brain metastasis, and may find wider application across more patients due to their multiple specificities.

6.5 Limitations and Considerations

An acknowledgement needs to be made to the limitation of the brain metastasis models used in this thesis. The question as to why the MDA-MB-231-Br breast cancer brain metastasis model showed higher expression of adhesion molecules and, thus, sensitivity to targeted MPIO contrast agents, may be explained by the high vascular density, co-optive growth pattern and higher doubling time of this cell line. This finding cannot be generalised for all breast cancer brain metastasis mouse models, as distinctive growth patterns and inherent heterogeneity have been demonstrated for different brain tropic human breast cancer cell lines (e.g. JMT-BR3 and SUM190-BR3) [238]. Moreover, expression of angiogenic factors such as VEGF-A and IL-8 governs the vascularisation pattern and invasion of brain tropic melanoma cell lines [239]. The melanoma brain metastasis cell line used in this thesis, H1_DL2, was found to have relatively low vascular density and in many instances, a distinctive lobular growth pattern [240]. In contrast, other brain tropic human melanoma cancer cell lines, such as A-07, D-12 and U-25, have been shown to have high microvessel density and to exhibit co-optive growth when injected intracardially into mice [239]. The same explanation may apply to the SEBTA-001 brain metastasis model, however the slow doubling time of this cell line prevented extensive study of this model in this thesis. Other human lung-derived brain metastasis cell lines, such as BT478 and BT530, could also be investigated for CAMs expression in the future [241]. Nevertheless, the results of this thesis suggest heterogeneity of brain metastases depending on their origin and are in line with the mounting evidence of genomic heterogeneity intratumourally, as well as across different primaries for brain metastasis in patients [242].

6.6 Clinical Translation

Preclinical brain metastasis models remain a vital tool for identifying and screening novel diagnostic avenues. Although *in vivo* models lack the successful replication of the microenvironment in which a human tumour grows in totality, and there are physiological differences between humans and rodents, these models have allowed major advances in understanding tumour biology, thus advancing diagnostic and treatment strategies. Two adhesion

molecules, ALCAM and E-selectin, that have been investigated thoroughly in this thesis were also found to be evident in all human brain metastasis biopsies from breast, melanoma and lung primaries. However, it should be acknowledged that due to the limited access to human brain metastases biopsies, the number of cases studied in this body of work was limited and the type of primary cancer (e.g. triple negative for breast cancer) was not provided. Further investigation and analyses of ALCAM and E-selectin upregulation in human brain metastases biopsies is required for future work.

As discussed in the Introduction Chapter, molecular imaging using SPECT and PET for diagnosis of neuroinflammation are currently performed in humans [243], [244], the clinical value of these methods is impeded by exposure to ionising radiation, low spatial resolution and low availability of the imaging agents. In contrast, molecular MRI overcomes these limitations. With the advent of biodegradable multimeric MPIO (mMPIO) [134], humanised ALCAM and E-selectin antibodies can be developed to be used in man.

One concern for translation of this approach is that the spatial resolution of MRI in mice is substantially higher than that currently achieved in the clinical setting. However, based on previous calculations, the smallest tumour detected with E-selectin-MPIO, 100 μm diameter (88 μm isotropic resolution), equates to detection of a 300-350 μm diameter tumour using a 3 T clinical MRI scanner (~1 mm isotropic resolution) [97]. This tumour size is considerably smaller than tumours that can be detected with current techniques requiring a permeable BBB (2-5 mm in diameter) [245]. Moreover, moving to lower clinical resolution would minimise the rate of false positive signals from non-specific MPIO retention, hence, improving visualisation of bound MPIO.

Further concern could be the sensitivity and specificity of targeting adhesion molecules for detection of brain micrometastases. As discussed previously, E-selectin is upregulated on cerebral vessels in a number of diseases, such as multiples sclerosis (MS), infection, stroke and many other inflammatory diseases [246], [247]. Therefore, the suggested technique is recommended for patients “at risk” of brain metastasis development, with a history of primary

cancer. This itself greatly increases the likelihood that MPIO "positive" signals reflect brain metastasis and not another inflammatory disease or a primary tumour. It should be noted that, the gold standard gadolinium-enhanced T_1-weighted MRI is not specific for detection of brain metastases, and there is diagnostic uncertainty between a cerebral abscess, metastatic tumour or primary malignancy as well as other neuroinflammatory diseases [248].

Finally, early detection of brain micrometastasis using adhesion molecule-MPIO would enable treatment decisions that are not currently possible, such as: (i) no brain metastases at diagnosis of primary tumour (e.g. breast cancer) - radical therapy of primary, with periodic screening for presentation of brain metastases; (ii) low brain metastasis burden at diagnosis of primary tumour - radical therapy of primary and aggressive treatment of brain metastasis(es); (iii) Large brain metastasis burden at diagnosis of primary tumour - decision to limit invasive therapy of primary and palliative care and maintaining quality of life as long as possible.

6.7 Future Directions

Further studies characterising adhesion molecules and their ligands in brain metastasis is warranted. Such studies may allow: (1) prevention of brain metastasis formation by blocking or disrupting adhesion of disseminated cancer cells to the brain; (2) further development of novel molecularly targeted imaging agents; (3) development of personalised theranostic tools for diagnosis and treatment of brain micrometastases in one package; and (4) use of molecularly targeted MRI agents as a tool to assess treatment response. These points are discussed in further detail below.

1) The prognostic significance of ALCAM expression in primary cancer cells (breast, melanoma and lung) and brain metastasis has not been shown previously. It has been suggested that the presence of ALCAM may indicate a more invasive phenotype of cancer cells [249], [250]. Blocking ALCAM expressed on primary cancer cells and/or circulating cancer cells may prevent distant metastasis formation. The same approach could be applied to the E-selectin ligands expressed on cancer cells (e.g. CLA, PSGL-1), thus preventing

adhesion of tumour cells to the endothelial cells and, consequently, blocking formation of brain metastases.

2) Advancing MPIO based contrast agents targeting multiple adhesion molecules may improve detection of brain micrometastases. More complex MPIO harbouring two/multiple antibodies on their surface could be developed. Moreover, these multiple targeted agents could be radiolabelled, and their application could be expanded to other imaging modalities such as PET or SPECT for detection of metastases in other sites (e.g. lungs).

3) Access to CNS immunity has now been accepted, and it has set the basis of development of novel targeted immunotherapy approaches (i.e. immune checkpoint inhibitors) [251]. The response to targeted agents in brain metastasis seems to be higher than for conventional chemotherapy drugs. The adhesion molecules presented in this work could be used as targets for theranostic applications. For instance, nanoparticles targeting adhesion molecules, and conveying two or more drugs simultaneously could bring opportunities to overcome the restriction of current treatment of brain micrometastasis.

4) Finally, as shown in this work, molecular imaging yields significant information about the pathobiology of brain metastases. This information could be used to advance personalised treatments. As an example, these molecular imaging contrast agents could be used as a tool to evaluate treatment response. Radiation therapy is still a mainstay treatment for cerebral metastases, and its effect on adhesion molecules in brain has not been explored. Improving our knowledge in this field would help to develop a pipeline where subjects are imaged with targeted MPIO prior to and after radiation therapy, therefore evaluating brain metastasis response to treatment *in vivo*.

6.8 Closing Remarks

The “Sword of Damocles” hangs over the head of patients diagnosed with brain metastasis. The lack of early detection of brain metastasis, hence, limited treatment strategies, is clearly reflected in the high mortality of these patients. The work presented in this thesis, introduced two

adhesion molecules, present on brain metastasis-associated vessels from breast, melanoma and lung primary cancers. Targeting these surrogates using MRI based contrast agents demonstrated that brain micrometastases could be detected before any current imaging technique is able, potentially opening a window of opportunity for earlier treatment interventions.

Bibliography

[1] K. Fink and J. Fink, “Imaging of brain metastases,” *Surg. Neurol. Int.*, vol. 4, no. 5, p. 209, 2013.

[2] T. N. Seyfried and L. C. Huysentruyt, “On the origin of cancer metastasis,” *Crit. Rev. Oncog.*, vol. 18, no. 1–2, pp. 43–73, 2013.

[3] C. L. Chaffer and R. A. Weinberg, “A perspective on cancer cell metastasis,” *Science*, vol. 331, no. 6024. pp. 1559–1564, 25-Mar-2011.

[4] N. G. Zaorsky, T. M. Churilla, B. L. Egleston, S. G. Fisher, *et al.*, “Causes of death among cancer patients,” *Ann. Oncol.*, vol. 28, no. 2, pp. 400–407, 2017.

[5] C. A. Klein, “Framework models of tumor dormancy from patient-derived observations,” *Current Opinion in Genetics and Development*, vol. 21, no. 1. pp. 42–49, Feb-2011.

[6] “https://seer.cancer.gov/statfacts.” .

[7] S. Paget, “The distribution of seconday growths in cancer of the breast.,” *Lancet*, vol. 133, no. 3421, pp. 571–573, Mar. 1889.

[8] J. E. Talmadge and I. J. Fidler, “AACR centennial series: The biology of cancer metastasis: Historical perspective,” *Cancer Research*, vol. 70, no. 14. pp. 5649–5669, 15-Jul-2010.

[9] I. J. Fidler and G. Poste, “The ‘seed and soil’ hypothesis revisited,” *The Lancet Oncology*, vol. 9, no. 8. p. 808, Aug-2008.

[10] P. W. Sperduto, S. T. Chao, P. K. Sneed, X. Luo, *et al.*, “Diagnosis-Specific Prognostic Factors, Indexes, and Treatment Outcomes for Patients With Newly Diagnosed Brain Metastases: A Multi-Institutional Analysis of 4,259 Patients,” *Int. J. Radiat. Oncol. Biol. Phys.*, vol. 77, no. 3, pp. 655–661, 2010.

[11] J. S. Barnholtz-sloan, A. E. Sloan, F. G. Davis, F. D. Vigneau, *et al.*, “Incidence Proportions of Brain Metastases in Patients Diagnosed (1973 to 2001) in the Metropolitan Detroit Cancer Surveillance System,” *J. Clin. Oncol.*, vol. 22, no. 14, pp. 2865–2872, 2004.

[12] K. E. Smedby, L. Brandt, M. L. Bäcklund, and P. Blomqvist, “Brain metastases admissions in Sweden between 1987 and 2006,” *Br. J. Cancer*, vol. 101, no. 11, pp. 1919–1924, Dec. 2009.

[13] I. T. Gavrilovic and J. B. Posner, “Brain metastases: Epidemiology and pathophysiology,” *J. Neurooncol.*, vol. 75, no. 1, pp. 5–14, 2005.

[14] C. Nieder, O. Spanne, M. P. Mehta, A. L. Grosu, and H. Geinitz, “Presentation, patterns of care, and survival in patients with brain metastases: What has changed in the last 20 years?,” *Cancer*, vol. 117, no. 11, pp. 2505–2512, 2011.

[15] A. S. Achrol, R. C. Rennert, C. Anders, R. Soffietti, *et al.*, “Brain metastases,” *Nat. Rev. Dis. Prim.*, vol. 5, no. 1, p. 5, Dec. 2019.

[16] L. Nayak, E. Q. Lee, and P. Y. Wen, “Epidemiology of brain metastases,” *Curr. Oncol. Rep.*, vol. 14, no. 1, pp. 48–54, 2012.

[17] A. E. Sloan, C. J. Nock, and D. B. Einstein, “Diagnosis and treatment of melanoma brain metastasis: A literature review,” *Cancer Control*, vol. 16, no. 3. H. Lee Moffitt Cancer Center and Research Institute, pp. 248–255, 2009.

[18] R. Soffietti, A. Ducati, and R. Rudà, *Neuro-Oncology Part II*. 2012.

[19] G. Sze, E. Milano, C. Johnson, and L. Heier, “Detection of brain metastases: comparison of contrast-enhanced MR with unenhanced MR and enhanced CT,” *AJNR Am J Neuroradiol*, vol. 11, no. 4, pp. 785–91, 1990.

[20] H. Mehrabian, J. Detsky, H. Soliman, A. Sahgal, and G. J. Stanisz, “Advanced Magnetic Resonance Imaging Techniques in Management of Brain Metastases,” *Front. Oncol.*, vol. 9, no. June, pp. 1–16, 2019.

[21] Y. Nomoto, T. Miyamoto, and Y. Yamaguchi, “Brain metastasis of small cell lung carcinoma: Comparison of gd-dtpa enhanced magnetic resonance imaging and enhanced

computerized tomography," *Jpn. J. Clin. Oncol.*, vol. 24, no. 5, pp. 258–262, 1994.
[22] W. A. Hall, "The safety and efficacy of stereotactic biopsy for intracranial lesions," *Cancer*, vol. 82, no. 9, pp. 1749–1755, May 1998.
[23] L. M. DeAngelis, J. Y. Delattre, and J. B. Posner, "Radiation-induced dementia in patients cured of brain metastases," *Neurology*, vol. 39, no. 6, pp. 789–796, 1989.
[24] J. A. Bovi, "Prevention of Brain Metastases," *Front. Neurol.*, vol. 9, p. 758, 2018.
[25] A. Shinde, D. Akhavan, M. Sedrak, S. Glaser, and A. Amini, "Shifting paradigms: whole brain radiation therapy versus stereotactic radiosurgery for brain metastases," *CNS Oncol.*, vol. 8, no. 1, p. CNS27, Mar. 2019.
[26] P. E. Fecci, C. D. Champion, J. Hoj, C. M. McKernan, *et al.*, "The Evolving Modern Management of Brain Metastasis," *Clin. Cancer Res.*, 2019.
[27] G. Minniti, D. Anzellini, C. Reverberi, G. C. A. Cappellini, *et al.*, "Stereotactic radiosurgery combined with nivolumab or Ipilimumab for patients with melanoma brain metastases: evaluation of brain control and toxicity," *J. Immunother. Cancer*, vol. 7, no. 1, p. 102, Dec. 2019.
[28] M. Preusser, F. Winkler, M. Valiente, C. Manegold, *et al.*, "Recent advances in the biology and treatment of brain metastases of non-small cell lung cancer: summary of a multidisciplinary roundtable discussion," *ESMO Open*, vol. 3, no. 1, p. e000262, 2018.
[29] T. K. Owonikoko, J. Arbiser, A. Zelnak, H.-K. G. Shu, *et al.*, "Current approaches to the treatment of metastatic brain tumours.," *Nat. Rev. Clin. Oncol.*, vol. 11, no. 4, pp. 203–22, 2014.
[30] S. Friberg and A. Nystrom, "Cancer Metastases: Early Dissemination and Late Recurrences," *Cancer Growth Metastasis*, vol. 8, p. CGM.S31244, Jan. 2015.
[31] K. L. Harper, M. S. Sosa, D. Entenberg, H. Hosseini, *et al.*, "Corrigendum: Mechanism of early dissemination and metastasis in Her2+ mammary cancer," *Nature*, vol. 553, no. 7688. NLM (Medline), p. 366, 18-Jan-2018.
[32] S. Turajlic and C. Swanton, "Metastasis as an evolutionary process," *Science*. 2016.
[33] D. R. Welch and D. R. Hurst, "Defining the Hallmarks of Metastasis," *Cancer Research*, vol. 79, no. 12. American Association for Cancer Research Inc., pp. 3011–3027, 15-Jun-2019.
[34] D. Hanahan and R. A. Weinberg, "Hallmarks of cancer: The next generation," *Cell*, vol. 144, no. 5. pp. 646–674, 04-Mar-2011.
[35] T. Brabletz, R. Kalluri, M. A. Nieto, and R. A. Weinberg, "EMT in cancer," *Nature Reviews Cancer*, vol. 18, no. 2. Nature Publishing Group, pp. 128–134, 25-Jan-2018.
[36] E. D. Hay, "Organization and fine structure of epithelium and mesenchyme in the developing chick embryo," *Ep. Interact.*, 1968.
[37] A. G. Clark and D. M. Vignjevic, "Modes of cancer cell invasion and the role of the microenvironment," *Current Opinion in Cell Biology*, vol. 36. Elsevier Ltd, pp. 13–22, 01-Oct-2015.
[38] S. Y. Wong and R. O. Hynes, "Lymphatic or hematogenous dissemination: How does a metastatic tumor cell decide?," *Cell Cycle*, vol. 5, no. 8, pp. 812–817, 2006.
[39] S. P. H. Chiang, R. M. Cabrera, and J. E. Segall, "Tumor cell intravasation," *American Journal of Physiology - Cell Physiology*, vol. 311, no. 1. American Physiological Society, pp. C1–C14, 01-Jul-2016.
[40] G. M. Saidel, "Quantitative Relationships of Intravascular Tumor Cells, Tumor Vessels, and Pulmonary Metastases following Tumor Implantation," *Cancer Res.*, vol. 34, no. 5, pp. 997–1004, 1974.
[41] Y. S. Chang, E. Di Tomaso, D. M. McDonald, R. Jones, *et al.*, "Mosaic blood vessels in tumors: Frequency of cancer cells in contact with flowing blood," *Proc. Natl. Acad. Sci. U. S. A.*, vol. 97, no. 26, pp. 14608–14613, Dec. 2000.
[42] D. Wirtz, K. Konstantopoulos, and P. C. Searson, "The physics of cancer: The role of physical interactions and mechanical forces in metastasis," *Nature Reviews Cancer*, vol. 11, no. 7. pp. 512–522, Jul-2011.
[43] M. J. Mitchell and M. R. King, "Computational and experimental models of cancer cell

response to fluid shear stress," *Frontiers in Oncology*, vol. 3. pp. 1–11, 2013.
[44] A. Steven and B. Seliger, "The Role of Immune Escape and Immune Cell Infiltration in Breast Cancer," *Breast Care*, vol. 13, no. 1. S. Karger AG, pp. 16–21, 01-Mar-2018.
[45] A. F. Chambers, A. C. Groom, and I. C. MacDonald, "Dissemination and growth of cancer cells in metastatic sites.," *Nat. Rev. Cancer*, vol. 2, no. 8, pp. 563–572, 2002.
[46] J. Y. Delattre, G. Krol, H. T. Thaler, and J. B. Posner, "Distribution of Brain Metastases," *Arch. Neurol.*, vol. 45, no. 7, pp. 741–744, 1988.
[47] B. Strilic and S. Offermanns, "Intravascular Survival and Extravasation of Tumor Cells," *Cancer Cell*, vol. 32, no. 3. pp. 282–293, 2017.
[48] C. T. Mierke, "Role of the Endothelium during Tumor Cell Metastasis: Is the Endothelium a Barrier or a Promoter for Cell Invasion and Metastasis?," *J. Biophys.*, vol. 2008, pp. 1–13, 2008.
[49] M. Nathoo, A. Chahlavi, G. H. Barnett, and S. A. Toms, "Pathobiology of brain metastases," *Journal of Clinical Pathology*, vol. 58, no. 3. pp. 237–242, 2005.
[50] J. L. Chitty, E. C. Filipe, M. C. Lucas, D. Herrmann, *et al.*, "Recent advances in understanding the complexities of metastasis," *F1000Research*, vol. 7. 2018.
[51] A. M. Chacko, C. Li, D. A. Pryma, S. Brem, *et al.*, "Targeted delivery of antibody-based therapeutic and imaging agents to CNS tumors: Crossing the blood-brain barrier divide," *Expert Opinion on Drug Delivery*, vol. 10, no. 7. pp. 907–926, 2013.
[52] I. Wilhelm, J. Molnár, C. Fazakas, J. Haskó, and I. A. Krizbai, "Role of the blood-brain barrier in the formation of brain metastases," *International Journal of Molecular Sciences*, vol. 14, no. 1. Multidisciplinary Digital Publishing Institute, pp. 1383–1411, 11-Jan-2013.
[53] S. Paku, B. Döme, R. Tóth, and J. Timár, "Organ-specificity of the extravasation process: An ultrastructural study," *Clin. Exp. Metastasis*, vol. 18, no. 6, pp. 481–492, 2000.
[54] Y. Kienast, L. Von Baumgarten, M. Fuhrmann, W. E. F. Klinkert, *et al.*, "Real-time imaging reveals the single steps of brain metastasis formation," *Nat. Med.*, vol. 16, no. 1, pp. 116–122, 2010.
[55] W. S. Carbonell, O. Ansorga, N. Sibson, and R. Muschel, "The vascular basement membrane as 'soil' in brain metastasis," *PLoS One*, vol. 4, no. 6, p. e5857, 2009.
[56] M. S. Soto, S. Serres, D. C. Anthony, and N. R. Sibson, "Functional role of endothelial adhesion molecules in the early stages of brain metastasis," *Neuro. Oncol.*, vol. 16, no. 4, pp. 540–551, 2014.
[57] A. S. Berghoff and M. Preusser, "Anti-angiogenic therapies in brain metastases," *Memo - Magazine of European Medical Oncology*, vol. 11, no. 1. Springer, pp. 14–17, 2018.
[58] C. Gaudy-Marqueste, A. S. Dussouil, R. Carron, L. Troin, *et al.*, "Survival of melanoma patients treated with targeted therapy and immunotherapy after systematic upfront control of brain metastases by radiosurgery," *Eur. J. Cancer*, vol. 84, pp. 44–54, Oct. 2017.
[59] Q. He, J. Liu, J. Liang, X. Liu, *et al.*, "Towards Improvements for Penetrating the Blood–Brain Barrier—Recent Progress from a Material and Pharmaceutical Perspective," *Cells*, vol. 7, no. 4, p. 24, 2018.
[60] J. J. Connell, G. Chatain, B. Cornelissen, K. A. Vallis, *et al.*, "Selective permeabilization of the blood-brain barrier at sites of metastasis," *J. Natl. Cancer Inst.*, vol. 105, no. 21, pp. 1634–1643, Nov. 2013.
[61] H. Togashi, T. Sakisaka, and Y. Takai, "Cell adhesion molecules in the central nervous system.," *Cell Adh. Migr.*, vol. 3, no. 1, pp. 29–35, 2009.
[62] G. Bendas and L. Borsig, "Cancer cell adhesion and metastasis: Selectins, integrins, and the inhibitory potential of heparins," *International Journal of Cell Biology*, vol. 2012. Hindawi, pp. 1–10, 12-Feb-2012.
[63] A. Fung, M. Vizcaychipi, D. Lloyd, Y. Wan, and D. Ma, "Central nervous system inflammation in disease related conditions: Mechanistic prospects," *Brain Research*, vol. 1446. Elsevier, pp. 144–155, 29-Mar-2012.

[64] Q. Ma, S. Chen, D. Klebe, J. H. Zhang, and J. Tang, "Adhesion molecules in CNS disorders: biomarker and therapeutic targets.," *CNS Neurol. Disord. Drug Targets*, vol. 12, no. 3, pp. 392–404, May 2013.
[65] W. A. Muller, "Getting Leukocytes to the Site of Inflammation," *Veterinary Pathology*, vol. 50, no. 1. pp. 7–22, Jan-2013.
[66] C. Strell and F. Entschladen, "Extravasation of leukocytes in comparison to tumor cells," *Cell Communication and Signaling*, vol. 6. BioMed Central, p. 10, 04-Dec-2008.
[67] G. Sökeland and U. Schumacher, "The functional role of integrins during intra- and extravasation within the metastatic cascade," *Molecular Cancer*, vol. 18, no. 1. 2019.
[68] B. R. Zetter, "Adhesion molecules in tumor metastasis," *Semin Cancer Biol*, vol. 4, no. 4, pp. 219–29, 1993.
[69] A. M. Khatib, M. Kontogiannea, L. Fallavollita, B. Jamison, *et al.*, "Rapid induction of cytokine and E-selectin expression in the liver in response to metastatic tumor cells," *Cancer Res.*, vol. 59, no. 6, pp. 1356–1361, Mar. 1999.
[70] H. ; Läubli and L. Borsig, "Selectins promote tumor metastasis," *Semin. Cancer Biol.*, vol. 20, no. 3, pp. 169–177, 2010.
[71] A. Aruffo, M. A. Bowen, G. C. Starling, J. A. Gebe, *et al.*, "CD6-ligand interactions: A paradigm for SRCR domain function?," *Immunol. Today*, vol. 18, no. 10, pp. 498–504, 1997.
[72] N. J. Hassan, A. N. Barclay, and M. H. Brown, "Frontline: Optimal T cell activation requires the engagement of CD6 and CD166," *Eur. J. Immunol.*, vol. 34, no. 4, pp. 930–940, 2004.
[73] G. W. M. Swart, P. C. Lunter, J. W. J. Van Kilsdonk, and L. C. L. T. Van Kempen, "Activated leukocyte cell adhesion molecule (ALCAM/CD166): Signaling at the divide of melanoma cell clustering and cell migration?," *Cancer and Metastasis Reviews*, vol. 24, no. 2. pp. 223–236, 2005.
[74] A. Masedunskas, J. A. King, F. Tan, R. Cochran, *et al.*, "Activated leukocyte cell adhesion molecule is a component of the endothelial junction involved in transendothelial monocyte migration," *FEBS Lett.*, vol. 580, no. 11, pp. 2637–2645, 2006.
[75] L. C. van Kempen, J. J. van den Oord, G. N. van Muijen, U. H. Weidle, *et al.*, "Activated leukocyte cell adhesion molecule/CD166, a marker of tumor progression in primary malignant melanoma of the skin," *Am. J. Pathol.*, vol. 156, no. 3, pp. 769–774, 2000.
[76] W. W. Zhang, S. H. Zhan, C. X. Geng, X. Sun, *et al.*, "Activated leukocyte cell adhesion molecule regulates the interaction between pancreatic cancer cells and stellate cells," *Mol. Med. Rep.*, vol. 14, no. 4, pp. 3627–3633, 2016.
[77] Y. J. Jeong, H. K. Oh, S. H. Park, and J. G. Bong, "Prognostic significance of activated leukocyte cell adhesion molecule (alcam) in association with promoter methylation of the ALCAM gene in breast cancer," *Molecules*, vol. 23, no. 1, 2018.
[78] J. A. King, S. F. Ofori-Acquah, T. Stevens, A. B. Al-Mehdi, *et al.*, "Activated leukocyte cell adhesion molecule in breast cancer: Prognostic indicator," *Breast Cancer Res.*, vol. 6, no. 5, 2004.
[79] Y. Zhang, C. Qian, L. Jing, J. Ren, and Y. Guan, "Meta-analysis indicating that high ALCAM expression predicts poor prognosis in colorectal cancer," *Oncotarget*, vol. 8, no. 29, pp. 48272–48281, 2017.
[80] S. F. Ofori-Acquah and J. A. King, "Activated leukocyte cell adhesion molecule: a new paradox in cancer," *Transl. Res.*, vol. 151, no. 3, pp. 122–128, 2008.
[81] U. H. Weidle, D. Eggle, S. Klostermann, and G. W. M. Swart, "ALCAM / CD166 : Cancer-related Issues," vol. 244, pp. 231–243, 2010.
[82] A. Roth, D. C. Drummond, F. Conrad, M. E. Hayes, *et al.*, "Anti-CD166 single chain antibody-mediated intracellular delivery of liposomal drugs to prostate cancer cells," *Mol. Cancer Ther.*, vol. 6, no. 10, pp. 2737–2746, 2007.
[83] M. T. Wiiger, H. B. Gehrken, Ø. Fodstad, G. M. Mælandsmo, and Y. Andersson, "A

novel human recombinant single-chain antibody targeting CD166/ALCAM inhibits cancer cell invasion in vitro and in vivo tumour growth," *Cancer Immunol. Immunother.*, vol. 59, no. 11, pp. 1665–1674, 2010.
[84] M. Uhlén, L. Fagerberg, B. M. Hallström, C. Lindskog, *et al.*, "Tissue-based map of the human proteome," *Science (80-.).*, vol. 347, no. 6220, 2015.
[85] R. Lyck, M. A. Lécuyer, M. Abadier, C. B. Wyss, *et al.*, "ALCAM (CD166) is involved in extravasation of monocytes rather than T cells across the blood–brain barrier," *J. Cereb. Blood Flow Metab.*, vol. 37, no. 8, pp. 2894–2909, 2017.
[86] H. Samaha, A. Pignata, K. Fousek, J. Ren, *et al.*, "A homing system targets therapeutic T cells to brain cancer," *Nature*, vol. 561, no. 7723, pp. 331–337, 2018.
[87] M. A. Lécuyer, O. Saint-Laurent, L. Bourbonnière, S. Larouche, *et al.*, "Dual role of ALCAM in neuroinflammation and blood-brain barrier homeostasis," *Proc. Natl. Acad. Sci. U. S. A.*, vol. 114, no. 4, pp. E524–E533, Jan. 2017.
[88] B. J. Graves, R. L. Crowther, C. Chandran, J. M. Rumberger, *et al.*, "Insight into E-selectin/ligand interaction from the crystal structure and mutagenesis of the lec/EGF domains," *Nature*, vol. 367, no. 6463, pp. 532–538, 1994.
[89] J. S. Merzaban, M. M. Burdick, S. Z. Gadhoum, N. M. Dagia, *et al.*, "Analysis of Glycoprotein E-selectin Ligands Expressed on Human and Mouse Hematopoietic Progenitor Cells," *Blood*, vol. 118, no. 7, pp. 1–29, 2011.
[90] R. B. Huang and O. Eniola-Adefeso, "Shear stress modulation of IL-1β-induced E-selectin expression in human endothelial cells," *PLoS One*, vol. 7, no. 2, pp. 1–9, 2012.
[91] S. R. Barthel, J. D. Gavino, L. Descheny, and C. J. Dimitroff, "Targeting selectins and selectin ligands in inflammation and cancer," *Expert Opinion on Therapeutic Targets*, vol. 11, no. 11. pp. 1473–1491, 2007.
[92] M. M. Burdick, K. A. Henson, L. F. Delgadillo, Y. E. Choi, *et al.*, "Expression of E-selectin ligands on circulating tumor cells: cross-regulation with cancer stem cell regulatory pathways?," *Front. Oncol.*, vol. 2, no. August, pp. 1–11, 2012.
[93] S. A. Jassam, Z. Maherally, J. R. Smith, K. Ashkan, *et al.*, "CD15s/CD62E interaction mediates the adhesion of non-small cell lung cancer cells on brain endothelial cells: Implications for cerebral metastasis," *Int. J. Mol. Sci.*, vol. 18, no. 1474, pp. 1–16, 2017.
[94] J. M. Cook-Mills, M. E. Marchese, and H. Abdala-Valencia, "Vascular cell adhesion molecule-1 expression and signaling during disease: regulation by reactive oxygen species and antioxidants.," *Antioxid. Redox Signal.*, vol. 15, no. 6, pp. 1607–38, Sep. 2011.
[95] M. E. Pueyo, W. Gonzalez, A. Nicoletti, F. Savoie, *et al.*, "Angiotensin II stimulates endothelial vascular cell adhesion molecule-1 via nuclear factor-κB activation induced by intracellular oxidative stress," *Arterioscler. Thromb. Vasc. Biol.*, vol. 20, no. 3, pp. 645–651, 2000.
[96] D.-H. Kong, Y. K. Kim, M. R. Kim, J. H. Jang, and S. Lee, "Emerging Roles of Vascular Cell Adhesion Molecule-1 (VCAM-1) in Immunological Disorders and Cancer.," *Int. J. Mol. Sci.*, vol. 19, no. 4, Apr. 2018.
[97] S. Serres, M. S. Soto, A. Hamilton, M. a. McAteer, *et al.*, "Molecular MRI enables early and sensitive detection of brain metastases," *Proc. Natl. Acad. Sci.*, vol. 109, pp. 6674–6679, 2012.
[98] V. W. T. Cheng, M. S. Soto, A. A. Khrapitchev, F. Perez-Balderas, *et al.*, "VCAM-1–targeted MRI Enables Detection of Brain Micrometastases from Different Primary Tumors," *Clin. Cancer Res.*, vol. 25, no. 2, pp. 533–534, 2019.
[99] M. Schlesinger and G. Bendas, "Vascular cell adhesion molecule-1 (VCAM-1)-An increasing insight into its role in tumorigenicity and metastasis," *Int. J. Cancer*, vol. 136, pp. 2504–2514, 2015.
[100] D. D. Eisenstat, J. Rak, S. Das, T. Charles, *et al.*, "Preclinical Modeling and Therapeutic Avenues for Cancer Metastasis to the Central Nervous System," vol. 7, p. 1, 2017.
[101] T. Yoneda, P. J. Williams, T. Hiraga, M. Niewolna, and R. Nishimura, "A bone-seeking clone exhibits different biological properties from the MDA-MB-231 parental human

breast cancer cells and a brain-seeking clone in vivo and in vitro.," *J. Bone Miner. Res.*, vol. 16, no. 8, pp. 1486–1495, 2001.
[102] D. A. Mankoff, "A definition of molecular imaging.," *J. Nucl. Med.*, vol. 48, no. 6, 2007.
[103] N. Nicastro, V. Garibotto, and P. R. Burkhard, "The role of molecular imaging in assessing degenerative parkinsonism – an updated review," *Swiss Med. Wkly.*, vol. 148, no. 1718, Apr. 2018.
[104] V. Valotassiou, J. Malamitsi, J. Papatriantafyllou, E. Dardiotis, *et al.*, "SPECT and PET imaging in Alzheimer's disease," *Ann. Nucl. Med.*, vol. 32, pp. 583–593, 2018.
[105] V. Narayanaswami, K. Dahl, V. Bernard-Gauthier, L. Josephson, *et al.*, "Emerging PET Radiotracers and Targets for Imaging of Neuroinflammation in Neurodegenerative Diseases: Outlook Beyond TSPO," *Mol. Imaging*, vol. 17, pp. 1–25.
[106] M. M. Khalil, J. L. Tremoleda, T. B. Bayomy, and W. Gsell, "Molecular SPECT Imaging: An Overview," *Int. J. Mol. Imaging*, vol. 2011, p. 15, 2011.
[107] L. Abou-Elkacem, S. V Bachawal, and J. K. Willmann, "Ultrasound molecular imaging: Moving toward clinical translation," *Eur. J. Radiol.*, vol. 84, no. 9, pp. 1685–1693, 2015.
[108] C. Wang, Z. Wang, T. Zhao, Y. Li, *et al.*, "Optical molecular imaging for tumor detection and image-guided surgery," *Biomaterials*, vol. 157, pp. 62–75, Mar. 2018.
[109] M. Gauberti, A. P. Fournier, D. Vivien, and S. M. de Lizarrondo, "Molecular magnetic resonance imaging (mMRI)," in *Methods in Molecular Biology*, vol. 1718, 2018, pp. 315–327.
[110] D. McRobbie, E. Moore, M. Graves, and M. Prince, *MRI from Picture to Proton*. Cambridge University Press, 2006.
[111] J. C. Böck, F. Kaufmann, and R. Felix, "Comparison of gadolinium-DTPA and macromolecular gadolinium-DTPA-polylysine for contrast-enhanced pulmonary time-of-flight magnetic resonance angiography.," *Invest. Radiol.*, vol. 31, no. 10, pp. 652–7, Oct. 1996.
[112] A. Matsumura, Y. Shibata, K. Nakagawa, and T. Nose, "MRI Contrast Enhancement by Gd-DTPA-Monoclonal Antibody in 9L Glioma Rats," in *Brain Edema IX*, Vienna: Springer Vienna, 1994, pp. 356–358.
[113] G. Strijkers, W. M. Mulder, G. F. van Tilborg, and K. Nicolay, "MRI Contrast Agents: Current Status and Future Perspectives," *Anticancer. Agents Med. Chem.*, vol. 7, no. 3, pp. 291–305, Apr. 2008.
[114] S. A. Anderson, R. K. Rader, W. F. Westlin, C. Null, *et al.*, "Magnetic resonance contrast enhancement neovasculature with α(v)β3-targeted nanoparticles," *Magn. Reson. Med.*, vol. 44, no. 3, pp. 433–439, 2000.
[115] J. Pellico, C. M. Ellis, and J. J. Davis, "Nanoparticle-Based Paramagnetic Contrast Agents for Magnetic Resonance Imaging," *Contrast Media Mol. Imaging*, vol. 2019, 2019.
[116] A. I. Journal, N. Naseri, E. Ajorlou, F. Asghari, and Y. Pilehvar-Soltanahmadi, "An update on nanoparticle-based contrast agents in medical imaging," *Nanomedicine, Biotechnol.*, vol. 46, no. 6, pp. 1111–1121, 2018.
[117] I. Milosevic, L. Motte, B. Aoun, T. Li, *et al.*, "Effects of coating spherical iron oxide nanoparticles," *Biochim. Biophys. Acta - Gen. Subj.*, vol. 1861, no. 1, pp. 3621–3626, Jan. 2017.
[118] R. Weissleder, G. Elizondo, J. Wittenberg, C. A. Rabito, *et al.*, "Ultrasmall superparamagnetic iron oxide: Characterization of a new class of contrast agents for MR imaging," *Radiology*, vol. 175, no. 2, pp. 489–493, May 1990.
[119] M. Gkagkanasiou, A. Ploussi, M. Gazouli, and E. P. Efstathopoulos, "USPIO-Enhanced MRI Neuroimaging: A Review," *J Neuroimaging*, vol. 26, no. 2, pp. 161–168, 2016.
[120] S. R. Alam, C. Stirrat, J. Richards, S. Mirsadraee, *et al.*, "Vascular and plaque imaging with ultrasmall superparamagnetic particles of iron oxide," *J. Cardiovasc. Magn. Reson.*, vol. 17, no. 1, p. 83, Dec. 2015.

[121] Y. X. J. Wáng and J.-M. Idée, “A comprehensive literatures update of clinical researches of superparamagnetic resonance iron oxide nanoparticles for magnetic resonance imaging,” *Quant. Imaging Med. Surg.*, vol. 7, no. 1, pp. 88–122, 2017.
[122] D. J. Korchinski, M. Taha, R. Yang, N. Nathoo, and J. F. Dunn, “Iron Oxide as an Mri Contrast Agent for Cell Tracking: Supplementary Issue,” *Magn. Reson. Insights*, no. 8, pp. 15–29, 2015.
[123] D. H. Murrell, N. Zarghami, M. D. Jensen, F. Dickson, *et al.*, “MRI surveillance of cancer cell fate in a brain metastasis model after early radiotherapy,” *Magn. Reson. Med.*, vol. 00, no. October, pp. 1–7, 2016.
[124] S. Namkung, C. J. Zech, T. Helmberger, M. F. Reiser, and S. O. Schoenberg, “Superparamagnetic iron oxide (SPIO)-enhanced liver MRI with ferucarbotran: Efficacy for characterization of focal liver lesions,” *J. Magn. Reson. Imaging*, vol. 25, no. 4, pp. 755–765, Apr. 2007.
[125] S. N. Gandhi, M. A. Brown, J. G. Wong, D. A. Aguirre, and C. B. Sirlin, “MR Contrast Agents for Liver Imaging: What, When, How,” *RadioGraphics*, vol. 26, no. 6, pp. 1621–1636, Nov. 2006.
[126] F. Goodfellow, G. A. Simchick, L. J. Mortensen, S. L. Stice, and Q. Zhao, “Tracking and Quantification of Magnetically Labeled Stem Cells using Magnetic Resonance Imaging,” *Adv. Funct. Mater.*, vol. 26, no. 22, p. 3899, 2016.
[127] E. M. Shapiro, S. Skrtic, and A. P. Koretsky, “Sizing it up: Cellular MRI using micron-sized iron oxide particles,” *Magn. Reson. Med.*, vol. 53, no. 2, pp. 329–338, 2005.
[128] E. M. Shapiro, S. Skrtic, K. Sharer, J. M. Hill, *et al.*, “MRI detection of single particles for cellular imaging.,” *Proc. Natl. Acad. Sci. U. S. A.*, vol. 101, no. 30, pp. 10901–10906, 2004.
[129] C. Heyn, C. V. Bowen, B. K. Rutt, and P. J. Foster, “Detection threshold of single SPIO-labeled cells with FIESTA,” *Magn. Reson. Med.*, vol. 53, no. 2, pp. 312–320, 2005.
[130] M. M. Chaumeil, B. Gini, H. Yang, A. Iwanami, *et al.*, “Longitudinal evaluation of MPIO-labeled stem cell biodistribution in glioblastoma using high resolution and contrast-enhanced MR imaging at 14.1Tesla,” *Neuro. Oncol.*, vol. 14, no. 8, pp. 1050–1061, 2012.
[131] Y. Yang, Y. Yang, N. Yanasak, A. Schumacher, and T. C. C. Hu, “Temporal and noninvasive monitoring of inflammatory-cell infiltration to myocardial infarction sites using micrometer-sized iron oxide particles,” *Magn. Reson. Med.*, vol. 63, no. 1, pp. 33–40, 2010.
[132] S. Melemenidis, A. Jefferson, N. Ruparelia, A. M. Akhtar, *et al.*, “Molecular magnetic resonance imaging of angiogenesis in vivo using polyvalent cyclic RGD-iron oxide microparticle conjugates,” *Theranostics*, vol. 5, no. 5, pp. 515–529, 2015.
[133] L. Liu, T. K. Hitchens, Q. Ye, Y. Wu, *et al.*, “Decreased reticuloendothelial system clearance and increased blood half-life and immune cell labeling for nano- and micron-sized superparamagnetic iron-oxide particles upon pre-treatment with Intralipid,” *Biochim. Biophys. Acta - Gen. Subj.*, vol. 1830, no. 6, pp. 3447–3453, 2013.
[134] F. Perez-Balderas, S. I. van Kasteren, A. A. A. Aljabali, K. Wals, *et al.*, “Covalent assembly of nanoparticles as a peptidase-degradable platform for molecular MRI,” *Nat. Commun.*, vol. 8, p. 14254, 2017.
[135] A. Jefferson, R. S. Wijesurendra, M. A. McAteer, J. E. Digby, *et al.*, “Molecular imaging with optical coherence tomography using ligand-conjugated microparticles that detect activated endothelial cells: Rational design through target quantification,” *Atherosclerosis*, vol. 219, no. 2, pp. 579–587, 2011.
[136] W. Y. K. Hwang and J. Foote, “Immunogenicity of engineered antibodies,” *Methods*, vol. 36, no. 1, pp. 3–10, May 2005.
[137] S. Serres, D. C. Anthony, Y. Jiang, K. A. Broom, *et al.*, “Systemic inflammatory response reactivates immune-mediated lesions in rat brain,” *J. Neurosci.*, vol. 29, no. 15, pp. 4820–4828, 2009.

[138] N. Sibson, D. Anthony, S. van Kasteren, A. Dickens, *et al.*, "Molecular MRI Approaches to the Detection of CNS Inflammation," in *Magnetic Resonance Neuroimaging*, 2010, pp. 397–396.
[139] M. a Mcateer, N. R. Sibson, C. Von Mühlen, J. E. Schneider, *et al.*, "In vivo magnetic resonance imaging of acute brain inflammation using microparticles of iron oxide," *Nat Med*, vol. 13, no. 10, pp. 1253–1258, 2007.
[140] A. Montagne, M. Gauberti, R. Macrez, A. Jullienne, *et al.*, "Ultra-sensitive molecular MRI of cerebrovascular cell activation enables early detection of chronic central nervous system disorders," *Neuroimage*, vol. 63, no. 2, pp. 760–770, 2012.
[141] L. C. Hoyte, K. J. Brooks, S. Nagel, A. Akhtar, *et al.*, "Molecular magnetic resonance imaging of acute vascular cell adhesion molecule-1 expression in a mouse model of cerebral ischemia," *J. Cereb. Blood Flow Metab.*, vol. 30, no. 6, pp. 1178–1187, 2010.
[142] M. Gauberti, A. Montagne, O. A. Marcos-Contreras, A. Le Béhot, *et al.*, "Ultra-sensitive molecular MRI of vascular cell adhesion molecule-1 reveals a dynamic inflammatory penumbra after strokes," *Stroke*, vol. 44, no. 7, pp. 1988–1996, 2013.
[143] S. Serres, S. Mardiguian, and S. Campbell, "VCAM-1-targeted magnetic resonance imaging reveals subclinical disease in a mouse model of multiple sclerosis," *FASEB J.*, vol. 25, no. 12, pp. 4415–4422, 2011.
[144] L. H. Deddens, G. A. F. van Tilborg, K. van der Marel, H. Hunt, *et al.*, "In Vivo Molecular MRI of ICAM-1 Expression on Endothelium and Leukocytes from Subacute to Chronic Stages After Experimental Stroke," *Transl. Stroke Res.*, vol. 8, no. 5, pp. 440–448, 2017.
[145] L. H. Deddens, G. A. F. Van Tilborg, A. Van Der Toorn, K. Van Der Marel, *et al.*, "MRI of ICAM-1 upregulation after stroke: The importance of choosing the appropriate target-specific particulate contrast agent," *Mol. Imaging Biol.*, vol. 15, no. 4, pp. 411–422, 2013.
[146] E. L. A. Blezer, L. H. Deddens, G. Kooij, J. Drexhage, *et al.*, "*In vivo* MR imaging of intercellular adhesion molecule-1 expression in an animal model of multiple sclerosis," *Contrast Media Mol. Imaging*, vol. 10, no. 2, pp. 111–121, 2015.
[147] A. P. Fournier, A. Quenault, S. M. De Lizarrondo, M. Gauberti, *et al.*, "Prediction of disease activity in models of multiple sclerosis by molecular magnetic resonance imaging of P-selectin," *Proc. Natl. Acad. Sci. U. S. A.*, vol. 114, no. 23, pp. 6116–6121, 2017.
[148] C. Von Zur Muhlen, N. R. Sibson, K. Peter, S. J. Campbell, *et al.*, "A contrast agent recognizing activated platelets reveals murine cerebral malaria pathology undetectable by conventional MRI," *J. Clin. Invest.*, vol. 118, 2008.
[149] C. Chapon, F. Franconi, F. Lacoeuille, F. Hindré, *et al.*, "Imaging E-selectin expression following traumatic brain injury in the rat using a targeted USPIO contrast agent," *Magn. Reson. Mater. Physics, Biol. Med.*, vol. 22, no. 3, pp. 167–174, 2009.
[150] M. Fréchou, V. Beray-Berthat, J.-S. Raynaud, S. Mériaux, *et al.*, "Detection of vascular cell adhesion molecule-1 expression with USPIO-enhanced molecular MRI in a mouse model of cerebral ischemia," *Contrast Media Mol. Imaging*, vol. 8, no. 2, pp. 157–164, 2013.
[151] A. K. Bindal, R. K. Bindal, K. R. Hess, A. Shiu, *et al.*, "Surgery versus radiosurgery in the treatment of brain metastasis," *J. Neurosurg.*, vol. 84, no. 5, pp. 748–754, 1996.
[152] P. Workman, E. O. Aboagye, F. Balkwill, A. Balmain, *et al.*, "Guidelines for the welfare and use of animals in cancer research," *British Journal of Cancer*. pp. 1555–1557, 2010.
[153] G. E. Orchard, "Heavily pigmented melanocytic neoplasms: comparison of two melanin-bleaching techniques and subsequent immunohistochemical staining," *Br. J. Biomed. Sci.*, vol. 56, pp. 188–193, 1999.
[154] G. E. Orchard, "Use of heat provides a fast and efficient way to undertake melanin bleaching with dilute hydrogen peroxide," *Br. J. Biomed. Sci.*, vol. 64, no. 2, pp. 89–91, 2007.

[155] V. Kersemans, S. Gilchrist, S. Wallington, P. D. Allen, *et al.*, "A Carbon-Fiber Sheet Resistor for MR-, CT-, SPECT-, and PET-Compatible Temperature Maintenance in Small Animals," *Tomogr. (Ann Arbor, Mich.)*, vol. 5, no. 2, pp. 274–281, Jun. 2019.
[156] S. Gilchrist, A. L. Gomes, P. Kinchesh, V. Kersemans, *et al.*, "An MRI-compatible high frequency AC resistive heating system for homeothermic maintenance in small animals," *PLoS One*, vol. 11, no. 11, Nov. 2016.
[157] J. W. M. Bulte and D. L. Kraitchman, "Iron oxide MR contrast agents for molecular and cellular imaging," *NMR Biomed.*, vol. 17, no. 7, pp. 484–499, 2004.
[158] D. J. Korchinski, M. Taha, R. Yang, N. Nathoo, and J. F. Dunn, "Iron Oxide as an MRI Contrast Agent for Cell Tracking," vol. 8, pp. 15–29, 2015.
[159] S. J. Dodd, M. Williams, J. P. Suhan, D. S. Williams, *et al.*, "Detection of single mammalian cells by high-resolution magnetic resonance imaging.," *Biophys. J.*, vol. 76, no. 1 Pt 1, pp. 103–9, 1999.
[160] A. K. Gupta and M. Gupta, "Synthesis and surface engineering of iron oxide nanoparticles for biomedical applications," *Biomaterials*, vol. 26, no. 18, pp. 3995–4021, 2004.
[161] G. Stoll and M. Bendszus, "New approaches to neuroimaging of central nervous system inflammation.," *Curr. Opin. Neurol.*, no. 3, pp. 282–6, 2010.
[162] R. Weissleder, A. Bogdanov, E. A. Neuwelt, and M. Papisov, "Long-circulating iron oxides for MR imaging," *Adv. Drug Deliv. Rev.*, vol. 16, no. 2–3, pp. 321–334, 1995.
[163] F. Deckers, B. Corthouts, Y. Nackaerts, O. Ozsarlak, *et al.*, "Original article The influence of MR field strength on the detection of focal liver lesions with superparamagnetic iron oxide," vol. 892, no. May 1996, pp. 887–892, 1997.
[164] C. T. Farrar, G. Dai, M. Novikov, A. Rosenzweig, *et al.*, "Impact of field strength and iron oxide nanoparticle concentration on the linearity and diagnostic accuracy of off-resonance imaging," vol. 21, no. 5, pp. 453–463, 2009.
[165] A. Tanimoto and S. Kuribayashi, "Application of superparamagnetic iron oxide to imaging of hepatocellular carcinoma," *Eur. J. Radiol.*, vol. 58, no. 2, pp. 200–216, 2006.
[166] O. M. Girard, J. Du, L. Agemy, K. N. Sugahara, *et al.*, "Optimization of iron oxide nanoparticle detection using ultrashort echo time pulse sequences: Comparison of T1, T2*, and synergistic T1 - T2* contrast mechanisms," *Magn. Reson. Med.*, vol. 65, no. 6, pp. 1649–1660, 2011.
[167] J. Huang, X. Zhong, L. Wang, L. Yang, and H. Mao, "Improving the magnetic resonance imaging contrast and detection methods with engineered magnetic nanoparticles," *Theranostics*, vol. 2, no. 1. pp. 86–102, 2012.
[168] K. Scheffler and S. Lehnhardt, "Principles and applications of balanced SSFP techniques," *Eur. Radiol.*, vol. 13, no. 11, pp. 2409–2418, 2003.
[169] D. H. Murrell, N. Zarghami, M. D. Jensen, A. F. Chambers, *et al.*, "Evaluating changes to blood-brain barrier integrity in brain metastasis over time and after radiation treatment," *Transl. Oncol.*, vol. 9, no. 3, pp. 219–227, 2016.
[170] S. H. Kim, S. N. Oh, H. S. Choi, H. S. Lee, *et al.*, "USPIO enhanced lymph node MRI using 3D multi-echo GRE in a rabbit model," *Contrast Media Mol. Imaging*, vol. 11, no. 6, pp. 544–549, 2016.
[171] L. Zheng, Z. Zhang, K. Khazaie, S. Saha, *et al.*, "MRI-monitored intra-tumoral injection of iron-oxide labeled Clostridium novyi-NT anaerobes in pancreatic carcinoma mouse model," *PLoS One*, vol. 9, no. 12, pp. 1–15, 2014.
[172] H. Wei, O. T. Bruns, M. G. Kaul, E. C. Hansen, *et al.*, "Exceedingly small iron oxide nanoparticles as positive MRI contrast agents," *Proc. Natl. Acad. Sci.*, vol. 114, no. 9, pp. 2325–2330, 2017.
[173] M. C. Evans, S. Serres, A. A. Khrapitchev, H. B. Stolp, *et al.*, "T_2-weighted MRI detects presymptomatic pathology in the SOD1 mouse model of ALS.," *J. Cereb. Blood Flow Metab.*, vol. 34, no. February, pp. 785–793, 2014.
[174] M. Gauberti, A. Montagne, A. Quenault, and D. Vivien, "Molecular magnetic resonance

imaging of brain-immune interactions.," *Front. Cell. Neurosci.*, vol. 8, no. November, p. 389, 2014.
[175] M. A. McAteer, K. Mankia, N. Ruparelia, A. Jefferson, *et al.*, "A leukocyte-mimetic magnetic resonance imaging contrast agent homes rapidly to activated endothelium and tracks with atherosclerotic lesion macrophage content," *Arterioscler. Thromb. Vasc. Biol.*, vol. 32, no. 6, pp. 1427–1435, 2012.
[176] E. M. Shapiro and A. P. Koretsky, "Micron-Sized Iron Oxide Particles (MPIOs) for Cellular Imaging: More Bang for the Buck," *Nanoparticles Biomed. Imaging*, pp. 141–161, 2008.
[177] C. Tassa, J. L. Duffner, T. A. Lewis, R. Weissleder, *et al.*, "Binding Affinity and Kinetic Analysis of Targeted Small Molecule-Modified," vol. 12, pp. 14–19, 2010.
[178] M. J. Pittet, F. K. Swirski, F. Reynolds, L. Josephson, and R. Weissleder, "Labeling of immune cells for in vivo imaging using magnetofluorescent nanoparticles.," *Nat. Protoc.*, vol. 1, no. 1, pp. 73–79, 2006.
[179] M. A. T. Bisschops, K. C. A. M. Luyben, and L. A. M. Van Der Wielen, "Generalized Maxwell-Stefan approach for swelling kinetics of dextran gels," *Ind. Eng. Chem. Res.*, vol. 37, no. 8, pp. 3312–3322, 1998.
[180] P. Wunderbaldinger, L. Josephson, and R. Weissleder, "Tat peptide directs enhanced clearance and hepatic permeability of magnetic nanoparticles," *Bioconjug. Chem.*, vol. 13, no. 2, pp. 264–268, 2002.
[181] K. A. Kelly, J. R. Allport, A. Tsourkas, V. R. Shinde-Patil, *et al.*, "Detection of vascular adhesion molecule-1 expression using a novel multimodal nanoparticle," *Circ. Res.*, vol. 96, no. 3, pp. 327–336, 2005.
[182] S. H. Kim, D. Choi, J. H. Lim, W. J. Lee, *et al.*, "Optimal Pulse Sequence for Ferumoxides-Enhanced MR Imaging Used in the Detection of Hepatocellular Carcinoma: A Comparative Study Using Seven Pulse Sequences," *Korean J. Radiol.*, vol. 3, no. 2, pp. 87–97, 2002.
[183] N. Schieda, L. Avruch, W. M. Shabana, and S. C. Malone, "Multi-echo gradient recalled echo imaging of the pelvis for improved depiction of brachytherapy seeds and fiducial markers facilitating radiotherapy planning and treatment of prostatic carcinoma," *J. Magn. Reson. Imaging*, vol. 41, no. 3, pp. 715–720, 2015.
[184] N. Martin, D. Malfair, Y. Zhao, D. Li, *et al.*, "Comparison of MERGE and axial T2-weighted fast spin-echo sequences for detection of multiple sclerosis lesions in the cervical spinal cord," *Am. J. Roentgenol.*, vol. 199, no. 1, pp. 157–162, 2012.
[185] N. K. Bangerter, B. A. Hargreaves, S. S. Vasanawala, J. M. Pauly, *et al.*, "Analysis of Multiple-Acquisition SSFP," *Magn. Reson. Med.*, vol. 51, no. 5, pp. 1038–1047, 2004.
[186] E. J. Ribot, D. Wecker, A. J. Trotier, B. Dallaudiere, *et al.*, "Water selective imaging and bSSFP banding artifact correction in humans and small animals at 3T and 7T, respectively," *PLoS One*, vol. 10, no. 10, pp. 1–16, 2015.
[187] S. Chen, F. Reynolds, L. Yu, R. Weissleder, and L. Josephson, "A screening paradigm for the design of improved polymer-coated superparamagnetic iron oxide nanoparticles," *J. Mater. Chem.*, vol. 19, no. 35, p. 6387, 2009.
[188] S. Delangre, Q. L. Vuong, D. Henrard, C. Po, *et al.*, "Bottom-up study of the MRI positive contrast created by the Off-Resonance Saturation sequence," *J. Magn. Reson.*, vol. 254, pp. 98–109, 2015.
[189] P. Reimer and T. Balzer, "Ferucarbotran (Resovist): a new clinically approved RES-specific contrast agent for contrast-enhanced MRI of the liver: properties, clinical development, and applications," *Eur. Radiol.*, vol. 13, no. 6, pp. 1266–1276, 2003.
[190] A. J. W. van der Kouwe, T. Benner, D. H. Salat, and B. Fischl, "Brain morphometry with multiecho MPRAGE," *Neuroimage*, vol. 40, no. 2, pp. 559–569, 2008.
[191] J. S. Choi, M. J. Kim, J. H. Kim, J. Y. Choi, *et al.*, "Comparison of multi-echo and single-echo gradient-recalled echo sequences for SPIO-enhanced Liver MRI at 3 T," *Clin. Radiol.*, vol. 65, no. 11, pp. 916–923, 2010.
[192] C. L. Mallett and P. J. Foster, "Optimization of the balanced steady state free precession

(bSSFP) pulse sequence for magnetic resonance imaging of the mouse prostate at 3T," *PLoS One*, vol. 6, no. 4, pp. 3–8, 2011.
[193] M. W. DiFrancesco, J. M. Rasmussen, W. Yuan, R. Pratt, *et al.*, "Comparison of SNR and CNR for in vivo mouse brain imaging at 3 and 7 T using well matched scanner configurations," *Med. Phys.*, vol. 35, no. 9, pp. 3972–3978, 2008.
[194] J. Biswas, C. B. Nelson, V. M. Runge, B. J. Wintersperger, *et al.*, "Brain tumor enhancement in magnetic resonance imaging: Comparison of signal-to-noise ratio (SNR) and contrast-to-noise ratio (CNR) at 1.5 versus 3 tesla," *Invest. Radiol.*, vol. 40, no. 12, pp. 792–797, 2005.
[195] K. Ley, C. Laudanna, M. I. Cybulsky, and S. Nourshargh, "Getting to the site of inflammation: the leukocyte adhesion cascade updated," *Nat. Rev. Immunol.*, vol. 7, no. 9, pp. 678–689, 2007.
[196] N. R. Sibson, A. M. Blamire, M. Bernades-Silva, S. Laurent, *et al.*, "MRI Detection of Early Endothelial Activation in Brain Inflammation," *Magn. Reson. Med.*, vol. 51, no. 2, pp. 248–252, 2004.
[197] S. Serres, S. Mardiguian, S. J. Campbell, M. A. McAteer, *et al.*, "VCAM-1-targeted magnetic resonance imaging reveals subclinical disease in a mouse model of multiple sclerosis.," *FASEB J.*, vol. 25, no. 12, pp. 4415–22, 2011.
[198] S. Mardiguian, S. Serres, E. Ladds, S. J. Campbell, *et al.*, "Anti-IL-17A treatment reduces clinical score and VCAM-1 expression detected by in vivo magnetic resonance imaging in chronic relapsing EAE ABH mice," *Am. J. Pathol.*, vol. 182, no. 6, pp. 2071–2081, 2013.
[199] A. M. Akhtar, J. E. Schneider, S. J. Chapman, A. Jefferson, *et al.*, "In vivo quantification of VCAM-1 expression in renal ischemia reperfusion injury using non-invasive magnetic resonance molecular imaging," *PLoS One*, vol. 5, no. 9, p. e12800, 2010.
[200] M.-A. Lécuyer, O. Saint-Laurent, L. Bourbonnière, S. Larouche, *et al.*, "Dual role of ALCAM in neuroinflammation and blood–brain barrier homeostasis," *Proc. Natl. Acad. Sci.*, vol. 114, no. 4, pp. E524–E533, 2017.
[201] N. Zarghami, A. A. Khrapitchev, F. Perez-balderas, M. S. Soto, *et al.*, "Optimization of molecularly targeted MRI in the brain : empirical comparison of sequences and particles," pp. 4345–4359, 2018.
[202] R. Cayrol, K. Wosik, J. L. Berard, A. Dodelet-Devillers, *et al.*, "Activated leukocyte cell adhesion molecule promotes leukocyte trafficking into the central nervous system.," *Nat. Immunol.*, vol. 9, no. 2, pp. 137–45, 2008.
[203] Smith, "Expression and regulation of activated leukocyte cell adhesion molecule in human retinal vascular endothelial cells," *Exp Eye Res*, vol. 29, no. 6, pp. 997–1003, 2012.
[204] P. Adisakwattana, N. Suwandittakul, S. Petmitr, S. Wongkham, *et al.*, "ALCAM is a novel cytoplasmic membrane protein in TNF-α stimulated invasive cholangiocarcinoma cells," *Asian Pacific J. Cancer Prev.*, vol. 16, no. 9, pp. 3849–3856, 2015.
[205] A. G. Hansen, S. A. Arnold, M. Jiang, T. D. Palmer, *et al.*, "ALCAM/CD166 is a TGF-b-responsive marker and functional regulator of prostate cancer metastasis to bone," *Cancer Res.*, vol. 74, no. 5, pp. 1404–1415, 2014.
[206] L. Xu, A. Nirwane, and Y. Yao, "Basement membrane and blood-brain barrier," *Stroke and Vascular Neurology*, vol. 4, no. 2. pp. 78–82, 2019.
[207] S. G. Patching, "Glucose Transporters at the Blood-Brain Barrier: Function, Regulation and Gateways for Drug Delivery," *Molecular Neurobiology*, vol. 54, no. 2. Humana Press Inc., pp. 1046–1077, 01-Mar-2017.
[208] M. P. Pusztaszeri, W. Seelentag, and F. T. Bosman, "Immunohistochemical expression of endothelial markers CD31, CD34, von Willebrand factor, and Fli-1 in normal human tissues," *J. Histochem. Cytochem.*, vol. 54, no. 4, pp. 385–395, Apr. 2006.
[209] N. V. Goncharov, A. D. Nadeev, R. O. Jenkins, and P. V. Avdonin, "Markers and Biomarkers of Endothelium: When Something Is Rotten in the State," *Oxidative*

Medicine and Cellular Longevity, vol. 2017. Hindawi Limited, 2017.
[210] M. P. Bevilacqua, "ENDOTHELIAL-LEUKOCYTE ADHESION MOLECULES," *Annu. Rev. Immunol.*, vol. 11, pp. 767–804, 1993.
[211] E. Jubeli, L. Moine, J. Vergnaud-Gauduchon, and G. Barratt, "E-selectin as a target for drug delivery and molecular imaging," *J. Control. Release*, vol. 158, no. 2, pp. 194–206, 2012.
[212] T. Garrood, M. Blades, D. O. Haskard, S. Mather, and C. Pitzalis, "A novel model for the pre-clinical imaging of inflamed human synovial vasculature."
[213] H. Hong, F. Chen, Y. Zhang, and W. Cai, "New Radiotracers for Imaging of Vascular Targets in Angiogenesis-related Diseases," 2014.
[214] J. M. Runnels, P. Zamiri, J. A. Spencer, I. Veilleux, *et al.*, "Imaging Molecular Expression on Vascular Endothelial Cells by In Vivo Immunofluorescence Microscopy."
[215] I. Spivak, A. Rix, G. Schmitz, S. Fokong, *et al.*, "Low-Dose Molecular Ultrasound Imaging with E-Selectin-Targeted PBCA Microbubbles," *Mol Imaging Biol*, vol. 18, pp. 180–190, 2016.
[216] P. A. Barber, T. Foniok, D. Kirk, A. M. Buchan, *et al.*, "MR molecular imaging of early endothelial activation in focal ischemia," *Ann. Neurol.*, vol. 56, no. 1, pp. 116–120, Jul. 2004.
[217] S. I. Van Kasteren, S. J. Campbell, S. Serres, D. C. Anthony, *et al.*, "Glyconanoparticles allow pre-symptomatic in vivo imaging of brain disease," *Proc. Natl. Acad. Sci. U. S. A.*, vol. 106, no. 1, pp. 18–23, 2009.
[218] C. W. Wyble, K. L. Hynes, J. Kuchibhotla, B. C. Marcus, *et al.*, "TNF-α and IL-1 upregulate membrane-bound and soluble E-selectin through a common pathway," *J. Surg. Res.*, vol. 73, no. 2, pp. 107–112, 1997.
[219] B. J. Ballermann, A. Dardik, E. Eng, and A. Liu, "Shear stress and the endothelium," in *Kidney International, Supplement*, 1998, vol. 54, no. 67, pp. S100–S108.
[220] J. J. Chiu and S. Chien, "Effects of disturbed flow on vascular endothelium: Pathophysiological basis and clinical perspectives," *Physiological Reviews*, vol. 91, no. 1. NIH Public Access, pp. 327–387, Jan-2011.
[221] N. Zarghami, "BioRender.com." .
[222] M. Nava Catorce and G. Gevorkian, "LPS-induced Murine Neuroinflammation Model: Main Features and Suitability for Pre-clinical Assessment of Nutraceuticals," *Curr. Neuropharmacol.*, vol. 14, no. 2, pp. 155–164, 2016.
[223] A. Vezzani, S. Balosso, and T. Ravizza, "Neuroinflammatory pathways as treatment targets and biomarkers in epilepsy," *Nat. Rev. Neurol.*, 2019.
[224] C. Yang, K. E. Hawkins, S. Doré, and E. Candelario-Jalil, "Neuroinflammatory mechanisms of blood-brain barrier damage in ischemic stroke," *Am. J. Physiol. - Cell Physiol.*, vol. 316, no. 2, pp. C135–C153, 2019.
[225] H. Läubli and L. Borsig, "Selectins as Mediators of Lung Metastasis," in *Cancer Microenvironment*, 2010, vol. 3, no. 1, pp. 97–105.
[226] M. Esposito, N. Mondal, T. M. Greco, Y. Wei, *et al.*, "Bone vascular niche E-selectin induces mesenchymal–epithelial transition and Wnt activation in cancer cells to promote bone metastasis," *Nat. Cell Biol.*, vol. 21, no. 5, pp. 627–639, May 2019.
[227] S. Hiratsuka, S. Goel, W. S. Kamoun, Y. Maru, *et al.*, "Endothelial focal adhesion kinase mediates cancer cell homing to discrete regions of the lungs via E-selectin up-regulation," *Proc. Natl. Acad. Sci. U. S. A.*, vol. 108, no. 9, pp. 3725–3730, Mar. 2011.
[228] R. P. McEver and C. Zhu, "Rolling Cell Adhesion," *Annu. Rev. Cell Dev. Biol.*, vol. 26, no. 1, pp. 363–396, Nov. 2010.
[229] E. B. Ehlerding, L. Sun, X. Lan, D. Zeng, and W. Cai, "Dual-targeted molecular imaging of cancer," *J. Nucl. Med.*, vol. 59, no. 3, pp. 390–395, 2018.
[230] R. S. Wijesurendra, A. Jefferson, and R. P. Choudhury, "Target: ligand interactions of the vascular endothelium. Implications for molecular imaging in inflammation.," *Integr. Biol. (Camb).*, vol. 2, pp. 467–482, 2010.

[231] K.-H. Song, B. K. Harvey, and M. A. Borden, "State-of-the-art of microbubble-assisted blood-brain barrier disruption.," *Theranostics*, vol. 8, no. 16, pp. 4393–4408, 2018.
[232] B. Luigi Biancone, M. Araki, K. Araki, and I. Stamenkovic, "Redirection of Tumor Metastasis by Expression of E-Selectin In Vivo," 1996.
[233] L. Zhong, B. Simoneau, P.-L. Tremblay, S. Gout, *et al.*, "E-Selectin-Mediated Adhesion and Extravasation in Cancer," in *Encyclopedia of Cancer*, 2014, pp. 1618–1624.
[234] S. Köhler, S. Ullrich, U. Richter, and U. Schumacher, "E-/P-selectins and colon carcinoma metastasis: first in vivo evidence for their crucial role in a clinically relevant model of spontaneous metastasis formation in the lung," *Br. J. Cancer*, vol. 102, no. 3, pp. 602–609, Feb. 2010.
[235] A. Gehad, M. Lichtman, C. Schmults, J. E. Teague, *et al.*, "Nitric oxide-producing myeloid-derived suppressor cells inhibit vascular E- selectin expression in human squamous cell carcinomas," *J. Invest. Dermatol.*, vol. 132, no. 11, p. 2642, 2012.
[236] S. Chien, S. U. Haq, M. Pawlus, R. T. Moon, *et al.*, "Adhesion Of Acute Myeloid Leukemia Blasts To E-Selectin In The Vascular Niche Enhances Their Survival By Mechanisms Such As Wnt Activation," *Blood*, vol. 122, no. 21, p. 61, 2013.
[237] A. Natoni, M. S. Macauley, and M. E. O'Dwyer, "Targeting selectins and their ligands in cancer," *Frontiers in Oncology*, vol. 6, no. APR. Frontiers Media SA, p. 93, 2016.
[238] D. H. Murrell, A. M. Hamilton, C. L. Mallett, R. van Gorkum, *et al.*, "Understanding Heterogeneity and Permeability of Brain Metastases in Murine Models of HER2-Positive Breast Cancer Through Magnetic Resonance Imaging: Implications for Detection and Therapy," *Transl. Oncol.*, vol. 8, no. 3, pp. 176–184, 2015.
[239] T. G. Simonsen, J.-V. Gaustad, and E. K. Rofstad, "Intertumor heterogeneity in vascularity and invasiveness of artificial melanoma brain metastases," 2015.
[240] F. Thorsen, B. Fite, M. Mahakia, J. Seo, *et al.*, "Multimodal imaging enables early detection and characterization of changes in tumor permeability of brain metastases," *Control. Release*, vol. 172, no. 3, pp. 812–822, 2014.
[241] M. Singh, C. Venugopal, T. Tokar, N. Mcfarlane, *et al.*, "Therapeutic targeting of the pre-metastatic stage in human lung-to-brain metastasis Running Title: Targeting of Pre-metastasis," 2018.
[242] C. H. Han and P. K. Brastianos, "Genetic Characterization of Brain Metastases in the Era of Targeted Therapy.," *Front. Oncol.*, vol. 7, p. 230, 2017.
[243] A. Varrone, V. Oikonen, A. Forsberg, J. Joutsa, *et al.*, "Positron emission tomography imaging of the 18-kDa translocator protein (TSPO) with [18 F]FEMPA in Alzheimer's disease patients and control subjects," *Eur J Nucl Med Mol Imaging*, vol. 42, pp. 438–446, 2015.
[244] E. Herranz, C. Giannì, C. Louapre, C. A. Treaba, *et al.*, "The neuroinflammatory component of gray matter pathology in multiple sclerosis HHS Public Access."
[245] J. Park, J. Kim, E. Yoo, H. Lee, *et al.*, "Detection of small metastatic brain tumors: comparison of 3D contrast-enhanced whole-brain black-blood imaging and MP-RAGE imaging.," *Invest. Radiol.*, vol. 47, no. 2, pp. 136–41, Feb. 2012.
[246] B. Rossi, S. Angiari, E. Zenaro, S. L. Budui, and G. Constantin, "Vascular inflammation in central nervous system diseases: adhesion receptors controlling leukocyte-endothelial interactions," *J. Leukoc. Biol*, vol. 89, pp. 539–556, 2011.
[247] S. Richard, L. Lagerstedt, P. R. Burkhard, M. Debouverie, *et al.*, "E-selectin and vascular cell adhesion molecule-1 as biomarkers of 3-month outcome in cerebrovascular diseases," 2015.
[248] S. J. Mills, G. Thompson, and A. Jackson, "Advanced magnetic resonance imaging biomarkers of cerebral metastases," *Cancer Imaging*, vol. 12, pp. 245–252, 2012.
[249] P. Donizy, M. Zietek, A. Halon, M. Leskiewicz, *et al.*, "Prognostic significance of ALCAM (CD166/ MEMD) expression in cutaneous melanoma patients," 2015.
[250] M. Ihnen, N. Köhler, J. F. Kersten, K. Milde-Langosch, *et al.*, "Expression levels of Activated Leukocyte Cell Adhesion Molecule (ALCAM/CD166) in primary breast carcinoma and distant breast cancer metastases," *Dis. Markers*, vol. 28, pp. 71–78,

2010.
[251] F. Franchino, R. Rudà, and R. Soffietti, “Mechanisms and Therapy for Cancer Metastasis to the Brain,” *Front. Oncol.*, vol. 8, p. 161, May 2018.

Appendices

Appendix A

The results presented in Appendix A were acquired as a part for the following study: S. Melemenidis, J.C. Knight, V. Kersemans, F. Perez-Balderas, N. Zarghami, M. Sarmiento Soto, B. Cornelissen, R.J. Muschel and N.R. Sibson as "*In vivo* PET detection of lung micrometastases by targeting endothelial VCAM-1" *under review* in the European Journal of Nuclear Medicine and Molecular Imaging.

A.1 Introduction

One of the limiting factors for the use of MPIO for molecular imaging applications is the possible iron toxicity. The dose of 4 mg Fe/kg body weight is usually used in preclinical models for targeted MRI applications [1], [2]. This dose is similar to the 2.6 mg Fe/kg body weight USPIO used for oncological imaging in humans [3], [4]. However, lower doses of iron (2 mg Fe/kg weight) have been suggested to be insufficient for discernible contrast on MRI in a mouse neuroinflammation model [5]. In the following study, the sensitivity of a reduced iron dose of VCAM-MPIO was tested for detection of brain micrometastases in a mouse syngeneic model.

A.2 Methods

Female BALB/c mice (7-10 weeks old, n = 4; Charles River, UK) were anaesthetised with isoflurane (2.0-3.0%) in oxygen. Mice were injected intracardially with 5×10^4 4T1-GFP (murine mammary carcinoma) into the left ventricle under ultrasound guidance to induce brain metastases, as described previously in the Methods chapter Section 2.4.2.2. The same mice were also injected with 5×10^4 4T1-GFP cells intravenously via a tail vein to develop lung metastases. This Appendix focuses on the brain metastasis formation in this model.

At day 14 after tumour cell injection, mice were anaesthetised and injected intravenously via a tail vein with VCAM-MPIO* (MyOne Tosylactivated Dynabeads, 1.6 mg Fe/kg in 100 µl sterile PBS). MRI data were acquired using a 9.4 T horizontal, wide-bore superconductive MRI system (Agilent Technologies Inc., Santa Clara, CA, USA). Approximately 1 hour after contrast agent administration, mice were imaged with T_2*W-MGE3D to detect bound MPIO in the brain. Following MRI, mice were perfusion-fixed, and brains were taken for immunohistochemistry. Sections were cut and stained for immunohistochemical detection of VCAM-1 on tumour associated vessels and their co-localisation with VCAM-MPIO.

A.3 Results and Discussion

In all tumour bearing mice, focal hypointensities were detected on T_2*W-MGE3D images, indicating binding of VCAM-MPIO, in accord with previous findings using VCAM-MPIO at the higher dose of 4 mg Fe/kg body weight [1], [6]–[8]. On histological assessment, co-localisation of the MRI-detectable hypointensities with micrometastases was evident (Figure A.1a, b) and the presence of MPIO was detected within VCAM-1 positive vessels (Figure A.1c, d). These data demonstrated efficacy and sensitivity of the lower dose (1.6 mg Fe/kg) of VCAM-1 targeted MPIO for detection of brain micrometastases. However, these results cannot be generalised for all preclinical molecular imaging applications. Therefore, further investigation is needed for optimising the dose of iron oxide contrast agents based on the pathological model, question and expression of endothelial biomarker.

* This agent was also conjugated with [^{89}Zr]-DFO for the molecular PET imaging.

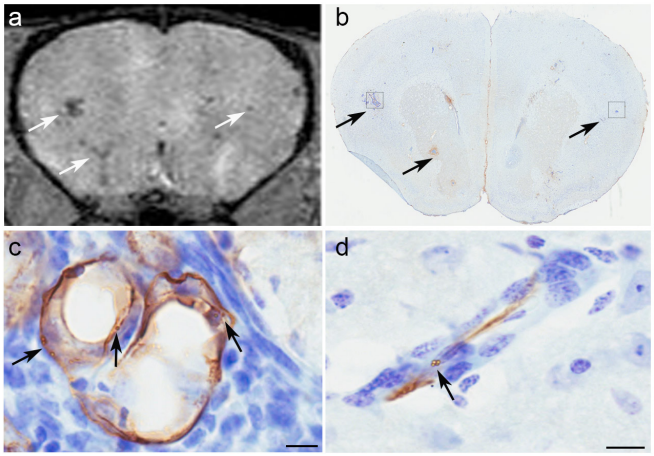


Figure A.1: Co-localisation of VCAM-MPIO and brain micrometastases in 4T1-GFP.
Co-localisation of focal hypointensities on a T_2*W-MGE3D (**a**; arrows) with histological detection of brain micrometastases (**b**; arrows); zoomed pictures of the insets are shown in **b** (**c, d**), arrows indicate MPIO on VCAM-1 positive (brown) vessel associated with micrometastasis. Scale bar = 10 µm.

Appendix B

B.1 Introduction

E-selectin is restrictively expressed on the endothelium and mediates slow rolling of leukocytes on inflamed vessels. E-selectin recognises a wide variety of fucosylated and sialylated glycolipids and glycoproteins [9]. Many glycostructures have been shown to recognise E-selectin, including P-selectin glycoprotein ligand (PSGL-1), E-selectin ligand (ESL-1; on mouse only), L-selectin (on human only), CD44 and CD43 [10]. Another counter ligand for E-selectin in humans, is cutaneous lymphocyte-associated antigen (CLA) [11]. CLA has a carbohydrate domain shared by sLe^X and requires glycosyltransferase α1,3-fucoyltransferase-VII (FucT-VII) for its biosynthesis. This ligand can be identified by the HECA-452 monoclonal antibody [11], [12]. This marker is primarily expressed on a subset of skin-homing memory T cells in skin inflamed diseases such as psoriasis lesions, and its expression has also been found on a subset of natural killer (NK) cells, monocytes, granulocytes, cutaneous T-cell neoplasia and infiltrating lymphocytes in Merkel cell carcinoma [13], [14]. Metastatic cells have shown high expression of glycans (e.g. sialic acid sugars) on their surface compared to primary tumours [15]–[17]. The presence of sLe^X and CD44 on breast cancer cells (MDA-MB-231) and their interactions with E-selectin have been shown *in vitro* [18]. Moreover, sLe^X (CD15s) has been shown on human brain metastases biopsies from non-small cell lung cancer and SEBTA-001 cancer cells *in vitro* [19]. However, CLA expression in brain metastases has not been demonstrated before. In Appendix B, I investigate CLA expression on mouse brain metastases tissues from breast, melanoma and lung, at various time-points post tumour cell injection.

B2. Methods

Tumour bearing mouse brain sections from breast (MDA-MB-231-Br), melanoma (H1_DL2) and lung (SEBTA-001) brain metastases models were immunohistochemically stained for CLA expression with the HECA-452 monoclonal antibody (details in Table 2.2 of the Methods Chapter) at various time-points after intracardiac tumour cell injection. Sections were also

fluorescently stained for CLA, the tumour-specific markers (GFP, Melan-A and cytokeratin) and CD31, following the same staining protocols as described in Sections 2.5.2 and 2.5.5, and using the antibodies in Table 2.2

B.3 Results and Discussion

CLA, with a distinctive perinuclear dot-like pattern, was present on some tumour cells in all three brain metastasis models, at all time-points studied (Figure B.1). These results show for the first time the presence of this marker on malignant cells. Furthermore, brain metastasis samples were fluorescently stained for CLA and endothelial marker (CD31). CLA expression on tumour cells from breast, melanoma and lung was confirmed immunofluorescently (Figure B.2). No co-localisation between CLA and endothelial cells (CD31) was found in these samples. Results presented here may suggest that brain metastatic cancer cells have acquired the machinery to mimic immune cells (i.e. T cells). Those tumour cells that express CLA, would be capable of binding to E-selectin when expressed on blood vessels. Further investigation of the role of CLA in tumour cells and its interaction with E-selectin (CLA and E-selectin co-localisation) is warranted for better understanding of the role of E-selectin in brain metastasis.

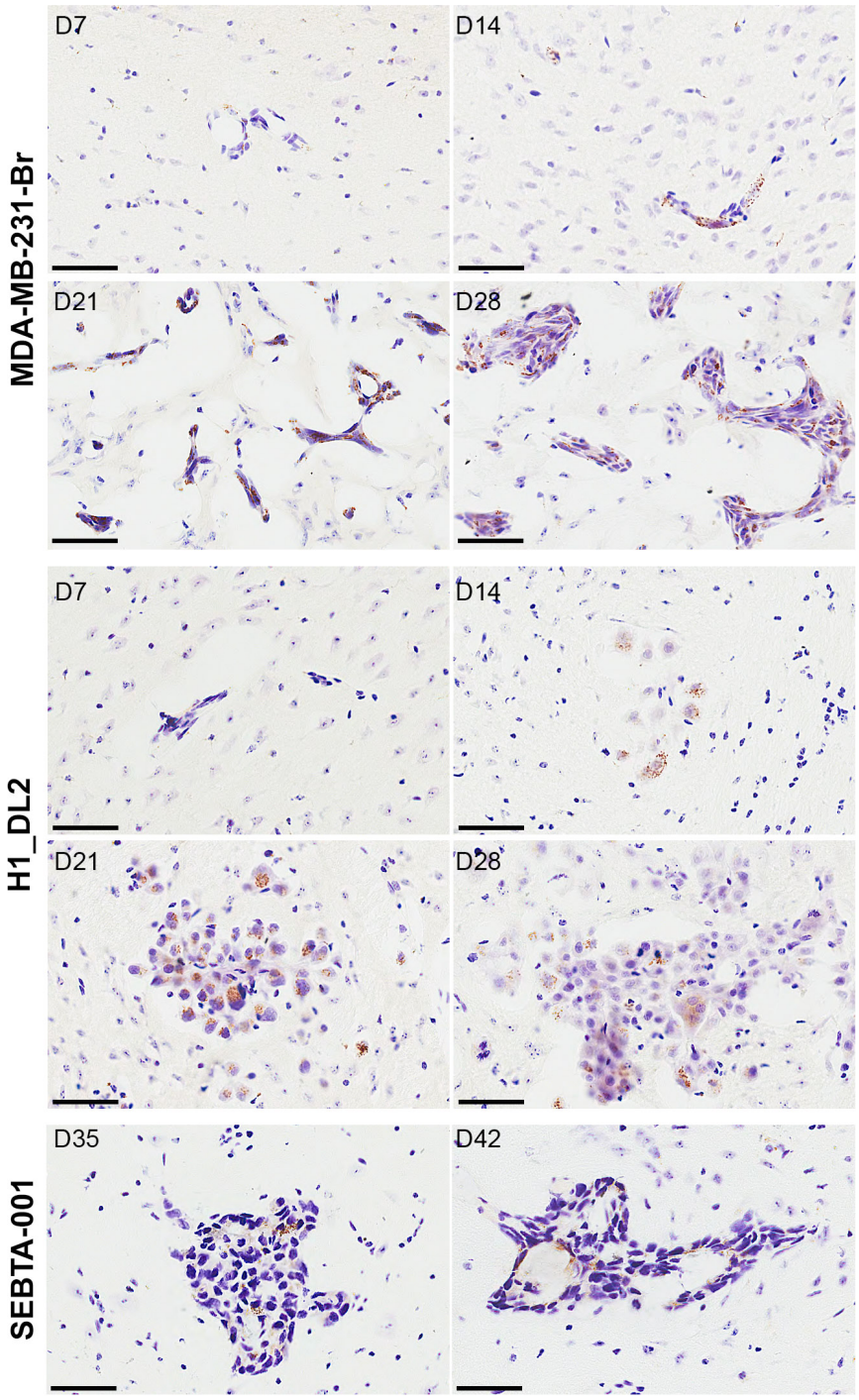


Figure B.1: CLA expression on brain metastasis cells.

Brain metastases samples from MDA-MB-231-Br, H1_DL2 and SEBTA-001 stained for CLA at different time-points post-intracardiac tumour injection. Perinuclear dotted expression of CLA (brown) was found on some of tumour cells at all the time-points studied. Cresyl violet: blue. Scale bars = 50 µm.

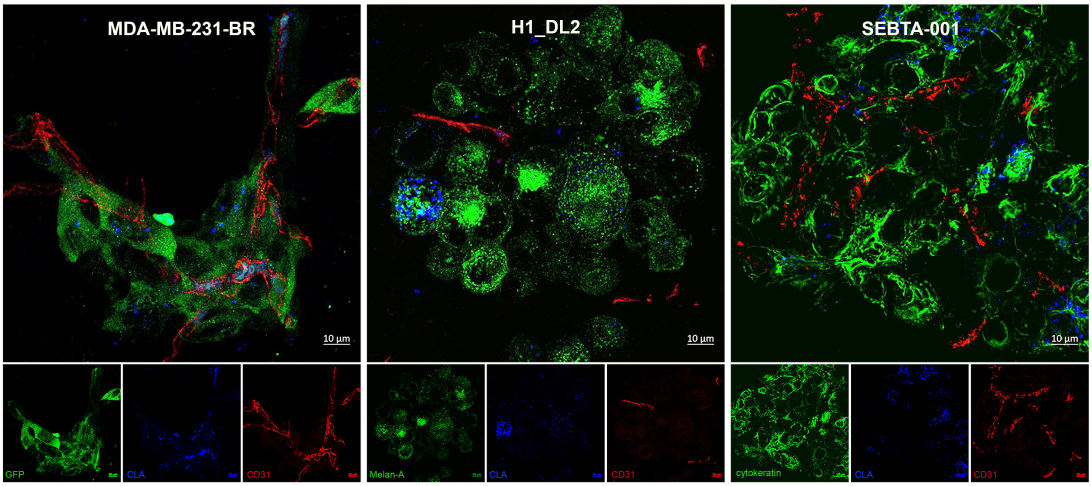


Figure B.2: CLA and endothelial cells (CD31) fluorescent staining in brain metastasis models. Immunofluorescence images from mouse brain sections stained for CLA (blue), endothelium (CD31; red) and metastatic tumours (green) for all three models. Although CLA was expressed in close proximity of vessels in some tumours (breast), no co-localisation was found between these two markers (CLA and CD31). MDA-MB-231-Br (day 21): GFP, H1_DL2 (day 21): Melan-A; SEBTA-001 (day42): cytokeratin.

Appendix C

In this thesis, Promag COOH MPIO were used for all *in vivo* molecular imaging experiments. In Appendix C, VCAM-Promag MPIO were used for imaging of two brain metastasis models (breast and melanoma), and MRI quantification results compared with the previous work published by Cheng *et.al* [8], who imaged these models using VCAM-carboxylic Dynabeads MPIO.

The VCAM-Promag MPIO contrast agent was injected intravenously in the breast cancer (MDA-MB-231-Br) and melanoma (H1_DL2) brain metastasis models at day 21 post-tumour cell injection (n = 3 per model). MPIO induced hypointensities were quantified on T_2*W-MGE3D images using the in-house MATLAB code, as previously described in the Methods Chapter Section 2.6.4 and using the same thresholding parameters as Cheng *et.al.* Hypointensity quantification showed a lower number of hypointense voxels for VCAM-Promag MPIO compared to the VCAM-carboxylic Dyna MPIO in both tumour models. This difference most likely reflects the different sizes of these beads; the Promag MPIO have a hydrodynamic diameter of 0.78 μm and Dynabeads carboxylic acid MPIO have a diameter of 1 μm. Consequently, Dynabeads should induce greater contrast per particle in neighbouring voxels compared to Promag. Moreover, as shown in Chapter 3 of this thesis, carboxylic Dynabeads show greater aggregation compared to Promag COOH, which may result in false positive voxels or larger clumps of VCAM-1 specific binding. Thus, less hypointensities from Promag COOH may likely to be more specific signal to brain metastases localisation

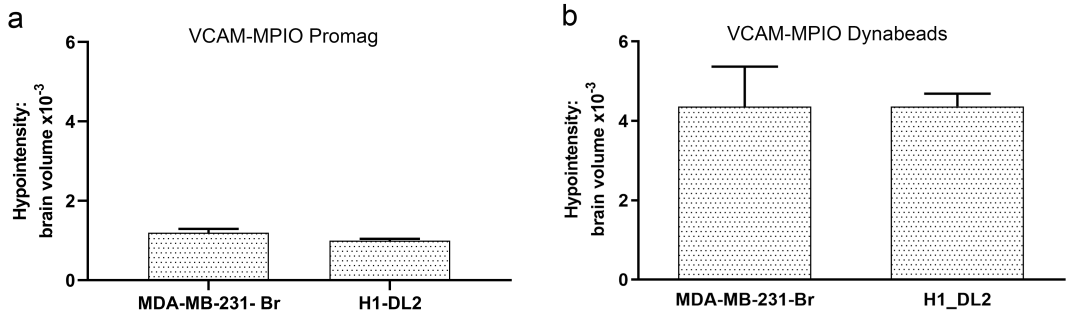


Figure C.1: Comparison of VCAM-Promag and VCAM-MyOne carboxylic acid MPIO. Hypointensities were quantified and normalised by brain volumes in breast (MDA-MB-231-Br) and melanoma (H1_DL2) brain metastasis models at day 21. **(a)** VCAM-Promag MPIO showed a lower number of hypointensities compared to **(b)** VCAM-Dynabeads MPIO. Plot **(b)** was extracted from Cheng *et al.* [8].

References

[1] M. a Mcateer, N. R. Sibson, C. Von Mühlen, J. E. Schneider, *et al.*, "In vivo magnetic resonance imaging of acute brain inflammation using microparticles of iron oxide," *Nat Med*, vol. 13, no. 10, pp. 1253–1258, 2007.

[2] S. Serres, M. S. Soto, A. Hamilton, M. a. McAteer, *et al.*, "Molecular MRI enables early and sensitive detection of brain metastases," *Proc. Natl. Acad. Sci.*, vol. 109, pp. 6674–6679, 2012.

[3] O. Will, S. Purkayastha, C. Chan, T. Athanasiou, *et al.*, "Diagnostic precision of nanoparticle-enhanced MRI for lymph-node metastases: A meta-analysis," *Lancet Oncol.*, vol. 7, no. 1, pp. 52–60, Jan. 2006.

[4] M. Gauberti, A. Montagne, A. Quenault, and D. Vivien, "Molecular magnetic resonance imaging of brain-immune interactions.," *Front. Cell. Neurosci.*, vol. 8, no. November, p. 389, 2014.

[5] N. Patel, B. A. Duffy, A. Badar, M. F. Lythgoe, and E. Årstad, "Bimodal Imaging of Inflammation with SPECT/CT and MRI Using Iodine-125 Labeled VCAM-1 Targeting Microparticle Conjugates," *Bioconjug. Chem.*, vol. 26, no. 8, pp. 1542–1549, 2015.

[6] S. Serres, S. Mardiguian, S. J. Campbell, M. A. McAteer, *et al.*, "VCAM-1-targeted magnetic resonance imaging reveals subclinical disease in a mouse model of multiple sclerosis.," *FASEB J.*, vol. 25, no. 12, pp. 4415–22, 2011.

[7] N. Zarghami, A. A. Khrapitchev, F. Perez-balderas, M. S. Soto, *et al.*, "Optimization of molecularly targeted MRI in the brain : empirical comparison of sequences and particles," pp. 4345–4359, 2018.

[8] V. W. T. Cheng, M. S. Soto, A. A. Khrapitchev, F. Perez-Balderas, *et al.*, "VCAM-1–targeted MRI Enables Detection of Brain Micrometastases from Different Primary Tumors," *Clin. Cancer Res.*, vol. 25, no. 2, pp. 533–534, 2019.
[9] S. D. Chase, J. L. Magnani, and S. I. Simon, "E-selectin ligands as mechanosensitive receptors on neutrophils in health and disease," *Annals of Biomedical Engineering*, vol. 40, no. 4. NIH Public Access, pp. 849–859, Apr-2012.
[10] A. Hidalgo, A. J. Peired, M. K. Wild, D. Vestweber, and P. S. Frenette, "Complete Identification of E-Selectin Ligands on Neutrophils Reveals Distinct Functions of PSGL-1, ESL-1, and CD44," *Immunity*, vol. 26, no. 4, pp. 477–489, 2007.
[11] L. W. Bergstresser, L. J. Terstappen, J. R. Picker, B. Treer, *et al.*, "skin-homing T cells. tissue-selective homing receptor for lymphocyte-associated antigen, a Differential regulation of the cutaneous Control of lymphocyte recirculation in man. II," 1993.
[12] K. Ohmori, F. Fukui, M. Kiso, T. Imai, *et al.*, "Identification of cutaneous lymphocyte-associated antigen as sialyl 6-sulfo Lewis X, a selectin ligand expressed on a subset of skin-homing helper memory T cells," 2006.
[13] C. Margo and M. Dyrsen, "Cutaneous lymphocyte antigen expression in benign and neoplastic cutaneous B - and T-cell lymphoid infiltrates," *J. Cutan. Pathol.*, vol. 35, pp. 1040–1049, 2008.
[14] O. K. Afanasiev, K. Nagase, W. Simonson, N. Vandeven, *et al.*, "Vascular E-selectin expression correlates with CD8 lymphocyte infiltration and improved outcome in Merkel cell carcinoma HHS Public Access," *J Invest Dermatol*, vol. 133, no. 8, pp. 2065–2073, 2013.
[15] J. W. Dennis, M. Granovsky, and C. E. Warren, "Glycoprotein glycosylation and cancer progression," *Biochimica et Biophysica Acta - General Subjects*, vol. 1473, no. 1. Elsevier, pp. 21–34, 17-Dec-1999.
[16] I. Häuselmann and L. Borsig, "Altered tumor-cell glycosylation promotes metastasis," *Frontiers in Oncology*, vol. 4. p. 28, 2014.
[17] C. Büll, M. A. Stoel, M. H. Den Brok, and G. J. Adema, "Sialic acids sweeten a tumor's life," *Cancer Research*, vol. 74, no. 12. American Association for Cancer Research Inc., pp. 3199–3204, 15-Jun-2014.
[18] Y. Geng, S. Chandrasekaran, J. W. Hsu, M. Gidwani, *et al.*, "Phenotypic Switch in Blood: Effects of Pro-Inflammatory Cytokines on Breast Cancer Cell Aggregation and Adhesion," *PLoS One*, vol. 8, no. 1, p. e54959, 2013.
[19] S. A. Jassam, Z. Maherally, J. R. Smith, K. Ashkan, *et al.*, "CD15s/CD62E interaction mediates the adhesion of non-small cell lung cancer cells on brain endothelial cells: Implications for cerebral metastasis," *Int. J. Mol. Sci.*, vol. 18, no. 1474, pp. 1–16, 2017.

Appendix D

International Journal of Nanomedicine

Dovepress
open access to scientific and medical research

Open Access Full Text Article

ORIGINAL RESEARCH

Optimization of molecularly targeted MRI in the brain: empirical comparison of sequences and particles

This article was published in the following Dove Press journal:
International Journal of Nanomedicine

Niloufar Zarghami[1]
Alexandre A Khrapitchev[1]
Francisco Perez-Balderas[1]
Manuel Sarmiento Soto[1]
James R Larkin[1]
Luca Bau[2]
Nicola R Sibson[1]

[1]Cancer Research UK and Medical Research Council Oxford Institute for Radiation Oncology, Department of Oncology, University of Oxford, Oxford, UK; [2]Institute of Biomedical Engineering, Department of Engineering Sciences, University of Oxford, Oxford, UK

Background: Molecular MRI is an evolving field of research with strong translational potential. Selection of the appropriate MRI sequence, field strength and contrast agent depend largely on the application. The primary aims of the current study were to: 1) assess the sensitivity of different MRI sequences for detection of iron oxide particles in mouse brain; 2) determine the effect of magnetic field strength on detection of iron oxide particles in vivo; and 3) compare the sensitivity of targeted microparticles of iron oxide (MPIO) or ultra-small superparamagnetic iron oxide (USPIO) for detection of vascular cell adhesion molecule-1 (VCAM-1) in vivo.

Methods: Mice were injected intrastriatally with interleukin 1β to induce VCAM-1 expression on the cerebral vasculature. Subsequently, animals were injected intravenously with either VCAM-MPIO or VCAM-USPIO and imaged 1 or 13 hours post-injection, respectively. MRI was performed at 4.7, 7.0, or 9.4 T, using three different T_2*-weighted sequences: single gradient echo 3D (GE3D), multi-gradient echo 3D (MGE3D) and balanced steady-state free precession 3D (bSSFP3D).

Results: MGE3D yielded the highest signal-to-noise ratio (SNR) and contrast-to-noise ratio (CNR) for the detection of iron oxide particles. All sequences showed a significant increase in SNR and CNR from 4.7 to 7.0 T, but no further improvement at 9.4 T. However, whilst targeted MPIO enabled sensitive detection of VCAM-1 expression on the cerebral vasculature, the long half-life (16.5 h vs 1.2 min) and lower relaxivity per particle (1.29×10^{-14} vs 1.18×10^{-9} Hz L/particle) of USPIO vs. MPIO rendered them impractical for molecular MRI.

Conclusion: These findings demonstrate clear advantages of MPIO compared to USPIO for molecularly-targeted MRI, and indicate that the MGE3D sequence is optimal for MPIO detection. Moreover, higher field strengths (7.0/9.4 T) showed enhanced sensitivity over lower field strengths (4.7 T). With the development of biodegradable MPIO, these agents hold promise for clinical translation.

Keywords: molecular imaging, preclinical MRI, VCAM-MPIO, VCAM-USPIO, multi gradient echo, bSSFP

Introduction

Preclinical molecular and cellular MRI is an evolving field of research with strong translational potential. Iron oxide particles are currently the preferred contrast platform for this application and have been thoroughly reviewed in the literature.[1–4] The magnetic core of these particles causes inhomogeneity in the local magnetic field, which leads to reduction of relaxation times of adjacent protons. Thus, the accumulation of iron oxide particles appears as dark (hypointense) regions on commonly used T_2*/T_2-weighted magnetic resonance images.[5] The degree of hypointense image contrast, or the susceptibility effect, is highly dependent on relaxivity values and the iron

Correspondence: Nicola R Sibson
Cancer Research UK and Medical Research Council Oxford Institute for Radiation Oncology, Department of Oncology, Old Road Campus Research Building, University of Oxford, Oxford OX3 7LJ, UK
Tel +44 186 522 5836
Fax +44 186 585 7127
Email nicola.sibson@oncology.ox.ac.uk

submit your manuscript | www.dovepress.com
Dovepress

http://dx.doi.org/10.2147/IJN.S158071

© 2018 Zarghami et al. This work is published by Dove Medical Press Limited, and licensed under a Creative Commons Attribution License. The full terms of the License are available at http://creativecommons.org/licenses/by/4.0/. The license permits unrestricted use, distribution, and reproduction in any medium, provided the original author and source are credited.

International Journal of Nanomedicine downloaded from https://www.dovepress.com/ by 192.76.8.80 on 27-Sep-2019
For personal use only.

International Journal of Nanomedicine downloaded from https://www.dovepress.com/ by 192.76.8.80 on 27-Sep-2019
For personal use only.

concentration of these agents,[6,7] as well as MRI parameters such as magnetic field strength[8,9] and pulse sequence.[8,10,11] However, although T_2-weighted spin-echo (SE) and T_2*-weighted gradient-echo (GRE) sequences are regarded as the gold standard for iron oxide-enhanced MRI,[12–14] and 7.0 T is the most commonly used field strength preclinically, a robust comparison of other sequences and/or magnetic field strengths has yet to be demonstrated.

Iron oxide agents are usually composed of a superparamagnetic core and a shell of varying thickness and material. In general, these particles are classified into 3 categories based on their hydrodynamic size. Ultra-small superparamagnetic iron oxide (USPIO; ~5–50 nm in diameter) particles are the smallest agents currently in use.[7,15] These particles typically exhibit a long (several hours) blood circulation half-life and have been clinically used for perfusion mapping and enhanced functional MRI activation detection.[16,17] USPIO have also shown potential for imaging brain tumors with an impaired blood–brain barrier (BBB).[18–20] Superparamagnetic iron oxide (SPIO; 50–150 nm in diameter) particles are slightly larger in size,[14,20,21] and have seen extensive clinical use for lymph node imaging in cancer patients.[22,23] Finally, microparticles of iron oxide (MPIO; ~1 µm[2,24,25]) have been used in a variety of preclinical molecular imaging,[25–29] but until recently[30] a clinically compatible MPIO platform has not existed. Innovations and developments in the field of molecular imaging and biodegradable iron oxide contrast agents have increased the potential for translation of preclinical research to clinic.[30–32] However, selection of the appropriate USPIO, SPIO, or MPIO contrast agent for imaging depends largely on the application and research or clinical question to be addressed.

Over the last decade, molecular MRI, of brain–immune system interactions, has been the subject of numerous studies,[27,33–38] with iron oxide particles being conjugated to a variety of different ligands (including proteins, peptides, antibodies, and carbohydrates) to target specific molecular epitopes expressed in disease. MPIO are often the agent of choice for such targeted molecular imaging studies, having several postulated advantages over UPSIO. The micron size of these particles enables assessment of specific binding to the endovasculature, unlike USPIO that are susceptible to macrophage uptake and passive diffusion into the brain parenchyma across a leaky BBB.[39,40] Moreover, the iron content of a single MPIO is 4.3 million times higher than that of a USPIO, yielding considerably greater contrast per particle, with the contrast effect extending up to 50 times the physical size of the particle.[6,24,41,42] Finally, the increased surface area of MPIO greatly increases labeling valency and, hence, binding affinity to the molecule of interest, while their short blood half-life (<5 min) compared to USPIO yields a high target-to-background ratio.[38,43,44] However, many of these advantages remain theoretical or have only been demonstrated in vitro, and a direct head-to-head in vivo comparison of molecularly targeted MPIO and USPIO has not previously been reported.[37,39]

The primary aims of the current study, therefore, were to 1) assess the relative sensitivities of 3 commonly used MRI sequences (single gradient echo 3D, multi-gradient echo 3D, and balanced steady-state free precession 3D) for the detection of iron oxide particles in mouse brain; 2) determine the effect of magnetic field strength on the detection of iron oxide particles in vivo; and 3) compare the specificity and sensitivity of vascular cell adhesion molecule (VCAM)-MPIO and VCAM-USPIO for the detection of VCAM-1 in a mouse model of neuroinflammation.

Materials and methods

VCAM-MPIO synthesis

Pro-mag™ carboxylic acid MPIO[45] (Cat. No. PMC1N, Lot 10892, Bangs Laboratory Inc., Fishers, IN, USA) were vortexed and 1 mg of MPIO transferred to a 2 mL plastic tube. 2-(N-morpholino)ethanesulfonic acid (MES) buffer was added (15 mM, 1 mL, pH: 6.0). MPIO were pelleted on a Dynal magnetic separator (Thermo Fisher Scientific, Waltham, MA, USA) for 2 min, and the supernatant discarded. For the amine coupling reaction, 100 µL MES buffer and 100 µL of a 10 mg/mL solution of 1-Ethyl-3-(3-dimethylaminopropyl)carbodiimide (EDC) (Cat. No. E6383, Sigma-Aldrich, St Louis, MO, USA) in 15 mM MES pH 6.0 were added to the pelleted MPIO, and the solution was incubated for 30 min at 25°C on a shaker (1,000 rpm). The solution was washed twice with 1 mL of 15 mM MES buffer and incubated with low endotoxin, 80 µL azide-free monoclonal rat antibody to mouse VCAM-1 (clone M/K-2, Cat. No. 1510-14, SouthernBiotech, Birmingham, AL, USA) for 24 h at 25°C on a shaker. Conjugates were washed twice with PBS/0.01% Tween and the supernatant containing any unbound antibody discarded. PBS was added to achieve the desired concentration of VCAM-MPIO.

VCAM-USPIO synthesis

Monocrystalline iron oxide nanocompounds (MION) were synthesized according to the published protocol.[46] Physicochemical properties of MION have been well investigated previously.[47] MION were converted into cross-linked iron oxide (CLIO)-NH_2 by reaction with epichlorohydrin and ammonium hydroxide.[48] CLIO-NH_2 were transformed into CLIO-COOH by reaction with succinic anhydride.[30] For VCAM-USPIO synthesis, MES (0.2 M, 100 µL, pH: 6.0) was added to the solution

International Journal of Nanomedicine downloaded from https://www.dovepress.com/ by 192.76.8.80 on 27-Sep-2019
For personal use only.

of CLIO-COOH (1 mg iron, 100 µL, 28.1 nm hydrodynamic diameter, 1.75×10^{14} particles/mg iron) and vortexed. Then, 10 µL of N-hydroxysulfosuccinimide sodium salt (sulfoNHS) (10 µmol; Cat. No. 56485, Sigma Aldrich) in MES buffer (1 M, pH 6.0) and 20 µL of EDC solution (10 µmol; Cat. No. E6383, Sigma Aldrich) in water were added. The mixture was incubated for 15 min at 25°C on a shaker (1,000 rpm), and excess of EDC was quenched by addition of 50 mg of HL-COOH (Tentagel, Cat. No. 86.333, Sigma-Aldrich) for 15 min. The sample was filtered and Tentagel was washed with 100 µL of MES buffer (0.2 M, pH: 6.0). To this solution, 80 µL of anti-mouse VCAM-1 antibody (same as MPIO) was added, and the reaction was incubated for 24 h at 25°C on a shaker. Subsequently, to quench any remaining activated carboxylic acid, 100 µL of borate buffer (1M, pH: 8.5) was added and the solution incubated for another 24 h at 25°C on a shaker. The sample was centrifuged at 186,000 *g* for 1.5 h, the supernatant discarded, and the pellet reconstituted in 1 mL of PBS. The sample was pelleted again (186,000 *g* for 1.5 h), then reconstituted in 1 mL of PBS and pelleted as before. This final pellet was reconstituted in 100 µL of PBS.

Physicochemical properties of VCAM-MPIO and VCAM-USPIO

The particle size of VCAM-USPIO was measured by dynamic light scattering on a Zetasizer Nano ZS (Malvern Panalytical Ltd, Malvern, UK), and reported as the *z*-average diameter. The polydispersity is reported as the coefficient of variation (CV) of the size distribution, which was calculated as the square root of the mean of the polydispersity index (for USPIO) or provided by the manufacturer (for MPIO). The zeta potential was measured on a Zetasizer Nano ZS in 0.1 M 4-(2-hydroxyethyl)piperazine-1-ethanesulfonic acid buffer at pH 7.0. The particle size of MPIO was provided by the manufacturer as a volume-weighted mean diameter measured with a Coulter counter. The iron content of VCAM-MPIO and VCAM-USPIO was measured by inductively coupled plasma optical emission spectrometry (ICP-OES) on a Varian Vista MPX (Varian, Palo Alto, CA, USA) after acid digestion. The upper limit of COOH loading was estimated from the nitrogen content of a freeze-dried sample, which was measured by combustion analysis. Results are reported as mean ± SD of repeated measurements on the same sample.

Iron content per particle and estimation of per-particle properties

The mass of iron per particle was used as a conversion factor to relate intrinsic properties relative to the amount of iron (value per mmol of iron) to per particle properties (value for one particle). The mass of iron per particle was calculated as

$$\text{pg Fe/particle} = 10^9 \times \frac{\%\text{Fe}}{100} \times (\text{particles/mg})^{-1}$$

where %Fe is the weight/weight concentration of iron in a dry sample measured by ICP-OES and particles/mg is the number of particles per mg of dry sample. The latter is provided by the manufacturer for MPIO, while for USPIO it is calculated as

$$\text{Particles/mg} = 10^{-3} \times \left[\frac{4}{3}\pi\left(\frac{d}{2}\right)^3 (\phi_{Fe_3O_4}\rho_{Fe_3O_4} + (1-\phi_{Fe_3O_4})\rho_{Dex})\right]^{-1}$$

where d is the particle diameter, $\phi_{Fe_3O_4}$ is the volume fraction of magnetite in a dry sample, $\rho_{Fe_3O_4}$ is the density of magnetite, and ρ_{Dex}=1.07 g/cm^3 is the density of hydrated cross-linked dextran.[49] The volume fraction of magnetite was calculated from the mass fraction of magnetite $\chi_{Fe_3O_4} = (\%\text{Fe}/100)\times[(3A_r(\text{Fe}) + 4A_r(\text{O}))/(3A_r(\text{Fe}))]$, where A_r(Fe)=55.845 u and A_r(O)=15.999 u are the atomic weights of iron and oxygen, respectively, and the density ratio $\rho_{Fe_3O_4}/\rho_{Dex}$.

Assessment of VCAM antibody loading on MPIO and USPIO

MPIO (10 µg) or USPIO (70 µg) were diluted in 200 of PBS buffer, and 2 µL of Alexa Fluor 647 goat anti-rat IgG (H+L) (Cat. No. A21091, 5 fluorophores per antibody, Invitrogen) was added. For MPIO, samples were shaken for 30 min, pelleted using a magnet, washed twice with PBS/0.01% Tween, and resuspended in 400 µL of PBS. Qifikit calibration beads (Dako, Agilent Technologies, Stockport, UK), used as a reference, were prepared according to the manufacturer's protocol, but substituting the provided fluorescently-conjugated antibody by Alexa Fluor 647 goat anti-mouse IgG (H+L) (Cat. No. A21050, 5 fluorophores per antibody, Invitrogen). Flow cytometry experiments were performed on a BD FACSCalibur flow cytometer, using channel FL4 (661/16 nm band pass filter). Calibration curve was performed, according to manufacturer protocol, by linear regression of the log–log plot of antibody loading versus fluorescence intensity. For USPIO, sample was centrifuged at 186,000 *g* for 1.5 h, the supernatant discarded, and the pellet reconstituted in 1 mL of PBST. The sample was pelleted again (186,000 *g* for 1.5 h) and reconstituted in 200 µL of PBS. Fluorescence intensity

International Journal of Nanomedicine downloaded from https://www.dovepress.com/ by 192.76.8.80 on 27-Sep-2019
For personal use only.

of the samples was measured and compared to a calibration curve composed of serial dilutions of Alexa Fluor 647 goat anti-rat IgG (H+L). Results are reported as mean ± SD.

Determination of MPIO and USPIO relaxivity in agarose gel

MRI phantoms were prepared as described previously.[30] Unconjugated MPIO and USPIO were embedded in 2% w/v agarose gels at iron concentrations of 0.0025–0.2 mM. Gels were prepared in 15 mL tubes and heated at 95°C. MPIO and USPIO particles were added to the tubes and dispersed for a homogenous mixture. Samples were sonicated and kept undisturbed at room temperature until cool. MPIO and USPIO relaxitivities were measured using a SE multi-slice sequence in a 7.0 T horizontal bore system (Agilent Technologies, Santa Clara, CA, USA) with a 26-mm birdcage RF coil (Rapid Biomedical, Rimpar, Germany). Sequence parameters for the T_2 maps were: repetition time (TR) =10 s, 12× echo time (TE) =[10–300] ms, spectral width (SW) =100 kHz, matrix =128×128, field of view (FoV) =72×72 mm, slice thickness =2 mm, and experimental time (Texp) =4 h 16 min. Sequence parameters for the T_1 maps were: TR =10 s, TE =10 ms, 12×Ti =[0.01–6.0] s, SW =100 kHz, matrix =128×128, FoV =72×72 mm, and slice thickness =2 mm, Texp =4 h 16 min.

Assessment of VCAM-MPIO and VCAM-USPIO circulatory half-life

To determine the blood half-life of VCAM-MPIO and VCAM-USPIO, the particles were injected via a tail vein into female BALB/c mice (6–7 weeks old, n=15, Charles River, UK, Kent, UK) at a constant dose of 4 mg Fe/kg in 100 µL sterile PBS. At 0, 0.8, 1, 2, 2.5, 3, 5, and 10 min after injection for VCAM-MPIO and 1, 6, 13, 24, 48 and 72, 96 h after VCAM-USPIO injection, the mice underwent anesthesia with 2%–3% isoflurane in 30% O_2 with 70% N_2 followed by thoracotomy. Blood was collected from the left ventricle using a 1 mL syringe with a 23G needle containing 1 µL of heparin sodium (25,000 I.U./mL, Wockhardt Ltd, Wrexham, UK). Blood samples (up to 1 mL) were oxygenated by placing in 15 mL tubes with a 100% O_2 atmosphere and inverting gently for 5 min until the color changed to bright red. Final blood volume (100 µL) was mixed with 1% agarose solution in PBS (100 µL), at 41°C and placed in 500 µL microcentrifuge tube. T_2 relaxivities of samples were immediately measured using a 7.0 T MRI. For T_2 relaxometery, a simple 90° and 180° pulse sequence were used with long TR (10 s) and adjusted array of TE for best fitting. Circulatory blood half-life was determined from the fitted 1 phase decay curve, constrained to a plateau at the average naive blood sample value (baseline). Blood samples from naïve mice were used as the baseline (n=6).

Mouse neuroinflammation model

All animal procedures were performed under the University of Oxford guidelines and approved by the UK Home Office. Female BALB/c mice (6–7 weeks old, n=24; Charles River, Kent, UK) were anesthetized with isoflurane (1.5%–2.0%) in 30% O_2: 70% N_2O, placed in a stereotaxic frame and a burr hole drilled above the injection site (co-ordinates from bregma: anterior +0.5 mm; left 2.0 mm; depth 2.5 mm). Using a glass microcannula (tip diameter *ca.* <50 µm), 1 ng of mouse recombinant interleukin-1β (IL-1β, Peprotech EC, London, UK) in 1 µL sterile PBS was injected into the left striatum to induce unilateral vascular activation.[25] The scalp incision was sutured, and the animals were recovered from anesthesia. Three hours after the surgery,[25] the mice were injected via tail vein with the dose of 4 mg Fe/kg of either (a) VCAM-MPIO (n=12) or (b) VCAM-USPIO (n=12).

MRI

All MRI experiments were performed using horizontal, wide-bore superconductive 4.7, 7.0, or 9.4 T MRI systems (Agilent Technologies Inc). The same size (ID =26 mm) transmit/receive birdcage RF coils were used in all experiments (Rapid Biomedical).

Mice injected intravenously with VCAM-MPIO (n=4 for each field strength) were imaged 1 h after contrast agent administration, as previously reported. An imaging time-point of 13 h post-injection was chosen for mice injected with VCAM-USPIO (n=4 for each field strength) to account for the longer circulation half-life.[50,51] All mice were imaged with both multi-gradient echo and balanced steady-state free precession 3D sequences (MGE3D and bSSFP3D, respectively). For MGE3D, the parameters were as follows: excitation angle =15°; TR =65.1 ms; time of the 1st echo (TE_1) =2.5 ms; echo separation time (TE_2) =4 ms (even echoes acquired in the reverse k-space direction, during opposite read gradient); SW =100 kHz (acquisition time =2.56 ms); and number of echoes =15. For bSSFP3D, the parameters were as follows: excitation angle =20°; TR/TE =8/4 ms; SW =147 kHz (acquisition time =1.74 ms); and number of excitation frequency offsets =8. The following parameters were consistent for both sequences: FoV =22.5×22.5×22.5 mm^3; acquisition matrix size =256×192×192 (final images zero-filled to

International Journal of Nanomedicine downloaded from https://www.dovepress.com/ by 192.76.8.80 on 27-Sep-2019
For personal use only.

256×256×256; final isotropic resolution =88 µm). Both MGE3D and bSSFP3D scans were run with a single average (NT =1), and the total acquisition time was ~40 min for each.

Image reconstruction

Images were reconstructed using home-built MATLAB (MathWorks, Natick, MA, USA) code. The final MGE3D images were reconstructed as the square root of sum of squares (SqrtSOS) of individual echoes.[52–54] Based on previous data, second single echo (TE =6.5 ms) was extracted from the MGE3D sequence to represent a single echo gradient echo (GE3D) dataset.[33,55] For bSSFP3D, the final images were reconstructed by adding the individual frequency offsets using the same SqrtSOS algorithm as above.[56,57]

Image and data analysis

For all datasets, brain masks were generated manually. Quantification of hypointense signals from MPIO and USPIO was performed using in-house MATLAB code. Signals arising from ventricles or sinuses, which naturally appear hypointense, were excluded.[27] The quantification of signal-to-noise (SNR) was performed by measuring the signal intensity (SI_{brain}) within the mouse brain (excluding hypointensities) and SD of background noise (SD_{noise}). For contrast-to-noise (CNR), we additionally measured the signal intensity coming from VCAM-MPIO or VCAM-USPIO (SI_{void}). Thus, SNR and CNR were estimated using the following calculations, respectively:

$$SNR = \frac{SI_{brain}}{SD_{noise}}$$

$$CNR = \frac{SI_{brain} - SI_{void}}{SD_{noise}}$$

Statistical analyses were performed using Prism software (GraphPad, San Diego, CA, USA). The normality of the measured variables was tested using the Shapiro–Wilk test. For multiple comparisons, analysis of variance (ANOVA) followed by Tukey post-hoc test were used.

Ex vivo assessment of VCAM-MPIO and USPIO binding

Following imaging, mice were transcardially perfused under terminal anesthesia with 0.9% heparinized saline followed by periodate-lysine-paraformaldehyde (PLP-light) containing 0.1% glutaraldehyde. Brains were harvested, post-fixed in PLP then placed in 30% sucrose solution until they sank to the bottom. Samples were frozen in isopentane at –80°C. Brains were cut at 10 µm and kept at –20°C until immunohistochemical staining for co-localization of VCAM-1 and iron oxide particles. Sections were quenched with 1% (v/v) hydrogen peroxide (30% w/v) in methanol (Sigma Aldrich), blocked with 10% goat serum in PBS for 1 h, and then incubated overnight at 4°C with the primary VCAM-1 antibody (1:100; SouthernBiotech). Sections were washed using PBS/0.01% Tween (Sigma Aldrich), and then incubated with a biotinylated rat polyclonal secondary antibody (1:200 Abcam, Cambridge, UK) for 1 h. Slides were washed and then incubated in Vectorelite ABC kit (1:1:100; Vector Laboratories, Peterborough, UK) for 45 min. The peroxidase was visualized using 3,3′-diaminobenzidine (Sigma Aldrich). To detect the iron oxide particles, sections were stained using Perls' Prussian blue. Positive control liver and spleen samples from mice injected intravenously with USPIO were included for Perls' Prussian blue staining. For fluorescent VCAM-1 staining, Tris-NaCl blocking buffer (TNB; PerkinElmer, Seer Green, UK) was used. Sections were subsequently incubated overnight at 4°C with the VCAM-1 primary antibody, as above. Sections were washed with PBS and incubated with biotinylated anti-goat secondary in TNB for 30 min. Sections were then washed with PBS, incubated with streptavidin–horseradish peroxidase (1:200; PerkinElmer) in TNB for 30 min, washed and incubated for 7 min in the dark with tyramide signal amplification (TSA)-biotin (1:100) in amplification buffer (PerkinElmer). Slides were washed and incubated with a streptavidin-DyLight 488 (1:200; Vector Laboratories). Samples were coverslipped, using Vectashield mounting medium containing DAPI (Vector Laboratories). Whole brain fluorescent images were taken at 20× magnification using an Aperio immunofluorescence slide scanner (Leica Biosystems, Milton Keynes, UK).

Results

Physicochemical properties of VCAM-MPIO and VCAM-USPIO

The *z*-average hydrodynamic diameter of VCAM-USPIO was 28.1 nm. The particle size distribution (Figure S1) is moderately polydisperse, with a CV of 36%. The particle size distribution of MPIO was narrower, with a CV of 15% and a mean diameter of 880 nm. Both USPIO and MPIO were negatively charged, with a zeta potential of –9.3±0.9 mV and –25.6±1.3 mV, respectively. The iron content of USPIO and MPIO was 30.6% w/w and 27.8% w/w, respectively, as measured by ICP-OES.

International Journal of Nanomedicine downloaded from https://www.dovepress.com/ by 192.76.8.80 on 27-Sep-2019
For personal use only.

Quantitation of antibody loading showed the density of VCAM antibody to be 10,490±450 molecules per particle (n=4) on MPIO and 7.4±3.1 molecules per particle on USPIO (n=3). Although the number of antibodies per particle differs by 3 orders of magnitude, the surface density (number of antibodies per unit area) is comparable, with 4,320±200 molecules/μm^2 on MPIO and 3,000±1,300 molecules/μm^2 on USPIO. The zeta potential of either agents does not change significantly after conjugation to the antibody (−10.3±1.1 mV for VCAM-USPIO and −26.4±1.4 mV for VCAM-MPIO), which is not entirely unexpected as the measurement pH falls within the isoelectric point range of rat IgG.[58]

The R_2 relaxivity of MPIO and USPIO, measured in agarose phantoms, was found to be 500 Hz L/mmol Fe and 126 Hz L/mmol Fe, respectively (Figure S2A and B). Both values are consistent with previous literature reports[30,37,59,60] and correspond to average relaxivitiy per particle of 1.18×10^{-9} Hz L/particle for MPIO and the much lower value of 1.29×10^{-14} Hz L/particle for USPIO. Properties of MPIO and USPIO are summarized in Table 1.

Comparison of MRI sequences and field strengths for detection of iron oxide particles

Representative images obtained using each of the 3 sequences (MGE3D, GE3D, and bSSFP3D) at 4.7, 7.0, and 9.4 T, with the same resolution and scan time, are shown in Figures 1A and 2A. Qualitatively, all 3 sequences enabled visualization of hypointense foci in the brains of mice injected with either VCAM-MPIO (Figure 1A) or VCAM-USPIO (Figure 2A). However, the T_2*-weighted MGE3D sequence appeared to reveal hypointensities more prominently than either the T_2*-weighted GE3D or the T_2/T_1-weighted bSSFP3D sequence. Quantitative assessment of SNR (Figure 3A and C) and CNR (Figure 3B and D) for all sequences at each magnetic field confirmed that the highest SNR was conferred by the MGE3D sequence compared with both the other sequences for both MPIO and USPIO (in all cases, ANOVA – $P<0.0001$, followed by Tukey's post-hoc test; Figure 3). The T_2/T_1-weighted bSSFP3D sequence also showed significantly greater CNR than the standard GE3D sequence for the USPIO (Figure 3D). When comparing SNR and CNR of the optimal MGE3D sequence at different magnetic field strengths, a significant increase in both SNR and CNR was evident from 4.7 to 7.0 T (in all cases, ANOVA – $P<0.05$, followed by Tukey's post-hoc test). However, no additional increase in either signal or contrast was gained by increasing field strength from 7.0 to 9.4 T.

Table 1 Physicochemical properties of MPIO and USPIO

Properties	MPIO	USPIO
Mean diameter (nm)	880[a]	28.1
Coefficient of variation[b] (%)	15[a]	36
Iron content (% w/w)	27.8	30.6
Core diameter (nm)	5.1[c]	9–14[d]
Saturation magnetization (emu/g Fe)	115[c]	62[e]
Zeta potential (mV)	−26.4±1.4[f]	−10.3±1.1[g]
COOH loading (μmol/mg Fe)	122[a]	<1.24
Surface area of 1 particle[e] (μm^2)	2.4	0.0025
Iron content per particle (pg Fe/particle)	0.13	5.7×10^{-6}
Antibody density per particle (Ab/particle)	10,490±450[g]	7.4±3.1[g]
Antibody density per unit area (Ab/μm^2)	4,320±200[g]	3,000±1,300[g]
Bulk relaxivity (Hz L/mmol Fe)	500	126
Particle relaxivity (Hz L/particle)	1.18×10^{-9}	1.29×10^{-14}

Notes: [a]Data provided by the manufacturer. [b]Relative SD of particle diameters within a sample. [c]From the study by Delangre et al.[59] [d]From the study by Perez-Balderas et al.[30] [e]From the study by Chen et al.[58] [f]Calculated from diameter assuming spherical particles. [g]Data are reported as mean ± SD of repeated measurements of the same sample.
Abbreviations: MPIO, microparticles of iron oxide; USPIO, ultra-small superparamagnetic iron oxide.

Comparing sensitivity and specificity of VCAM-MPIO and VCAM-USPIO

Immunohistochemically, unilateral upregulation of VCAM-1 was evident in mice injected intracerebrally with IL-1β and intravenously with VCAM-MPIO (Figure 1B–D). In accord with this unilateral upregulation, a marked unilateral contrast effect was evident in brain images at all field strengths and with all 3 sequences (Figure 1A). In contrast, in mice injected intracerebrally with IL-1β and intravenously with VCAM-USPIO, bilateral contrast effects were evident in all animals, with no differences between the hemispheres (Figure 2A). Immunohistochemistry confirmed unilateral VCAM-1 upregulation (Figure 2B–D). Quantitative analysis of hypointense voxels (mean ± SE) for all 3 field strengths showed a significant difference between the number of hypointense voxels in the injected and contralateral hemispheres for mice injected with VCAM-MPIO (4.7 T: 446±119 vs 229±30; 7.0 T: 430±47 vs 253±47; 9.4 T: 425±98 vs 214±58; n=4 per group, $P<0.05$; Figure 4A), but no significant difference for VCAM-USPIO-induced hypointensities (4.7 T: 1,444±75 vs 1,213±125; 7.0 T: 1,244±90 vs 1,138±36; 9.4 T: 1,058±28 vs 933±95; n=4 per group). Immunohistochemically, VCAM-1 and Perls' Prussian blue staining revealed the presence of VCAM-MPIO in the lumen of VCAM-1-positive vessels following MRI. However, despite intense bilateral contrast effects observed by MRI, no VCAM-USPIO were detected on VCAM-1 positive vessels or within the brain parenchyma following MRI (Figure 4B). To test that Perls' Prussian blue

International Journal of Nanomedicine downloaded from https://www.dovepress.com/ by 192.76.8.80 on 27-Sep-2019
For personal use only.

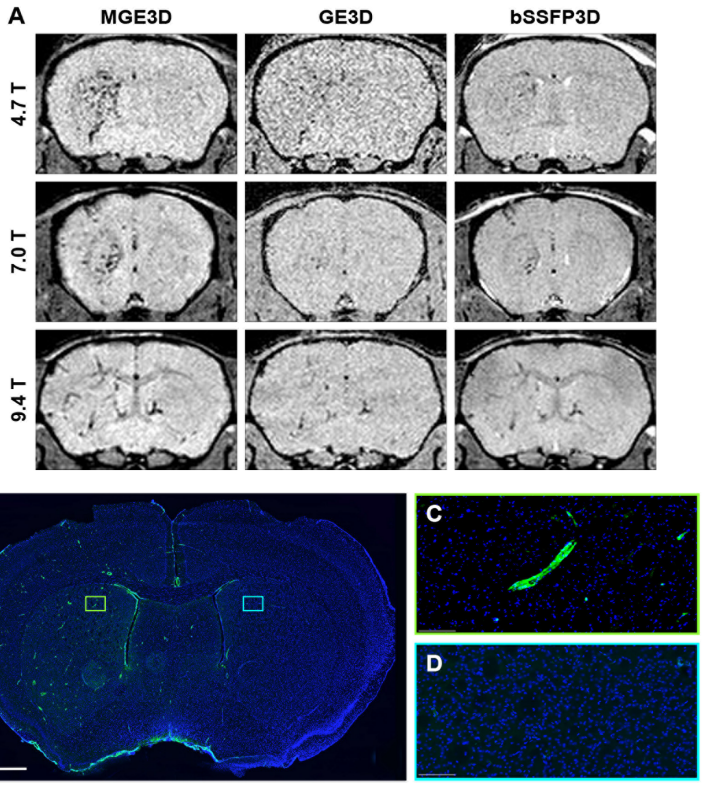


Figure 1 (**A**) Representative in vivo images of mice 1 h post-VCAM-MPIO injection at different magnetic fields. Three sequences of MGE3D, GE3D, and bSSFP3D are shown from a 3D dataset. Intense low signal areas on the left side of the brain reflect the specific retention of MPIO on acutely activated vascular endothelium with visually absent contrast effect in the contralateral control hemisphere. MGE3D demonstrates better visualization of hypointensities compared with other sequences. (**B**–**D**) Histological assessment of VCAM upregulation at the injection side.
Notes: Green vessels show unilateral upregulation of VCAM, nuclei are shown in blue. Scale bar: 1 mm.
Abbreviations: bSSFP3D, balanced steady-state free precession 3D; GE3D, gradient echo 3D; MGE3D, multi-gradient echo 3D; MPIO, microparticles of iron oxide; VCAM, vascular cell adhesion molecule.

stain can, in fact, stain and detect USPIO, positive control samples (liver and spleen) from mice injected with USPIO were stained. The results indicate that it is possible to detect USPIO (Figure S3) histologically.[61]

To determine whether contrast effects could be arising from unbound VCAM-USPIO within the blood, the half-life of VCAM-USPIO in the circulation was measured and found to be 16.5 h, in comparison to 1.2 min for VCAM-MPIO (Figure 4C). Consequently, the bilateral contrast effects arising from VCAM-USPIO administration was further investigated in both naïve mice and mice injected intracerebrally with IL-1β. Mice were injected intravenously with VCAM-USPIO and imaged at different time points (1, 13, and 80 h) after injection, as above (Figure 4D). Results showed bilateral contrast effects and, hence, presence of VCAM-USPIO, in both cohorts at 1 and 13 h after injection. In both naïve and IL-1β injected mice, contrast effects arising from VCAM-USPIO were no longer evident 80 h after injection (ie, *ca.* 5× blood half-life of VCAM-USPIO).

Discussion

In this study, we have demonstrated that the T_2*-weighted multi-gradient echo sequence provides the highest SNR and CNR for detection of targeted iron oxide particles in mouse brain. All sequences showed an improvement in both SNR and CNR on increasing field strength from 4.7 to 7.0 T, but

International Journal of Nanomedicine downloaded from https://www.dovepress.com/ by 192.76.8.80 on 27-Sep-2019
For personal use only.

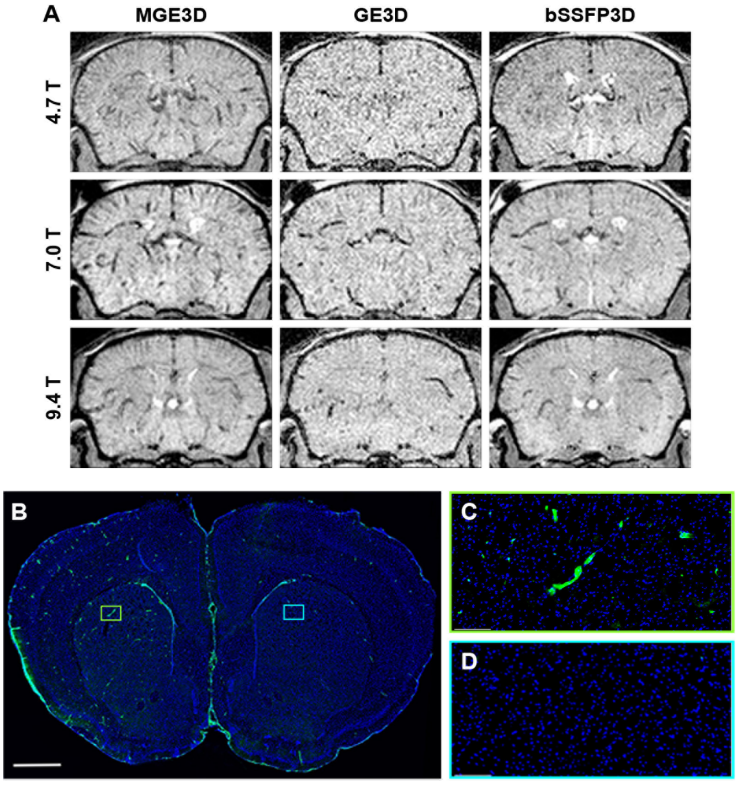


Figure 2 (**A**) Representative in vivo images of mice 13 h post-VCAM-USPIO injection at different magnetic fields. Three sequences of MGE3D, GE3D, and bSSFP3D are shown from a 3D dataset. Hypointensities were detected in both hemispheres of the brains. (**B**–**D**) Histological assessment of VCAM upregulation at the injection side.
Notes: Green vessels show unilateral upregulation of VCAM, nuclei are shown in blue. Scale bar: 1 mm.
Abbreviations: bSSFP3D, balanced steady-state free precession 3D; GE3D, gradient echo 3D; MGE3D, multi-gradient echo 3D; USPIO, ultra-small superparamagnetic iron oxide; VCAM, vascular cell adhesion molecule.

no further improvements in these parameters were observed on going to higher field. Finally, we have shown that while targeted MPIO enable selective and specific detection of target expression on the cerebral vasculature, the long half-life and lower relaxivity, and hence CNR, per particle of the targeted USPIO will likely render these particles impractical for most applications of molecular MRI targeting endovascular ligands.

Several different MRI approaches have been used previously for mouse neuroimaging of iron oxide contrast effects. As the transverse magnetization decays with T_2*, it distorts the gradient echo and, therefore, induces geometrical distortions.[62] Hence, conventional T_2*-weighted gradient echo (GE3D) is the most commonly used sequence for imaging of these particles.[36] This sequence uses a single echo sampled per line in k-space. In contrast, for T_2*-weighted multi-echo gradient echo (MGE3D), the recovery time is used to acquire additional echoes without increasing the total experimental time. Thus, a series of echoes at different TE are recorded for each line in k-space. This additional information can be used in a number of different ways, such as applying a SqrtSOS algorithm on the magnitude images from each echo to obtain MGE3D images.[63] The bSSFP3D sequence also has been used previously for tracking cells labeled with iron oxide particles and has shown advantages over conventional T_2- and T_2*-weighted sequences.[29,41,64]

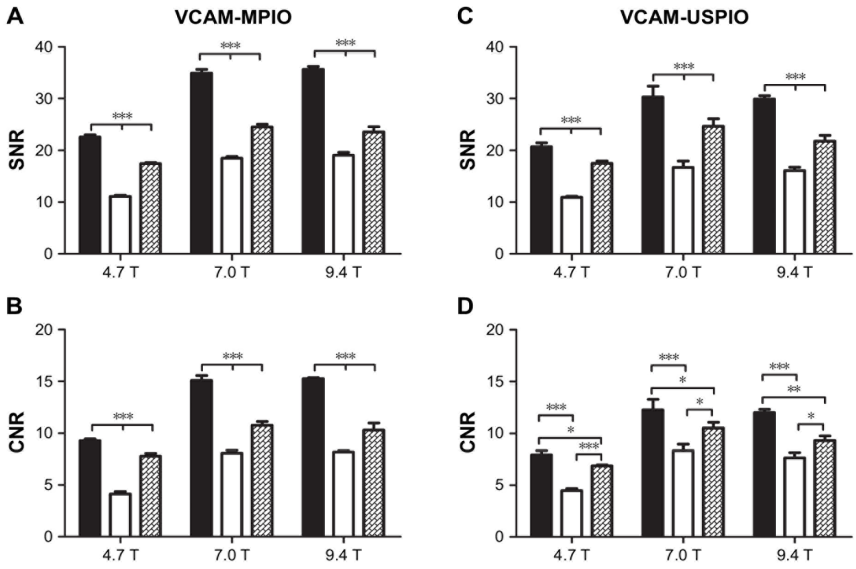


Figure 3 Quantitative comparison of MGE3D (■), GE3D (□), and bSSFP3D (▨) sequences for detection of MPIO and USPIO at different magnetic field strengths.
Note: MGE3D yielded significantly higher SNR (**A**, **C**) and CNR (**B**, **D**) compared with other sequences at all field strengths for both MPIO and USPIO detection (*$P<0.05$, **$P<0.01$, ***$P<0.001$).
Abbreviations: bSSFP3D, balanced steady-state free precession 3D; CNR, contrast-to-noise ratio; GE3D, gradient echo 3D; MGE3D, multi-gradient echo 3D; MPIO, microparticles of iron oxide; SNR, signal-to-noise ratio; USPIO, ultra-small superparamagnetic iron oxide; VCAM, vascular cell adhesion molecule.

However, this sequence is highly sensitive to local field inhomogeneities and the resulting "banding artifact" worsens at higher magnetic fields.[65,66]

The results of the current study suggest that by combining echoes in the MGE3D dataset, both SNR and CNR show significant improvements. Thus, MGE3D provides better depiction of both VCAM-MPIO and VCAM-USPIO contrast effects and greater overall image quality and sharpness compared to conventional GE3D and bSSFP3D. Consequently, quantitation of contrast effects will be improved significantly using the MGE3D sequence.

With regard to field strength, theoretically, an improvement in SNR would be anticipated with increasing field strength. However, many factors can limit the results observed in practice. In this study, improvements in both SNR and CNR were achieved for all sequences between 4.7 and 7.0/9.4 T, in accord with other rodent neuroimaging studies.[67,68] Although a significant improvement was observed between 4.7 and 7.0 T, no significant gain was obtained by increasing field strength further to 9.4 T in the current study. One possible reason for this lack of further SNR benefit is that magnetic susceptibility inherent in a mouse brain produce field-dependent perturbations in B_0 homogeneity, which result in degradation of SNR at 9.4 T. However, direct comparison of different magnetic field strengths suffers from several practical limitations.[67] For example, one consideration is the effect of different bore sizes. For the systems used in this study, the 9.4 T scanner had the smallest bore size (ID 160 mm), only allowing the use of a gradient coil with lower performance (gradient coil dimensions: OD 156 mm, ID 100 mm) than the 210 mm bore 7.0 T and 310 mm bore 4.7 T systems (gradient coil dimensions in both cases: OD 205 mm, ID 120 mm). Although it is not possible to generalize these results to all MRI scanners, given the vast array of different set-ups, our findings suggest that improved detection of iron oxide particles will be obtained by working at 7.0 T compared to lower field strengths. Beyond this field strength, the negative impact of field inhomogeneities and system constraints may counteract the benefits of higher field.

It has been shown that in response to disease, injury, and inflammation, VCAM-1 upregulates rapidly on activated

International Journal of Nanomedicine downloaded from https://www.dovepress.com/ by 192.76.8.80 on 27-Sep-2019
For personal use only.

International Journal of Nanomedicine downloaded from https://www.dovepress.com/ by 192.76.8.80 on 27-Sep-2019
For personal use only.

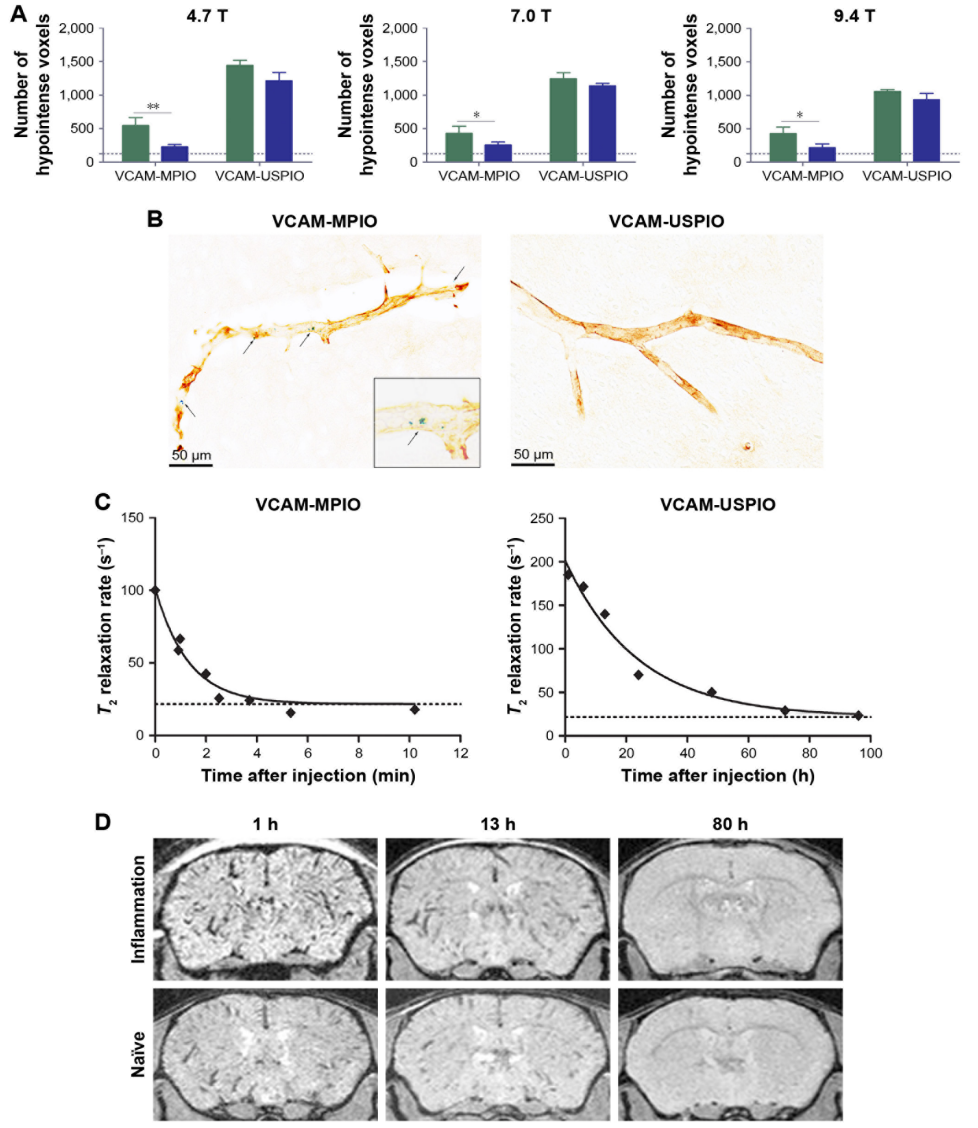


Figure 4 (**A**) Graph showing quantitation of MPIO- and USPIO-induced hypointensities in injected (green bar) and contralateral (blue bar) hemispheres using MGE3D sequence. Baseline level of endogenous hypointensities is shown with the dotted line. A significant difference was evident between the 2 hemispheres for VCAM-MPIO-injected mice at all field strengths. No significant difference was found for VCAM-USPIO. N=4 per group; *$P<0.05$, **$P<0.01$. (**B**) Histological staining for VCAM-1 (brown) and iron beads (Perls' Prussian blue) demonstrating upregulation of VCAM-1 on endothelial cells together with VCAM-MPIO binding (arrows). VCAM-USPIO was not detected in brain samples after perfusion, error bar=50 um (**C**) Graph showing the decay curve of the biological clearance of VCAM-MPIO and VCAM-USPIO, at a constant dose of 4 mg Fe/kg of body weight over time after injection. Graph shows T_2 relaxivity values of blood samples at different time points after administration. Curve is fitted as a single-phase exponential decay constrained to a plateau at the average naïve blood sample values (baseline; dotted lines). (**D**) MGE3D images of mice injected with VCAM-USPIO at different time-points acquired at 7.0 T – images show the presence of VCAM-USPIO in an inflammation model (top row) and naïve mouse (bottom row) at 1 and 13 h after contrast agent administration. No signal was detected 80 h after injection in both cohorts.

Abbreviations: MGE3D, multi-gradient echo 3D; MPIO, microparticles of iron oxide; USPIO, ultra-small superparamagnetic iron oxide; VCAM, vascular cell adhesion molecule.

International Journal of Nanomedicine downloaded from https://www.dovepress.com/ by 192.76.8.80 on 27-Sep-2019
For personal use only.

endothelial cells of the brain.[69] VCAM-1-targeted MPIO have been widely studied by a number of groups for detection of VCAM-1 in preclinical models of disease and have shown high sensitivity and specificity for detecting this biomarker in vivo.[25,33–35,37,70–73] As a simple model for inducing endothelial activation, we have previously demonstrated that a focal unilateral injection of IL-1β causes unilateral hemispheric upregulation of adhesion molecules on the endovascular surface, including VCAM-1.[25,70] We, therefore, used this model to determine the relative sensitivity and specificity of VCAM-MPIO and VCAM-USPIO for detection of target expression in vivo and found dramatically different results. For VCAM-MPIO, a combination of high valency targeted delivery of a high payload of iron oxide to sites of inflammation, and rapid clearance of MPIO from the blood conferred a high degree of specificity and sensitivity for target detection, as reported previously.[25,30,33,39] These properties are crucial in detecting biomarkers such as VCAM-1, that have relatively low abundance on endothelial cells[74] and may only be detectable using particles with higher contrast owing to their greater iron payload.

In contrast to VCAM-MPIO, no target-specific binding was detected by either MRI or histology (using Perls' Prussian blue staining) in mice injected with VCAM-USPIO. Moreover, our data show that VCAM-USPIO were still present in the blood circulation 13 h post-administration, in both naïve and IL-1β injected mice. As a consequence of this long circulation time, marked background contrast effects were evident, which preclude detection of target-specific binding in the injected hemisphere. This is not to say that target-specific binding is entirely absent in the case of VCAM-USPIO, but rather that it is undetectable owing to the continuing presence of circulating agent and the low relaxivity, and hence CNR, of the particles that are bound. Although, theoretically, it may be possible to identify an imaging window at which point all circulating USPIO have been eliminated, it is unlikely that specific binding will still be present and detectable at that time point. Moreover, the necessity for a long time window between contrast administration and imaging would also be less favorable for downstream clinical use, than an agent that allowed administration and rapid imaging within a short timeframe thereafter. In practice, we were unable to detect any VCAM-USPIO binding on the activated endothelium 13 h after injection histologically, and no specific VCAM-USPIO contrast effects were visible by MRI at 80 h after injection when the blood pool has cleared.

These findings demonstrate empirically that MPIO provide significant benefits for molecularly targeted MRI in brain and exhibit higher sensitivity than USPIO. While for USPIO many effective applications have been reported, the small size of these particles is likely to be limiting for their application in molecular MRI studies, particularly of endovascular targets. One of the drawbacks of MPIO that is often discussed, is their limited translational capacity to the clinic. However, with the new generation of degradable biocompatible particles,[30] this platform now has realizable translational potential.

Conclusion

The overall goal of this work was to identify the optimal pulse sequence, field strength, and particle size for molecular MRI in mice. Our results demonstrate clear advantages of the MGE3D sequence over bSSFP3D and GE3D for detection of iron oxide particles in vivo. Further, the specificity and sensitivity of VCAM-MPIO, compared with VCAM-USPIO, for delineation of activated endothelium in a mouse model of acute inflammation has been shown. With advances in the generation of biodegradable micrometer-sized iron oxide particles, these agents look promising for clinical translation in a broad range of central nervous system diseases, including inflammation and cancer.

Acknowledgments

This work was funded by Cancer Research UK (grant number C5255/A15935 to NRS). The authors would like to thank Karla Miller, Paul Kinchesh, Sean Smart, and Emeline Ribot for assistance in MRI sequence development. NZ was funded by a studentship from the CRUK & EPSRC Cancer Imaging Centre, in Oxford, UK (grant number C5255/A16466), and a Radcliffe Scholarship from University College, Oxford, UK.

Author contributions

NZ and NRS proposed and designed the study. NZ performed the experiments and data analysis. AAK developed sequences and image post-processing algorithms. FP-B developed and guided the generation of conjugates. LB assisted with physiochemical properties of conjugates. JRL assisted with blood half-life measurements. MSS assisted with the animal model. NRS supervised assembly of manuscript and NZ wrote the manuscript. All authors contributed to drafting and editing the manuscript and agreed to be accountable for all aspects of the work. All authors contributed toward data analysis, drafting and revising the paper and agree to be accountable for all aspects of the work.

Disclosure

The authors report no conflicts of interest in this work.

International Journal of Nanomedicine downloaded from https://www.dovepress.com/ by 192.76.8.80 on 27-Sep-2019
For personal use only.

References

1. Bulte JW, Kraitchman DL. Iron oxide MR contrast agents for molecular and cellular imaging. *NMR Biomed*. 2004;17(7):484–499.
2. Korchinski DJ, Taha M, Yang R, Nathoo N, Dunn JF. Iron oxide as an MRI contrast agent for cell tracking. *Magn Reson Insights*. 2015; 8(Suppl 1):15–29.
3. Dodd SJ, Williams M, Suhan JP, Williams DS, Koretsky AP, Ho C. Detection of single mammalian cells by high-resolution magnetic resonance imaging. *Biophys J*. 1999;76(1 Pt 1):103–109.
4. Gupta AK, Gupta M. Synthesis and surface engineering of iron oxide nanoparticles for biomedical applications. *Biomaterials*. 2005;26(18): 3995–4021.
5. Stoll G, Bendszus M. New approaches to neuroimaging of central nervous system inflammation. *Curr Opin Neurol*. 2010;23(3):282–286.
6. Shapiro EM, Skrtic S, Sharer K, Hill JM, Dunbar CE, Koretsky AP. MRI detection of single particles for cellular imaging. *Proc Natl Acad Sci U S A*. 2004;101(30):10901–10906.
7. Weissleder R, Bogdanov A, Neuwelt EA, Papisov M. Long-circulating iron oxides for MR imaging. *Adv Drug Deliv Rev*. 1995;16(2–3): 321–334.
8. Deckers F, Corthouts B, Nackaerts Y, Ozsarlak O, Parizel PM, De Schepper AM. Original article the influence of MR field strength on the detection of focal liver lesions with superparamagnetic iron oxide. *Eur Radiol*. 1997;7(6):887–892.
9. Farrar CT, Dai G, Novikov M, et al. Impact of field strength and iron oxide nanoparticle concentration on the linearity and diagnostic accuracy of off-resonance imaging. *NMR Biomed*. 2009;21(5):453–463.
10. Tanimoto A, Kuribayashi S. Application of superparamagnetic iron oxide to imaging of hepatocellular carcinoma. *Eur J Radiol*. 2006; 58(2):200–216.
11. Girard OM, Du J, Agemy L, et al. Optimization of iron oxide nanoparticle detection using ultrashort echo time pulse sequences: comparison of T1, T2*, and synergistic T1–T2* contrast mechanisms. *Magn Reson Med*. 2011;65(6):1649–1660.
12. Kim SH, Oh SN, Choi HS, et al. USPIO enhanced lymph node MRI using 3D multi-echo GRE in a rabbit model. *Contrast Media Mol Imaging*. 2016;11(6):544–549.
13. Zheng L, Zhang Z, Khazaie K, et al. MRI-monitored intra-tumoral injection of iron-oxide labeled Clostridium novyi-NT anaerobes in pancreatic carcinoma mouse model. *PLoS One*. 2014;9(12):e116204.
14. Wei H, Bruns OT, Kaul MG, et al. Exceedingly small iron oxide nanoparticles as positive MRI contrast agents. *Proc Natl Acad Sci U S A*. 2017; 114(9):2325–2330.
15. Modo MMJ, Bulte JWM. *Molecular and Cellular MR Imaging*. Boca Raton: CRC Press; 2007;4(3):458.
16. Christen T, Pannetier NA, Ni W, et al. MR vascular fingerprinting: a new approach to compute cerebral blood volume, mean vessel radius, and oxygenation maps in the human brain. *Neuroimage*. 2014;89:262–270.
17. Qui D, Zaharchul G, Christen T, Ni WW, Moseley ME. Contrast-Enhanced Functional Blood Volume Imaging (CE-fBVI): enhanced sensitivity for brain activation in humans using the ultrasmall superparamagnetic iron oxide agent ferumoxytol. *Neuroimage*. 2012;62(3): 1726–1731.
18. Neuwelt EA, Várallyay P, Bagó AG, Muldoon LL, Nesbit G, Nixon R. Imaging of iron oxide nanoparticles by MR and light microscopy in patients with malignant brain tumours. *Neuropathol Appl Neurobiol*. 2004;30(5):456–471.
19. Neuwelt EA, Hamilton BE, Varallyay CG, et al. Ultrasmall superparamagnetic iron oxides (USPIOs): a future alternative magnetic resonance (MR) contrast agent for patients at risk for nephrogenic systemic fibrosis (NSF)? *Kidney Int*. 2009;75(5):465–474.
20. Weinstein JS, Varallyay CG, Dosa E, et al. Superparamagnetic iron oxide nanoparticles: diagnostic magnetic resonance imaging and potential therapeutic applications in neurooncology and central nervous system inflammatory pathologies, a review. *J Cereb Blood Flow Metab*. 2010; 30(1):15–35.
21. Wang YX. Superparamagnetic iron oxide based MRI contrast agents: current status of clinical application. *Quant Imaging Med Surg*. 2011; 1(1):35–40.
22. Motomura K, Ishitobi M, Komoike Y, et al. SPIO-enhanced magnetic resonance imaging for the detection of metastases in sentinel nodes localized by computed tomography lymphography in patients with breast cancer. *Ann Surg Oncol*. 2011;18(12):3422–3429.
23. Pouw JJ, Grootendorst MR, Bezooijen R, et al. Pre-operative sentinel lymph node localization in breast cancer with superparamagnetic iron oxide MRI: the SentiMAG multicentre trial imaging subprotocol. *Br J Radiol*. 2015;88(1056):20150634.
24. Shapiro EM, Skrtic S, Koretsky AP. Sizing it up: cellular MRI using micron-sized iron oxide particles. *Magn Reson Med*. 2005;53(2): 329–338.
25. McAteer MA, Sibson NR, von Mühlen C. In vivo magnetic resonance imaging of acute brain inflammation using microparticles of iron oxide. *Nat Med*. 2007;13(10):1253–1258.
26. Chaumeil MM, Gini B, Yang H, et al. Longitudinal evaluation of MPIO-labeled stem cell biodistribution in glioblastoma using high resolution and contrast-enhanced MR imaging at 14.1 tesla. *Neuro Oncol*. 2012;14(8):1050–1061.
27. Serres S, Mardiguian S, Campbell SJ. VCAM-1-targeted magnetic resonance imaging reveals subclinical disease in a mouse model of multiple sclerosis. *FASEB J*. 2011;25(12):4415–4422.
28. Murrell DH, Zarghami N, Jensen MD, et al. MRI surveillance of cancer cell fate in a brain metastasis model after early radiotherapy. *Magn Reson Med*. 2017;78(4):1506–1512.
29. Murrell DH, Zarghami N, Jensen MD, Chambers AF, Wong E, Foster PJ. Evaluating changes to blood-brain barrier integrity in brain metastasis over time and after radiation treatment. *Transl Oncol*. 2016;9(3): 219–227.
30. Perez-Balderas F, van Kasteren SI, Aljabali AA, et al. Covalent assembly of nanoparticles as a peptidase-degradable platform for molecular MRI. *Nat Commun*. 2017;8:14254.
31. Ahmed N, Ahmad NM, Fessi H, Elaissari A. In vitro MRI of biodegradable hybrid (iron oxide/polycaprolactone) magnetic nanoparticles prepared via modified double emulsion evaporation mechanism. *Colloids Surf B Biointerfaces*. 2015;130:264–271.
32. Ahmed N, Jaafar-Maalej C, Eissa MM, Fessi H, Elaissari A. New oil-in-water magnetic emulsion as contrast agent for in vivo magnetic resonance imaging (MRI). *J Biomed Nanotechnol*. 2013;9(9): 1579–1585.
33. Serres S, Soto MS, Hamilton A, et al. Molecular MRI enables early and sensitive detection of brain metastases. *Proc Natl Acad Sci U S A*. 2012; 109(17):6674–6679.
34. Hoyte LC, Brooks KJ, Nagel S, et al. Molecular magnetic resonance imaging of acute vascular cell adhesion molecule-1 expression in a mouse model of cerebral ischemia. *J Cereb Blood Flow Metab*. 2010; 30(6):1178–1187.
35. Evans MC, Serres S, Khrapitchev AA, et al. T_2-weighted MRI detects presymptomatic pathology in the SOD1 mouse model of ALS. *J Cereb Blood Flow Metab*. 2014;34(5):785–793.
36. Gauberti M, Montagne A, Marcos-Contreras OA, Le Béhot A, Maubert E, Vivien D. Ultra-sensitive molecular MRI of vascular cell adhesion molecule-1 reveals a dynamic inflammatory penumbra after strokes. *Stroke*. 2013;44(7):1988–1996.
37. Montagne A, Gauberti M, Macrez R, et al. Ultra-sensitive molecular MRI of cerebrovascular cell activation enables early detection of chronic central nervous system disorders. *Neuroimage*. 2012;63(2): 760–770.
38. Yang Y, Yang Y, Yanasak N, Schumacher A, Hu TC. Temporal and noninvasive monitoring of inflammatory-cell infiltration to myocardial infarction sites using micrometer-sized iron oxide particles. *Magn Reson Med*. 2010;63(1):33–40.
39. Gauberti M, Montagne A, Quenault A, Vivien D. Molecular magnetic resonance imaging of brain-immune interactions. *Front Cell Neurosci*. 2014;8:389.

International Journal of Nanomedicine downloaded from https://www.dovepress.com/ by 192.76.8.80 on 27-Sep-2019
For personal use only.

40. McAteer MA, Mankia K, Ruparelia N, et al. A leukocyte-mimetic magnetic resonance imaging contrast agent homes rapidly to activated endothelium and tracks with atherosclerotic lesion macrophage content. *Arterioscler Thromb Vasc Biol*. 2012;32(6):1427–1435.
41. Heyn C, Bowen CV, Rutt BK, Foster PJ. Detection threshold of single SPIO-labeled cells with FIESTA. *Magn Reson Med*. 2005;53(2):312–320.
42. Shapiro EM, Koretsky AP. Micron-sized iron oxide particles (MPIOs) for cellular imaging: more bang for the buck. *Nanoparticles Biomed Imaging*. Fundamental Biomedical Technologies, Springer. 2008;102:141–161.
43. Tassa C, Duffner JL, Lewis TA, et al. Binding affinity and kinetic analysis of targeted small molecule-modified. 2010;21(1):14–19.
44. Liu L, Hitchens TK, Ye Q, et al. Decreased reticuloendothelial system clearance and increased blood half-life and immune cell labeling for nano- and micron-sized superparamagnetic iron-oxide particles upon pre-treatment with Intralipid. *Biochim Biophys Acta*. 2013;1830(6):3447–3453.
45. Mabray MC, Lillaney P, Sze CH, et al. In vitro capture of small ferrous particles with a magnetic filtration device designed for intravascular use with intraarterial chemotherapy: proof-of-concept Study. *J Vasc Interv Radiol*. 2016;27(3):426–432.
46. Bayburtskiy F, Semenova G, Brusentsov N, et al. Studying of a Magnetic Resonance in Contrasting Agents on the Basis of Biodecomposed Magnetic Fluid. *Oxidation Communications*. 2007;30(2):466–471.
47. Shen T, Weissleder R, Papisov M, Bogdanov A Jr, Brady TJ. Monocrystalline iron oxide nanocompounds (MION): physicochemical properties. *Magn Reson Med*. 1993;29(5):599–604.
48. Pittet MJ, Swirski FK, Reynolds F, Josephson L, Weissleder R. Labeling of immune cells for in vivo imaging using magnetofluorescent nanoparticles. *Nat Protoc*. 2006;1(1):73–79.
49. Bisschops MAT, Luyben KCAM, Van Der Wielen LAM. Generalized Maxwell–Stefan approach for swelling kinetics of dextran gels. *Ind Eng Chem Res*. 1998;37(8):3312–3322.
50. Wunderbaldinger P, Josephson L, Weissleder R. Tat peptide directs enhanced clearance and hepatic permeability of magnetic nanoparticles. *Bioconjug Chem*. 2002;13(2):264–268.
51. Kelly KA, Allport JR, Tsourkas A, Shinde-Patil VR, Josephson L, Weissleder R. Detection of vascular adhesion molecule-1 expression using a novel multimodal nanoparticle. *Circ Res*. 2005;96(3):327–336.
52. Kim SH, Choi D, Lim JH, et al. Optimal pulse sequence for ferumoxides-enhanced MR imaging used in the detection of hepatocellular carcinoma: a comparative study using seven pulse sequences. *Korean J Radiol*. 2002;3(2):87–97.
53. Schieda N, Avruch L, Shabana WM, Malone SC. Multi-echo gradient recalled echo imaging of the pelvis for improved depiction of brachytherapy seeds and fiducial markers facilitating radiotherapy planning and treatment of prostatic carcinoma. *J Magn Reson Imaging*. 2015;41(3):715–720.
54. Martin N, Malfair D, Zhao Y, et al. Comparison of MERGE and axial T2-weighted fast spin-echo sequences for detection of multiple sclerosis lesions in the cervical spinal cord. *AJR Am J Roentgenol*. 2012;199(1):157–162.
55. Melemenidis S, Jefferson A, Ruparelia N, et al. Molecular magnetic resonance imaging of angiogenesis in vivo using polyvalent cyclic RGD-iron oxide microparticle conjugates. *Theranostics*. 2015;5(5):515–529.
56. Bangerter NK, Hargreaves BA, Vasanawala SS, Pauly JM, Gold GE, Nishimura DG. Analysis of multiple-acquisition SSFP. *Magn Reson Med*. 2004;51(5):1038–1047.
57. Ribot EJ, Wecker D, Trotier AJ, et al. Water selective imaging and bSSFP banding artifact correction in humans and small animals at 3T and 7T, respectively. *PLoS One*. 2015;10(10):e0139249.
58. Chen S, Reynolds F, Yu L, Weissleder R, Josephson L. A screening paradigm for the design of improved polymer-coated superparamagnetic iron oxide nanoparticles. *J Mater Chem*. 2009;19(35):6387.
59. Delangre S, Vuong QL, Henrard D, Po C, Gallez B, Gossuin Y. Bottom-up study of the MRI positive contrast created by the Off-Resonance saturation sequence. *J Magn Reson*. 2015;254:98–109.
60. Reimer P, Balzer T. Ferucarbotran (Resovist): a new clinically approved RES-specific contrast agent for contrast-enhanced MRI of the liver: properties, clinical development, and applications. *Eur Radiol*. 2003;13(6):1266–1276.
61. Klohs J, Deistung A, Ielacqua GD, et al. Quantitative assessment of microvasculopathy in arcAβ mice with USPIO-enhanced gradient echo MRI. *J Cereb Blood Flow Metab*. 2016;36(9):1614–1624.
62. van der Kouwe AJW, Benner T, Salat DH, Fischl B. Brain morphometry with multiecho MPRAGE. *Neuroimage*. 2008;40(2):559–569.
63. Choi JS, Kim MJ, Kim JH, et al. Comparison of multi-echo and single-echo gradient-recalled echo sequences for SPIO-enhanced liver MRI at 3 T. *Clin Radiol*. 2010;65(11):916–923.
64. Mallett CL, Foster PJ. Optimization of the balanced steady state free precession (bSSFP) pulse sequence for magnetic resonance imaging of the mouse prostate at 3T. *PLoS One*. 2011;6(4):e18361.
65. Scheffler K, Lehnhardt S. Principles and applications of balanced SSFP techniques. *Eur Radiol*. 2003;13(11):2409–2418.
66. Huang SY, Seethamraju RT, Patel P, Hahn PF, Kirsch JE, Guimaraes AR. Body MR Imaging: Artifacts, k-Space, and Solutions. *RadioGraphics*. 2015;35(5):1439–1460.
67. DiFrancesco MW, Rasmussen JM, Yuan W, et al. Comparison of SNR and CNR for in vivo mouse brain imaging at 3 and 7 T using well matched scanner configurations. *Med Phys*. 2008;35(9):3972–3978.
68. Biswas J, Nelson CB, Runge VM, et al. Brain tumor enhancement in magnetic resonance imaging: comparison of signal-to-noise ratio (SNR) and contrast-to-noise ratio (CNR) at 1.5 versus 3 tesla. *Invest Radiol*. 2005;40(12):792–797.
69. Ley K, Laudanna C, Cybulsky MI, Nourshargh S. Getting to the site of inflammation: the leukocyte adhesion cascade updated. *Nat Rev Immunol*. 2007;7(9):678–689.
70. Sibson NR, Blamire AM, Bernades-Silva M, et al. MRI detection of early endothelial activation in brain inflammation. *Magn Reson Med*. 2004;51(2):248–252.
71. Serres S, Mardiguian S, Campbell SJ, et al. VCAM-1-targeted magnetic resonance imaging reveals subclinical disease in a mouse model of multiple sclerosis. *FASEB J*. 2011;25(12):4415–4422.
72. Mardiguian S, Serres S, Ladds E, et al. Anti-IL-17A treatment reduces clinical score and VCAM-1 expression detected by in vivo magnetic resonance imaging in chronic relapsing EAE ABH mice. *Am J Pathol*. 2013;182(6):2071–2081.
73. Akhtar AM, Schneider JE, Chapman SJ, et al. In vivo quantification of VCAM-1 expression in renal ischemia reperfusion injury using non-invasive magnetic resonance molecular imaging. *PLoS One*. 2010;5(9):e12800.
74. Jefferson A, Wijesurendra RS, McAteer MA, et al. Molecular imaging with optical coherence tomography using ligand-conjugated microparticles that detect activated endothelial cells: rational design through target quantification. *Atherosclerosis*. 2011;219(2):579–587.